Performance and Micro-Vibrations in Magnetic Bearings for Space Actuators

Guzmán BORQUE GALLEGO

École
polytechnique
fédérale
de Lausanne

2021

En memoria de Eliseo,
Clemente, Sandra y Pablo…

Acknowledgements

Acknowledgements

more generally to all colleagues at LAI for the fun moments and discussions.

I would also like to express my sincere gratitude to ESA's René Seiler for his technical support, knowledge and motivation to pursue this work, and in general to all the Mechanisms Section for their warm welcoming and help during the 3-month stay at ESA/ESTEC and the following years.

Por último, pero no por ello menos importante, me gustaría agradecer el inmenso apoyo recibido por parte de mi familia, Marco, Elisa, Ruth y Lucía, y por parte de mis amigos, por haber soportado todos estos años de duro trabajo, mostrando la incondicionalidad de vuestro apoyo y amistad, por la cual no podría sentirme más afortunado.

Neuchâtel, February 11, 2021   Guzmán Borque Gallego

Abstract

The development of new space missions with novel high-performance and very sensitive payloads for Earth observation or scientific missions has imposed considerably tougher requirements in terms of the satellite's pointing accuracy and stability, and thus on the maximum allowed on-board micro-vibrations. The main sources of on-board disturbances are any moving or rotating parts in the satellite, such as cryocoolers, momentum or reaction wheels (RWs) and control moment gyroscopes (CMGs). These actuators generate narrow-band harmonic vibrations dependent on the actuator's speed, which are transmitted and amplified through the satellite's structure and reach the sensitive payload such as high-resolution cameras, mirror structures or telescopes.

A very promising alternative to overcome these limitations is the use of magnetic bearings (MBs), as identified by the European Space Agency (ESA), to levitate the rotor during operation, and thus allow a contact- and friction-less operation with virtually infinite life-time. Furthermore, due to the active control of the position of the rotor it is possible to actively suppress any other rotor vibrations such as exported forces due to rotor residual unbalance, creating a very-low disturbance actuator that can satisfy the needs of future high-performance space missions.

In the present dissertation, a study of the main aspects of magnetic bearings for space applications is undertaken, and more specifically of a promising magnetic bearing reaction wheel configuration: a fully active, Lorentz-type, self-bearing, slotless magnetic bearing and permanent magnet synchronous motor. The main goal of this thesis is to identify the key factors and characteristics of a magnetic bearing system, for its use in reaction wheels for attitude control of satellites, in terms of requirements and performance criteria, and undertake the required analysis and modifications in order to address such aspects.

As a result of requirements from in-orbit conditions and on-ground qualification and testing, the key features of magnetic bearings in reaction wheels are: generated micro-vibrations during operation, magnetic bearing and motor efficiency affecting power consumption and heat dissipation, and system complexity linked to the actuator's failure risk and cost.

Regarding micro-vibration generation it is necessary to study its sources, countermeasures and active suppression control techniques, to materialise the advantages of magnetic bear-

Abstract

ings and achieve very-low disturbances. Through the micro-vibration characterisation of the studied magnetic bearing system, the main sources of vibrations are identified and several countermeasures are undertaken: highly-symmetric bearing and motor windings reduce cross-couplings and asymmetries in the bearing and motor forces, and a multi-harmonic force rejection control technique is proposed and successfully implemented, achieving a reduction in the generated vibrations of at least one order of magnitude.

In order to limit in-orbit power consumption and guarantee on-ground testing, a high magnetic bearing and motor efficiency should be sough, minimising thermal and power consumption constraints. For this reason an accurate electromagnetic modelling of the studied slotless magnetic bearings and motor, combined with a general optimisation technique allowing the maximisation of the overall machine efficiency, and resulting in important reductions of power consumption during operation ranging from 30 % to 60 % and its associated losses.

Lastly, system complexity should be addressed for missions in which risk and cost are key drivers for technology selection. A simplification of the studied system is proposed by employing iron-less passive magnetic bearings which can reduce the number of actuators, sensors, power electronics and computational power, and its viability is verified through simulation.

The work and results presented in this dissertation show the great potential of employing magnetic bearings in reaction wheels for attitude control of satellites, due to their very low exported vibrations, through the removal contact between moving parts and the use of multi-harmonic force rejection control. Moreover, the proposed optimisation process for active magnetic bearings and motor shows the great margin of improvement in terms of efficiency that can facilitate the mitigation of thermal and power consumption concerns for space applications, and the addition of iron-less passive magnetic bearing can greatly simplify the overall system complexity and cost if needed.

Keywords: satellite attitude control, reaction wheel, magnetic bearing, micro-vibrations, vibration control, electromagnetic modelling, slotless windings, force and torque models, optimisation.

Résumé

Le développement de nouvelles missions spatiales avec de nouvelles charges utiles très performantes et très sensibles pour l'observation de la Terre ou les missions scientifiques a imposé des exigences considérablement plus strictes en termes de précision de pointage et de stabilité du satellite, et donc sur le niveau maximal autorisé de micro-vibrations. Les sources principales de perturbations à bord du satellite sont tous les actionneurs qui disposent des pièces mobiles ou rotatives, telles que les compresseurs dans des systèmes cryogéniques, les roues de réaction et les actionneurs gyroscopiques faisant partie du système de commande d'attitude et d'orbite (SCAO). Ces actionneurs génèrent des vibrations harmoniques dépendantes de la vitesse de l'actionneur, qui sont transmises et amplifiées par la structure du satellite et atteignent la charge utile, comme caméras de haute résolution, structures de miroirs ou les télescopes.

Une alternative très prometteuse pour éliminer ces limitations est l'utilisation de paliers magnétiques pour soutenir le rotor en levitation pendant le fonctionnement, et permettre ainsi un fonctionnement sans contact et sans friction avec une durée de vie pratiquement infinie. En outre, grâce au contrôle actif de la position du rotor, il est possible de supprimer activement toute autre vibration du rotor, comme les forces exportées dues au balourd résiduel du rotor, créant ainsi un actionneur à très faible perturbation qui peut satisfaire les besoins des futures missions spatiales à haute performance.

Dans cette thèse, une étude des principaux aspects techniques des paliers magnétiques pour les applications spatiales est entreprise, et plus particulièrement, d'une configuration prometteuse de roue de réaction à paliers magnétiques : un moteur synchrone à aimants permanents et à paliers magnétiques sans fente, entièrement actif et bassé sur les forces de Lorentz. L'objectif principal de cette thèse est d'identifier les facteurs et les caractéristiques clés d'un système à paliers magnétiques, pour son utilisation dans les roues de réaction pour le contrôle d'attitude des satellites, en termes d'exigences et de critères de performance, et d'entreprendre l'analyse et les modifications nécessaires afin de traiter ces aspects.

En raison des conditions et des exigences en orbite et sur Terre pour sa qualification, les principales caractéristiques des paliers magnétiques pour des roues de réaction sont les suivantes : les micro-vibrations générées pendant son fonctionnement, le rendement des paliers magnétiques et moteur affectant la consommation de puissance et la dissipation de chaleur,

Résumé

et la complexité du système liée au risque de malfonctionnement de l'actionneur et au coût.

En ce qui concerne la génération de micro-vibrations, il est nécessaire d'étudier ses sources, les contre-mesures et les techniques de régulation pour la suppression active des vibrations. Grâce à la caractérisation des micro-vibrations du système étudié à paliers magnétiques, les principales sources de vibrations sont identifiées et les contre-mesures suivants sont prises : les bobines symétriques des paliers et des moteurs réduisent les couplages et les asymétries dans les forces des paliers et des moteurs, et une nouvelle technique de régulation est proposée pour rejeter les forces harmoniques, permettant d'obtenir une réduction des vibrations générées d'au moins un ordre de grandeur.

Afin de limiter la consommation d'énergie en orbite et de garantir les essais au sol, une modélisation électromagnétique précise des paliers magnétiques et du moteur sans fente est faite, et combinée avec une technique d'optimisation générale permettant de maximiser le rendement global de la machine, des réductions de consommation de puissance de 30 à 60 % et donc d'augmentation du rendement, sont obtenues.

Pour conclure l'analyse, la complexité du système doit être prise en compte pour les missions dans lesquelles le risque et le coût sont les principaux facteurs de sélection des actionneurs. Une simplification du système étudié est proposée en utilisant des paliers magnétiques passifs sans fer qui peuvent réduire le nombre d'actionneurs, de capteurs, d'éléments dans l'électronique de puissance et la puissance de calcul. La viabilité d'une telle configuration est vérifiée par simulation.

Les travaux et les résultats présentés dans cette thèse montrent le grand potentiel des paliers magnétiques pour son utilisation dans les roues de réaction pour le contrôle d'attitude des satellites, grâce au très faible niveau de vibrations exportées. De plus, le processus d'optimisation proposé pour les paliers magnétiques actifs et le moteur montre la grande marge d'amélioration en termes de rendement permettant la reduction des problèmes thermiques et de consommation de puissance électrique pour les applications spatiales, et l'ajout de paliers magnétiques passifs sans fer peut grandement simplifier la complexité et le coût du système si nécessaire.

Mots-clés : contrôle d'attitude des satellites, roue de réaction, paliers magnétiques, micro-vibrations, contrôle des vibrations, modélisation électromagnétique, bobinage autoportant, modèles de force et de couple, optimisation de machines eéléctriques.

Contents

Contents

List of Figures

List of Figures

List of Tables

Notation

Symbols

a	Rotor shaft bow magnitude
A, B, C, D	Continuous-time state-space matrices
α, β	Polar angle at which rotor mass eccentricity and axis of inertia tilt occur
α_a, β_a	Polar angle at which linear and angular shaft bow occur
$A_\perp$	Winding phase perpendicular phase belt area
A_{wire}	Winding wire cross-sectional area
$B, \boldsymbol{B}$	Magnetic flux density magnitude and vector
B_M	Projection of external field over permanent magnet magnetisation vector
B_{rem}	Permanent magnet remanent flux density
c_c	Rate of convergence of generalised notch filter
$\check{c}_c$	Modified rate of convergence of generalised notch filter
χ	Rotor main axis of inertia tilt with respect to symmetry axis
χ_a	Rotor shaft bow angular misalignment
d^{ax}	Axial winding coils separation
δ	Virtual stiffness coefficient of generalised notch filter
d_F, d_T	Actuator force and torque disturbance
D_q	Rotordynamics model passive damping matrix
d_r, d_n	Rotating and non-rotating damping coefficients
$E(m_{jk})$	Complete elliptic integral of the second kind
ϵ	Rotor centre of mass eccentricity with respect to geometric centre
ϵ_w	Current space vector phase angle
$\boldsymbol{e}_v$	Unitary directing vector of winding parametrisation
$F, \boldsymbol{F}$	Force component and vector
$\boldsymbol{f}$	Rotordynamics model generalised force vector
$\boldsymbol{f}_a$	Generalised shaft bow force vector
$\boldsymbol{f}_b$	Active magnetic bearing generalised active force vector
$\boldsymbol{f}_g$	Generalised gravity force vector
$f_i(\cdot)$	Optimisation objective function
$\boldsymbol{f}_u$	Generalised unbalance force vector

Symbols

g	Earth's gravity
$g_{ij}(\cdot)$	Optimisation inequality constraints
G_q	Rotordynamics model gyroscopic matrix
$H, \boldsymbol{H}$	Magnetic field magnitude and vector
$h_{ij}(\cdot)$	Optimisation equality constraints
$H(\omega)$	Dynamic response of measurement test bench structure
H_q	Rotordynamics model circulatory matrix
i	Magnetic bearing or motor current
$\Im(\cdot)$	Imaginary part of complex magnitude
I_p, I_t	Rotor's polar and transverse moments of inertia
$\hat{i}_s$	Phase current amplitude
$J, \boldsymbol{J}$	Current density magnitude and vector in winding
$j = \sqrt{-1}$	Imaginary unit
k	Mechanical and electromagnetic stiffness
κ	Amplification force and torque factor due to reluctance forces
κ_F, κ_T	Actuator force and torque constants
K_B, K_M	Bearing and motor constants
$K(m_{jk})$	Complete elliptic integral of the first kind
K_p, K_i, K_d	Proportional, integral and derivative gain matrices of PID or LQG controller
K_q	Rotordynamics model passive stiffness matrix
K_{SF}	State feedback gain matrix
L	Loop transfer function matrix
λ, Λ	Single-component and matrix correcting factor for B-field with back iron
L_{pc}	Position control state estimator dynamic system
L_p, L_d	Proportional and derivative gain matrices of LQG observer
L_{ph}	Winding phase wire length
L_{pm}	Permanent magnet axial length
L_s	Hexagonal axial segment length
L_{SF}	State estimator gain matrix
l_s, l_b	Distance of position sensor and bearing to machine's centre
L_{st}	Stator back iron axial length
L_w	Winding active axial length
$M_0, \boldsymbol{M}_0$	Material magnetisation magnitude and vector
m	Rotor mass
m_{jk}, n_j	Elliptic integrals parameters
M_q	Rotordynamics model mass matrix
μ_0	Magnetic permeability in vacuum
μ_r	Relative permeability of material
m_w	Number of winding phases
N_f	Generalised notch filter dynamic system
n_h	Number of harmonics to be suppressed by generalised notch filter
n_q	Number of harmonics to be suppressed by generalised notch filter

N	Number of winding turns per phase
Ω	Rotor speed
P	Continuous-time plant (rotor)dynamic model
ϕ_c	Radial tilting of rotor in complex coordinates
Φ_M	Magnetic scalar potential
ϕ_s	Hexagonal and rhombus opening angle
$\phi_{x'}, \phi_{y'}, \phi_{z'}$	Rotor rigid body orientation
$\Pi(n_j, m_{jk})$	Complete elliptic integral of the third kind
P_{Joule}	Joule losses in winding
P_w	Active power consumption
p_w	Number of winding pole pairs
$\boldsymbol{q}$	Rotordynamics model generalised coordinate vector
Q_K, R_K, N_K	State, input and crossed weighting factor matrices for LQG controller
q_{Kp}, q_{Ki}, q_{Kd}	Proportional, integral and derivative state weighting factors for LQG controller
Q_L, R_L, N_L	State, input and crossed weighting factor matrices for LQG observer
q_{Lp}, q_{Li}, q_{Ld}	Proportional, integral and derivative state weighting factors for LQG observer
Q_w	Reactive power consumption
$r_1.r_2, r_3, r_4$	Radial dimensions of passive magnetic bearing
ρ, ϕ, α	Winding parametrisation variables
r_c	Radial displacement of rotor's centre of mass in complex coordinates
R_{cc}	Current control dynamic system
R	Combined position control and observer dynamic system
$\Re(\cdot)$	Real part of complex magnitude
r_F, r_T	Actuator force and torque ripple
ρ_{Cu}	Copper resistivity
R_{pc}	Position control dynamic system
R_{ph}	Winding phase resistance
R_{pm}	Permanent magnet radius
r, φ, z	Cylindrical coordinates
R_{st}	Stator back iron radius
R_w	Winding radius
S	Sensitivity transfer function matrix of closed-loop system
$|S_w|$	Apparent power consumption
$T, \boldsymbol{T}$	Torque component and vector
t	Instant t, moment in time
$\mathscr{T}$	Maxwell stress tensor
$T_N(\Omega)$	Speed-dependent complex gain matrix of conventional generalised notch filter
$T_J = \Im(T_N)$	Imaginary part of complex gain matrix of conventional generalised notch filter
$T_R = \Re(T_N)$	Real part of complex gain matrix of conventional generalised notch filter
T_s, f_s	Sampling period and frequency
$\boldsymbol{u}$	Dynamic system input vector
U_q	Magnetic bearing active force matrix

$v, \boldsymbol{v}$	Winding parametrisation component and vector
$V, \mathrm{d}V$	Total and infinitesimal winding volume
V_q	Unbalance magnitude matrix
V_q'	Shaft bow magnitude matrix
w_i	Optimisation objective function weight
W_q	Position sensor output matrix
$\boldsymbol{x}$	State-space state vector
$\hat{\boldsymbol{x}}$	State estimation vector
$\boldsymbol{x}_i$	Optimisation variables
$\boldsymbol{x}_{ref}$	Reference set-point for position controller
x, y, z	Cartesian coordinates
x_c, y_c, z_c	Rotor centre of mass position
$\boldsymbol{y}$	Position sensors measurement vector
$\check{\boldsymbol{y}}$	Filtered position sensors measurement vector
$z_1. z_2, z_3, z_4$	Axial dimensions of passive magnetic bearing
z_c	Axial displacement of rotor's centre of mass

Subscripts

11	Matrix element referred to radial displacement of rotordynamics model
$12, 13, 23$	Crossed matrix element referred of rotordynamics model
22	Matrix element referred to radial tilting of rotordynamics model
33	Matrix element referred to axial displacement of rotordynamics model
A, B, C	A, B, or C phase components of vector
d, q	Direct and quadrature components of vector
i, o	Lower and top integration limits
L	Matrix, vector or variable referred to state estimator
lor	Lorentz component of force or torque
N	Matrix, vector or variable referred to generalised notch filter
P	Matrix, vector or variable referred to plant dynamics
R	Matrix, vector or variable referred to controller
rel	Reluctance component of force or torque
r, φ, z	Cylindrical components of vector
x, y, z	Cartesian components of vector

Superscripts

ax	Parameter or variable referred to axial winding type
$\ddot{}$	Second time derivative of a magnitude
$\dot{}$	First time derivative of a magnitude

he	Parameter or variable referred to heteropolar side of the machine
ho	Parameter or variable referred to homopolar side of the machine
hx	Parameter or variable referred to hexagonal winding type
rh	Parameter or variable referred to rhombic winding type
sk	Parameter or variable referred to skewed winding type
˜	Discrete-time counterpart of matrix or dynamic system
+	Optimisation variable referred to manufactured configuration
∗	Optimisation variable referred to optimum configuration
o	Optimisation variable referred to original configuration

Abbreviations

2D	Two Dimensions
3D	Three Dimensions
AC	Alternating Current
ADCS	Attitude Determination and Control System
AFW	Astro- und Feinwerktechnik Adlershof GmbH
AMB	Active Magnetic Bearing
AOCS	Attitude and Orbit Control System
BBRW	Ball Bearing Reaction Wheel
BUAA	Beihang University
C2F	Current-to-Force
CEL	Celeroton AG
CMG	Control Moment Gyroscope
CSEM	Swiss Center for Electronics and Microtechnology
DC	Direct Current
DoF	Degree of Freedom
DSP	Digital Signal Processor
DYN	Dynamometer
EO	Earth Observation
EPFL	Swiss Federal Institute of Technology in Lausanne
ESA	European Space Agency
ETHZ	Swiss Federal Institute of Technology in Zurich
FEA	Finite Element Analysis
FEM	Finite Element Method
FFT	Fast Fourier Transform
FOC	Field-Oriented Control
FPGA	Field-Programmable Gate Array
GNC	Guidance, Navigation and Control
HMB	Hybrid Magnetic Bearing
HTS	High-Temperature Superconducting materials

Abbreviations

ISS	International Space Station
LHP	Left Half-Plane
LPV	Linear Parameter-Varying
LQE	Linear-Quadratic Estimator
LQG	Linear-Quadratic-Gaussian
LQR	Linear-Quadratic Regulator
MAGLEV	Magnetic Levitation
MB	Magnetic Bearing
MBRW	Magnetic Bearing Reaction Wheel
MELCO	Mitsubishi Electric Corporation
MIMO	Multiple-Input Multiple-Output
NAL	National Aerospace Laboratory in Japan
NASA	National Aeronautics and Space Administration
PCB	Printed-Circuit-Board
PD	Proportional-Derivative
PI	Proportional-Integral
PID	Proportional-Integral-Derivative
PM	Permanent Magnet
PMB	Passive Magnetic Bearing
PMSM	Permanent Magnet Synchronous Motor
PWM	Pulse-Width Modulation
RHP	Right Half-Plane
RMS	Root Mean Square
RW	Reaction Wheel
SISO	Single-Input Single-Output
SQP	Sequential Quadratic Programming
SSC	Surrey Space Centre
TFM	Transfer Function Matrix
UFRC	Unbalance Force Rejection Control
WDE	Wheel Drive Electronics

1 Introduction

The development of new space missions with novel high-performance and very sensitive payloads for Earth observation [1]–[3] or scientific missions [4]–[6] has imposed considerably tougher requirements in terms of the satellite's pointing accuracy and stability, and thus on the maximum allowed on-board micro-vibrations.

The main sources of on-board disturbances are any moving or rotating parts in the satellite, such as cryocoolers, momentum or reaction wheels (RWs) and control moment gyroscopes (CMGs). These actuators generate narrow-band harmonic vibrations dependent on the actuator's speed, which are transmitted and amplified through the satellite's structure and reach the sensitive payload like high-resolution cameras, mirror structures or telescopes. Missions with very strict requirements either mount these actuators over isolation platforms, as in the James Webb Space Telescope [6], or force the actuators vibrations to be outside the frequency range of interest during measurement by adjusting the rotor speed, as done in the SWOT mission [3], or force the actuators to be completely stopped during measurement phases, as in Euclid mission [5], or even not mounting any of these actuators to avoid moving parts, as in Gaia mission [4].

Long before the use of rotating machinery in space applications, the vibrations generated by these actuators have been an important field of study in engineering since the industrial revolution due to the importance of steam machines and turbines in the development of modern technology [7]–[9]. These vibrations generate mechanical disturbances that create stresses in the actuator's housing, rotor and environment that may result in a system failure, and thus they need to be minimised to guarantee a substantial life-time of the machine.

Extensive studies have been performed to analyse the main sources and propose counter-measures for these vibrations for both space [10], [11] and terrestrial applications [12], [13], being identified to be linked to rotor residual unbalance, bearing disturbances and motor noise [11]. Whereas rotor balancing can considerably reduce the magnitude of vibrations, allowing the operation of the machine for much longer time and at higher speeds, in practice it is impossible to achieve a perfectly balanced rotor [14] and thus some residual vibrations will

always be present. Furthermore, the use of conventional ball bearings will generate additional vibrations, in the form of higher harmonic narrow-band disturbances, resulting from ball bearing imperfections such as uneven bearing race and rolling element sizing. Also, the use of ball bearings impose strict requirements on the lubricant, specially for space applications, where temperature, vacuum and micro-gravity may significantly limit the expected life-time of the actuator.

A very promising alternative to overcome these limitations is the use of magnetic bearings (MBs) to support the rotor during operation, and thus allow a contact- and friction-less operation with virtually infinite life-time. Furthermore, due to the active control of the position of the rotor it is possible to actively suppress any other rotor vibrations such as exported forces due to rotor unbalance, creating a very-low disturbance actuator that can satisfy the needs of future high-performance space missions. Magnetic bearings are identified by the European Space Agency (ESA) as the most promising technology that will greatly enhance the characteristics of actuators such as reaction wheels [15].

While magnetic bearing reaction wheels (MBRWs) saw an initial interest and developments in the decade of 1980 and 1990, due to the broader extension of rare-earth magnets that greatly improved the efficiency of such machines, being successfully used in the French Earth observation SPOT [1], [2], HELIOS and ENVISAT missions [16], the limited computational power and high cost caused most developments to stop. The availability in recent years of high-performance and cost-effective embedded controllers, digital signal processors (DSPs) and even field-programmable gate arrays (FPGAs) with more than sufficient computational power, combined with novel motor and bearing control techniques [15], make magnetic bearings a competitive solution to enable novel agile and high-performance missions.

In this thesis a study of the main aspects of magnetic bearings for space applications is undertaken, and more specifically of a promising magnetic bearing reaction wheel configuration, focusing on micro-vibrations, machine efficiency, power consumption, and system complexity. In the following sections an overview of the available actuators employed in space applications is performed, and more specifically for attitude control of satellites, which can most profit from the advantages of MBs. Subsequently, the main scientific contributions and outline of the thesis are detailed.

1.1   Space Actuators for Attitude Control of Satellites

As described in [17], the attitude determination and control system (ADCS), is in charge of controlling the orientation (attitude) of a satellite, or in the case of a guidance, navigation and control, or attitude and orbit control system (GNC/AOCS), the orientation and linear velocity (attitude and orbit). Depending on the goals and requirements of the space mission, the attitude can be uncontrolled, simply passively stabilised by spin stabilisation or interaction with Earth's magnetic or gravitational fields, or actively controlled, usually three-axis stabilised, by a system of sensors, controller and actuators.

The main actuators employed for attitude control are:

- *Thrusters*: eject a propellant at a certain speed creating a reaction force on the satellite. Multiple thruster types exist such as chemical (hot or cold gas) or electric (ion) propulsion [18], [19]. Both linear and angular thrust can be achieved at the cost of consuming fuel.

- *Momentum wheels*: in momentum-biased satellites, a wheel with big inertia is kept at high and almost constant speed [10], usually with spin axis normal to the orbit plane, to provide gyroscopic stiffness to the satellite, in a similar way to spin stabilisation techniques.

- *Reaction wheels (RW)*: big inertial wheels similar to momentum wheels, but operated at varying speeds, applying reaction torques during acceleration or deceleration to the satellite to counteract disturbances [10]. Generally three or more RWs are employed, eventually requiring desaturation manoeuvres to avoid the saturation of the wheel and bring its speed back to zero using thrusters or magnetic torquers [17].

- *Control moment gyroscopes (CMG)*: a big inertial wheel rotating at high speeds and mounted over one- or two-axis gimbals, which apply torque to the satellite by changing the direction of the spin axis of the wheel and generating gyroscopic forces. The torque applied by CMGs is significantly higher than the one of RW, allowing for mass and power consumption reduction [20] and at least two units are required for three-axis stabilisation.

- *Magnetic torquers or magnetotorquers*: coils or permanent magnets that generate a magnetic dipole on the satellite and by interaction with external magnetic fields, such as Earth's field, they exert a moment to the satellite. Magnetotorquers are usually employed for reaction wheel desaturation and attitude control [21].

Due to fuel consumption in thrusters, low or limited torques in magnetotorquers, and complexity and big torques applied by CMGs, making them mainly employed in very large platforms such as the international space station (ISS), reaction/momentum wheels are the most common actuator type used for three-axis attitude control of satellites [17].

The main drawbacks of RWs are the relatively high power consumption and the micro-vibrations originated from the rotating body, mainly due to rotor unbalance, bearing disturbances, motor noise or structural resonances [10], which greatly affects the pointing stability that the satellite can achieve [22]. For this reason, in some missions with high sensitive payloads, such as ESA's Gaia space astrometric mission [4] where rotating and moving parts are strictly minimised, RWs are either directly avoided. Other options rely on mounting the RWs over some complex passive [6], [22] or active [23] isolation or damping platforms.

The main limitation in the level of vibrations and limited life-time of reaction wheels resides in the conventional ball bearings that are commonly employed. As mentioned before, the

rotating bodies in the bearings generate high-harmonic disturbances, require lubrication and extensive tribological studies, which limit its expected life-time in space due to temperature changes and wear [24]. As clearly stated by ESA in its AOCS Sensors and Actuators Harmonisation Dossier [15], the technology featured in reaction wheels has remained greatly unchanged in the last 20 years, and thus there is a clear need to develop novel state-of-the-art technologies to greatly overcome these limits in conventional designs.

Other alternative bearings exist to achieve contact-less, vibration-free rotation, such as gas/air bearings or magnetic bearings, which will be briefly described in the following section, including a comparison between these technologies. Magnetic bearings are identified by ESA in [15] as the most promising and ground-braking technology for RWs to achieve these high performance goals of vibrations and life-time, due to recent developments in electronics, materials and control theory, while keeping complexity and cost in reasonable levels. An overview and classification of the different types of magnetic bearings is shown in the next section to understand their basic principles and available options.

1.2 Magnetic Bearing Systems

As previously mentioned, several approaches can be followed to achieve a contact-less levitation of a rotor or body, and overcome the limitations imposed by conventional ball bearings. It is possible to generate the levitation forces through high-pressure fluids, as performed in gas or air bearings, or by electromagnetic interaction between static and moving parts, yielding magnetic bearings. Each of the bearing options, ball, gas and magnetic bearings have their respective advantages and disadvantages, as summarised in [25].

Gas bearings allow rotation with very-low friction and a passive stabilisation of the rotor (self-acting) and they are best suited in applications where the rotating machine already employs some gas, such as compressors or pumps [26], [27]. In self-acting machines the fluid pressure is generated by the rotation of the rotor inside a stator, both of which generally feature thin patterns of grooves to help the pressure increase, and thus it can only be operated above certain speeds, and the bearing properties like stiffness and damping greatly depend on the speed [28]. This is generally not an issue in applications where a more or less constant regime is employed, such as turbomachinery, but it considerably limits the use in cases where constant acceleration or deceleration of the rotor are required, such as reaction wheels. Other possibility is to conceive an externally pressurised bearing that will allow a stable levitation even at standstill, but at the expense of increasing the system complexity.

In any case, the use of pressurised fluids in space applications can be achieved but may not be the most appropriate choice due to vacuum in space. Magnetic levitation is perfectly compatible with these conditions as no matter is required to transmit electromagnetic fields. In this case the levitation can be achieved by a combination of permanent magnets or electromagnets in rotor and stator, yielding a friction- and contact-less operation. A great variety of configurations exists to achieve the magnetic levitation, and thus it is necessary to identify the
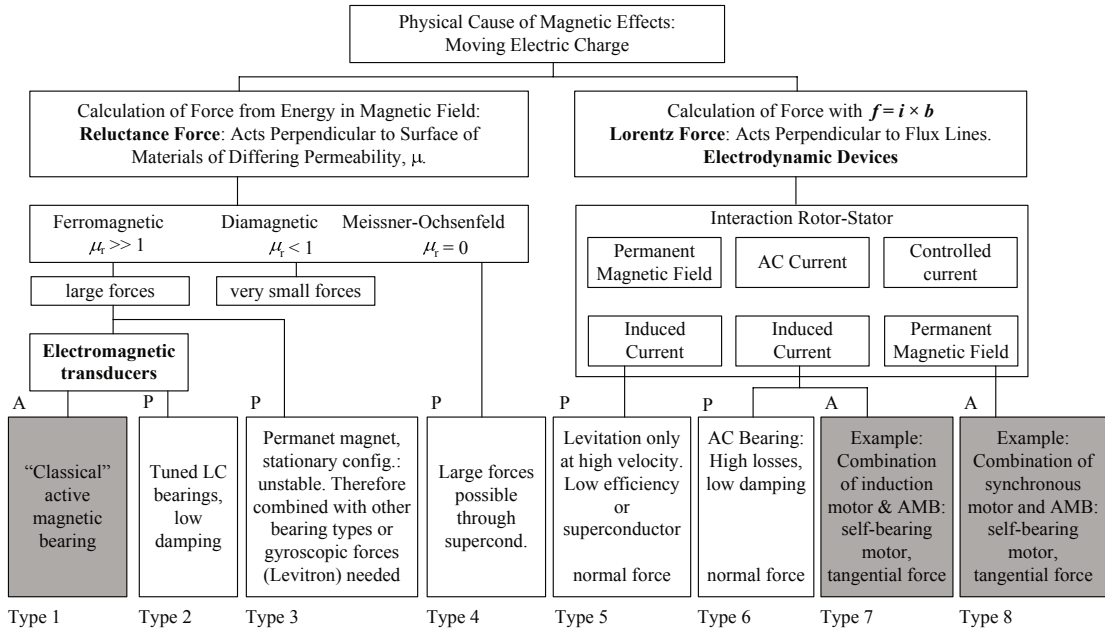
Figure 1.1 – Classification of main types of magnetic bearings according to its physical principle, based on reluctance or Lorentz forces, and identifying active (A) and passive(P) types (Source: [29], [30]).

most appropriate topologies for space applications.

Whereas multiple ways of classifying magnetic bearings (MBs) exist, such as by their need of active control or not for stabilisation, by application field or by number of degrees of freedom (DoF) it is able to control, the most useful classification was originally performed in [29] and later included in [30], which organises the multiple types of magnetic levitation systems according to their physical principle, as summarised in figure 1.1. All magnetic bearings can be classified in two main groups: *reluctance-force* or *Lorentz-force* types, depending on the origin of the levitation forces.

For the first group, the *reluctance forces* are the electromagnetic forces appearing at the interface of two materials, normal to the surface, with different relative permeability μ_r, such as iron and air, as a result of the minimisation of the energy contained in the magnetic field. Depending on the type of materials and configurations, reluctance-force magnetic bearings can be classified in:

- *Type 1*: active reluctance-force bearings, in which the strength of the magnetic field and forces are actively controlled by an electromagnet and both rotor and stator and composed of ferromagnetic ($\mu_r \gg 1$) materials. This corresponds to the most extended magnetic bearing type. Power consumption can be considerably reduced if permanent magnets are also included in the magnetic circuit, creating a constant bias flux over which the electromagnet actuates to stabilise the system, as identified in early developments of magnetic bearings for space applications [31].

5

- *Type 2*: a passive levitation system can be achieved by a simple tuned LCR circuit composed by the electromagnet with iron core ($\mu_r \gg 1$), bearing coil and a capacitor operated near resonance. This type is rarely used due to its intrinsic lack of damping and requiring other auxiliary system for consistent stability.

- *Type 3*: another passive levitation system can be obtained by a combination of permanent magnets ($\mu_r \approx 1$). Due to Earnshaw's theorem, only some DoF can be passively stabilised and they need to be combined with other active magnetic bearings for the unstable directions.

- *Type 4*: complete passive stabilisation can be achieved by superconductive materials ($\mu_r = 0$) as a result of the Meissner–Ochsenfeld effect. These superconductive magnetic bearings have seen an increasing interest in the last years as a result of recent high-temperature superconductive (HTS) materials, including in space applications [32]–[34], but with limited applicability due to the very low temperatures required.

For the second group, the *Lorentz forces* are the electromagnetic forces generated between the interaction of a moving charge in a magnetic field. As before, depending on the employed materials and arrangements, Lorentz-force bearings, also known as electrodynamic bearings, can be classified as follows:

- *Type 5*: passive levitation forces can occur in a conductor, in which electric currents are induced, moving at high speeds relative to a magnetic field generated by permanent magnets. This electrodynamic levitation has been studied in the frame of magnetically-levitated (MAGLEV) vehicles [35]–[37] and rotating machinery [38], [39]. This bearings are only stable above a certain threshold speed, and usually feature very low damping.

- *Type 6*: a passive levitation system can be achieved if a conductor is placed inside a magnetic field generated by an alternating current (AC), generating induced currents in the conductor and repelling forces. In general this bearing type, commonly known as AC bearing, features low forces and efficiency and poor damping behaviour [40].

- *Type 7*: an active magnetic levitation can be achieved in the same configuration as type 6 when the AC current is actively controlled, resulting in induction magnetic bearings. This configuration is equivalent to induction motors, and are both usually combined to create magnetic bearing inductions motors [41]. If both magnetic bearing and motor actuators are combined, sharing the same magnetic circuit, the machine is generally known as self-bearing motor.

- *Type 8*: another active magnetic levitation system is obtained if the magnetic flux density generated by permanent magnets located in the rotor or moving body are combined with an actively controlled current flowing through a conductor in the stator. This same principle is employed in permanent-magnet synchronous motors (PMSMs), and can be combined with this types of bearings to create a self-bearing motor [42].

When considering combined motor and magnetic bearing systems (self-bearing or bearingless) another possible classification of the magnetic bearing types is by considering the electrical type of actuator [43], similar to the classification of electric motors: induction, switched reluctance, synchronous reluctance, permanent magnet or homopolar. All these types of self-bearing motors can be classified as in figure 1.1, being switched reluctance, synchronous reluctance and homopolar of *type 1*, induction of *type 7*, and permanent magnet of *type 8*. In any case, the parallelisms between magnetic bearings and motors are clear, consisting both of electrical machines that generate forces or torques to the rotor by electromagnetic interactions. In self-bearing machines, the bearing and motor actuators are simply differentiated by the combination of number of poles of rotor and stator [30], [43].

Having identified the different types of magnetic bearings available, an overview of the past developments of magnetic bearing actuators for space applications, and more specifically in reaction wheels, will be undertaken in chapter 2, where the different advantages and drawbacks of each configuration will be identified in order to appropriately select the most promising one for the studied application.

In the following sections, the work undertaken in this thesis is presented, describing the general structure of the document and highlighting the main scientific contributions, also including the list of publications.

1.3 Outline of the Thesis

In the present dissertation, a study of the main aspects of magnetic bearings for space applications is undertaken, and more specifically of a promising magnetic bearing reaction wheel configuration. The main goal of this thesis is to identify the key factors and characteristics of a magnetic bearing system for its use in reaction wheels for attitude control of satellites in terms of requirements and performance criteria, and undertake the required analysis and modifications in order to address such aspects.

The presentation of the work developed throughout the present thesis is structured in a total of eight chapters that deal with the characterisation, modelling, optimisation, and control of magnetic bearing systems for space applications. The overall thesis structure can be summarised as follows:

- In *chapter 1*, an introduction to the work presented in this thesis is included, describing more in detail the context and main goals of the present investigations.

- A review of the past investigations linked to the present research is detailed in *chapter 2*. This chapter more specifically highlights the most important magnetic bearing actuators for space applications and their main limitations that justify the present work. Furthermore the chapter briefly describes the actuator in which this thesis is based on.

- In *chapter 3*, an overview of the main identified sources of micro-vibrations for magnetic

bearing systems can be found, from the sources themselves to the possible approaches to measure them. A novel micro-vibration measurement method for active magnetic bearing reaction wheels called current-to-force is detailed, also described in [44]. These sources are then included into a modular closed-loop simulation model, based upon the work presented in [45], which combines rotordynamics, bearing, sensor and control models to perform performance and stability analysis.

- In order to be able to quantify the efficiency of the machine and perform its design, the electromagnetic modelling of the studied slotless active magnetic bearings and motor is detailed in *chapter 4*. Due to the different combinations existing in the machine, a modular approach is employed, capable of calculating the electromagnetic forces and torques generated by different permanent magnet arrangements, with and without back iron, and different slotless winding types, as also described in [46] and [47]. Moreover, the electromagnetic model of iron-less passive magnetic bearings is also presented, making use of equivalent magnetic flux density models employed for the active bearings, as also detailed in [48].

- Having defined the electromagnetic models of both active and passive magnetic bearings required for machine design, in *chapter 5*, an optimisation procedure is proposed for both fully active and hybrid magnetic bearing systems. For the former, a global efficiency optimisation is undertaken to minimise the machine losses in all actuators while also reducing bearing-dependent disturbances by appropriate winding selection, as also described in [49], and for the latter, a design procedure that guarantees the stability and quantifies the expected performance of the closed-loop system is executed.

- In *chapter 6*, a multi-harmonic force rejection control technique is presented and analysed. The general structure of the technique is introduced and its stability is studied for general control systems and more specifically for magnetic bearing systems, enabling a substantial reduction of vibrations generated by the machine during operation, as also shown in [50].

- All experimental measurements and validation of models, measurement methods and control techniques are included in *chapter 7*. All employed test equipments are first detailed, followed by the validation of all models presented in previous chapters, concluding with the micro-vibration characterisation of the studied fully active magnetic bearing system and the quantification of the impact of the implemented improvements and modifications.

- Finally, in *chapter 8*, a summary of all the work presented in this thesis is included, and an overview of the identified future work that would be of great interest to continue the research undertaken in the frame of the thesis.

1.4 Contributions of the Thesis

The main scientific contributions of the work undertaken in the frame of the present thesis are the following:

- A novel micro-vibration measurement method for active magnetic bearings is proposed and validated. The proposed current-to-force method is based on the measurement of the forces directly applied by the active magnetic bearing currents. As such measurements are already available for control purposes, the measured vibrations and forces are directly obtained in real-time, allowing its use for monitoring purposes of control parameter adaptation for optimal performance. The current-to-force method is successfully validated by comparison to a reference multi-component dynamometer commonly employed for micro-vibration characterisation and qualification of space equipment.

- The main sources of micro-vibrations for magnetic bearing actuators are identified and detailed. Due to the particularities of magnetic bearing systems, when compared to conventional and very well studied actuators with ball bearings, disturbances of different nature need to be analysed and accounted for to characterise their sources of micro-vibrations. These sources can be as diverse as rotor unbalance, sensor noise, winding and permanent magnet imperfections and asymmetries, high-frequency inverter noise in power electronics, computation delays or fixed-point rounding errors in controller implementation.

- A modular closed-loop simulation model for active and passive magnetic bearing capable of studying stability and general behaviour of rotating systems. The model combines multiple options of rotordynamics, bearing, sensing and control models with different possible levels of complexity or simplification to analyse the impact of specific factors in the closed-loop system. Frequency and time-based analysis tools are available to determine stability, micro-vibration or general performance of a given system.

- An accurate and computationally efficient electromagnetic model for slotless active magnetic bearings and motors is proposed and validated. The model employs elliptic integrals to define the three-dimensional magnetic flux density distribution in the machine's airgap for several possible combinations of permanent magnet arrangements with and without back iron, and combined with a selection of slotless winding types, like skewed, rhombic, hexagonal and axial, it is capable of accurately calculate the force and torque applied by the actuator.

- A general efficiency optimisation procedure for active magnetic bearing motors is detailed, allowing the simultaneous consideration of multiple actuators for global optimisation of magnetic bearing machines. This optimisation technique enables the possibility of selecting the appropriate permanent magnet, winding and back iron dimensions and parameters by means of a global constrained multi-objective optimisation that seeks

the maximisation of the machine overall efficiency, defined by the linear combination of motor and bearing constants, i.e. ratio between applied force/torque and Joule losses.

- A multi-harmonic force rejection control technique for unbalance and other synchronous vibration suppression in magnetic bearing systems. The proposed generalised notch filter features improved stability properties enabling easier design of multi-harmonic suppression when compared to conventional techniques, which usually require gain-scheduling internal parameters to maintain stability. This technique is successfully implemented on the studied magnetic bearing system for the first three harmonics achieving at least one order of magnitude reduction in vibrations.

- An electromagnetic model for ironless passive magnetic bearings is developed and validated. The model is based on the formulation of the magnetic flux density distribution of permanent magnet rings using computationally-efficient elliptic integrals, resulting in an accurate calculation of the passive magnetic stiffness of massive magnetic bearing arrangements.

- Several hybrid magnetic bearing configurations, combining active and passive magnetic bearings, are proposed to reduce the complexity of fully active configurations while retaining most of the high performance and low vibrations. The stability and general behaviour of such configurations is validated and proven using the developed closed-loop simulation models showing promising capabilities.

1.5   List of Publications

Throughout the development of the present thesis several conference and journal articles have been submitted for publication and published or are currently under review. The complete list of publications is included hereafter.

Conference Papers

[45]   G. Borque Gallego, L. Rossini, E. Onillon, T. Achtnich, C. Zwyssig, R. Seiler, D. Martins Araujo, and Y. Perriard, "Magnetic Bearing Reaction Wheel Micro-Vibration Signature Prediction", in *18th European Space Mechanisms and Tribology Symposium*, Munich, Germany, Sep. 2019.

[46]   G. Borque Gallego, L. Rossini, T. Achtnich, C. Zwyssig, D. Martins Araujo, and Y. Perriard, "Force Analysis of a Slotless Lorentz-Type Active Magnetic Bearing Actuator", in *2018 21st International Conference on Electrical Machines and Systems (ICEMS)*, IEEE, Oct. 2018, pp. 75–80, ISBN: 978-89-86510-20-1. DOI: 10.23919/ICEMS.2018.8549038.

[48]   ——, "Force and Torque Model of Ironless Passive Magnetic Bearing Structures", in *2019 IEEE International Electric Machines & Drives Conference (IEMDC)*, IEEE, May 2019, pp. 507–514, ISBN: 978-1-5386-9350-6. DOI: 10.1109/IEMDC.2019.8785411.

Journal Articles

[44] G. Borque Gallego, L. Rossini, E. Onillon, T. Achtnich, C. Zwyssig, R. Seiler, D. Martins Araujo, and Y. Perriard, "On-line micro-vibration measurement method for Lorentz-type magnetic-bearing space actuators", *Mechatronics*, vol. 64, p. 102 283, Dec. 2019, ISSN: 09574158. DOI: 10.1016/j.mechatronics.2019.102283.

[47] G. Borque Gallego, L. Rossini, T. Achtnich, D. Martins Araujo, and Y. Perriard, "Three-Dimensional Force and Torque Models of Slotless Magnetic Bearing Machines", *IEEE/ASME Transactions on Mechatronics*, May 2020, under review.

[49] ——, "Efficiency Optimisation and Vibration Reduction in Slotless Magnetic Bearing Machines", *IEEE/ASME Transactions on Industry Applications, Special Issue on Magnetically Levitated Motor Systems*, Nov. 2020, under review.

[50] ——, "Novel Generalised Notch Filter for Harmonic Vibration Suppression in Magnetic Bearing Systems", *IEEE/ASME Transactions on Industry Applications, Special Issue on Magnetically Levitated Motor Systems*, Dec. 2020, under review.

2 Magnetic Bearing Actuators for Space Applications

As mentioned in the previous chapter, magnetic bearings are identified as a key technology in the development of very-low disturbance actuators, and more specifically for reaction and momentum wheels, of strategic interest for the European Space Agency (ESA). For this reason, it is necessary to identify the state of the art in terms of past activities that have targeted to integrate magnetic bearings into reaction or momentum wheels for attitude control of satellites, in order to better focus the present research.

Firstly, an overview of the previously developed magnetic bearing reaction wheels (MBRWs) is performed in section 2.1, identifying its main target applications in terms of satellite size and characteristics through the analysis of the physical characteristics of the reaction wheels (RWs). Furthermore, the topology and configuration of the magnetic bearings (MBs) employed in these actuators is studied to identify the limitations seen in these past developments. Finally, in section 2.2, the magnetic bearing reaction wheel demonstrator developed by Celeroton (CEL) is described, including the general MB topology, the actuator, sensor and control algorithm, which will be the base for the investigations undertaken in this thesis.

2.1   Magnetic Bearing Reaction Wheels for Satellite Attitude Control

This section will focus on the different magnetic actuators developed for attitude control of satellites. Firstly, acknowledging that similar devices exist in attitude and orbit control systems (AOCS), as reviewed in chapter 1, such as control moment gyroscopes (CMGs), the literature overview included hereafter will only cover magnetic bearing reactions wheels (MBRWs), due to being this the main target application highlighted by the ESA in [15]. Moreover, exclusively the actuators that are equipped with a full magnetic suspension system (active or passive) are considered.

2.1.1 General Overview

The main potential advantages, such as virtually infinite life-time due to friction-less operation or better control of bearing dynamic properties, and the progress in some technological aspects, like the development of rare-earth magnets (i.e. samarium-cobalt magnets), from other applications of magnetic bearings in rotating machinery resulted in the first efforts of developing magnetically-suspended reaction wheel systems for attitude control of satellites simultaneously in different parts of the world between the end of the decade of 1960 and beginning of the 1970 decade, mainly by the National Aeronautics and Space Administration (NASA) [31], [51], [52], and many other contractors [53]–[56] in the United States; by Aerospatiale [57]–[59] in France; and by TELDIX (currently Collins Aerospace) [60], [61] in Germany. These last designs by Aerospatiale [16], [62]–[65] and TELDIX [66]–[70] were improved and continued in the following decades.

Several of these Magnetic Bearing Reaction Wheels designed and manufactured by Aerospatiale (currently Thales Alenia Space) were used in different space missions, starting from a 1-DoF axially active MBRW that was sent to space in the French Earth Observation satellite SPOT 1 in 1986, and then used in others like SPOT 2 and 3, ERS (European Radar Observation Satellites) 1 and 2. Then a 2-DoF radially active MBRW was developed, also by Aersopatiale, and launched into space in SPOT 4 and 5, HELIOS 1A and 1B, and ENVISAT satellites, until the development was discontinued in early 2000.

Since the beginning of 1980, in Japan, the National Aerospace Laboratory in Japan (NAL), in collaboration with Mitsubishi Electric Corporation (MELCO) and Toshiba, started different research and development activities that resulted in the generation of several Magnetic Bearing Reaction Wheel designs [71]–[75]. These activities were undertaken for two decades, and one of them, a radially-active MBRW was launched to space in the JINDAI platform in 1986 for in-space testing that lasted three days. Other major developments by NAL and MELCO are a three-axis active magnetic bearing, with axial and gimballing capabilities [71], [72], and the most recent five-axis active MBRW, which started focusing on the study of micro-vibration exported to the satellite's structure [75].

During the 90's, other efforts on implementing magnetic bearings in momentum or reaction wheels for satellite attitude control were undertaken. On the one hand, one of the first research activities with a main focus on small satellites, was developed by Scharfe *et al.* for the Dresden University of Technology in Germany [76]–[79] during mid 90's and the beginning of 2000's, initially intended for the AMSAT Phase 3-D satellite and then miniaturised for its used in small satellites. On the other hand, a conical MBRW topology was designed and tested by the Mechatronics Laboratory of the Technical University of Turin (*Politecnico di Torino*) [80]–[82]. These two projects were discontinued during the decade of 2000.

The most recent developments of magnetic bearings for reaction wheels known by the author were undertaken in [83], [84] at the Surrey Space Centre (SSC) of Surrey University in the United Kingdom until 2011, and more recently by Beihang University (BUAA) in China [85]–[94]. Lastly,
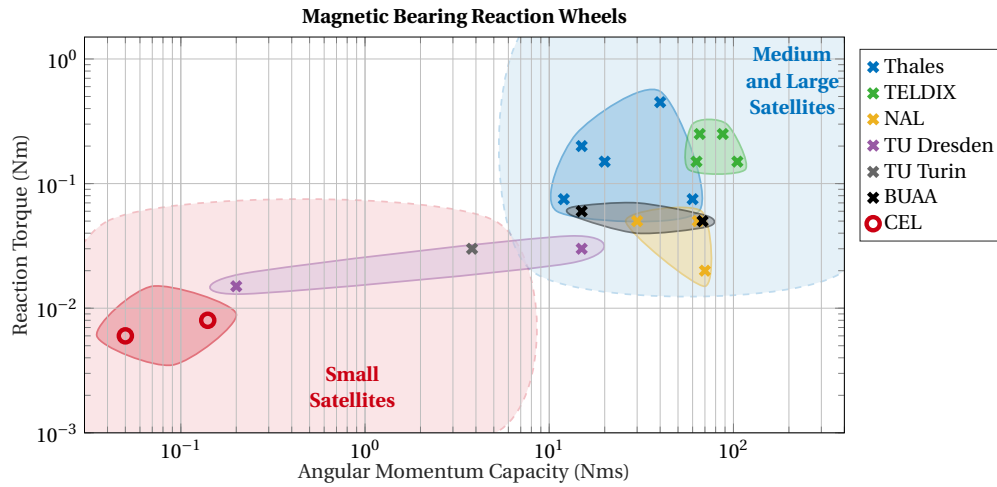
Figure 2.1 – Comparison of the main physical characteristics, reaction torque and angular momentum storage capacity, of past magnetic bearing reaction wheels which define the possible use and target application of such actuator.

originated from very-high-speed motors, Celeroton AG (CEL) developed a magnetic bearing reaction wheel demonstrator to prove the viability of its fully active Lorentz-type magnetic bearing topology for its use in space applications, and more specifically for small satellites.

2.1.2   Magnetic Bearing Comparison

The main characteristics of a reaction wheel actuator that determines the size of the satellites in which it can operate are the reaction torque and momentum storage capacity. Even though the exact RW selection will depend on the specific mission requirements such as agility, reliability or pointing stability, some examples of missions are given as a reference for RW sizing:

- *Small satellites* (<500 kg): the TET-1 mission with around 120 kg of mass, use RWs with 0.34 N m s of momentum storage, and 0.015 N m of reaction torque [95].

- *Medium satellites* (500 kg to 1000 kg): the AMSAT phase 3-D with 500 kg of mass, feature RWs in the range of 13 N m s of momentum storage and 0.03 N m of torque [76].

- *Large satellites* (>1000 kg): earth observation (EO) Sentinel-2 satellite, with 1225 kg of mass, employ RWs of 18 N m s of momentum storage, and 0.3 N m of torque [96].

In order to identify the sizing of the aforementioned MBRWs, in table 2.1 and their possible target missions, a comparison between the main technical parameters, such as number of active DoF, magnetic bearing type, angular momentum storage capacity, reaction torque and power consumption, is performed. Moreover a graphical comparison in included in figure 2.1, in terms of reaction torque and angular momentum storage capacity.

Table 2.1 – Magnetic bearing reaction wheel (MBRW) overview with main technical characteristics, including number of active degrees of freedom (DoF), magnetic bearing type (number according to figure 1.1, reluctance or Lorentz), maximum rotational speed, angular momentum storage, reaction motor (Mot.) and gimballing (Gim.) torque and power consumption in steady state (S.S.) or maximum (Max.) for both bearings (Bear.) and motor (Mot.).

Developer	Active DoF	Type	Speed (krpm)	Ang. Mom. (N m s)	Torque (N m)	Power (W)
Thales Alenia (Aerospatiale)	1 (Ax.)	1+3 (Rel.)	2-24	1-100	0.05-0.1	3-25 (S.S.)
	2 (Rad.)	1+3 (Rel.)	2.4	40	0.45	13 (Bear.) 80 (Mot.)
	2 (Rad.)	1+3 (Rel.)	6-10.3	12-60	0.075-0.15	120
Collins Aerosp. (TELDIX)	5 (All)	8 (Lor.)	12	100	0.05 (Mot.) 2 (Gim.)	150
	5 (All)	8 (Lor.)	5-8	30-150	0.1 (Mot.) 4 (Gim.)	70-120
	5 (All)	8 (Lor.)	6-10	63-105 (Mot.) 2 (Gim.)	0.25 (Mot.) 0.6 (Gim.)	14 (S.S.)
	5 (All)	8 (Lor.)	6-8	65-87 (Mot.) 2-2.6 (Gim.)	0.1 (Mot.) 0.6 (Gim.)	18-25 (S.S.) 140 (Max.)
NAL Japan	1 (Ax.)	1+3 (Rel.)	10	34	-	-
	2 (Rad.)	1+3 (Rel.)	3	7.5	-	3 (S.S.)
	3 (Ax. & Gim.)	1+3 (Rel.)	10	70	0.02 (Mot.) 4 (Gim.)	8 (Bear.) 50 (Mot.)
	5 (All)	1+3 (Rel.)	5-8	30-64	0.05	15 (S.S.)
TU Dresden	2 (Rad.)	1+3 (Rel.)	3	15	0.03	5 (Bear.) 15 (Mot.)
	2 (Rad.)	1+3 (Rel.)	5	0.2	0.01	5 (S.S.) 20 (Max.)
TU Turin	5 (All)	1+3 (Rel.)	10	3.81	0.03	6 (S.S.) 40 (Max.)
Beihang Univ. (BUAA)	5 (All)	1+3 (Rel.)	6	15	0.06	-
	5 (All)	1+3 (Rel.) & 8 (Lor.)	5	68	0.05 (Mot.) 3.3 (Gim.)	-

In both figure 2.1 and table 2.1, it can be clearly seen that most previous developments in magnetic bearings were targeted to medium to large satellites, whereas only few efforts by TU Dresden and Celeroton focused on the growing sector of small satellites. This can be explained

by the fact that it is generally large satellites the ones that feature high-precision and highly sensitive payloads for scientific and Earth observation missions, where very-low disturbance actuators are of most importance [15].

Nevertheless, due to the lower size, mass and inertia of small satellites, its structure is more sensitive to existing on-board disturbances, which mainly limits the precision and accuracy of the payloads that the satellite can carry [97]. The use of magnetic bearing, which will considerably reduce these perturbations, combined with the recent tendency to equip small satellites with high-performance payloads [15], [97] will enable new missions that previously may have not been viable.

Another important aspect to analyse is the type of magnetic bearing that is employed. Independently of the chosen magnetic bearing type, the actuator should be able to withstand all load cases that the system will be subject to in-orbit, and allow sufficient on-ground testing for qualification, including basic functionality checks, requirement and performance verifications, such as basic levitation, reaction torque, micro-vibration generation, or torque stability. Due to the micro-gravity conditions in-orbit, the main forces that the bearings will cope with are the gyroscopic forces during satellites manoeuvres. On-ground, the gravitational forces during levitation are the most important loads. The dimensioning of the magnetic bearing system according to the gravitational loads will result in a considerably oversized actuator for in-orbit conditions, resulting in weight increase due to bigger MBs and power electronics, and thus increasing system cost, volume and weight, which are also important magnitudes to limit in space applications. An intermediate solution can be found: it is possible to perform the actuator dimensioning for in-orbit conditions, while still guaranteeing sufficient testing in on-ground conditions, by either employing auxiliary cooling or levitation system only for testing, or by limiting the configurations used for testing, for instance, testing for a limited time or orientation.

In table 2.1, it can be seen that most developments are based on magnetic bearings of reluctance-force type, and more specifically, of a combination of types 1 and 3 (PM-bias active reluctance-force type) according to the classification shown in figure 1.1. This situation can be justified by two main factors: the fact that most reluctance force bearings feature much higher load capacities, facilitating the on-ground testing of the heavy MBRW, and because these configurations enable the active control of some given DoF while passively stabilising other, greatly simplifying the overall system complexity and making allowing a very compact actuator.

Even though these advantages allowed the development of a broad selection of magnetic bearing configurations, some key drawbacks of reluctance-force types are the much higher passive stiffness due to the attraction between rotor and stator in small air-gaps, compromising the possibility of achieving a perfect vibration suppression through control techniques, as any rotor displacement will generate a disturbance force, and due to the fact that these configurations feature ferromagnetic and generally conductive materials in both rotor and

stator parts, greater eddy current or iron losses will limit the efficiency and maximum speed of the actuators. Also, the passive stabilisation of some degrees of freedom will never allow a perfect vibration suppression, limiting the maximum performance that can be achieved, but considerably reducing the system's complexity.

When considering Lorentz-force-based magnetic bearing machines, either slotted or slotless configurations can be employed. The former features high load and torque capacities with high passive magnetic stiffness due to small air-gaps, but high-harmonic disturbances due to uneven field distribution resulting from stator slots that generate force and torque ripples are unavoidable. Slotless machines are known for its good dynamic response, good linearity and high reliability [98], featuring very smooth operation due to the absence of stator slots, and thus reduced force and torque ripple, and very low magnetic stiffness, as a result of the fact that motor and bearing windings are located in the air-gap. However, this bigger air-gap also imposes as a result limited load capacities [30]. This limitation can be reduced by employing high-efficiency slotless winding types, such as rhombic and hexagonal, or even optimised winding shapes on flexible PCBs [99], [100].

The main difference between the topologies proposed by TELDIX and CEL is the use of independent actuators of axial, radial and motor, and a homopolar configuration of permanent magnets in the rotor for the former, and a compact self-bearing heteropolar motor and radial bearing machine combined with homopolar radial and axial bearing machine for the latter. Furthermore, due to the fact that the permanent magnets are located at the outer rim of the wheel for TELDIX' MBRW and multiple pole-pairs are employed, the field is generated by discrete permanent magnet blocks in the rotor, which combined with several individual air-core concentrated windings in stator, allows for greater forces and torques, but generating high-harmonic field distortions due to discrete magnets and coils. In CEL's MBRW demonstrator, the use of self-bearing machine with slotless windings, with single cylindrical PMs in the rotor, generates a very smooth operation due to the absence of most bearing and motor disturbances, and showing good properties for very-low disturbance reaction wheels. The main limitation of such configuration is the limited load capacities due to thermal constraints for on-ground testing.

On the one hand, if small satellites are targeted, the smaller size of the RW will greatly relax the common load capacity limitations of Lorentz-type MBs. On the other hand, if medium or large satellites are targeted, with much larger RWs, due to the micro-gravity conditions in-orbit, limiting the bearing actuation to sustaining the gyroscopic forces during satellites manoeuvres, the load conditions that the levitation system needs to withstand are also considerably reduced. In any case, as previously mentioned, some on-ground levitation capabilities need to be guaranteed for functional and qualification testing. However, by limiting the configurations in which the system can be tested or by using auxiliary test systems it is possible to considerably reduce the constraints imposed on the bearing load capacity, facilitating the design and dimensioning of the actuators.

Figure 2.2 – Rotor (left), stator (middle) and controller and power electronics (right) of Celeroton's Lorentz-type, dual hetero/homopolar, slotless, self-bearing, fully active magnetic bearing system.

For these reasons, in applications where very-low disturbance actuators are required, fully active, self-bearing, slotless, Lorentz-force type magnetic bearings (*type 8*) like the one proposed by CEL show very promising capabilities and advantages over the other available alternatives. During the present thesis, as a detailed study of the aforementioned main aspects in MBRWs, such as efficiency, complexity and micro-vibrations, will be undertaken for this configuration, a description of the studied topology is included hereafter, which corresponds with the starting point of the research.

2.2 Celeroton's Magnetic Bearing Reaction Wheel Demonstrator

A compact ultra-high-speed magnetic bearing and motor topology was proposed and developed by the Swiss Federal Institute of Technology in Zurich (ETHZ) and Celeroton AG (CEL) [42], [101]–[103], with promising capabilities for space applications, such as reaction wheels for attitude and orbit control systems (AOCS). For studying its capabilities, a magnetic bearing reaction wheel demonstrator, shown in figure 2.2, has been developed [104], [105]. The topology of the aforementioned demonstrator, as schematically shown in figure 2.3, is a Lorentz-type, dual hetero/homopolar, slotless, self-bearing, fully active magnetic bearing and permanent-magnet synchronous motor (PMSM).

The main aspects of the studied configuration, important for understanding the overall working principle and the work undertaken in the present thesis, are included hereafter. The complete description of all the elements can be found in [42] and [104].

2.2.1 Topology Overview

On the one hand, the heteropolar side is responsible for generating radial forces and motor torque to the rotor, by means of the interaction between the magnetic flux created by a diametrically-magnetised permanent magnet (PM) and the current applied to a radial bearing for force generation and to a motor winding for torque generation. The heteropolar configuration of this part of the machine requires a synchronous modulation of both motor and bearing currents with rotor's orientation, typical in any field-oriented control (FOC) of PMSMs. The
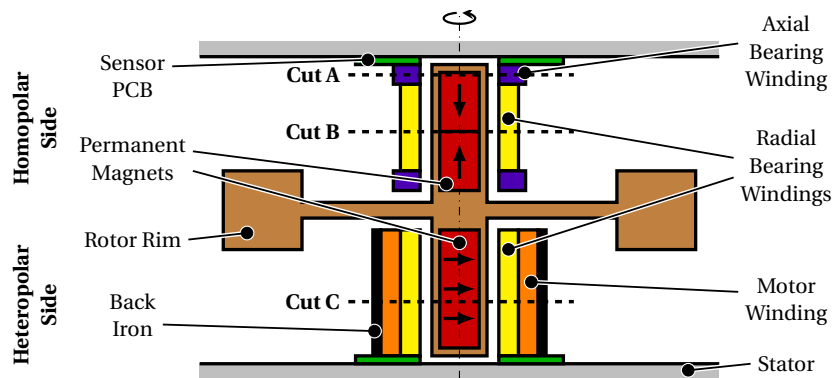
Figure 2.3 – Schematic cross-sectional view of the initial configuration of the slotless permanent-magnet magnetic bearing reaction wheel demonstrator, including heteropolar side that generates radial force and motor torque, and homopolar side that exerts radial and axial forces.

magnetic circuit is shared by both, motor and bearing windings (self-bearing), located in the machine's air-gap (slotless design), and depending on the application, it can be closed by a stator core.

On the other hand, the homopolar side is responsible for generating axial and radial forces. These forces result from the Lorentz force between the magnetic field created by two axially-magnetised PMs pointing towards each other and two separated ring-wound coils for the axial forces, and with a radial bearing winding. A combined magnetic circuit is shared between axial and radial bearings. Nevertheless, the homopolar configuration is independent from rotor's orientation, and thus, actuation control loop is simplified, as no field-oriented control is required. As before, depending on the application, the machine can be enclosed by a stator core.

2.2.2 Electromagnetic Actuator

All bearings and motor are slotless and of the Lorentz-type, and thus, the main part of the force and torque is generated by the Lorentz force resulting from the electromagnetic interaction between the magnetic flux density distribution in the air-gap created by the rotor's permanent magnet, and the current density distribution in the windings.

More precisely, these actuators feature the following characteristics:

- *Homopolar axial bearing*: a two-piece slotless single-phase ring-wound winding that generates axial force as shown in figure 2.4.a.

- *Homopolar radial bearing*: a slotless three-phase winding with a single pole-pair and also of skewed type. The axially symmetric flux density distribution in the homopolar air-gap, combined with a winding with one pole-pair results in a radial force, as schematically represented in figure 2.4.b.

20

(a) Homopolar axial force generation.

(b) Homopolar radial force generation.

(c) Heteropolar radial force generation.

(d) Heteropolar motor torque generation.
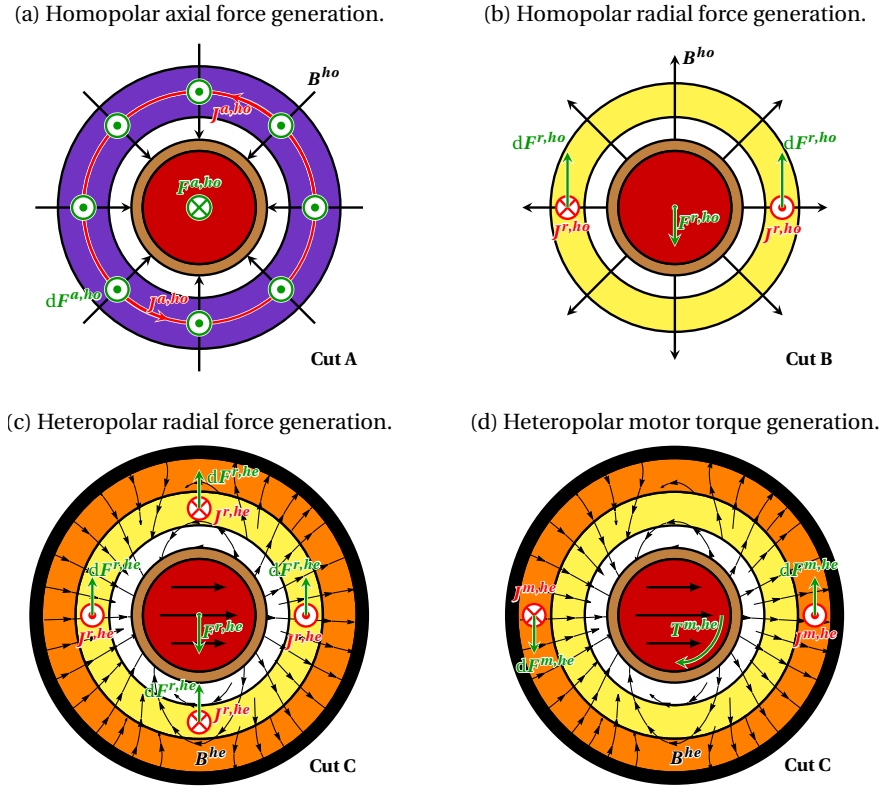
Figure 2.4 – Schematic representation of Lorentz forces generated in homopolar axial and radial bearing windings and heteropolar radial bearing and motor windings at cutting planes A, B and C defined in figure 2.3. (Source: Celeroton AG)

- *Heteropolar radial bearing*: a slotless three-phase winding with two pole-pairs of skewed type. The two pole pairs in the winding combined with a flux generated by a permanent magnet with a single pole-pair generates a radial force, as schematically shown in figure 2.4.c. Furthermore, due to the presence of back iron, the flux in it will also contribute to the total radial force [27], [42], a term commonly known as reluctance force.

- *Heteropolar motor*: a slotless three-phase winding with one pole-pair of skewed type, generating the motor torque as schematically shown in figure 2.4.d. In this case, due to the axial symmetry of the back iron surface, no reluctance torque is generated.

The cut planes of all cross sections included in figure 2.4 are identified in figure 2.3.

2.2.3 Control Architecture

The magnetic bearing control is implemented as a cascaded control loop, as commonly done for motor control applications, where an inner loop, with much faster dynamics is used for current control, and an outer one for position control, as shown in figure 2.5. The fast current control loops are ideally executed synchronously. This approach allows minimising
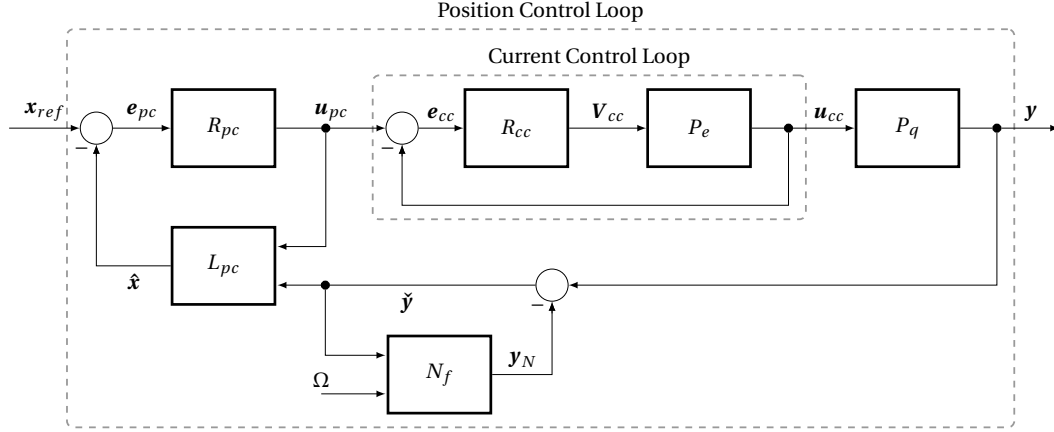
Figure 2.5 – Closed-loop scheme of control architecture featuring cascaded control with outer rotor position control loop and inner actuator current control loop. The closed-loop system is composed of position controller R_{pc} and observer L_{pc}, generalised notch filter for unbalance force rejection N_f, current controller R_{cc}, plant electrical dynamics P_e and mechanical system rotordynamics P_q.

the possible error in applied currents and thus reducing its influence in position control, but requires parallel computation capabilities, as 10 currents have to be accurately controlled with minimum delay.

Current Control

The force and torque applied to the rotor under levitation is directly controlled by the current applied to the windings. In the studied topology, three three-phase windings and one single-phase winding need to be accurately controlled. For the heteropolar side, a modulation of the three-phase winding currents needs to be performed to apply force or torque in the desired direction. For the homopolar side, due to the axial symmetry of the magnetic field, no modulation is needed.

In order to remove this angle-dependency from the current and position controllers, a field-oriented control (FOC) technique is employed for all three-phase windings. A given electrical magnitude x, such as phase currents and voltages, can be converted from alternating ABC-coordinates to the angle-invariant rotor-fixed DQ-coordinates [106] employing an amplitude-invariant Park transformation

$$\begin{bmatrix} x_d \\ x_q \end{bmatrix} = \frac{2}{3} \begin{bmatrix} \cos(\phi_{z'}) & \cos\left(\phi_{z'} - \frac{2\pi}{3}\right) & \cos\left(\phi_{z'} + \frac{2\pi}{3}\right) \\ -\sin(\phi_{z'}) & -\sin\left(\phi_{z'} - \frac{2\pi}{3}\right) & -\sin\left(\phi_{z'} + \frac{2\pi}{3}\right) \end{bmatrix} \begin{bmatrix} x_A \\ x_B \\ x_C \end{bmatrix}, \tag{2.1}$$

being $\phi_{z'}$ the rotor polar angle, and *vice versa* using the inverse transform

$$
\begin{bmatrix} x_A \\ x_B \\ x_C \end{bmatrix} = \begin{bmatrix} \cos(\phi_{z'}) & -\sin(\phi_{z'}) \\ \cos\left(\phi_{z'} - \frac{2\pi}{3}\right) & -\sin\left(\phi_{z'} - \frac{2\pi}{3}\right) \\ \cos\left(\phi_{z'} + \frac{2\pi}{3}\right) & -\sin\left(\phi_{z'} + \frac{2\pi}{3}\right) \end{bmatrix} \begin{bmatrix} x_d \\ x_q \end{bmatrix}.
\tag{2.2}
$$

Employing Park's direct and inverse transformations on current sensors measurements and terminal phase voltages, respectively, all control loops are implemented making use of DQ-coordinates, executed in parallel in a field-programmable gate array (FPGA) to minimise execution delays, and using a simple proportional-integral (PI) controller.

All currents are sampled at 800 kHz using magneto-resistive current sensors, and controlled using the actuating voltage on three-phase DC/AC inverters using pulse-width modulation (PWM). The combination of a FPGA-based current control for synchronous and parallel execution of the current control with high sampling rate enables the possibility of having sufficient controller bandwidth for implementing a successful cascaded control.

In order to drive all windings, a three-phase two-level voltage source inverter (2LVSI) is employed to apply the terminal phase voltages of each three-phase winding and a full bridge inverter for the axial single-phase winding, powered by two DC/DC converters for motor and bearings, as schematically represented in figure 2.6.

This way, the position controller simply needs to specify the reference currents in DQ-coordinates.

Position Control

The position controller architecture is based on a linear-quadratic-gaussian (LQG) observer and controller, and its detailed design is presented in [103]. For the design of the position controllers, radial and axial dynamics are considered decoupled, allowing the independent design of both controllers. The position control is implemented on a digital signal processor (DSP) and executed at a sampling rate of 20 kHz.

The control loop for the multiple-input multiple-output (MIMO) dynamic system for the radial position, and single-input single-output (SISO) for the axial position, are composed of a controller R_{pc}, a Kalman filter state-space observer L_{pc}, a current limiter and its associated anti-windup to avoid problems with the integral state during saturation. A generalised notch filter, N_f, is enabled above 50 krpm to reject exported forces due to rotor unbalance, being 1 krpm one thousand revolutions per minute.

In order to extract the state vector from the noisy sensor measurements, a Kalman filter of the form

$$
\hat{\boldsymbol{x}}(t_k) = L_{pc} \begin{bmatrix} \hat{\boldsymbol{x}}(t_{k-1}) \\ \boldsymbol{u}(t_{k-1}) \\ \check{\boldsymbol{y}}(t_k) \end{bmatrix},
\tag{2.3}
$$
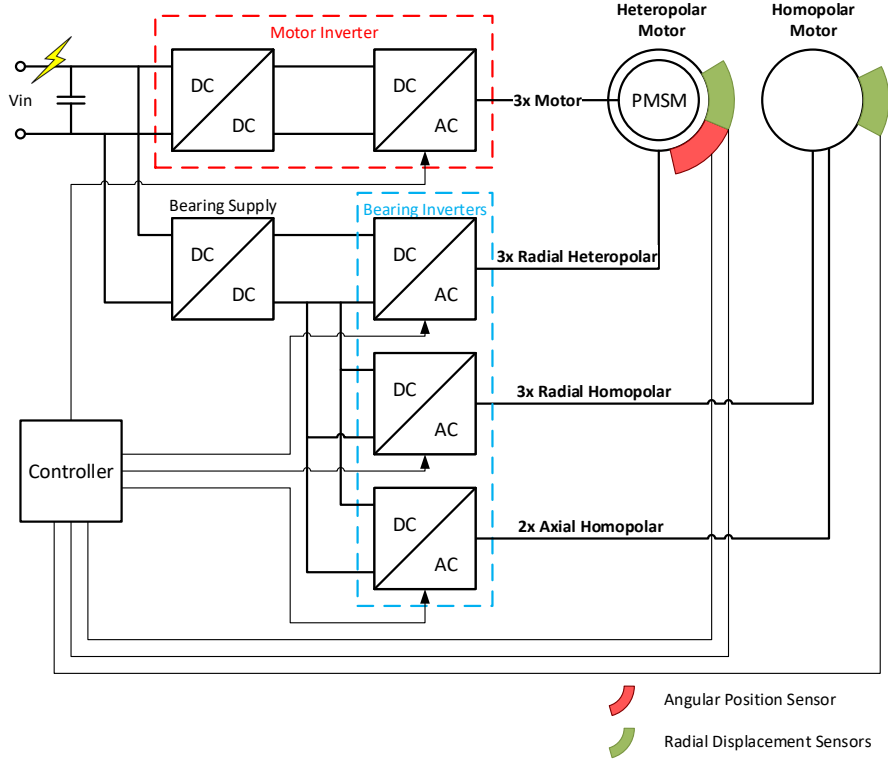
Figure 2.6 – Block diagram of power electronics configuration for active control of three-phase motor and radial bearing currents and single-phase axial bearing current (Source: Celeroton AG).

is used. The estimated state $\hat{x}$ at time t_k is updated by using the estimated state at the previous sample time t_{k-1}, previous controller output $\boldsymbol{u}$, and filtered sensor measurements $\check{\boldsymbol{y}}$, multiplied by the observer gain matrix L_{pc}.

Considering a reference position $\boldsymbol{x}_{ref} = 0$, to fix the rotor at the geometrical centre of the air-gap, the full state feedback LQG controller

$$\boldsymbol{u}_{pc}(t_k) = R_{pc}\left(\boldsymbol{x}_{ref} - \hat{\boldsymbol{x}}(t_k)\right) \tag{2.4}$$

is employed, composed of proportional, integral and derivative states. The controller matrix gain R_{pc} is obtained by minimising a quadratic cost function dependent on states and currents, as typically done for LQG control.

In order to limit the overheating in the bearings, the maximum Joule losses in windings are fixed by imposing a quadratic limit, $\boldsymbol{u}_{max}$, to the input currents $\boldsymbol{u}_{pc}$. Whenever the threshold is reached the current is limited by imposing $\boldsymbol{u}_{pc} = \boldsymbol{u}_{max}$, and integration in (2.4) is stopped. This behaviour, due to its non-linearity, is only present in the time based analysis of the closed-loop system.

2.2.4 Position Sensors

The information regarding rotor position and orientation is obtained via two printed-circuit-board (PCB)-based sensors placed at the two axial extremes of the stator.

On the one hand, the radial position measurements are via eddy-current sensors, more specifically by transverse flux sensors that can be implemented on a PCB as detailed in [107]. On the other hand, two different axial position sensors are available, using either an Eddy-current sensor, or the magnitude of the stray field measured by Hall-effect sensors, as detailed in [42].

The angular position of the rotor $\phi_{z'}$ is obtained by two pairs of orthogonal Hall sensors in differential connection, which directly yield components that are proportional to $\sin(\phi_{z'})$ and $\cos(\phi_{z'})$.

2.3 Conclusions

In this chapter, a review of the past magnetic bearing reaction wheels developed for attitude control of satellites, where the advantages of magnetic bearings are of most interest, is performed. In this overview the main characteristics of these past developments are analysed to identify the remaining open points to this technology, which shows that the configuration studied in this thesis features some important and promising advantages for its implementation in very-low disturbance actuators for space applications.

Finally, the fully active magnetic bearing system studied in this thesis is detailed, including a description of its magnetic bearing topology, actuator, sensor, power electronics, and control configurations.

3 Closed-Loop Magnetic Bearing Model and Micro-Vibration Characterisation

In order to quantify the impact of the different modifications and correcting measures implemented and proposed throughout this thesis, it is first necessary to define the different figures of merit and analysis tools required to quantitatively assess some characteristics such as stability, performance and vibrations.

In this chapter, two main aspects of the analysis are covered. On the one hand, a presentation of the different sources and measurement tools available for evaluating the vibrations generated by rotating machinery is performed. On the other hand, a closed-loop magnetic bearing simulation model is developed and presented, which will be employed as a benchmark for the different control measures and evaluate the impact on the stability, performance and vibrations generated by the system. Furthermore, a measurement method for active magnetic bearings, called current-to-force method, is presented and compared to state-of-the-art vibration measurement techniques.

Both the simulation model and the new measurement technique are experimentally validated in chapter 7. Earlier versions of the model and measurement method were presented in [45] and [44], respectively.

3.1 Micro-Vibration Sources for Magnetic Bearing Reaction Wheels

Due to the high impact of reaction wheels (RW) on satellite's pointing accuracy, the noise signature and the main sources of these disturbances for common ball bearing reaction wheels (BBRWs) have been extensively addressed in the past [10], [11]. These disturbances are commonly known as micro-vibrations, due to their low amplitude and periodic components, dependent on rotor's speed, and are common to any rotating machinery.

The main sources of periodic reaction wheel micro-vibration can be classified, as performed in [10], according to their origin or cause in: unbalance-driven , bearing-driven, and motor-driven disturbances. These type of disturbances for magnetic bearing systems are detailed hereafter.

3.1.1 Unbalance-Driven Disturbances

This component of the micro-vibrations is caused by uneven distribution of mass in the rotor around its geometrical axis, and it is acknowledged to be the most significant disturbance in reaction wheels. It consists of two types of unbalances: static unbalance, which appears as a periodic force perpendicular to the rotation axis, and dynamic unbalance, measurable as a radial torque, also perpendicular to the spin axis.

The common definition of the unbalance in unbalance measurement equipment and balancing machines is expressed as an additional mass at a certain radial position, being

$$\boldsymbol{F_s} = \begin{bmatrix} F_x \\ F_y \end{bmatrix} = m_s r_s \Omega^2 \begin{bmatrix} \cos(\Omega t + \alpha) \\ \sin(\Omega t + \alpha) \end{bmatrix},$$
$$\boldsymbol{T_d} = \begin{bmatrix} T_x \\ T_y \end{bmatrix} = m_d r_d d_d \Omega^2 \begin{bmatrix} \sin(\Omega t + \beta) \\ \cos(\Omega t + \beta) \end{bmatrix},$$

(3.1)

where Ω is the wheel rotation speed, m_s and m_d are the static and dynamic unbalance point-masses, respectively, r_s and r_d the radius between the geometric axis of rotation and the static and dynamic masses, and d_d the axial distance between the dynamic unbalance masses. These unbalance models consider a centrifugal force and torque in radial direction (F_x, F_y, T_x, T_y), synchronous with rotation speed. Due to the interaction with other bodies of the stator, other modulations of these unbalance can be measured, appearing as higher integer harmonic orders of the rotation frequency.

One of the main advantages of magnetic bearings, due to the lack of physical contact between rotor and stator, is the possibility of including active unbalance control, that would considerably reduce the exported vibrations of the reaction wheel.

3.1.2 Bearing-Driven Disturbances

For conventional reaction wheels (RWs) featuring ball bearings, other non-integer modulations of the harmonic micro-vibrations appear as a result of imperfections in the bearing components, originated from the manufacturing process, such as waviness or geometrical irregularities in the surface of bearing parts. Ball bearings also generate random/transient disturbances, mainly due to lubrication issues, such as performance deterioration at speeds close to zero, limited number of zero-crossings, momentary non-homogeneous oil distribution inside the bearings that generate additional friction force or other disturbances originated from ageing lubricant.

All these disturbances will not appear in a magnetic bearing reaction wheels (MBRWs), due to the contactless, and thus, frictionless operation of these actuators. In practice, some permanent magnet and winding imperfections, power electronics and sensors will generate some parasitic forces to the rotor and stator, appearing as integer or non-integer harmonic

orders of the rotation frequency. The characteristics of such forces will greatly depend on the magnetic bearing topology and control approach employed, as happens for the motor-driven disturbances.

For the studied fully active Lorentz-type magnetic bearing system it can be seen that the bearing disturbances appear at several integer harmonic orders. As it will be analytically studied in chapter 4 and experimentally shown in chapter 7, the main sources of bearing disturbances are permanent magnet and back iron attraction, permanent magnet imperfections and winding asymmetries.

3.1.3 Motor-Driven Disturbances

Torque ripple and torque instabilities are the main components of motor-dependent disturbances that appear about rotation axis as a distorting motor torque (M_z). The former is understood as any periodic/deterministic torque disturbance derived from power electronics switching, variation in airgaps between permanent magnets, current measurement errors and cogging torque [11]. The latter is referred to as any random or transient disturbance on the motor torque, such as random torque noise.

3.2 Micro-Vibration Measurement Techniques

3.2.1 Analysis Techniques

In order to characterise the level of vibrations generated by rotating machinery, independently of the chosen measurement approach, it is necessary to study its behaviour for its whole speed range. This will allow identifying the behaviour of the machine for every possible working condition and thus identify possible critical speeds and structural resonances. The common test procedure is undertaken as follows: the wheel is driven from minimum to maximum rotation speed by either small and constant acceleration or by small speed steps. This way a transformation to the frequency or order domain can be performed by applying a fast Fourier transform (FFT) assuming a constant speed for each window of the time series data.

The main difference between frequency and order domain analysis relies on the fact that the time signal is re-sampled at constant angle steps of the rotor for the latter, instead of a signal sampled at constant time steps for the former. This allows the easier identification of the harmonic orders of the speed-dependent disturbances.

Once the signal is available in frequency or order domain, the following plots are commonly employed to study the level of vibrations generated by the machine:

- *Waterfall plot*: a three-dimensional plot of the force or torque amplitude as a function of frequency/order and rotor speed, as shown, as an example, in figure 3.1.a in the frequency domain, and in figure 3.1.b in the order domain for the studied fully active

magnetic bearing reaction wheel. In this plot it is possible to identify both structural resonances, that appear at constant frequency, and harmonic disturbances dependent on speed, that appear at constant order. Note that both frequency and order plots are complementary as all information can be found in both approaches, and thus it is a matter of preference to use one or another.

- *Worst-case plot*: a two-dimensional plot of the maximum amplitude at each frequency, figure 3.1.c, or order, figure 3.1.d, for all the measured speeds. As the limitations on allowed vibrations is given as a function of frequency [10], [97], this plots allows the verification of such constraints independently of the rotating speed.

- *Noise-vs-speed plot*: a two-dimensional plot of the root mean square of the force amplitude for all frequencies, figure 3.1.e, or orders, figure 3.1.f, at each rotor speed. This plot is commonly employed to identify the speeds that feature higher level of vibrations, that usually excite one of the main resonance modes and have higher disturbance amplitudes.

3.2.2   Measurement Techniques

For space applications, in the qualification process of any reaction wheel assembly, the exported micro-vibrations to the satellite's structure have to be estimated, in order to guarantee that they satisfy the requirements stipulated for the space mission.

In practice, all on-ground qualification process of any reaction wheel is performed using a state-of-the-art multi-component dynamometer, capable of measuring all exported forces and torques. Nevertheless, due to the new possibilities provided by the internal measurement capabilities of a fully active magnetic bearing, it is possible to estimate such vibrations by employing current measurement data. This measurement technique is named current-to-force.

Both micro-vibration measurement methods employed throughout this thesis are explained hereafter. As a comparison, the required steps for calculating the generated vibrations using a multi-component dynamometer or the current-to-force method are graphically shown in figure 3.2.

For both cases, it is necessary to first multiply current or voltage measurements by a constant to obtain the raw force measurements, then a geometric transformation is required to express the measurements in a desired reference frame, and finally a Fourier transform is applied to convert the signal into the frequency domain. If order domain is employed a resampling in angle steps instead of time steps is required before computing the Fourier transform.
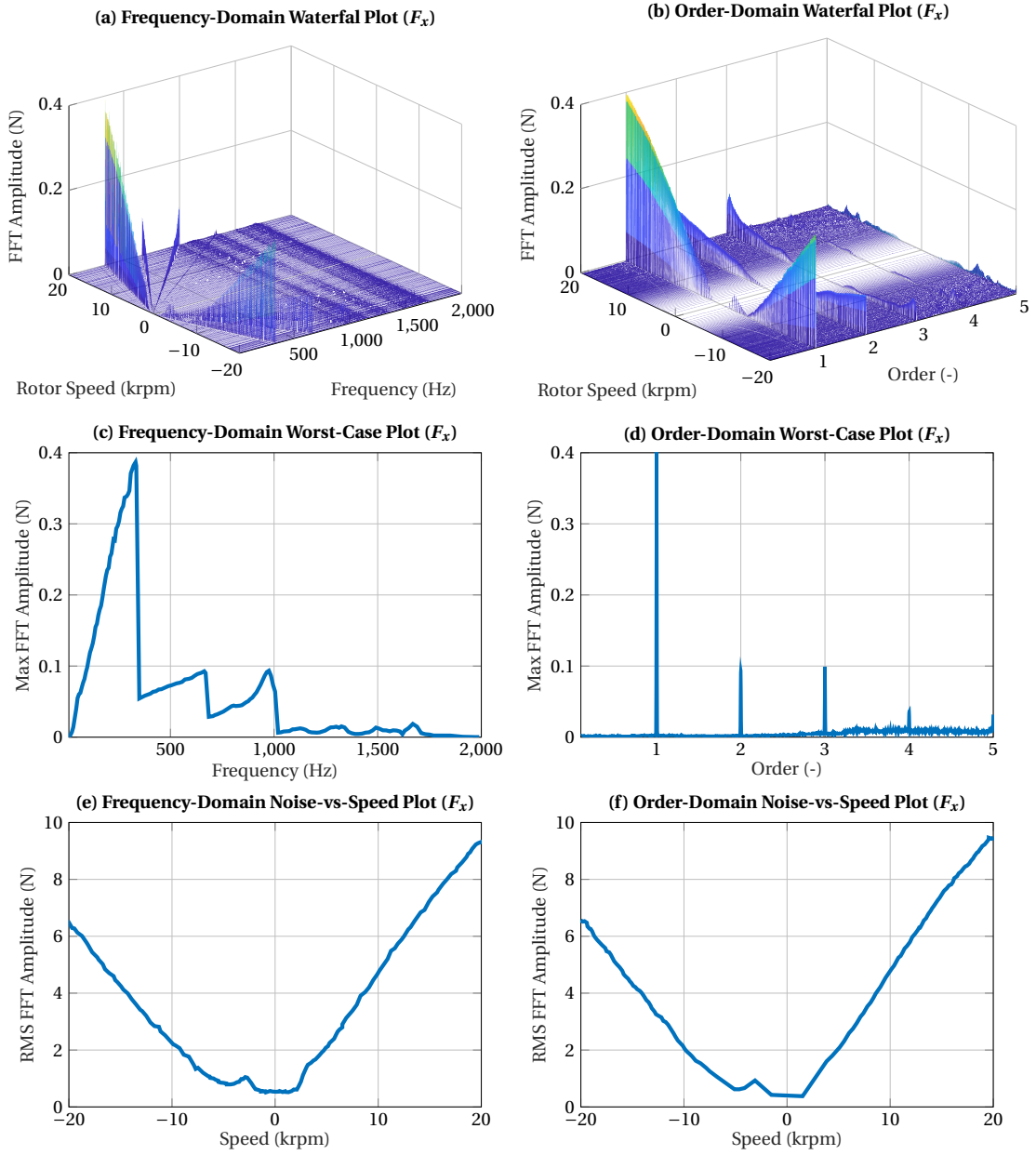
Figure 3.1 – Waterfall, worst-case and noise-vs-speed plots in frequency and order domains of micro-vibration measurements of studied fully active magnetic bearing system using multi-component dynamometer at CSEM.

Multi-component dynamometer

The state-of-the-art micro-vibration qualification equipment relies on the use of a piezoelectric-based multi-component dynamometric platform, fixed over a seismic mass and isolators, as shown in figure 3.3, representing the equipment available at the Swiss Centre for Electronics and Microtechnology (CSEM) in Neuchâtel, Switzerland, during the test campaign of the studied fully active magnetic bearing reaction wheel demonstrator. This multi-component
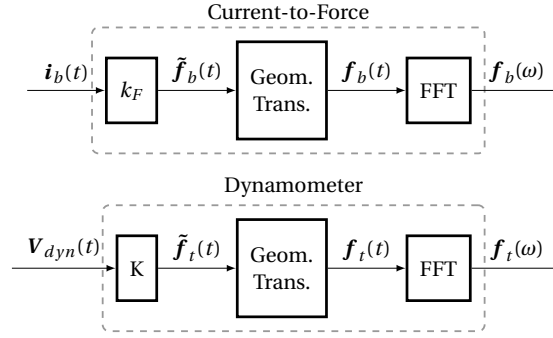
Figure 3.2 – Schematic information flow to obtain the exported micro-vibrations of measured equipment for the proposed current-to-force method and the multi-component dynamometer.

dynamometer consists of four pre-loaded three-axis piezoelectric sensors that measure the strain resulting from the forces generated by the measured equipment. By a simple geometric transformation of the measurements of the four sensors it is possible to reconstruct the total force and torque generated during the experiment.

The measurement procedure is simple: during the operation of the motor, the charge output from the load on the piezoelectric sensors is conditioned and amplified by a charge amplifier and then sampled by an acquisition system, resulting in a series of measurements in the time domain. The output voltage v_{dyn} of the charge amplifier is simply multiplied by the configured sensitivity to obtain the measured forces $\tilde{f}_t$ and geometrically combined to obtain forces and torques with respect to the dynamometer's centre or mounting plane f_t. Then, any analysis technique previously defined can be employed.

Current-to-Force for Magnetic Bearing Systems

This approach is based on the estimation of the electromagnetic forces applied to the rotor via the measurement of the currents and the use of the bearings' electromagnetic models. In some cases, specially on electrodynamic bearings with slotless windings, whose principle is based on Lorentz-force law, a linear relation can be considered between currents and forces, and only a simple multiplication by a constant is required to estimate the applied bearing forces, giving the possibility of having a real-time measurement of the micro-vibrations for control or monitoring purposes. Reluctance-force magnetic bearing types could be also considered for the proposed micro-vibration measurement method, but a more complex relation between actuator's currents, displacements and applied forces may be present.

For the studied system, as it is shown in [47], [101] and in chapter 7, the relation between winding currents, i_b and bearing forces, f_b is linear, of the form $f_b = \kappa_F i_b$, being κ_F the bearing's force constant that can be calculated analytically using the electromagnetic models described in chapter 4.

Then, the measurement procedure is again simple: during the operation of the motor, the

Figure 3.3 – Multi-component dynamometer mounted over isolation platform, consisting of a seismic mass over pneumatic isolator, during micro-vibration characterisation of the studied fully active magnetic bearing reaction wheel (MBRW) demonstrator.

currents i_b applied to the motor and bearing windings are logged using Celeroton's CC-AMB-500 power converter and controller, resulting in a series of measurements in the time domain. The measured currents are transformed into forces $\tilde{f}_b$ by multiplying by the bearing force constant κ_F and geometrically transformed to obtain forces and torques with respect to the stator's centre or mounting plane f_b. As before, any analysis technique previously defined can be employed.

This micro-vibration measurement technique is validated in chapter 7 and in [44] by comparing the current-to-force micro-vibration measurements with two multi-component dynamometers.

3.3 Complete Closed-Loop Magnetic Bearing Simulation Model

The developed closed-loop model of the magnetic bearing system is intended for studying not only the stability of the system but also the general behaviour and identify possible sources of instabilities and micro-vibrations. The followed approach corresponds to a general closed-loop model, as shown in figure 3.4, where each block is modular, and different models of each component can be considered in order to simplify or study more in detail the effect and influence of each one of them.

The different implemented options for each component in figure 3.4 will be described here-
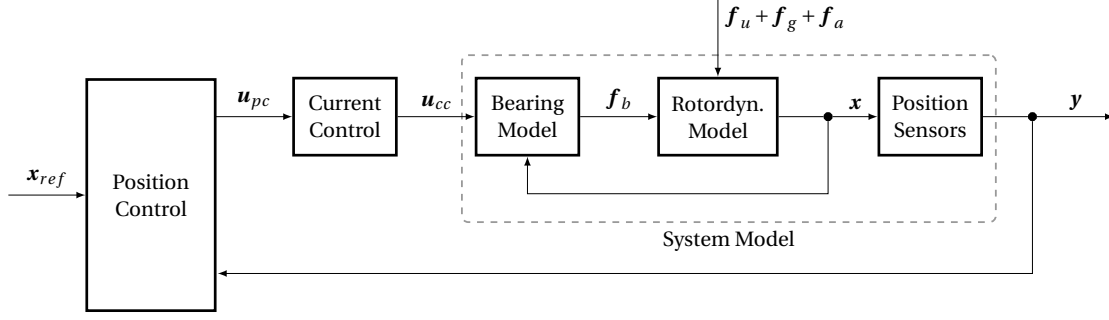
Figure 3.4 – Block diagram of closed-loop simulation model for magnetic bearing systems.

after. For the definition of all the following equations, only the formulation using complex coordinates will be shown due to its more compact and simple form, under the assumption that the system has axial symmetry.

3.3.1 Rotordynamic Models

The dynamics of rotating bodies have been extensively studied in the past with multiple approaches and notations. In this work the approach and notation presented in [108] is followed with some minor adaptations to avoid naming collision with other sections. Considering a rigid body with mass m and moments of inertia $I_{x'}$, $I_{y'}$ and $I_{z'}$ referred to a non-inertial reference frame $S\{O', x', y', z'\}$ fixed to the body, the equations of motion of the system subject to some general forces $\boldsymbol{F} = [F_x, F_y, F_z]^\top$ and torques $\boldsymbol{T} = [T_{x'}, T_{y'}, T_{z'}]^\top$ under an inertial $S\{O, x, y, z\}$ and non-inertial $S\{O', x', y', z'\}$ reference frames, respectively, can be described using classical mechanics as follows

$$
\begin{cases}
F_x = m\ddot{x}, \\
F_y = m\ddot{y}, \\
F_z = m\ddot{z},
\end{cases}
\qquad
\begin{cases}
T_{x'} = \dot{\Omega}_{x'} I_{x'} + \Omega_{y'}\Omega_{z'}(I_{z'} - I_{y'}), \\
T_{y'} = \dot{\Omega}_{y'} I_{y'} + \Omega_{x'}\Omega_{z'}(I_{x'} - I_{z'}), \\
T_{z'} = \dot{\Omega}_{z'} I_{z'} + \Omega_{x'}\Omega_{y'}(I_{y'} - I_{x'}),
\end{cases}
\tag{3.2}
$$

known as Newton-Euler equations of motion. For the rotational dynamics the equations are heavily non-linear and are rarely directly employed to study rotordynamics behaviour. Generally, the axis of rotation is well defined and coincides with one of the axis of inertia of the rotor (small unbalance assumption) and the displacements and velocities other than the rotation about the main axis are small (small displacement assumption), which allows the simplification and linearisation of the equations of motion as explained hereafter.

Furthermore, it is assumed that the rotor rotational speed Ω is constant or its variation is considerably slower than the radial and axial dynamics, allowing for the definition of the rotordynamics model as a linear parameter-varying (LPV) model. Different levels of complexity can be considered, depending on further simplifications in the model, for the study of the dynamics of the rotor during operation. Three main models have been implemented and

employed for the study of the magnetic bearing systems in this work:

- *Jeffcott Rotor Model*: point-mass model of the rotor where no gyroscopic effect is considered. Presenting only two degrees of freedom corresponding to the linear displacements of the center of gravity [7], it is mainly employed for the design of the radial controller for the proposed hybrid magnetic bearing system.

- *Four Degrees-Of-Freedom Model*: rigid model of the rotor with consideration of gyroscopic effect [108]. This model is employed for the radial controller design of the fully active magnetic bearing system as well as the closed-loop analysis of all systems.

- *Five Degrees-Of-Freedom Model*: four degrees-of-freedom model augmented with axial dynamics as point-mass model. This model considers uncoupled radial and axial dynamics [108], but allows incorporating couplings in the remaining blocks of the simulation model. This model is employed for the full system closed-loop analysis.

Independently of the level of simplification, the general linearised equations of motion of the rotating body, considering a given set of generalised coordinates $\boldsymbol{q}(t)$, result in

$$M_q\ddot{\boldsymbol{q}}(t) + \left(D_q + G_q(\Omega)\right)\dot{\boldsymbol{q}}(t) + \left(K_q + H_q(\Omega)\right)\boldsymbol{q}(t) = \boldsymbol{f}(t), \tag{3.3}$$

being M_q the mass matrix, D_q the passive damping matrix, $G_q(\Omega)$ the gyroscopic matrix, K_q the passive stiffness matrix, $H_q(\Omega)$ the circulatory matrix, and $\boldsymbol{f}$ a generalised force vector. The exact form of the matrices are detailed hereafter for the different studied models.

Motor control and dynamics are not considered in the closed-loop simulation and analysis, and thus the rotational speed of the rotor Ω is externally imposed.

Jeffcott Rotor Model

As detailed in [108], the simplest model of a rotor spinning at constant angular speed Ω is the consideration of a rotating point mass attached to a massless shaft suspended by some axially symmetric compliant supports or bearings with stiffness k and damping d, as graphically represented in figure 3.5.a. Defining the generalised coordinates as the radial displacements of the rotor in complex coordinates, i.e. $\boldsymbol{q}(t) = r_c(t) = x_c(t) + jy_c(t)$, being j the imaginary unit, x_c and y_c the positions of the rotor's centre C, the equations of motion of such a system can be expressed as in (3.3), being the system matrices (single elements in this case)

$$M_q = m, \quad D_q = d_n + d_r, \quad G_q(\Omega) = 0, \quad K_q = k, \quad H_q(\Omega) = -j\Omega d_r, \tag{3.4}$$

with m the mass of the rotor, d_n and d_r the non-rotating and rotating damping of shaft and bearings, k the stiffness of shaft and bearings, and f the generalised (external) forces acting on the rotor.

(a) Jeffcott rotor model **(b) Four and Five Degrees-of-Freedom model**
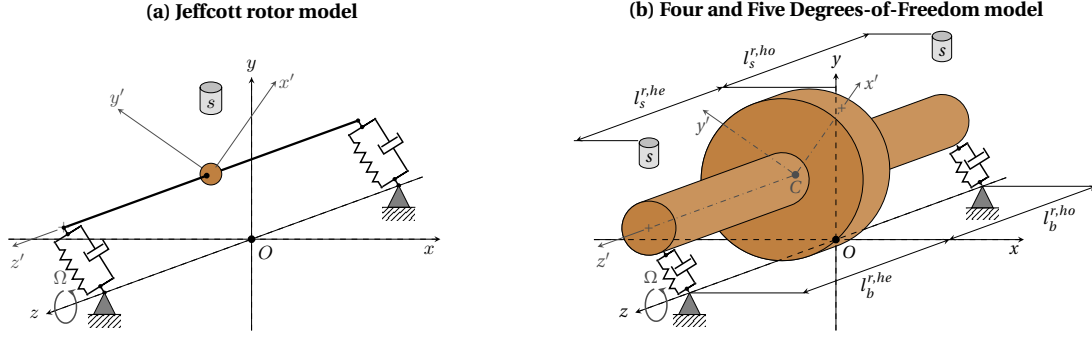
Figure 3.5 – Schematic representation of main rotordynamics models: (a) Jeffcott rotor and (b) four/five degrees-of-freedom models, consisting of a point-mass (left) or rigid body (right) rotor over compliant bearings with passive stiffness and damping, and position sensors.

As it commonly happens in practice, if the rotor is not perfectly balanced, the centre of gravity or location of the point mass, P, is located at a distance ϵ from the geometric centre, C, the rotor will be subject to unbalance forces f_u dependent on the rotation speed. If the rotor shaft is not perfectly straight and features a bow of magnitude a, the rotor will be subject to some synchronous disturbances f_a. Furthermore, when considering active bearings, apart from the passive stiffness and damping, some active forces f_b can be applied to the rotor, resulting in generalised forces f of the form

$$f(t) = f_b(t) + f_u(t) + f_a(t) + f_g(t) = f_b(t) + V_q e^{j\Omega t} + V_q' e^{j\Omega t} + mg(t) =$$
$$= f_b(t) + \left(m\epsilon\Omega^2 e^{j\alpha} \right) e^{j\Omega t} + \left(kae^{j\alpha_a} \right) e^{j\Omega t} + mg(t), \tag{3.5}$$

being V_q and V_q' the unbalance and shaft bow matrices, α the angle with respect to the x-axis of the line $C - P$ in the XY plane, α_a the phase angle of the shaft bow with respect to the x-axis, f_g the gravitational forces, and g the acceleration of gravity in complex coordinates.

The compact formulation of the equations of motion in complex coordinates reduces the number of solutions by two and allows identifying the direction (forward or backward) of the rotordynamic modes by the sign of the poles and solutions of the equation.

Four Degrees-of-Freedom Model

In order to study the behaviour of the rotor and identify some phenomena that depends on the rotor speed, the Jeffcott rotor cannot be employed. Instead of a point mass, the rotor can be considered as a rigid body of mass m with non-vanishing moments of inertia, being I_p and I_t its polar and transverse moments of inertia. As developed in [108], when considering again compliant bearings with damping behaviour, as graphically represented in figure 3.5.b, it is possible to define the equations of motion as in (3.3) by defining the generalised coordinate vector as $\boldsymbol{q} = [r_c, \phi_c]^\top$, being composed of the radial displacements of the geometric centre in complex coordinates $r_c = x_c + jy_c$ as well as the tilting of the rigid body about X and Y axes,

also in complex coordinates, $\phi_c = \phi_{y'} - j\phi_{x'}$. The resulting system matrices are defined as

$$
M_q = \begin{bmatrix} m & 0 \\ 0 & I_t \end{bmatrix}, \quad D_q = \begin{bmatrix} d_{n11} & d_{n12} \\ d_{n12} & d_{n22} \end{bmatrix} + \begin{bmatrix} d_{r11} & d_{r12} \\ d_{r12} & d_{r22} \end{bmatrix}, \quad G_q = -j\Omega \begin{bmatrix} 0 & 0 \\ 0 & I_p \end{bmatrix},
$$
$$
K_q = \begin{bmatrix} k_{11} & k_{12} \\ k_{12} & k_{22} \end{bmatrix}, \quad H_q = -j\Omega \begin{bmatrix} d_{r11} & d_{r12} \\ d_{r12} & d_{r22} \end{bmatrix},
$$
(3.6)

being subscripts $11, 12, 22$ referred to linear r, angular ϕ or crossed elements $r\phi$ of the matrices respectively. A comprehensive derivation of the previous equations can be found in [108].

Due to the consideration of a rigid rotor, the stiffness and damping coefficients consider only the bearings' passive behaviour, such as the attraction of the permanent magnet to the back iron appearing as stiffness, and the dissipation of energy due to induced eddy currents in bearing coils as damping.

In this case, an unbalanced rotor would result in forces $\boldsymbol{f}_u$ not only in an eccentricity ϵ but also in a tilt χ between the main axis of inertia and the symmetry axis of the rotor. Additionally, when the shaft of the rotor is not perfectly straight, its arc or bow a and angular misalignment χ_a will also result in additional excitation forces and torques $\boldsymbol{f}_a$. Including also the active bearing forces and torques $\boldsymbol{f}_b$ and gravitational forces $\boldsymbol{f}_g$, the generalised force vector $\boldsymbol{f}$ results in

$$
\boldsymbol{f}(t) = \boldsymbol{f}_b(t) + \boldsymbol{f}_u(t) + \boldsymbol{f}_a(t) + \boldsymbol{f}_g(t) = \boldsymbol{f}_b(t) + V_q e^{j\Omega t} + V_q' e^{j\Omega t} + \boldsymbol{f}_g(t) =
$$
$$
= \begin{bmatrix} f_{b,r}(t) \\ f_{b,\phi}(t) \end{bmatrix} + \Omega^2 \begin{bmatrix} m\epsilon e^{j\alpha} \\ \chi(I_t - I_p)e^{j\beta} \end{bmatrix} e^{j\Omega t} + K \begin{bmatrix} a e^{j\alpha_a} \\ \chi_a e^{j\beta_a} \end{bmatrix} e^{j\Omega t} + \begin{bmatrix} mg(t) \\ 0 \end{bmatrix},
$$
(3.7)

being V_q and V_q' the unbalance and shaft bow matrices, $\{\alpha, \beta\}$ and $\{\alpha_a, \beta_a\}$ the polar angles at which the unbalance and bow forces/torques appear, and K the stiffness matrix defined in (3.6). It can be seen that the forces due to the shaft bow are equivalent to an harmonic excitation with constant amplitude, whereas the unbalance ones are proportional to the square of the speed. The force due to rotor eccentricity is generally known as *static unbalance* and the torque generated by the tilt of main axis of inertia *couple unbalance*.

Such a model is used for the design of the radial position controller of the fully active magnetic bearing system and to study the behaviour of the closed loop system.

Five Degrees-of-Freedom Model

For a complete description of the rotor's behaviour, it is needed to also consider the axial dynamics, which is not possible with the four degrees-of-freedom model. In many situations, due to the small displacement assumption and having a mainly straight rotor, it is possible to decouple the radial dynamics from the torsional and axial dynamics of the rotor and study them independently, as it has been considered in the previous models. While this mainly still holds true for the studied configurations, some components of the closed-loop system can

feature cross-couplings between radial and axial dynamics, such as the geometric configuration of the eddy current axial displacement sensor or asymmetries in bearing windings. For this reason, the four degrees-of-freedom model previously presented is extended with the consideration of axial dynamics as a point-mass system.

Augmenting the generalised coordinate vector with the axial position of the geometric centre as $\boldsymbol{q} = [r_c, \phi_c, z_c]^\top$, the equations of motion of such a system are defined in (3.3) with matrices

$$
M_q = \left[\begin{array}{cc|c} m & 0 & 0 \\ 0 & I_t & 0 \\ \hline 0 & 0 & m \end{array} \right], \quad
D_q = \left[\begin{array}{cc|c} d_{n11} & d_{n12} & d_{n13} \\ d_{n12} & d_{n22} & d_{n23} \\ \hline d_{n13} & d_{n23} & d_{n33} \end{array} \right] + \left[\begin{array}{cc|c} d_{r11} & d_{r12} & d_{r13} \\ d_{r12} & d_{r22} & d_{r23} \\ \hline d_{r13} & d_{r23} & d_{r33} \end{array} \right],
$$

$$
G_q = -j\Omega \left[\begin{array}{cc|c} 0 & 0 & 0 \\ 0 & I_p & 0 \\ \hline 0 & 0 & 0 \end{array} \right], \quad
K_q = \left[\begin{array}{cc|c} k_{11} & k_{12} & k_{13} \\ k_{12} & k_{22} & k_{23} \\ \hline k_{13} & k_{23} & k_{33} \end{array} \right], \quad
H_q = -j\Omega \left[\begin{array}{cc|c} d_{r11} & d_{r12} & d_{r13} \\ d_{r12} & d_{r22} & d_{r23} \\ \hline d_{r13} & d_{r23} & d_{r33} \end{array} \right],
$$

(3.8)

being the subscript 3 referred to the axial behaviour. This formulation enables the possibility of studying the closed-system behaviour with couplings between radial and axial dynamics. These couplings can be due to non-zero stiffness or damping elements in positions 13 and 23, or due to some other components such as position sensors or bearing models with couplings between radial and axial directions, e.g. radial tilting that generates an axial displacement or a radial bearing generating axial forces.

3.3.2 Bearing Models

The detailed electromechanical models of the studied magnetic bearings are presented in chapter 4. Nevertheless, such a level of detail is not necessary for the study of the closed-loop behaviour of the magnetic bearing system during operation.

For this reason, the main characteristics of the magnetic bearings obtained through the analytical model are extracted and employed in the simulation model. Such parameters are, for instance, the relation between input current and force (force constant) κ_F for active magnetic bearings, cross couplings between radial and axial bearings and forces, and some possible dependency of this factor with the torsional angle of the rotor $\kappa_F(\phi_{z'})$, as it can be seen in the experimental measurements detailed in chapter 7. Apart from the electromagnetic characteristics of the bearings, a geometric transformation is required to convert the generated forces at the bearing planes to the forces and torques at centre of mass reference frame. To summarise, the implemented models of the magnetic bearing actuators are:

- *Ideal bearings*: simplest model consisting of a diagonal bearing force constants. Model employed for controller design and frequency-based analysis, bearings independent design of axial and radial controllers.

- *Non-ideal actuators with radial-axial cross-couplings*: model considering linearised transformation but with cross-couplings between radial and axial bearings and forces.

- *Non-ideal bearings with angle-dependent force constants*: model considering again either linearised or trigonometric transformations with bearing forces dependent on rotor torsional angle $\phi_{z'} = \Omega t$. The considered dependency is harmonic, with either first and/or second harmonics of the rotational speed.

Considering the bearing currents also in complex coordinates $\boldsymbol{u}_{cc}(t) = [i^{r,he}(t), i^{r,ho}(t), i^{a,ho}(t)]^{\top}$, where the superscripts r and a denote the current referred to radial or axial bearing, and he and ho to heteropolar and homopolar sides, respectively, the general model of the actuators can be defined as follows

$$\boldsymbol{f}_b(t) = U_q \boldsymbol{u}(t) = \left[\begin{array}{cc|c} 1 & 1 & 0 \\ l_b^{r,he} & -l_b^{r,ho} & 0 \\ \hline 0 & 0 & 1 \end{array} \right] \boldsymbol{\kappa}_F(\phi_{z'}) \left[\begin{array}{c} i^{r,he}(t) \\ i^{r,ho}(t) \\ \hline i^{a,ho}(t) \end{array} \right], \tag{3.9}$$

being U_q the bearing active force matrix, $l_b^{r,he}$ and $l_b^{r,ho}$ the axial distance between the bearing planes and the centre of mass, $\boldsymbol{\kappa}_F(\phi_{z'})$ the linear or non-linear bearing force constants, and $\boldsymbol{u}$ the input currents to the magnetic bearings. The three-phase currents of the radial bearing windings are expressed here in a field-oriented manner, by employing an amplitude-invariant Park transformation, as commonly done for rotational machinery [101] and defined in equation (2.1). In complex coordinates, $i^{r,he}$ and $i^{r,ho}$ will then be composed of the DQ components $i = i_d + j i_q$.

Ideal Bearings

Considering the ideal actuators, the geometric transformation matrix R and the bearing force factor matrix $\boldsymbol{\kappa}_F$ are independent of the rotor angle $\phi_{z'}$ and are defined as

$$\boldsymbol{\kappa}_F = \left[\begin{array}{cc|c} \kappa_F^{r,he} & 0 & 0 \\ 0 & \kappa_F^{r,ho} & 0 \\ \hline 0 & 0 & \kappa_F^{a,ho} \end{array} \right], \tag{3.10}$$

where $\kappa_F^{r,he}$, $\kappa_F^{r,ho}$ and $\kappa_F^{a,ho}$ the force constants of each magnetic bearing, namely, radial heteropolar, radial homopolar, and axial homopolar as described in chapter 2. The same nomenclature employed in the electromagnetic bearing models and design is employed here.

Non-Ideal Bearings (Cross-Couplings and Angle-Dependency)

For the case of studying bearing cross-couplings, the bearing force matrix $\boldsymbol{\kappa}_F$ remains independent of the rotor angle $\phi_{z'}$, but features now some non-zero elements outside the diagonal. The off-diagonal elements of $\boldsymbol{\kappa}_F$ can be either analytically or experimentally estimated.

For the most general case with also angle-dependency, some harmonic disturbances dependent on $\phi_{z'}$ will be present. The amplitude of such harmonic disturbances can be analytically estimated when considering some winding asymmetries or by fitting a sinusoidal from the experimental measurements shown in chapter 7. The sinusoidal modulation can be performed not only on the diagonal elements of matrix $\boldsymbol{\kappa}_F$ but also on the off-diagonal ones, as it is shown to happen in experimental measurements.

These models are employed for studying the impact of non-ideal characteristics of the bearings in the closed-loop behaviour. Due to the non-linear aspects of such studies, it is mainly exclusive to the time-based analysis of the system.

3.3.3 Position Sensor Models

The position sensors in the model will transform the state of the rotor, expressed under its centre of mass reference frame, to the radial displacements at the sensor planes located at the two axial extremes of the shaft, as schematically shown in figure 2.3, and to the axial displacement measured at the face of the inertia disk.

As in the previous case, several options have been implemented and are available for controller design and closed-loop analysis. These options can be summarised, similarly to the bearing models, as:

- *Ideal sensors*: simplest model consisting of a linearised geometric transformation with ideal uncoupled sensors. This model is employed for controller design and frequency-based analysis, allowing independent design of axial and radial controllers.

- *Non-linear sensors with radial-axial cross-couplings*: similar to previous model, but considering transformation dependent on trigonometric functions. Model employed for closed-loop time-based analysis.

Ideal Sensors

Assuming small maximum values of ϕ_c due to the small available clearance between rotor and emergency bearings, it is possible to obtain a linearised transformation of rotor states $\boldsymbol{q}$ and displacements at sensor planes $\boldsymbol{y}$, in complex coordinates, resulting in

$$\boldsymbol{y}(t) = W_q \boldsymbol{q}(t) = \left[\begin{array}{cc|c} 1 & l_s^{r,he} & 0 \\ 1 & -l_s^{r,ho} & 0 \\ \hline 0 & 0 & 1 \end{array} \right] \left[\begin{array}{c} r_c(t) \\ \phi_c(t) \\ \hline z_c(t) \end{array} \right], \tag{3.11}$$

being $l_s^{r,he}$ and $l_s^{r,ho}$ the axial position of the radial position sensor planes.

Non-Linear Sensors with Cross-Couplings

Dropping the small-angle assumption, a more precise geometric transformation can be defined. Considering that the axial eddy-current sensor is located at a radial distance $l_s^{a,ho}$, e.g. at point $[-l_s^{a,ho}, 0, 0]$, some couplings will result from the non-centred location of the axial sensor and from combination of tilting and displacements, being more precisely

$$
\boldsymbol{y}(t) = \left[\begin{array}{c} r_c(t) + \left(l_s^{r,he} - z_c(t) \right) \tan\left(\phi_c(t) \right) \\ r_c(t) - \left(l_s^{r,ho} + z_c(t) \right) \tan\left(\phi_c(t) \right) \\ \hline z_c(t) + \left(\Re\left(r_c(t) \right) + l_s^{a,ho} \right) \tan \Re\left(\phi_c(t) \right) \end{array} \right].
\tag{3.12}
$$

Depending on the radial direction in which the axial sensor is located, either $\Re(r_c)$, $\Re(\phi_c)$ or $\Im(r_c)$, $\Im(\phi_c)$, or a combination of both will appear in (3.12), being $\Re$ and $\Im$ the real and imaginary parts of the variables.

3.3.4 Position Control

The most general configuration of the position control is graphically shown in figure 3.6, which features a controller R_{pc}, estimator L_{pc} and a generalised notch filter N_f for harmonic or unbalance force rejection.

Different alternatives exist for stabilising a magnetically levitated rotor [30]. For the proposed model two main control techniques are considered depending on the application:

1. *PID or PD Controller*: the simplest controller structure that can be implemented is a decentralised and diagonal proportional-derivative (PD) or proportional-integral-derivative (PID) controller R_{pc}.

2. *State Feedback Controller*: if an accurate model of the dynamic system to control is available, it is possible to include such model in the design of a controller R_{pc} and observer L_{pc} in order to have some desired closed-loop performance through a pole-placement technique, or by solving the linear-quadratic-gaussian (LQG) problem for optimal control. This technique corresponds to a centralised and coupled control of the rotor.

In order to be included in the closed-loop model, the previous controllers are defined in a state-space formulation hereafter. Also, the generalised notch filter is independent from the employed position control technique and it is included to suppress synchronous vibrations resulting from rotor unbalance or other possible sources. Its structure is also briefly introduced here, and detailed in chapter 6.
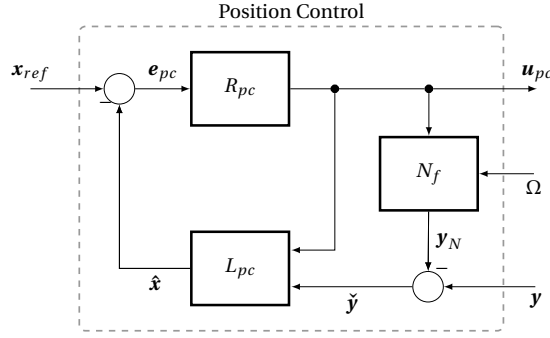
Figure 3.6 – Block diagram of position controller.

PID Controller

Considering a parallel structure of a PID with proportional k_p, integral k_i and derivative k_d gains, and a decentralised and decoupled configuration if a multiple-input and multiple-output (MIMO) system is considered, the resulting transfer function matrix (TFM) of the controller is

$$L_{pc}(s) = O, \qquad R_{pc}(s) = k_p I + \frac{k_i}{s} I + k_d \frac{w_d s}{s + w_d} I, \tag{3.13}$$

where I and O are identity and zero matrices, respectively, no state estimator L_{pc} is required, as the PID directly takes the error signal $\boldsymbol{e}_{pc}$ as input, and a first-order derivative filter with cut-off frequency w_d is considered instead of the non-causal ideal derivative s. The state-space representation of such a PID controller can then be defined in continuous-time by considering a state-space vector $\boldsymbol{x}_R$ that accounts for the derivative and integral states, resulting in

$$R_{pc} = \begin{cases} \dot{\boldsymbol{x}}_R(t) = A_R \boldsymbol{x}_R(t) + B_R \boldsymbol{e}_{pc}(t) = \begin{bmatrix} O & O \\ O & -w_d I \end{bmatrix} \boldsymbol{x}_R(t) + \begin{bmatrix} I \\ -w_d I \end{bmatrix} \boldsymbol{e}_{pc}(t), \\ \boldsymbol{u}_{pc}(t) = C_R \boldsymbol{x}_R(t) + D_R \boldsymbol{e}_{pc}(t) = \begin{bmatrix} k_i I & k_d w_d I \end{bmatrix} \boldsymbol{x}_R(t) + (k_p + k_d w_d) I \boldsymbol{e}_{pc}(t), \end{cases} \tag{3.14}$$

Furthermore, for the implementation on a digital controller it is necessary to perform the discretisation of expression (3.14), which can be done considering a first-order Euler discretisation with sampling period T_s, obtaining

$$\tilde{R}_{pc} = \begin{cases} \boldsymbol{x}_R[k+1] = \tilde{A}_R \boldsymbol{x}_R[k] + \tilde{B}_R \boldsymbol{e}_{pc}[k] = (I + T_s A_R) \boldsymbol{x}_R[k] + T_s B_R \boldsymbol{e}_{pc}[k], \\ \boldsymbol{u}_{pc}[k] = \tilde{C}_R \boldsymbol{x}_R[k] + \tilde{D}_R \boldsymbol{e}_{pc}[k] = C_R \boldsymbol{x}_R[k] + D_R \boldsymbol{e}_{pc}[k]. \end{cases} \tag{3.15}$$

State Feedback Controller

Combining the rotordynamics, sensor and bearing models defined in the previous sections, it is possible to define the dynamic system to be controlled P_q in continuous-time state-space

representation as follows

$$P_q = \begin{cases} \dot{\boldsymbol{x}}_P(t) = A_P \boldsymbol{x}_P(t) + B_P \boldsymbol{u}(t), \\ \boldsymbol{y}(t) = C_P \boldsymbol{x}_P(t), \end{cases} \tag{3.16}$$

where the state-space vector $\boldsymbol{x}_P = [\boldsymbol{q}^\top, \dot{\boldsymbol{q}}^\top]^\top$ considers the generalised coordinates and their derivative defined in the rotordynamics model. Note that for the controller design, linear and ideal bearing and sensor models as per (3.10) and (3.11) are considered.

As before, for the implementation of the controller into a digital processor it is necessary to perform the design process in discrete-time. For this reason, the dynamic system P_q is discretised using a first-order Euler discretisation with sampling period T_s, resulting in

$$\tilde{P}_q = \begin{cases} \boldsymbol{x}_P[k+1] = \tilde{A}_P \boldsymbol{x}_P[k] + \tilde{B}_P \boldsymbol{u}[k] = (I + T_s A_P)\boldsymbol{x}_P[k] + T_s B_P \boldsymbol{u}[k], \\ \boldsymbol{y}[k] = \tilde{C}_P \boldsymbol{x}_P[k] = C_P \boldsymbol{x}_P[k]. \end{cases} \tag{3.17}$$

It is then possible to define a controller R_{pc} and observer L_{pc} to stabilise the closed-loop system. The state estimator or observer is required in this case as no direct measurement of the system states, notably velocities $\dot{\boldsymbol{q}}$ and thus it needs to be estimated from the sensor measurements $\boldsymbol{y}$.

The system states can then be estimated $\hat{\boldsymbol{x}} = [\hat{\boldsymbol{q}}^\top, \hat{\dot{\boldsymbol{q}}}^\top]^\top$ considering the system dynamics (3.17), controller output signal $\boldsymbol{u}_{pc}$, measured signal $\tilde{\boldsymbol{y}}$, and an observer gain matrix L_{SF}, such that the error between measured and estimated measured signal $\boldsymbol{y} - \hat{\boldsymbol{y}}$ is minimised, resulting in

$$\tilde{L}_{pc} = \begin{cases} \hat{\boldsymbol{x}}[k+1] = \tilde{A}_L \hat{\boldsymbol{x}}[k] + \tilde{B}_L \begin{bmatrix} \boldsymbol{u}_{pc}[k] \\ \boldsymbol{y}[k] \end{bmatrix} = (\tilde{A}_P - L_{SF}\tilde{C}_P)\hat{\boldsymbol{x}}[k] + \begin{bmatrix} \tilde{B}_P & L_{SF} \end{bmatrix} \begin{bmatrix} \boldsymbol{u}_{pc}[k] \\ \boldsymbol{y}[k] \end{bmatrix}, \\ \hat{\boldsymbol{x}}[k] = \tilde{C}_L \hat{\boldsymbol{x}}[k] = I\hat{\boldsymbol{x}}[k]. \end{cases} \tag{3.18}$$

Then the actuation signal $\boldsymbol{u}_{pc}$ can be computed by considering a full-state feedback control with gain matrix K_{SF} such that $\boldsymbol{u}_{pc} = K_{SF}(\boldsymbol{x}_{ref} - \hat{\boldsymbol{x}})$. Additionally, an integral state can be included in order to counteract constant disturbances such as gravity, and thus controller gain matrix can be partitioned into $K_{SF} = [K_i, K_p, K_d]$, with integral K_i, proportional K_p and derivative K_d gain matrices, which results in a dynamic system with the following discrete-time state-space representation

$$\tilde{R}_{pc} = \begin{cases} \boldsymbol{x}_R[k+1] = \tilde{A}_R \boldsymbol{x}_R[k] + \tilde{B}_R \boldsymbol{e}_{pc}[k] = I\boldsymbol{x}_R[k] + \begin{bmatrix} T_s I & O \end{bmatrix} \boldsymbol{e}_{pc}[k], \\ \boldsymbol{u}_{pc}[k] = \tilde{C}_R \hat{\boldsymbol{x}}[k] + \tilde{D}_R \boldsymbol{e}_{pc}[k] = K_i \boldsymbol{x}_R[k] + \begin{bmatrix} K_p & K_d \end{bmatrix} \boldsymbol{e}_{pc}[k]. \end{cases} \tag{3.19}$$

Note that here again, a first-order Euler discretisation is employed to perform the integration of the position error $\boldsymbol{q}_{ref} - \hat{\boldsymbol{q}}$. Furthermore, if no integral state is considered in the controller,

R_{pc} is reduced to $\tilde{A}_R = \tilde{B}_R = \tilde{C}_R = O$ and simply $\tilde{D}_R = [K_p, K_d]$.

Then, the selection of observer and controller gain matrices L_{SF} and K_{SF} will depend on the chosen design approach, such as pole-placement to obtain desired closed-loop dynamics or by solving the linear-quadratic-gaussian (LQG) problem for optimal control [30].

Generalised Notch Filter

Lastly, a generalised notch filter for harmonic disturbance suppression is also considered. The implemented approach takes the estimation of the bearing forces as input, which are in this case the currents $\boldsymbol{u}_{pc}$, to generate an harmonic signal that will remove the harmonic part of the measurements $\boldsymbol{y}$ and thus avoiding reacting to the unbalance or other excitation at the rotation frequency and higher harmonics. This is achieved for the l-th harmonic by considering the following state-space dynamic system

$$\dot{\boldsymbol{x}}_{Nl}(t) = A_{Nl}\boldsymbol{x}_{Nl}(t) + B_{Nl}\boldsymbol{u}_{pc}(t) = \begin{bmatrix} jl\Omega I & O \\ O & -jl\Omega I \end{bmatrix} \boldsymbol{x}_{Nl}(t) + c_c \frac{\Omega}{|\Omega|} \begin{bmatrix} jI \\ -jI \end{bmatrix} \boldsymbol{u}_{pc}(t),$$

$$\boldsymbol{y}_{Nl}(t) = C_{Nl}\boldsymbol{x}_{Nl}(t) = \frac{1}{2}\begin{bmatrix} I & I \end{bmatrix} \boldsymbol{x}_{Nl}(t),$$

(3.20)

being I an identity matrix, O a zero matrix, c_c the convergence rate of the filter, which also defines its bandwidth, and combining for all $l \in \{1, 2, \ldots, n_h\}$ harmonics that will be suppressed results in

$$N_f = \begin{cases} \dot{\boldsymbol{x}}_N(t) = A_N\boldsymbol{x}_N(t) + B_N\boldsymbol{u}_{pc}(t) = \begin{bmatrix} A_{N1} & \cdots & O \\ \vdots & \ddots & \vdots \\ O & \cdots & A_{Nn_h} \end{bmatrix} \boldsymbol{x}_N(t) + \begin{bmatrix} B_{N1} \\ \vdots \\ B_{Nn_h} \end{bmatrix} \boldsymbol{u}_{pc}(t), \\ \boldsymbol{y}_N(t) = C_N\boldsymbol{x}_N(t) = \begin{bmatrix} C_{N1} & \cdots & C_{Nn_h} \end{bmatrix} \boldsymbol{x}_N. \end{cases}$$

(3.21)

A more detailed description of the proposed generalised notch filter is performed in chapter 6.

3.3.5 Current Control

As shown in figure 3.4, the magnetic bearing system features a cascaded control loop of position and currents. Due to the much faster dynamics of the electrical system (current control) with respect to the mechanical system (position control) it is possible to consider for the position controller design that the currents circulating through the bearing windings are exactly the output of the controller.

A detailed description of the dynamics of the electrical system and the design of the current controller R_{cc} is performed in [103]. Its execution on the real system is performed on a field-programmable gate array (FPGA), allowing a parallel and fast execution of the controller

at 800 kHz. The design of the current controller is performed to guarantee a closed-loop bandwidth of >10 kHz in order to minimise its impact on the position control that will be executed at 20 kHz.

Under these conditions, it is considered for the complete closed-loop system model that the electrical system behaves like a low-pass filter with cutoff frequency, ω_{bw}, equal to the current control bandwidth, and a delay, τ_{cc}, equal to the execution time of the controller in the FPGA. The exact model of the controlled currents is then obtained as a transfer unction of the form

$$R_{cc}(s) = \frac{1}{\frac{s}{\omega_{bw}} + e^{-s\tau_{cc}}}. \tag{3.22}$$

3.4 Stability Analysis

The previous rotor, bearings, sensor and controller dynamic equations are combined in a simulation model implemented using MATLAB. This simulation environment is capable of performing the controller design and analyse the closed-loop behaviour of the system. Two types of studies are available:

1. *Frequency-based analysis*: study of the closed-loop stability and performance in the frequency domain, representative for the steady-state behaviour of the linear/linearised system.

2. *Time-based analysis*: study of the closed-loop behaviour in the time domain, capable of assessing the stability and performance of the system including non-linearities and transient responses.

For both types of analysis, each component is transformed into a state-space representation of its dynamics, and each block connected to each other as graphically shown in figure 3.4. If the considered models are linear, both analysis should provide similar results, but the time domain study enables the possibility of considering non linearities in the system and thus making it more versatile.

In both cases, torsional dynamics are not considered, and thus the rotating speed is imposed externally. In order to study the behaviour and stability of the rotating system, the simulation is run for several speed steps until the whole speed range of the motor is covered.

3.4.1 Frequency-Based Analysis

A multiple-input multiple-output (MIMO) analysis technique is required for the study of the dynamics. The analysis in the frequency domain provides a description of the stability and behaviour of the closed-loop system in steady state and is the common approach used for control design. As previously mentioned, the use of complex coordinates for the radial
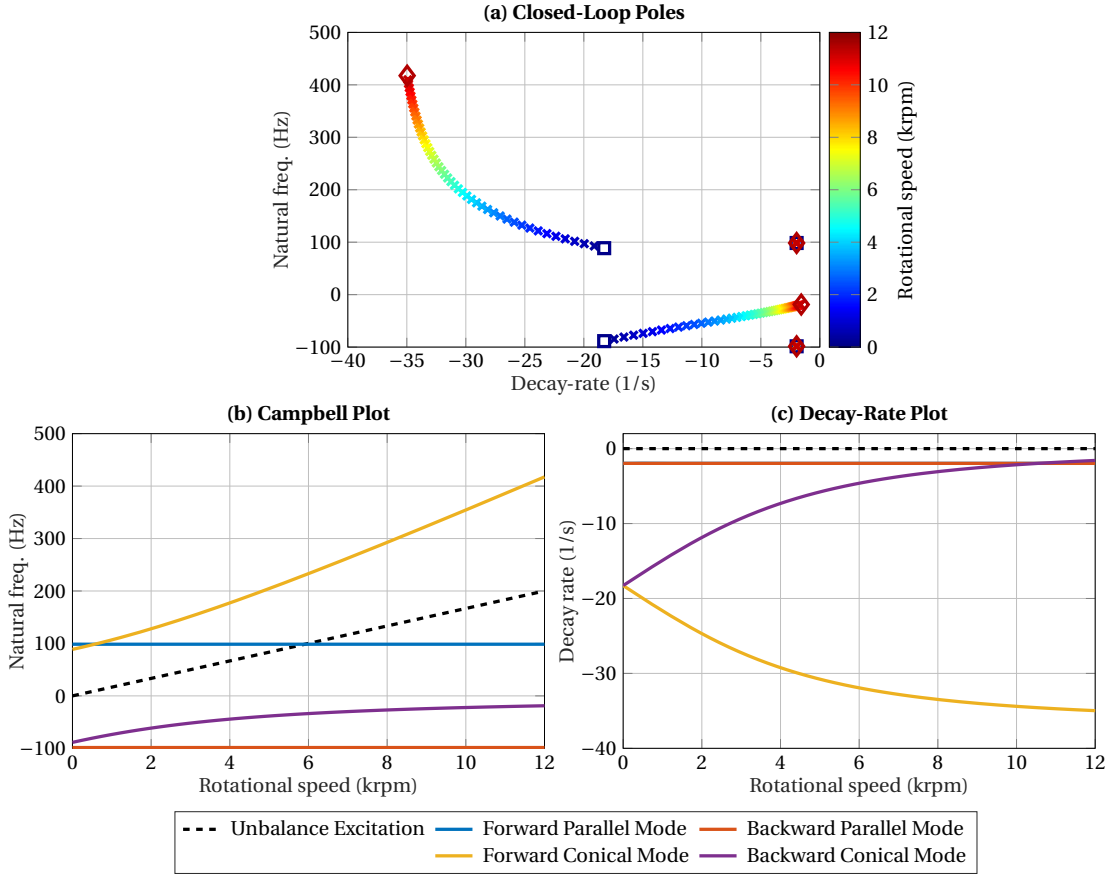
Figure 3.7 – Example of frequency-based analysis results: closed-loop poles, Campbell and decay-rate plots.

rotordynamics is preferred to facilitate the identification and differentiation of the different whirling modes. All analyses shown hereafter are valid under the assumption of constant or relatively slow varying rotational speed Ω.

The main tools employed for the frequency-based analysis are the following:

- *Closed-loop poles*: it is possible to study the stability and main behaviour of the system by analysing its closed-loop poles for the whole speed range. This analysis is commonly done in the form of a pole-zero map, figure 3.7.a, as well as a Campbell diagram, figure 3.7.b, combined with a decay-rate plot, figure 3.7.c. As it can be seen in the example figures, both represent the same results but arranged in a different manner, and thus the Campbell-decay-rate plots allow clearly identifying the dependency of the different whirling modes' natural frequency and decay rates on the rotating speed Ω.

  By employing complex coordinates the different whirling modes are clearly differentiated by an opposite natural frequency: forward whirling modes are identified by a positive sign of the natural frequency, whereas the backward whirling modes have negative frequency, implying the same or opposite rotating direction with respect to Ω,
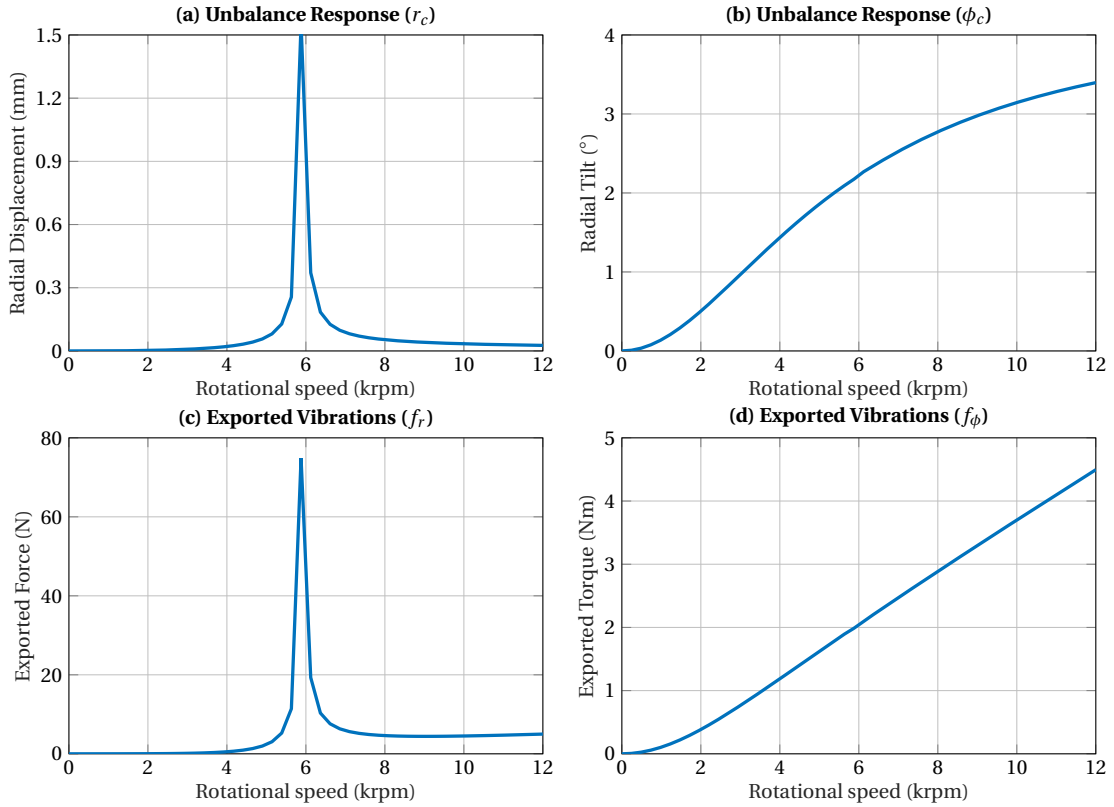
Figure 3.8 – Example of frequency-based analysis results: unbalance response and exported vibrations.

respectively.

In figure 3.7, it is shown as an example, the results of a fully passive and stable system, with positive values of stiffness, k and non-rotating damping, d_n, that could represent a ball bearing motor. This system is considered for its simplicity to show the possibilities of the developed modelling and design tools.

- *Steady-state harmonic disturbance response*: when considering a set of harmonic disturbances as described in equation (3.7) it is possible to simulate the response of the system in the frequency domain. The main results of such an analysis would be the displacements of the system, generally at the sensor planes to verify that the mechanical clearings in the stator are sufficient to avoid any crash, or the generated vibrations.

  In figures 3.8.a and 3.8.b, the unbalance response of the same simple fully passive system is shown. It can be seen that at the speed where one of the whirling modes in figure 3.7.b crosses the rotation frequency a critical speed is present, with big displacements and forces. This is due to the fact that the unbalance excitation is an harmonic disturbance with frequency equal to the rotation as shown in expression (3.7).

- *Steady-state exported micro-vibrations*: performing the same calculations as for the harmonic disturbance response, but considering the forces appearing between rotor

47

and stator, such as stiffness and damping passive forces, as well as active bearing forces, it is possible to calculate the level of vibrations that the machine will generate during operation.

As before, the same passive system is considered, and in figures 3.8.c and 3.8.d the exported forces and torques per speed, respectively, are shown. With this type of analysis it is possible to verify not only if the system is unstable, but also if some allowable limits in displacements or generated forces are satisfied or not.

3.4.2 Time-Based Analysis

In this case, any desired combination of rotordynamic, sensor and bearing models with position and current controller are employed in the time domain to study the evolution of the closed-loop system. All dynamic equations are numerically integrated employing a fourth-order Runge-Kutta method to obtain the evolution of the system with time and investigate its stability and general behaviour. As previously mentioned, this approach allows for the consideration of non-linearities in the models for a more precise study of the system.

Furthermore, due to the resulting signals in the time domain, similar analysis techniques to the ones employed in experimental vibration measurements of rotating machinery can be employed, such as waterfall or worst-case plots, and thus obtain a more clear comparison between real and simulated systems.

The time-domain simulation is implemented by considering an initial system state, $\boldsymbol{x}_0$, constant rotor speed, Ω, and evaluating system state at every controller period (20 kHz) and numerically integrating the system dynamics between sample times, t_k and t_{k-1}, until a maximum time is reached. This process is repeated for different speeds until the whole speed range of the wheel is studied.

Then, to complete the stability and performance studies of the closed-loop system, the following time-based analysis tools are used:

- *Harmonic disturbance response*: obtained by considering as input the generalised force amplitude and direction specified in the rotordynamics models for each speed, as defined in expression (3.7), and showing the amplitude of the maximum rotor displacements and tilts.

  If the considered system model is linear, and the final simulation time is long enough to reach steady-state, as it is the case for the simple passive system considered as example, the results obtained here are equivalent to the ones shown in figures 3.8.a and 3.8.b.

- *Exported micro-vibrations*: obtained by considering the forces appearing between rotor and stator of the closed-loop system under harmonic disturbance excitation, namely: bearing passive stiffness and damping, and active bearing forces.

On the one hand, it can be considered, as before, the maximum value of the forces and torques generated at each speed, which would result in an equivalent result to the one obtained using frequency-based analysis in figures 3.8.c and 3.8.d.

On the other hand, as it will be shown in chapter 7 for the validation of the closed-loop model, due to the availability of a time series of a force and torque signal for the whole speed range, as generally happening in an experimental vibration measurement campaign, the same tools employed for analysing machine vibrations [10], [11] can be employed. These tools have been detailed in section 3.2, and correspond to waterfall, worst-case and noise-vs-speed plots, which rely on the calculation of a fast Fourier transform (FFT) of the signal for each speed to convert it to the frequency or order domain.

Due to the possibility of directly comparing experimental measurements with simulation results in the time domain, these analysis tools will be employed for the validation of the simulation model for the studied fully active magnetic bearing system in chapter 7. The vibration measurements obtained from a multi-component dynamometer and the rotor orbits measured with the internal displacement sensors will be compared to the simulation results for validation.

3.5 Conclusions

In this chapter a complete closed-loop simulation model of a magnetic bearing system capable of analysing the stability, performance and generated vibrations during operation of the system is presented. Furthermore, an overview of the micro-vibration sources for magnetic bearing system is performed, and a set of micro-vibration measurement techniques are introduced.

The main contributions of this chapter are:

- The main vibration sources of magnetically levitated systems have been identified and described. The quantification of the sources is performed for Celeroton's magnetic bearing system in chapter 7.

- A novel micro-vibration measurement approach for active magnetic bearing systems is presented. Its validation is described in chapter 7.

- A modular closed-loop simulation model is developed and presented. The modularity relies on the possibility of incorporating more detailed or ideal models for elements such as rotordynamics, bearing, sensors or controller models.

- A comprehensive analysis toolbox is developed in MATLAB and its main characteristics are described. This toolbox is employed for position, current controllers and unbalance control design, and its use is shown in chapters 5 and 6.

4 Magnetic Bearing and Motor Electromagnetic Modelling

In order to be able to accurately design and optimise the desired actuators, it is necessary to have a detailed model of the components. In this chapter, all the required electromagnetic models of the different studied actuators such as active or passive magnetic bearings and motor will be presented and developed.

Firstly, in section 4.1, the electromagnetic models of the active slotless magnetic bearings and motor is detailed, enabling the possibility of calculating the main characteristics of the actuators, such as force or torque constants, winding resistance for Joule loss estimation, as well as the force disturbances for some cases. Secondly, in section 4.2, the electromagnetic models of several iron-less passive magnetic bearing structures are developed, providing a force, torque and passive stiffness calculation for characterising the bearings. Lastly, in section 4.3, the numerical validation of some core elements of the defined models is performed by comparing it to a reference finite element model of each studied configuration.

A preliminary version of the active magnetic bearing models is presented in [46] for skewed and axial windings, and has been completed in [47] for rhombic and hexagonal windings. Also, the passive magnetic bearing models have been introduced in [48]. The remaining validation of the models is experimentally performed and detailed in chapter 7.

4.1 Active Magnetic Bearing and Motor Force and Torque Models

The electromagnetic force and torque applied in a electric machine can be calculated by integrating the electromagnetic force $\mathrm{d}\boldsymbol{F}$ and torque $\mathrm{d}\boldsymbol{T}$ density over the stator volume V and back iron inner surface S, where the force density can be divided according to its origin

$$\boldsymbol{F} = \iiint_V \mathrm{d}\boldsymbol{F} = \iiint_V (\mathrm{d}\boldsymbol{F}_{lor} + \mathrm{d}\boldsymbol{F}_{rel}) = \iiint_V \boldsymbol{J} \times \boldsymbol{B}\,\mathrm{d}V + \oint_S \mathscr{T} \cdot \boldsymbol{n}\,\mathrm{d}S, \tag{4.1a}$$

$$\boldsymbol{T} = \iiint_V \boldsymbol{v} \times \mathrm{d}\boldsymbol{F} = \iiint_V \boldsymbol{v} \times (\mathrm{d}\boldsymbol{F}_{lor} + \mathrm{d}\boldsymbol{F}_{rel}), \tag{4.1b}$$

being $\mathrm{d}\boldsymbol{F}_{lor}$ the Lorentz force generated in the stator winding, $\mathrm{d}\boldsymbol{F}_{rel}$ the reluctance force generated by the armature flux in the back iron in the machine due to a change in magnetic permeability, $\boldsymbol{J}$ the current density vector, $\boldsymbol{B}$ the magnetic flux density vector, $\mathscr{T}$ the Maxwell stress tensor, and $\boldsymbol{n}$ normal surface vector of the back iron over which $\mathscr{T}$ is integrated.

In order to obtain the expression of the force and torque as a function of the controlled currents, the following steps need to be undertaken:

1. Definition of the magnetic flux density distribution, $\boldsymbol{B}$, for each configuration: homopolar and heteropolar sides with and without back iron.

2. Definition of the current density distribution, $\boldsymbol{J}$, in the winding volumes for each employed winding type: skewed, rhombic, hexagonal and axial.

3. Perform integration of Lorentz force, $\boldsymbol{F}_{lor}$, and torque, $\boldsymbol{T}_{lor}$, over the whole winding volume.

4. If the configuration features back iron, calculate the amplification factor due to the reluctance forces, $\boldsymbol{F}_{rel}$.

All these steps are detailed hereafter.

4.1.1 Magnetic Flux Density Distribution

The accuracy and computational time required to evaluate the electromechanical models of every actuator will greatly depend on the employed magnetic flux density model, and thus it is crucial to select the appropriate one depending on the needs. Furthermore, as there are two sides with different arrangement of the magnets, heteropolar and homopolar, and each of them can feature or not soft magnetic materials (back iron), the field models will have to be specific for each of the cases, so no general model will be possible.

In this section, an overview of some of the possible magnetic flux density models will be performed for each of the cases: heteropolar and homopolar sides with and without back iron. The procedure shown here below should not be considered an exhaustive overview of possible modelling alternatives. A more detailed overview can be found in [109].

For all the configurations, only the magnetostatic case is studied due to the following assumptions:

1. All materials are linear, i.e. $\boldsymbol{B} = \mu_0 \mu_r \boldsymbol{H}$, being μ_0 the magnetic permeability in vacuum, and μ_r the relative permeability of the material.

2. The only source of magnetic field is the permanent magnet, which is considered to be a hard ferromagnet with magnetisation $\boldsymbol{M}_0$, i.e. $\boldsymbol{B} = \mu_0 \mu_r \boldsymbol{H} + \mu_0 \boldsymbol{M}_0$.
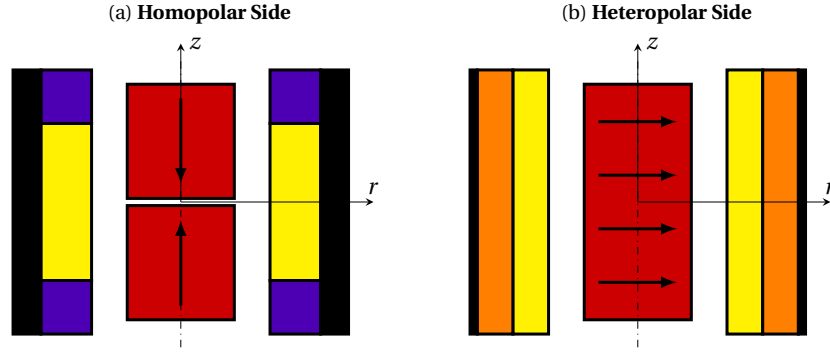
Figure 4.1 – Schematic cross-sectional representation of homopolar and heteropolar sides with back iron and its associated reference frames. For heteropolar side the cross-section is shown for $\varphi = 0$.

3. All materials are non-conductive (no eddy currents).

4. Any dependency in time of the field is neglected (static conditions).

The magnetic field generated by the winding current and its interaction with the back iron will be considered in section 4.1.4.

Due to the assumption of absence of current sources for the definition of the field in the machine's air-gap, the easiest approach is the consideration of the total scalar potential Φ_M, such that $\boldsymbol{H} = -\nabla\Phi_M$, for solving magnetostatic Maxwell's equations [110], resulting in Poisson's and Laplace's equations inside and outside the permanent magnet, respectively:

$$\Delta\Phi_M = \nabla^2\Phi_M = \begin{cases} \frac{1}{\mu_r}\nabla \cdot \boldsymbol{M}_0, & \text{inside magnet,} \\ 0, & \text{outside magnet.} \end{cases} \tag{4.2}$$

Depending on the imposed boundary conditions and the performed assumptions, the different cases for each configuration can be considered. For the studied fully active magnetic bearing system, as described in chapters 2 and 5, four different configurations need to be analysed: homopolar side (two facing axially-mangetised permanent magnets) without and with back iron in stator, and heteropolar side (single diametrically-magnetised permanent magnet) without and with back iron. These configurations are studied more in detail hereafter.

Homopolar side without back iron

This configuration is modelled as two facing axially-magnetised permanent magnets of cylindrical shape with remanent flux density B_{rem}, radius R_{pm}^{ho} and length L_{pm}^{ho} surrounded by air. It can then be assumed that no boundaries are present, and thus the free-space Green's function can be employed for defining the field around the magnet [110]:

- *2D axisymmetric flux density with elliptic integrals*: The potential at position $\boldsymbol{r} = (r, \varphi, z)$

is defined as the integral over the magnet volume V_M

$$\Phi_M(\boldsymbol{r}) = -\frac{1}{4\pi} \iiint_{V_M} \frac{\nabla' \cdot \boldsymbol{M}_0}{|\boldsymbol{r} - \boldsymbol{r}'|} d^3 r', \tag{4.3}$$

which is also known as the Coulomb model of a permanent magnet [111]. This integral can then be transformed into the magnetic flux density $\boldsymbol{B}$ using the definition of the magnetic potential in vacuum $\boldsymbol{B} = -\mu_0 \nabla \Phi_M$ and reformulating it by using elliptic integrals for a fast implementation without any loss in accuracy [112], as already validated in [47] and in section 4.3.

Following the procedure performed in [112], with some small modifications for a more homogeneous notation with the passive bearing models by considering $r_j = \{r_1, r_2\} = \{0, R_{pm}^{ho}\}$ and $z_k = \{z_1, z_2\} = \{-L_{pm}^{ho}/2, L_{pm}^{ho}/2\}$, the magnetic flux density distribution generated by a single magnet can be reformulated using elliptic integrals and some auxiliary parameters, resulting in

$$B_{ri}^{ho}(r,z) = \frac{B_{rem}}{\pi} \sum_{j=1}^{2} \sum_{k=1}^{2} (-1)^{j+k} \frac{r_j}{\sigma_{jk}} \left[\left(1 - \frac{2}{m_{jk}}\right) K(m_{jk}) + \frac{2}{m_{jk}} E(m_{jk}) \right], \tag{4.4a}$$

$$B_{zi}^{ho}(r,z) = \frac{B_{rem}}{\pi} \sum_{j=1}^{2} \sum_{k=1}^{2} (-1)^{j+k} \frac{r_j}{\sigma_{jk}} \frac{(z+z_k)(1+\xi_j)}{(r+r_j)n_j} \left[K(m_{jk}) - \xi_j \Pi(n_j, m_{jk}) \right], \tag{4.4b}$$

being the auxiliary parameters σ_{jk}, ξ_j, m_{jk} and n_j defined as

$$\xi_j = \frac{r - r_j}{r + r_j}, \qquad n_j = 1 - \xi_j^2 = \frac{4rr_j}{(r+r_j)^2},$$

$$\sigma_{jk} = \sqrt{(z+z_k)^2 + (r+r_j)^2}, \quad m_{jk} = \frac{4rr_j}{(z+z_k)^2 + (r+r_j)^2}. \tag{4.5}$$

Note that for this case no summation in j is necessary and can be omitted here, but it allows the possibility of considering hollow cylindrical permanent magnets by using $r_j = \{r_1, r_2\} = \{R_{pmi}^{ho}, R_{pmo}^{ho}\}$. These functions are a combination of complete elliptic integrals of the first, K, second, E, and third kind Π, as mathematically defined in appendix A. Due to the axial symmetry of the domain, the azimuthal component vanishes $B_{\varphi}^{ho} = 0$ and no dependency on φ is present.

Finally, the total magnetic flux density generated by the pair of facing axially-magnetised permanent magnets that compose the homopolar side of the machine can be calculated by using the superposition principle and considering the axial half distance between both magnets z_0, resulting in the expression, in cylindrical coordinates,

$$\boldsymbol{B}^{ho}(r,z) = \begin{bmatrix} B_{ri}^{ho}(r, z+z_0) + B_{ri}^{ho}(r, z_0 - z) \\ 0 \\ B_{zi}^{ho}(r, z+z_0) - B_{zi}^{ho}(r, z_0 - z) \end{bmatrix}. \tag{4.6}$$

Heteropolar side without back iron

This configuration can be modelled as one diametrically-magnetised permanent magnet of cylindrical shape with remanent flux density B_{rem}, radius R_{pm}^{he} and length L_{pm}^{he} surrounded by air. The same approach defined for the homopolar side without back iron can be applied here:

- *3D flux density with elliptic integrals*: by simply changing the magnetisation direction of the permanent magnet in (4.3), it is also possible to reformulate the expression in terms of elliptic integrals, as performed in [112], being its applicability for force/torque models validated in [47].

  The expression of the magnetic flux density distribution, employing the same approach defined in [112], being in this case $r_j = \{r_1, r_2\} = \{0, R_{pm}^{he}\}$ and $z_k = \{z_1, z_2\} = \{-L_{pm}^{he}/2, L_{pm}^{he}/2\}$ and auxiliary parameters from (4.5), results in

$$B_r^{he}(r, \varphi, z) = \frac{B_{rem}}{2\pi r} \cos\varphi \sum_{j=1}^{2} \sum_{k=1}^{2} (-1)^{j+k} \frac{r_j}{\sigma_{jk}} (z + z_k) \left[\left(\frac{2}{m_{jk}} - \frac{2\xi_j}{n_j} - 1 \right) K(m_{jk}) - \right.$$
$$\left. - \frac{2}{m_{jk}} E(m_{jk}) + \frac{\xi_j + \xi_j^3}{n_j} \Pi(n_j, m_{jk}) \right], \tag{4.7a}$$

$$B_\varphi^{he}(r, \varphi, z) = \frac{B_{rem}}{\pi r} \sin\varphi \sum_{j=1}^{2} \sum_{k=1}^{2} (-1)^{j+k} \frac{r_j}{\sigma_{jk}} (z + z_k) \left[\left(\frac{1}{m_{jk}} + \frac{\xi_j^2}{n_j} \right) K(m_{jk}) - \right.$$
$$\left. - \frac{1}{m_{jk}} E(m_{jk}) - \frac{\xi_j^3}{n_j} \Pi(n_j, m_{jk}) \right], \tag{4.7b}$$

$$B_z^{he}(r, \varphi, z) = \frac{B_{rem}}{\pi} \cos\varphi \sum_{j=1}^{2} \sum_{k=1}^{2} (-1)^{j+k} \frac{r_j}{\sigma_{jk}} \left[\left(1 - \frac{2}{m_{jk}} \right) K(m_{jk}) + \frac{2}{m_{jk}} E(m_{jk}) \right]. \tag{4.7c}$$

  It has been considered, for simplicity, that the magnetisation direction is along the X-axis. Note again that no summation in j is necessary for this case and it can be omitted, but it allows the possibility of considering hollow cylindrical permanent magnet by using $r_j = \{r_1, r_2\} = \{R_{pmi}^{he}, R_{pmo}^{he}\}$.

Homopolar side with back iron

It can be modelled as two facing axially-magnetised permanent magnets of cylindrical shape with radius R_{pm}^{ho} and length L_{pm}^{ho} surrounded by air and a cylindrical shell of radius R_{sti}^{ho}-R_{sto}^{ho} and length L_{st}^{ho} made of soft magnetic material. Different assumptions can be considered in this case:

- *2D axisymmetric flux density by Fourier series expansion*: considering the most complete problem, it is possible to solve (4.2) by separation of variables, performing the Fourier series expansion of the magnet magnetisation and then connecting the solutions in the

different regions [110], [113]. A general method is described in [113], [114] which is used for solving the boundary value problem for the homopolar configuration.

- *2D axisymmetric flux density with elliptic integrals*: the expression derived using elliptic integrals can then be generalised to account for the effect of the back iron by a linear correcting factor $\Lambda = \text{diag}(\lambda_r, \lambda_\varphi, \lambda_z)$.

The effect of the back iron is quantified by evaluating the relative increase or reduction of the radial, azimuthal and axial components of the magnetic flux density in the air-gap using a magnetostatic Finite Element Model (FEM) or Fourier series expansion [113], [115]. The magnetic flux density distribution in cylindrical coordinates in an air-gap with back iron, $\boldsymbol{B}|_{R_{sti}}$, is approximated by considering the magnetic flux density without back iron, $\boldsymbol{B}|_{R_{sti} \to \infty}$, and a constant coefficient matrix Λ,

$$\boldsymbol{B}|_{R_{sti}}(r,\varphi,z) = \Lambda \, \boldsymbol{B}|_{R_{sti} \to \infty}(r,\varphi,z) = \begin{bmatrix} \lambda_r & 0 & 0 \\ 0 & \lambda_\varphi & 0 \\ 0 & 0 & \lambda_z \end{bmatrix} \begin{bmatrix} B_r(r,\varphi,z) \\ B_\varphi(r,\varphi,z) \\ B_z(r,\varphi,z) \end{bmatrix}\Bigg|_{R_{sti} \to \infty}, \qquad (4.8)$$

where Λ is obtained using the expressions

$$\lambda_r = \frac{\iiint_V B_r|_{R_{sti}}}{\iiint_V B_r|_{R_{sti} \to \infty}}, \quad \lambda_\varphi = \frac{\iiint_V B_\varphi|_{R_{sti}}}{\iiint_V B_\varphi|_{R_{sti} \to \infty}}, \quad \lambda_z = \frac{\iiint_V B_z|_{R_{sti}}}{\iiint_V B_z|_{R_{sti} \to \infty}}, \qquad (4.9)$$

calculated over each winding's volume V using a reference magnetic model. In this case the reference model obtained using separation of variables and Fourier series expansion, as described in [113], [115], is used. The advantage of employing such an approximation is the possibility of exploiting the fast calculations of elliptic integrals for the calculation of the winding forces and torques, enabling its use in the optimisation process and design of the actuator, and only requiring the computationally expensive evaluation of Λ when the dimensions of the domains are modified. This approach has been validated in [47] and included in section 4.3.

Heteropolar side with back iron

This configuration can be modelled as one diametrically-magnetised permanent magnet of cylindrical shape with radius R_{pm}^{he} and length L_{pm}^{he} surrounded by air and a cylindrical shell of radius R_{sti}^{he}-R_{sto}^{he} and length L_{st}^{he} made of soft magnetic material. The options for this case will be again similar to the ones defined for the homopolar side:

- *3D flux density by Fourier series expansion*: as with the homopolar configuration, it is possible to solve (4.2) by separation of variables, performing the Fourier series expansion of the magnet magnetisation and then connecting the solutions in the different regions [110], [113]. This approach is derived in [115] for slotless machines with diametrical or radial magnetisation considering a back iron with infinite length and permeability and

can be directly employed for this configuration.

- *3D flux density with elliptic integrals*: exploiting the linear properties of the Lorentz force it is possible to express $\boldsymbol{B}$ using the expressions of the case without iron [112], and account for the effect of the back iron in the flux distribution by a linear correcting factor $\Lambda = \mathrm{diag}(\lambda_r, \lambda_\varphi, \lambda_z)$, as also done for the 2D approximation, calculated using (4.9). This approach is equivalent to the one described for the homopolar side and is validated in [47] and section 4.3.

- *2D flux density*: assuming a sufficiently long machine, the effect of the end of the permanent magnet ends can be neglected, resulting in a 2D polar (r, φ) flux model that can be solved by separation of variables [109], [116]. To consider the effect of the ends of the magnet (stray flux), it is possible to include a linear correcting factor $\Lambda = \mathrm{diag}(\lambda_r, \lambda_\varphi, \lambda_z)$ that will amplify or decrease each component $\boldsymbol{B} = \Lambda \boldsymbol{B}_{2D}$, which is calculated for each radial, azimuthal and axial component as in (4.9). The reference model can be calculated by FEA or as described in [113], [115].

Due to the cylindrical geometry of the studied problems, all the previous models will be expressed in cylindrical coordinates, and can thus be transformed to Cartesian coordinates, $(r, \varphi, z) \mapsto (x, y, z)$, as follows

$$\boldsymbol{B} = \begin{bmatrix} B_x \\ B_y \\ B_z \end{bmatrix} = \begin{bmatrix} cos(\varphi) & -sin(\varphi) & 0 \\ sin(\varphi) & cos(\varphi) & 0 \\ 0 & 0 & 1 \end{bmatrix} \begin{bmatrix} B_r \\ B_\varphi \\ B_z \end{bmatrix}, \tag{4.10}$$

for its introduction in the Force/Torque models presented in the next sections.

4.1.2 Winding Models

Due to the slotless topology of the magnetic bearings and motor, the force and torque will be mainly generated by the Lorentz force acting on the air-gap windings. There exists a broad variety of slotless windings that can be studied, such as straight windings [27], skewed or Faulhaber windings of figure 4.2.a [101], [117], rhombic windings of figure 4.2.b [101], hexagonal windings of figure 4.2.c [118], [119], toroidal windings among many others, that can be manufactured using self-bonding wire or even flexible PCB technology [99].

The procedure that must be undertaken to define the current density distribution was initially defined in [101] mainly for skewed windings, and in [47] for the remaining winding types. For all the winding types, it is necessary to perform the following steps:

- Define the parametric curve in space $\boldsymbol{\nu}$ that specifies the position of an infinitesimal winding volume. Considering three parameters (ρ, ϕ, α) to fully define winding volume with the parametric curve $\boldsymbol{\nu}$, in which one of them, ϕ defines the shape of the winding

loop, and the other two, ρ and α, the initial position of such a winding loop, the position in space in Cartesian coordinates of a point in the winding will be defined by a function of the form

$$\boldsymbol{v}(\rho,\phi,\alpha) = \begin{bmatrix} v_x(\rho,\phi,\alpha) \\ v_y(\rho,\phi,\alpha) \\ v_z(\rho,\phi,\alpha) \end{bmatrix}. \tag{4.11}$$

- The unitary tangential vector $\boldsymbol{e}_v$ that will define the direction of the current density vector can be directly computed from the winding parametrisation by computing the derivatives of each component $\{v'_x, v'_y, v'_z\}$ with respect to the parameter that defines the curve direction, being ϕ for all the parametrisations defined hereafter. It can be calculated as

$$\boldsymbol{e}_v(\rho,\phi,\alpha) = \frac{\boldsymbol{v}'(\rho,\phi,\alpha)}{\|\boldsymbol{v}'(\rho,\phi,\alpha)\|} = \frac{1}{\|\boldsymbol{v}'\|}\begin{bmatrix} v'_x \\ v'_y \\ v'_z \end{bmatrix} = \frac{\frac{\partial \boldsymbol{v}}{\partial \phi}}{\left\|\frac{\partial \boldsymbol{v}}{\partial \phi}\right\|}. \tag{4.12}$$

- Transform the infinitesimal winding volume in Cartesian coordinates $\mathrm{d}V = \mathrm{d}x\mathrm{d}y\mathrm{d}z$ to the infinitesimal volume with respect to the winding parameters (ρ,ϕ,α) through a change of variables

$$\mathrm{d}V = \mathrm{d}x\mathrm{d}y\mathrm{d}z = \left|\frac{\partial(v_x, v_y, v_z)}{\partial(\rho,\phi,\alpha)}\right|\mathrm{d}\rho\mathrm{d}\phi\mathrm{d}\alpha, \tag{4.13}$$

being $\left|\partial(v_x, v_y, v_z)/\partial(\rho,\phi,\alpha)\right|$ the determinant of the Jacobian matrix of the transformation $(x, y, z) \mapsto (\rho,\phi,\alpha)$.

- Define the area $A_\perp$ perpendicular to $\boldsymbol{e}_v$ in order to calculate the homogenised current density distribution in the windings. It can be calculated as the division of an infinitesimal winding volume $\mathrm{d}V$ and the length of an infinitesimal arc segment $\|\boldsymbol{v}'\|$

$$A_\perp = \iint \frac{\mathrm{d}V}{\|\boldsymbol{v}'\|\mathrm{d}\phi}. \tag{4.14}$$

- Calculate the winding phase length in order to be able to estimate the winding resistance by calculating the arc length of the previously defined winding parametrisation

$$L_{ph} = N\int \|\boldsymbol{v}'(\rho,\phi,\alpha)\|\mathrm{d}\phi, \tag{4.15}$$

being N the number of turns per phase of the winding.

Then the current density distribution can be defined for phase $n \in \{0, 1, \ldots, m_w - 1\}$ using the expression

$$\boldsymbol{J} = \frac{N\hat{i}_S}{A_\perp}\cos\left(\epsilon_w - \frac{2\pi n}{m_w}\right)\boldsymbol{e}_v = J\boldsymbol{e}_v, \tag{4.16}$$

where the current density magnitude is defined by the number of turns per phase, N, the phase
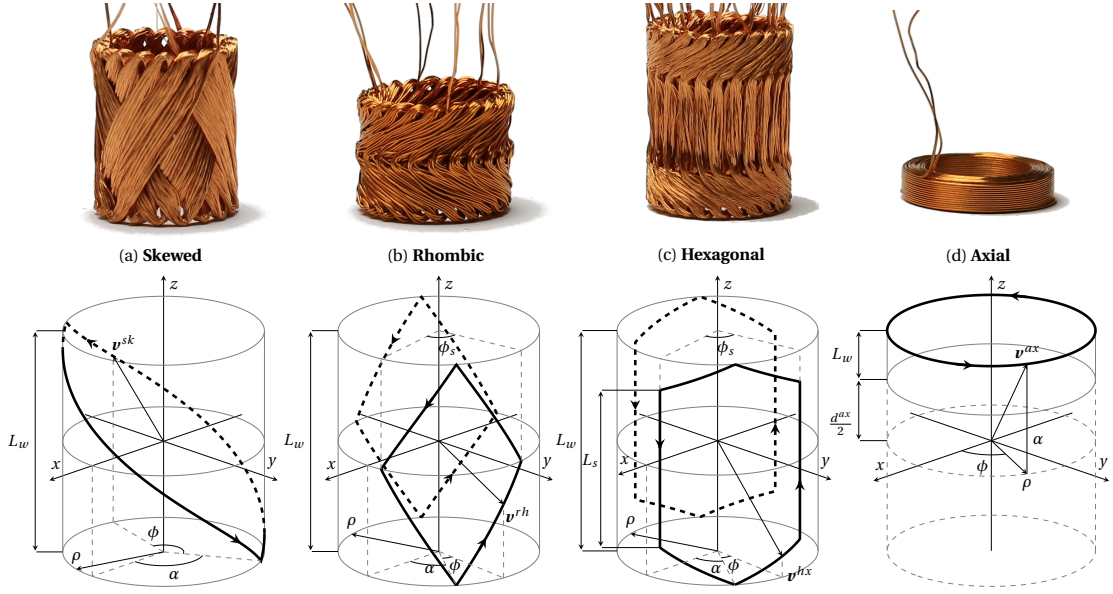
Figure 4.2 – Manufactured windings (top) and their parametrisation (bottom) employed to define the model's current density distribution (here shown for $p_w = 1$).

current amplitude, $\hat{\imath}_S$, the phase belt area perpendicular to $\boldsymbol{e}_v$, $A_\perp$, the number of phases of the winding, m_w, and the current space vector phase angle, ϵ_w.

The parametrisation of each winding type, $\boldsymbol{v}$, shown in figure 4.2 will be detailed hereafter, namely: skewed, rhombic, hexagonal and axial slotless windings. The remaining auxiliary parameters necessary for the calculation of the current density distribution, such as $\boldsymbol{e}_v$, $A_\perp$, $\mathrm{d}V$ and L_{ph}, are detailed in appendix B.

Skewed Winding

Following an equivalent parametrisation to the one shown in [101], a skewed winding can be described by the number of pole-pairs p_w and number of phases m_w. For this type of winding, a phase belt spreads over an angle $\alpha \in [-\pi/(m_w p_w), \pi/(m_w p_w)]$. A parametrisation vector $\boldsymbol{v}^{sk}(\cdot)$, as shown in figure 4.2.a, that defines the winding loop, in Cartesian coordinates, can be defined as follows

$$\boldsymbol{v}^{sk}(\rho,\phi,\alpha) = \begin{bmatrix} v_x^{sk}(\rho,\phi,\alpha) \\ v_y^{sk}(\rho,\phi,\alpha) \\ v_z^{sk}(\phi) \end{bmatrix} = \begin{bmatrix} \rho\cos(\phi+\alpha) \\ \rho\sin(\phi+\alpha) \\ v_z^{sk}(\phi) \end{bmatrix}, \tag{4.17}$$

being ρ the radius of the winding turn, which can vary from R_{wi}, the inner winding radius, to R_{wo}, the outer winding radius, ϕ the azimuthal component w.r.t. the initial angle of the winding turn α, and $v_z^{sk}(\cdot)$ the z coordinate defined as

$$v_z^{sk}(\phi) = L_w \cdot \begin{cases} -\frac{1}{2} + \frac{p_w}{\pi}\phi & \phi \in \left(0, \frac{\pi}{p_w}\right] \\ \frac{1}{2} - \frac{p_w}{\pi}\left(\phi - \frac{\pi}{p_w}\right) & \phi \in \left(\frac{\pi}{p_w}, \frac{2\pi}{p_w}\right] \end{cases}, \tag{4.18}$$

59

being L_w the winding length, and resulting in the curve shown in figure 4.2.a for $p_w = 1$.

Rhombic Winding

A slotless rhombic winding of active length L_w, inner and outer radii R_{wi} and R_{wo}, respectively, can be fully defined by the number of winding pole-pairs p_w, number of phases m_w, and the total opening angle of the rhombus including both legs ϕ_s. The number of pole-pairs in this winding is forced by including a winding loop with opposite polarisation every π/p_w, which results in a highly symmetric winding. This also results in a phase belt that spreads over an angle $\alpha \in [-\pi/(2m_w p_w), \pi/(2m_w p_w)]$. The winding loop parametrisation $\boldsymbol{v}^{rh}(\cdot)$, which is graphically shown in figure 4.2.b for $p_w = 1$, can be defined in Cartesian coordinates as follows

$$\boldsymbol{v}^{rh}(\rho,\phi,\alpha) = \begin{bmatrix} v_x^{rh}(\rho,\phi,\alpha) \\ v_y^{rh}(\rho,\phi,\alpha) \\ v_z^{rh}(\phi) \end{bmatrix} = \begin{bmatrix} \rho\cos(v_\varphi^{rh}(\phi,\alpha)) \\ \rho\sin(v_\varphi^{rh}(\phi,\alpha)) \\ v_z^{rh}(\phi) \end{bmatrix}, \tag{4.19}$$

being ρ the radius of the winding loop, and the azimuthal v_φ^{rh} and axial v_z^{rh} components

$$v_\varphi^{rh}(\phi,\alpha) = \begin{cases} \phi + \alpha, & \phi \in \left(0, \frac{\phi_s}{2}\right], \\ -\phi + \phi_s + \alpha, & \phi \in \left(\frac{\phi_s}{2}, \frac{3\phi_s}{2}\right], \\ \phi - 2\phi_s + \alpha, & \phi \in \left(\frac{3\phi_s}{2}, 2\phi_s\right], \end{cases} \tag{4.20a}$$

$$v_z^{rh}(\phi) = L_w \cdot \begin{cases} -\frac{1}{2} + \frac{\phi}{\phi_s}, & \phi \in \left(0, \phi_s\right], \\ \frac{1}{2} - \frac{\phi - \phi_s}{\phi_s}, & \phi \in \left(\phi_s, 2\phi_s\right]. \end{cases} \tag{4.20b}$$

The graphical representation of the winding parametrisation is shown in figure 4.2.b.

Hexagonal Winding

A similar parametrisation as the rhombic one can be performed for a slotless hexagonal winding. This winding can be fully defined by its active length L_w, inner and outer radii R_{wi} and R_{wo}, p_w number of winding pole-pairs, m_w phases, a total opening angle of the hexagon including both legs of ϕ_s, and a straight (axial) segment of length L_s. As with the rhombic winding, the number of pole-pairs is forced by winding loops of inverse polarity every π/p_w, resulting in a highly symmetric winding, and in a phase belt that spreads over an angle $\alpha \in [-\pi/(2m_w p_w), \pi/(2m_w p_w)]$. In this case the additional degree of freedom L_s is included allowing a higher force and torque density thanks to the purely axial segments of the hexagon. The winding loop parametrisation $\boldsymbol{v}^{hx}(\cdot)$, graphically shown in figure 4.2.c for $p_w = 1$, can be

defined in Cartesian coordinates as follows

$$\boldsymbol{v}^{hx}(\rho,\phi,\alpha) = \begin{bmatrix} v_x^{hx}(\rho,\phi,\alpha) \\ v_y^{hx}(\rho,\phi,\alpha) \\ v_z^{hx}(\phi) \end{bmatrix} = \begin{bmatrix} \rho\cos(v_\varphi^{hx}(\phi,\alpha)) \\ \rho\sin(v_\varphi^{hx}(\phi,\alpha)) \\ v_z^{hx}(\phi) \end{bmatrix}, \tag{4.21}$$

being ρ the radius of the winding loop, and the azimuthal v_φ^{hx} and axial v_z^{hx} components

$$v_\varphi^{hx}(\phi,\alpha) = \begin{cases} \phi + \alpha, & \phi \in \left(0,\frac{\phi_s}{2}\right] \subset \mathcal{D}, \\ \frac{\phi_s}{2} + \alpha, & \phi \in \left(\frac{\phi_s}{2},\frac{\phi_s L_w}{L_w - L_s} - \frac{\phi_s}{2}\right] \subset \mathcal{S}, \\ \frac{\phi_s L_w}{L_w - L_s} - \phi + \alpha, & \phi \in \left(\frac{\phi_s L_w}{L_w - L_s} - \frac{\phi_s}{2},\frac{\phi_s L_w}{L_w - L_s} + \frac{\phi_s}{2}\right] \subset \mathcal{D}, \\ \alpha - \frac{\phi_s}{2}, & \phi \in \left(\frac{\phi_s L_w}{L_w - L_s} + \frac{\phi_s}{2}, 2\frac{\phi_s L_w}{L_w - L_s} - \frac{\phi_s}{2}\right] \subset \mathcal{S}, \\ \phi - 2\frac{\phi_s L_w}{L_w - L_s} + \alpha, & \phi \in \left(2\frac{\phi_s L_w}{L_w - L_s} - \frac{\phi_s}{2}, 2\frac{\phi_s L_w}{L_w - L_s}\right] \subset \mathcal{D}, \end{cases} \tag{4.22a}$$

$$v_z^{hx}(\phi) = \begin{cases} -\frac{L_w}{2} + \frac{\phi}{\phi_s}(L_w - L_s), & \phi \in \left(0,\frac{\phi_s L_w}{L_w - L_s}\right], \\ \frac{3L_w}{2} - \frac{\phi}{\phi_s}(L_w - L_s), & \phi \in \left(\frac{\phi_s L_w}{L_w - L_s}, 2\frac{\phi_s L_w}{L_w - L_s}\right]. \end{cases} \tag{4.22b}$$

In figure 4.2.c, the graphical representation of the winding parametrisation is shown.

Axial Winding

A ring-wound winding, of length L_w, inner and outer radii R_{wi} and R_{wo} respectively, separated by an axial distance d^{ax} from the centre of each other that ideally only features an azimuthal component, can be parametrised $\boldsymbol{v}^{ax}$, following the graphical definition of figure 4.2.d in Cartesian coordinates, as

$$\boldsymbol{v}^{ax}(\rho,\phi,\alpha) = \begin{bmatrix} v_x^{ax}(\rho,\phi) \\ v_y^{ax}(\rho,\phi) \\ v_z^{ax}(\alpha) \end{bmatrix} = \begin{bmatrix} \rho\cos(\phi) \\ \rho\sin(\phi) \\ \alpha \end{bmatrix}. \tag{4.23}$$

Such a winding parametrisation is graphically shown in figure 4.2.d.

4.1.3 Lorentz Force and Torque

Having defined the magnetic flux density distribution for the heteropolar and homopolar sides of the machine and the current density distribution for each type of winding, the total force and torque can be calculated by substituting the corresponding expressions into (4.1a) and (4.1b) and integrating over the winding volume V. Due to the presence of elliptic integrals in the integrand of the force and torque, this last integration needs to be performed numerically, and thus no closed-form solution can be obtained.

The general form of the Lorentz force and torque generated by a general winding will result in the sum of the force generated by each winding phase $n \in \{0,\ldots,m_w - 1\}$ and pole-pair

$h \in \{0, \ldots, p_w - 1\}$

$$\boldsymbol{F}_{lor} = \sum_{n=0}^{m_w-1} \sum_{h=0}^{p_w-1} \iiint\limits_{V_{n,h}} J \boldsymbol{e}_v(\rho, \phi, \alpha) \times \boldsymbol{B}(\rho, \phi, \alpha) \, \mathrm{d}V, \tag{4.24a}$$

$$\boldsymbol{T}_{lor} = \sum_{n=0}^{m_w-1} \sum_{h=0}^{p_w-1} \iiint\limits_{V_{n,h}} J \boldsymbol{v}(\rho, \phi, \alpha) \times \boldsymbol{e}_v(\rho, \phi, \alpha) \times \boldsymbol{B}(\rho, \phi, \alpha) \, \mathrm{d}V. \tag{4.24b}$$

The particular expressions for each winding type are detailed in appendix B.

4.1.4 Reluctance Force and Torque

Apart from Lorentz forces, an additional electromagnetic force will appear at the interface between two materials with different magnetic permeability generally known as reluctance force. Considering the configuration of a slotless machine, the presence of a back iron will result in an increase of the total force due to the additional armature field created by the windings. In slotless permanent-magnet machines this armature field is comparably lower than the one generated by the permanent magnets and usually neglected, also as a result of the vanishing surface integral due to the problem's symmetry when the motor torque is studied. For magnetic bearing systems this component can result in a noticeable increase of total electromagnetic force in radial direction, and thus for a correct estimation of forces and torques it should be included in the models.

Reluctance forces can be obtained independently from other sources when integrating the Maxwell stress tensor $\mathcal{T}$ over the back iron interface surface S as in (4.1a), or combined with Lorentz forces when integrating over rotor's interface [27].

In [27], a closed-form solution was found for an ideal radial bearing straight winding, resulting in a force in the same direction as Lorentz forces. Using this finding as an approximation, the total force generated in the machine can be calculated including the amplification factor κ as follows

$$\boldsymbol{F} = \boldsymbol{F}_{lor} + \boldsymbol{F}_{rel} = \boldsymbol{F}_{lor} + \frac{\left(R_{wo}^4 - R_{wi}^4\right)}{4 R_{sti}^4 \log(R_{wo}/R_{wi})} \boldsymbol{F}_{lor} = \kappa \boldsymbol{F}_{lor}, \tag{4.25}$$

where it is found that κ gets higher when winding outer radius, R_{wo}, and stator back iron inner radius, R_{sti}, are closer to each other, and κ can hold a maximum value of 2. It is also worth mentioning that due to symmetry only radial forces and torques feature reluctance forces.

The complete validation of the force and torque electromechanical models for the active magnetic bearings and motor is experimentally performed employing a dedicated force and torque measurement test bench, and its results are included in chapter 7.
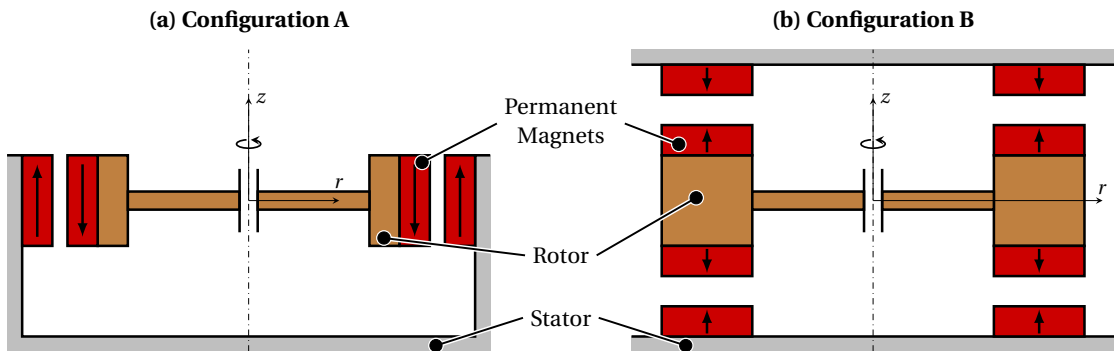
Figure 4.3 – Studied passive bearing configurations.

4.2 Passive Magnetic Bearing Force and Torque Models

In some cases it may be preferable to have some degrees of freedom of the rotor passively stabilised, in order to considerably reduce cost and complexity of the system. The simplification of the studied fully active magnetic bearing system can be performed by removing some of the actuators and including an arrangement of permanent magnets to stabilise the remaining degrees of freedom. Due to the use of Lorentz-type active magnetic bearings in the system, with limited force and torque constants when compared to reluctance-types, it is chosen not to employ any iron in the passive bearing structure and only permanent magnet rings. This will results in lower passive bearing stiffness and load capacity in the stable direction, e.g. axial stiffness for an axial bearing, but also in lower force disturbances on the unstable directions, e.g. negative radial stiffness for the axial bearing.

For any given passive bearing, two main configurations can be envisioned depending on the magnetisation direction of the permanent magnet rings:

- *Configuration A*: Attractive. The stabilisation of the rotor is achieved by attraction between stator and rotor permanent magnets. If the desired passive stabilisation is axial (axial bearing) a configuration as shown in figure 4.3.a can be employed.

- *Configuration B*: Repulsive. The stabilisation is achieved by repulsion between rotor and stator permanent magnets. If an axial bearing is desired, a configuration as shown in figure 4.3.b can be used.

Note that only passive axial bearings are shown in figure 4.3, as they are the only configurations employed for the design in chapter 5. If passive radial bearings would be studied, the magnetisation of stator permanent magnet rings can be inverted, and figure 4.3.a would be transformed into a repulsive passive radial bearing, and figure 4.3.b into an attractive passive radial bearing.

Furthermore, note that due to the fact that the permanent magnet rings are located at the outer part of the rotor instead of close to the rotation axis, the axial bearing will also passively

stabilise any radial tilting in the rotor.

For these configurations, the previously defined electromagnetic models are not valid, and thus some new models are required. Considering the Ampere's model (current-loop equivalent) of a permanent magnet located at the rotor and an external magetic flux density distribution, created for example by a stator permanent magnet, it is possible to calculate the resulting Lorentz force applied between magnets. The electromagnetic force $\boldsymbol{F}$ and torque $\boldsymbol{T}$ applied to a permanent magnet can be calculated by integrating over the whole permanent magnet volume V the gradient of the external B-field, $\boldsymbol{B}_{st}$, projected over the magnetisation direction, $\boldsymbol{M}_{rot}$,

$$\boldsymbol{F} = \iiint_V \mathrm{d}\boldsymbol{F} = \iiint_V \nabla(\boldsymbol{M}_{rot} \cdot \boldsymbol{B}_{st})\mathrm{d}V = \iiint_V \nabla B_M \mathrm{d}V, \tag{4.26a}$$

$$\boldsymbol{T} = \iiint_V \boldsymbol{r} \times \mathrm{d}\boldsymbol{F} = \iiint_V \boldsymbol{r} \times \nabla(\boldsymbol{M}_{rot} \cdot \boldsymbol{B}_{st})\mathrm{d}V. \tag{4.26b}$$

being $\boldsymbol{r} = (r, \varphi, z)$ the position vector of every point of the rotor permanent magnet volume V. As no actuation is possible for the passive magnetic bearings, the main result of the models is the calculation of the passive stiffness resulting from a given rotor displacement or tilting.

Thus, in order to calculate the force, torque and stiffness resulting from the interaction between the permanent magnet rings composing the passive bearings, the following steps are undertaken:

1. Definition of the magnetic flux density distribution, $\boldsymbol{B}_{st}$, generated by stator's permanent magnet rings.

2. Consider exclusively the component aligned with the magnetisation of the rotor's permanent magnet ring, $\boldsymbol{M}_{rot} \cdot \boldsymbol{B}_{st}$.

3. Calculate the partial derivatives of the projection and calculate the force $\mathrm{d}\boldsymbol{F}$ and torque $\mathrm{d}\boldsymbol{T}$ at an infinitesimal volume $\mathrm{d}V$ of the rotor permanent magnets.

4. Integrate the force and torque over the rotor magnet volume V.

5. Repeat the previous calculations for several given displacements and tilting to calculate the passive stiffness k_r, k_ϕ and k_z.

All these steps are detailed hereafter. This approach has been presented and validated in [48] for the repulsive configuration. Apart from axially magnetised permanent magnets, a Halbach configuration was initially studied, but due to the manufacturing limitations of radially magnetised permanent magnets, such a study is not included here.

(a) Configuration A **(b) Configuration B**
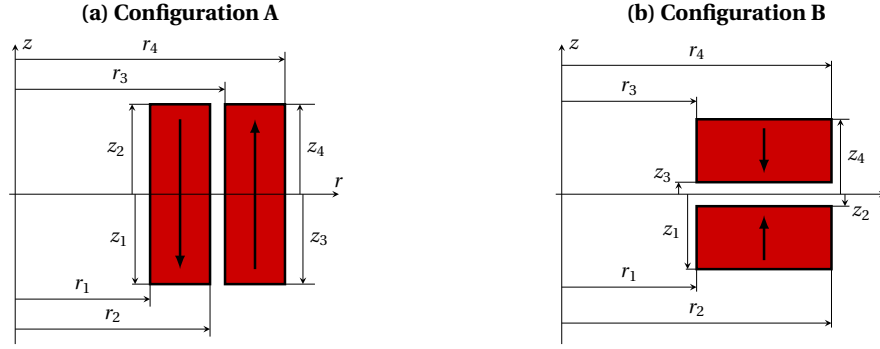
Figure 4.4 – Studied passive bearing configurations with associated reference frames and permanent magnet dimension parameters.

4.2.1 Magnetic Flux Density Distribution

Firstly, the magnetic flux density distribution generated by the stator permanent magnet rings need to be specified. The same assumptions previously defined for the B-field distribution in the active magnetic bearings are considered here, namely: linear and non-conductive materials, hard ferromagnets, and no dependency in time.

Due to the absence of iron in the passive bearing structures, and thus no external boundary is considered, Poisson's and Laplace's equations defined in (4.2) can be solved employing the free-space Green's function and the same formulation of the flux density distribution as a combination of elliptic integrals presented in [112].

As shown in figures 4.3 and 4.4, all magnets feature axial magnetisation, and thus the same models employed for the homopolar side of the fully active machine can be employed here. By considering a remanent magnetisation B_{rem} and dimensions $r_j = \{r_1, r_2\}$ and $z_k = \{z_1, z_2\}$ as defined in figure 4.4 for a general pair of permanent magnet rings, the magnetic flux density distribution generated by a single magnet results in (4.4a) and (4.4b). These expressions are repeated hereafter for convenience:

$$B_r^{pb}(r,z) = \frac{B_{rem}}{\pi} \sum_{j=1}^{2} \sum_{k=1}^{2} (-1)^{j+k} \frac{r_j}{\sigma_{jk}} \left[\left(1 - \frac{2}{m_{jk}}\right) K(m_{jk}) + \frac{2}{m_{jk}} E(m_{jk}) \right], \qquad (4.27a)$$

$$B_z^{pb}(r,z) = \frac{B_{rem}}{\pi} \sum_{j=1}^{2} \sum_{k=1}^{2} (-1)^{j+k} \frac{r_j}{\sigma_{jk}} \frac{(z+z_k)(1+\xi_j)}{(r+r_j)n_j} \left[K(m_{jk}) - \xi_j \Pi(n_j, m_{jk}) \right], \qquad (4.27b)$$

being the auxiliary parameters $\sigma_{jk}, \xi_j, m_{jk}$ and n_j defined as

$$\xi_j = \frac{r - r_j}{r + r_j}, \qquad n_j = 1 - \xi_j^2 = \frac{4rr_j}{(r+r_j)^2},$$
$$\sigma_{jk} = \sqrt{(z+z_k)^2 + (r+r_j)^2}, \quad m_{jk} = \frac{4rr_j}{(z+z_k)^2 + (r+r_j)^2}. \qquad (4.28)$$

These expressions are then validated in section 4.3 by comparison to a reference finite element

model of the magnet rings.

4.2.2 Passive Magnetic Force and Torque

The magnetic force and torque generated at an infinitesimal volume dV of the rotor's permanent magnet rings, can be estimated assuming that the external field is lower than the material coercivity and by considering the interaction between the rotor magnetisation and stator's magnetic flux density distribution as follows

$$
d\boldsymbol{F}(r,\varphi,z) = \begin{bmatrix} dF_r(r,z) \\ 0 \\ dF_z(r,z) \end{bmatrix} dV = \nabla(\boldsymbol{M}_{rot} \cdot \boldsymbol{B}_{st}) dV = \nabla B_M dV = \begin{bmatrix} \frac{\partial B_M}{\partial r} \\ 0 \\ \frac{\partial B_M}{\partial z} \end{bmatrix} dV, \tag{4.29a}
$$

$$
d\boldsymbol{T}(r,\varphi,z) = \boldsymbol{r} \times d\boldsymbol{F}, \tag{4.29b}
$$

being $\boldsymbol{r}$ the position vector of the infinitesimal volume dV with respect to the centre of the rotor and B_M the projection of the stator magnetic flux density over the rotor magnetisation. The exact expression of B_M will depend on the relative position between both permanent magnets, subject to possible radial displacements or tilting or axial displacements. In any case, B_M will be a linear combination of B_r^{pb} or B_z^{pb} defined in (4.27a) and (4.27b), respectively. Thus, in order to estimate the magnetic force, the partial derivatives of the radial and axial components of the magnetic flux density with respect to r and z are needed. Their partial derivatives can be computed analytically by making use of the mathematical properties and derivatives of elliptic integrals with respect to their parameters, as defined in appendix A.

The partial derivatives of the B-field generated by axially-magnetised rings result in another linear combination of complete elliptic integrals of the first, $K(m)$, and second kind, $E(m)$, as follows

$$
\frac{\partial B_r^{pb}}{\partial r}(r,z) = \frac{B_{rem}}{2r^2\pi} \sum_{j=1}^{2} \sum_{k=1}^{2} (-1)^{(j+k+1)} \left[\frac{(z+z_k)^4 + (r^2 + 2r_j^2)(z+z_k)^2 - r_j^2(r^2 - r_j^2)}{\sigma_{jk}\left((r-r_j)^2 + (z+z_k)^2\right)} E(m_{jk}) - \right.
$$
$$
\left. - \frac{r_j^2 + (z+z_k)^2}{\sigma_{jk}} K(m_{jk}) \right],
$$
$$
\tag{4.30a}
$$

$$
\frac{\partial B_r^{pb}}{\partial z}(r,z) = \frac{B_{rem}}{2r\pi} \sum_{j=1}^{2} \sum_{k=1}^{2} (-1)^{(j+k)} \frac{(z+z_k)}{\sigma_{jk}} \left[\frac{r^2 + r_j^2 + (z+z_k)^2}{(r-r_j)^2 + (z+z_k)^2} E(m_{jk}) - K(m_{jk}) \right], \tag{4.30b}
$$

$$
\frac{\partial B_z^{pb}}{\partial r}(r,z) = \frac{B_{rem}}{2r\pi} \sum_{j=1}^{2} \sum_{k=1}^{2} (-1)^{(j+k)} \frac{(z+z_k)}{\sigma_{jk}} \left[\frac{r^2 + r_j^2 + (z+z_k)^2}{(r-r_j)^2 + (z+z_k)^2} E(m_{jk}) - K(m_{jk}) \right], \tag{4.30c}
$$

$$
\frac{\partial B_z^{pb}}{\partial z}(r,z) = \frac{B_{rem}}{2\pi} \sum_{j=1}^{2} \sum_{k=1}^{2} (-1)^{(j+k+1)} \frac{1}{\sigma_{jk}} \left[\frac{r^2 - r_j^2 + (z+z_k)^2}{(r-r_j)^2 + (z+z_k)^2} E(m_{jk}) - K(m_{jk}) \right], \tag{4.30d}
$$

being m_{jk} and σ_{jk} as defined in (4.28).

Total Force and Torque

Finally, for a given relative position and orientation between magnets, the total force and torque between them can be calculated by simply integrating expressions (4.29a) and (4.29b) over the rotor's permanent magnet volume $V = [r_i, r_o] \times [\varphi_i, \varphi_o] \times [z_i, z_o] = [r_3, r_4] \times [0, 2\pi] \times [z_3, z_4]$, as schematically defined in figure 4.4.

Given that the field at point P is expressed under stator's reference frame, in cylindrical coordinates $P = [r', \varphi', z']$, and that the integral limits are expressed under rotor's reference frame, in cylindrical coordinates $P = [r, \varphi, z]$, a geometric transformation is needed to convert from one system to the other. Different cases of relative displacements, such as axial, radial displacement and radial tilting, and their associated transformations are studied in appendix C.

Considering the transformation $(r, \varphi, z) \mapsto (r', \varphi', z')$, the integral over the rotor's volume V' expressed under the stator's reference frame can be evaluated using integration by substitution, with expressions (4.26a) and (4.26b) resulting in

$$
\boldsymbol{F} = \begin{bmatrix} F_x \\ F_y \\ F_z \end{bmatrix} = \iiint\limits_{V'} \mathrm{d}\boldsymbol{F}(r', \varphi', z') r' \mathrm{d}r' \mathrm{d}\varphi' \mathrm{d}z' = \iiint\limits_{V'} \mathrm{d}\boldsymbol{F}(r', \varphi', z') r' \left| \frac{\partial(r', \varphi', z')}{\partial(r, \varphi, z)} \right| \mathrm{d}r \mathrm{d}\varphi \mathrm{d}z =
$$

$$
= \int\limits_{r_3}^{r_4} \int\limits_{0}^{2\pi} \int\limits_{z_3}^{z_4} \begin{bmatrix} \mathrm{d}F_r(r', z') \cos\varphi' \\ \mathrm{d}F_r(r', z') \sin\varphi' \\ \mathrm{d}F_z(r', z') \end{bmatrix} r \mathrm{d}r \mathrm{d}\varphi \mathrm{d}z,
$$

(4.31a)

$$
\boldsymbol{T} = \begin{bmatrix} T_x \\ T_y \\ T_z \end{bmatrix} = \iiint\limits_{V'} \mathrm{d}\boldsymbol{T}(r', \varphi', z') r' \mathrm{d}r' \mathrm{d}\varphi' \mathrm{d}z' = \iiint\limits_{V'} \mathrm{d}\boldsymbol{T}(r', \varphi', z') r' \left| \frac{\partial(r', \varphi', z')}{\partial(r, \varphi, z)} \right| \mathrm{d}r \mathrm{d}\varphi \mathrm{d}z =
$$

$$
= \int\limits_{r_3}^{r_4} \int\limits_{0}^{2\pi} \int\limits_{z_3}^{z_4} \begin{bmatrix} r' \cos\varphi' \\ r' \sin\varphi' \\ z' \end{bmatrix} \times \begin{bmatrix} \mathrm{d}F_r(r', z') \cos\varphi' \\ \mathrm{d}F_r(r', z') \sin\varphi' \\ \mathrm{d}F_z(r', z') \end{bmatrix} r \mathrm{d}r \mathrm{d}\varphi \mathrm{d}z,
$$

(4.31b)

and being $|\partial(r', \varphi', z')/\partial(r, \varphi, z)| = r/r'$ the determinant of the Jacobian matrix of the transformation.

Due to the presence of elliptic integrals inside the integrand, a numerical integration to calculate the total force and torque is required and thus no closed-form solution can be extracted. The numerical validation of the generated force and torque as a function of axial, Δz, and radial displacement, Δx, as well as radial tilting, $\Delta\phi_y$, is included in section 4.3.

4.2.3 Passive Magnetic Stiffness

In order to estimate forces, torque and stiffness generated in the bearing in all directions, three different cases will be studied, corresponding to the different possible rotor displacements: axial displacement Δz, radial displacement, i.e. Δx, and radial tilting $\Delta \phi_y$. The geometric transformations required to project the external flux density distribution over the rotor's permanent magnet will depend on the studied configuration (attractive or repulsive), as the arrangement of permanent magnets is specific to each of them. The exact transformations are detailed in appendix C.

Having expressed the total force and torque as a function of small rotor displacements in radial, Δx, or axial, Δz, directions, as well as small radial tilting $\Delta \phi_y$, the magnetic stiffness of the bearing can be calculated by

$$k_r = -\frac{\mathrm{d}F_x}{\mathrm{d}\Delta x} = k_{11}, \quad k_z = -\frac{\mathrm{d}F_z}{\mathrm{d}\Delta z} = k_{33}, \quad k_{\phi_y} = -\frac{\mathrm{d}T_y}{\mathrm{d}\Delta \phi_y} = k_{22}, \tag{4.32}$$

where the relation with the 5-DoF rotordynamics model defined in chapter 3 is specified, and more specifically in equation (3.8), being the rest of the elements zero as a result of symmetry. Due to the numerical integration performed for calculating the force at each displacement and tilt, the derivative shown in the previous expression is also implemented numerically. The validation of the calculated stiffness by comparison to a finite-element model of the passive bearings is shown in the next section.

4.3 Numerical Validation

In this section, the some elements of the previously developed electromechanical models for slotless motor and bearings and iron-less passive bearings will be validated using finite element models of the different configurations, implemented using COMSOL Multiphysics. Firstly, the proposed three-dimensional magnetic field distribution models are validated, and secondly, the passive force and stiffness of the passive bearing configurations are also validated. The experimental validation of the models is performed in chapter 7, and this only numerical validations are performed here.

4.3.1 Magnetic Flux Density Validation

In order to validate the magnetic flux density distribution defined in sections 4.1 and 4.2, the analytical expressions using elliptic integrals will be compared to the magnetic flux density distribution estimated using the aforementioned finite element model of each of the six studied configurations: homopolar side of the active magnetic bearing with and without back iron, heteropolar side of active machine with and without back iron, and iron-less passive bearing attractive and repulsive configurations.
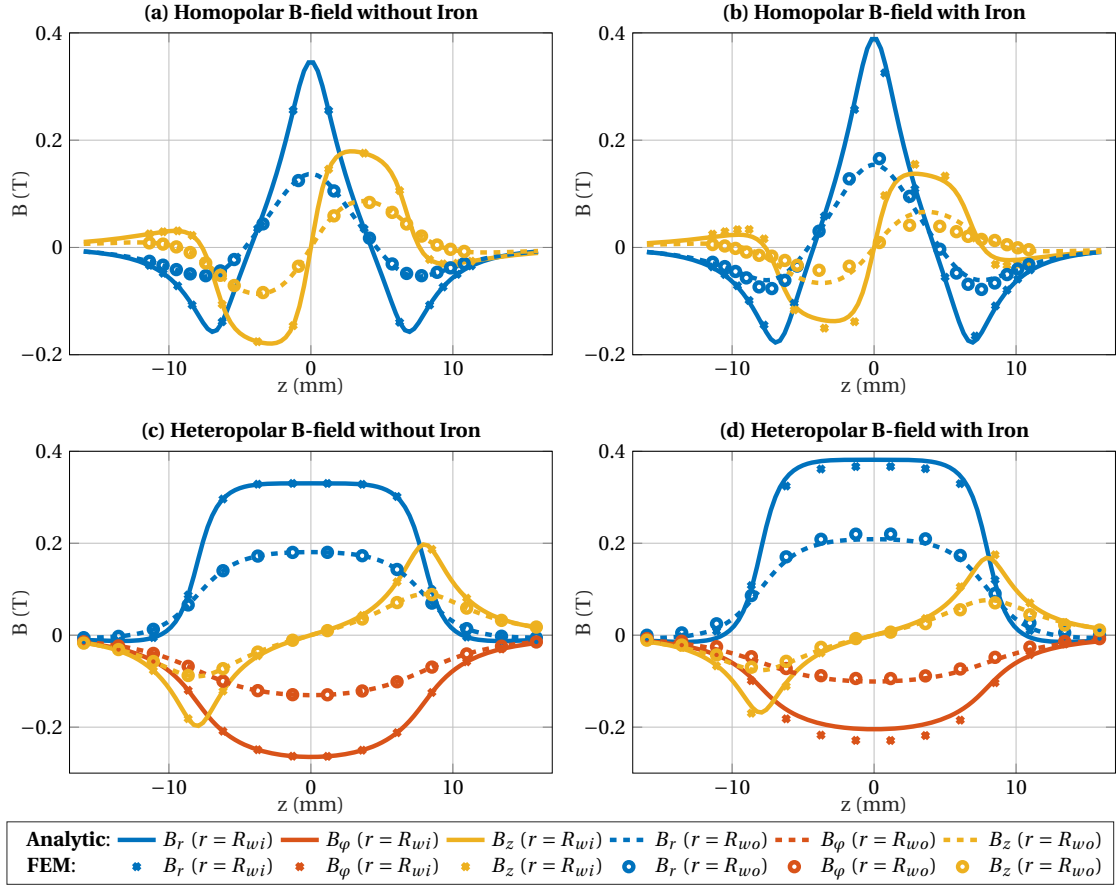
Figure 4.5 – Analytic and FEM validation results for the magnetic flux density distribution in homopolar and heteropolar air-gaps. Lines denote the analytical results and the markers the FEM results. For both cases, the continuous lines and crosses are considered at $r = R_{wi}$, and dashed lines and circles at $r = R_{wo}$. For the heteropolar side, the magnetic flux is evaluated at the azimuthal coordinate where each component is maximum ($\varphi = 0$ for B_r and B_z, and $\varphi = -\pi/2$ for B_φ).

Regarding the models of the active parts, four comparisons are performed and included in figure 4.5, namely: the magnetic flux density distribution of homopolar side without back iron, figure 4.5.a, with back iron, figure 4.5.b, and heteropolar side without, figure 4.5.c, and with back iron, figure 4.5.d. For the heteropolar side, each component is evaluated at the azimuthal coordinate where its maximum amplitude is reached ($\varphi = 0$ for B_r and B_z, and $\varphi = -\pi/2$ for B_φ).

It can be seen that the magnetic flux density distribution without back iron in figure 4.5.a and 4.5.c perfectly matches the simulation results of the FEM for both heteropolar and homopolar sides. This is expected, as the exact B-field has been simply reformulated using complete elliptic integrals (no simplification was considered in their derivation). Regarding the magnetic flux density with back iron in figure 4.5.b and 4.5.d, the employed approximation with the factor Λ is visible in the results, being higher than the FEM simulations at $r = R_{wi}$ and lower at $r = R_{wo}$. Nevertheless, due to the required integration in the winding volume needed for
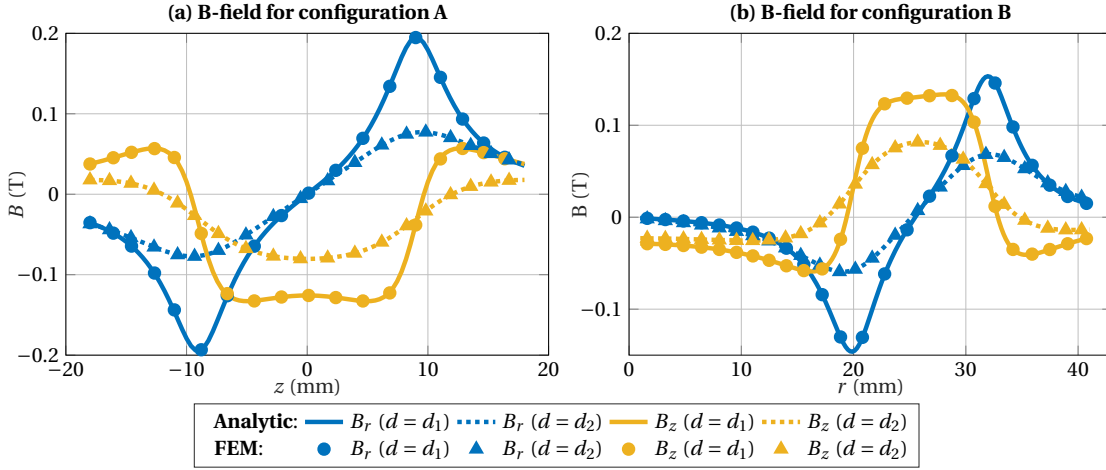
Figure 4.6 – Analytic and FEM magnetic flux density distribution comparison for axially-magnetised permanent magnet rings for passive bearing models.

calculating the total force and torque, these errors at individual points are compensated thanks to the integration approach proposed for calculating Λ, as it will be shown in the validation of the winding forces and torques.

Regarding the model of the passive bearings, it corresponds to a similar configuration to the homopolar side without back iron, but with permanent magnet rings instead of full cylinders. The comparison of the analytical models of the flux density distribution with the FEM counterpart is shown in figure 4.6.a for the attractive configuration, and figure 4.6.b for the repulsive one, as presented in figure 4.3.

The plots show the evaluation of the radial and axial flux density components at distance d_1 and d_2 from the permanent magnet ring. This distance is measured radially for configuration A and axially for configuration B, as it will represent positions of the rotor's permanent magnet. As in the case of the homopolar side without back iron, the analytical model with elliptic integrals perfectly match the FEM results, as it represents an exact solution of the electromagnetic problem previously defined.

Furthermore, the magnetic flux density distribution created by heteropolar and homopolar sides without back iron will be experimentally measured in chapter 7 using a three-axis hall probe and compared to the ideal models presented here for asymmetry detection in the real magnets.

4.3.2 Passive Bearing Force and Torque Model Validation

Finally, to validate the proposed models for passive stiffness, all three displacement cases (axial, radial and tilting) are compared with the simulation results of force and torque obtained using FEM of configurations A (attractive) and B (repulsive) as shown in figure 4.3. Due to the
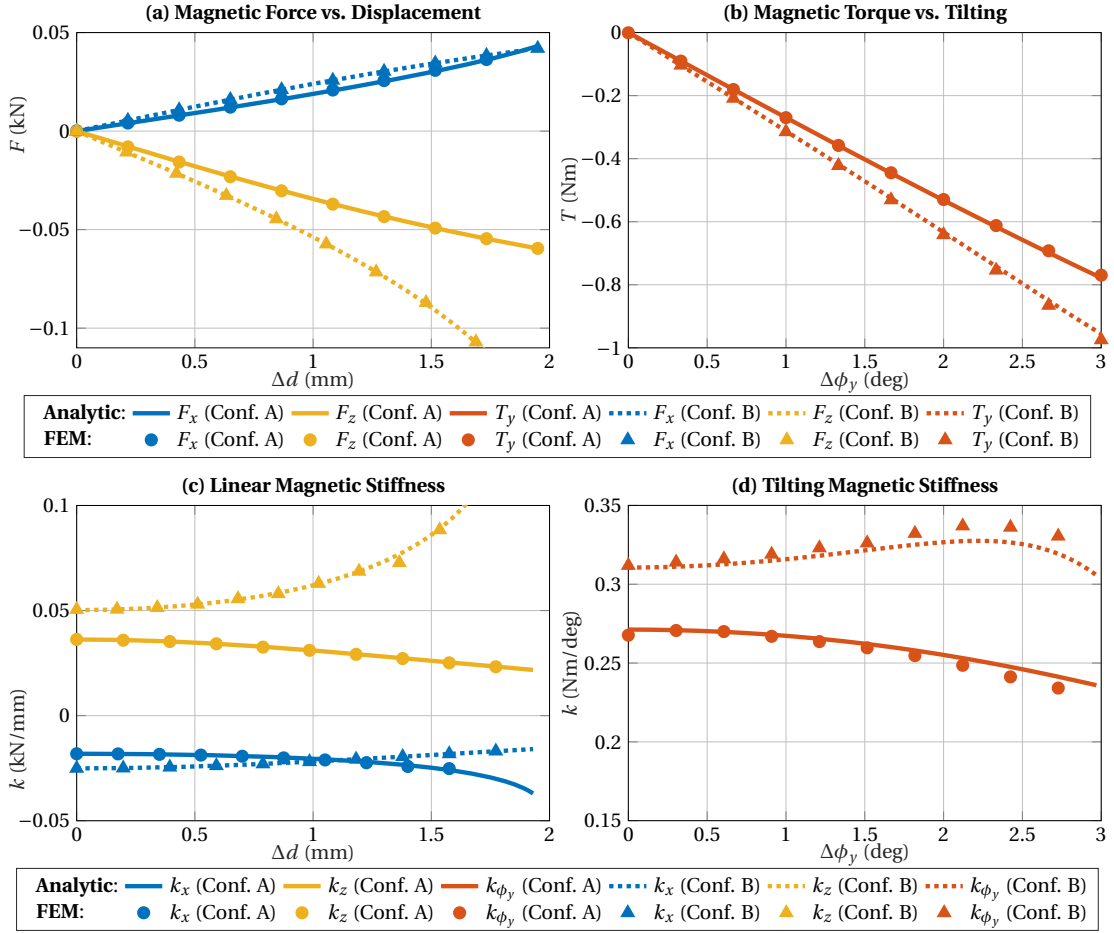
Figure 4.7 – Magnetic force/torque and stiffness generated by passive magnetic bearing configurations A (attractive) and B (repulsive). Δd represents the displacement in the same direction in which the force is calculated, being $\Delta d = \Delta x$ for F_x and k_x, and $\Delta d = \Delta z$ for F_z and k_z.

lost of symmetry when radial displacement or tilting is present, a full three-dimensional FEM simulation is employed for the comparison.

As shown in figure 4.7, a good agreement is obtained between analytical and simulation results for all radial, axial and angular displacements for both force/torque and stiffness. Due to the low number of displacement samples when employing the FEM for computational reasons, the derivation for estimating the FEM stiffness is computed by considering an cubic spline interpolation between evaluation points, allowing a lower numerical error in the derivation.

As for the evaluation of the flux density distribution, it is worth mentioning the low computational cost of the proposed analytical method based on elliptic integrals, requiring from just a few seconds to a few minutes of computation in a general-purpose dual-core CPU, depending on the symmetry and available simplifications of each studied case.

In table 4.1, the difference between the analytical and numerical forces, torques and stiffness

Table 4.1 – Maximum absolute ($e_{abs} = f_{an} - f_{FEM}$) and relative ($e_{rel} = (f_{an} - f_{FEM})/f_{FEM}$) error between semi-analytical model and FEM.

max	e_{Fx} (N)	e_{Fz} (N)	e_{Ty} (Nm)	e_{kx} (N/mm)	e_{kz} (N/mm)	$e_{k\phi}$ (Nm/deg)
Conf. A	0.208	0.144	0.002	0.226	0.207	0.002
	2.28%	1.04%	0.61%	0.92%	0.72%	2.13%
Conf. B	0.011	0.530	0.010	0.025	3.993	0.016
	0.05%	0.62%	1.42%	0.12%	5.46%	2.91%

for both configurations is included. When evaluating the force and torque using FEM, some numerical instabilities are seen at high displacements when no sufficient air-gap is present, being more visible for the evaluation of F_x for config. A, and F_z and T_y for config. B. To minimise its impact, the comparison is performed without considering the last FEM evaluation point. It can be seen that for all cases, the deviation with respect to the finite element results is always lower than 6%, showing a good correlation between analytical model and FEM results.

4.4 Conclusions

In this chapter, the analytical electromagnetic models of the active and passive magnetic bearings are detailed. These models will be employed for the optimisation and design of the fully active and hybrid magnetic bearing systems studied in this work.

The main contributions of this chapter can be summarised as follows:

- A modular electromechanical model for magnetic bearings and motor is presented:
  - The model allows the calculation of the magnetic flux density distribution of a selection of arrangements of permanent magnets with or without back iron.
  - For active magnetic bearings and motors, the model can consider a wide variety of slotless winding topologies, such as skewed, rhombic, hexagonal or axial windings.
  - As results for active bearings, it is capable of accurately estimating electromagnetic forces, torques and Joule losses.
  - As results for passive bearings, the model is capable of calculating the electromagnetic forces, torques and passive stiffness.
  - The model is numerically efficient thanks to the use of elliptic integrals for the definition of the three-dimensional field distribution, instead of relying on Fourier series expansions or FEM. It features also increased accuracy when compared to two-dimensional approximations of the field distribution.

- The different configurations for the model are numerically validated. Experimental validation is performed in chapter 7 including both accuracy and computational efficiency when compared to other analytical approaches.

5 Magnetic Bearing and Motor Electromagnetic Optimisation

Having defined both the closed-loop and electromagnetic models in previous chapters, it is possible to proceed with the detailed design and optimisation of the magnetic bearing system. Depending on the requirements of a given application, different magnetic bearing topologies may be better adapted for the needs of each situation and thus two main configurations are studied hereafter.

For applications that have more strict requirements in terms of performance or allowed vibrations, a fully active magnetic bearing configuration is proposed, allowing the active control of all degrees of freedom, and thus enabling the possibility of active vibration suppression in any direction. This comes at the expense of a higher complexity and cost of the systems. For applications in which requirements are either not as strict, or the increased complexity makes the system much less competitive, a simpler hybrid magnetic bearing configuration is presented, featuring the active control of only three out of six degrees of freedom of the rotor, thanks to the passive stabilisation of axial and tilting dynamics. This configuration allows the active suppression of the main disturbances, which appear in radial direction, such as the rotor unbalance, and thus not excessively compromising the system's performance.

In section 5.1, a general optimisation procedure is presented for active magnetic bearings and motor, based on the maximisation of the actuators efficiency, which is then applied to the studied fully active magnetic bearing motor. This optimisation procedure is also presented in [49]. Subsequently, in section 5.2, the design and optimisation of a hybrid magnetic bearing motor is presented, which combines the optimised active motor and bearings with the passive stabilisation of some degrees of freedom to obtain a significant simplification of the system with respect to the fully active configuration.

5.1 Fully Active Magnetic Bearing Motor Optimisation

As it is shown in chapter 7 in the experimental validation of the electromechanical models of the active magnetic bearings (AMBs), the originally employed skewed windings and its
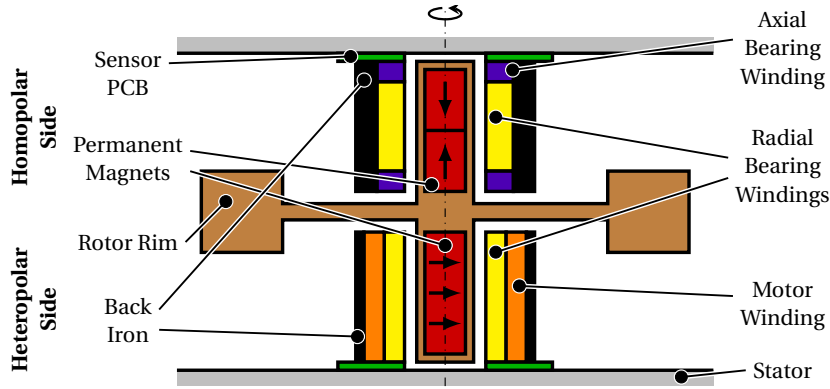
Figure 5.1 – Schematic cross-sectional view of the optimised configuration of the slotless permanent-magnet magnetic bearing reaction wheel demonstrator. The system consists of hexagonal, rhombic and axial windings with back iron in homopolar and heteropolar sides.

associated manufacturing process results in some winding asymmetries and disturbances. Furthermore, due to the use of skewed windings, the axial component of the wire is limited by the winding length L_w and the number of pole pairs p_w, and thus the efficiency and force capacity of such windings is fixed by these parameters.

Due to these limitations, a new manufacturing process has been developed for manufacturing highly symmetric and efficient winding types, such as rhombic and hexagonal. These winding types include some additional degrees of freedom in which the resulting force capacity and efficiency are no longer limited in the same way by winding length and pole pairs, allowing for an improved and optimised design of all the actuators. This efficiency can be further improved by including a back iron for both heteropolar and homopolar sides, as shown for the newer revision of the fully active machine in figure 5.1, and by optimising all winding and stator parameters for this configuration.

One of the main advantages of having an analytical model of the windings is the possibility of performing an optimisation of different bearing and motor winding parameters. This allows to obtain a desired performance and efficiency without a high computational cost, when compared to other numerical or finite element methods (FEM). In this section both the efficiency of the machine and the generated vibrations will be optimised, and the parameters employed for the evaluation of such characteristics (figures of merit), the followed procedure and the optimisation itself are explained here below.

All expressions and figures hereafter, including the ones in the results section, are expressed under the reference frames defined for each winding, as shown in figure 4.2, being the X and Y components radial, and the Z component referred to as axial. Furthermore, the same expressions are employed for the experimental validation of the optimisation results.

5.1.1 Figures of Merit

Efficiency

As commonly done for electric machines, a notable figure of merit for the efficiency of the machine is the ratio between the applied mechanical force or torque and the power losses in the winding (Joule losses). For electric motors the ratio is generally known as the motor constant K_M (Nm/$\sqrt{\text{W}}$), while for bearings can be defined as bearing constant K_B (N/$\sqrt{\text{W}}$). The figures can be calculated, for a three phase machine, as follows

$$K_B = \frac{F}{\sqrt{P_{Joule}}} = \frac{\kappa_F \hat{i}_s}{\sqrt{R_{ph}\hat{i}_s^2}} = \frac{\kappa_F}{\sqrt{R_{ph}}}, \tag{5.1a}$$

$$K_M = \frac{T}{\sqrt{P_{Joule}}} = \frac{\kappa_T \hat{i}_s}{\sqrt{R_{ph}\hat{i}_s^2}} = \frac{\kappa_T}{\sqrt{R_{ph}}}, \tag{5.1b}$$

where F (N) and T (Nm) denote the force and torque applied by the bearing and motor windings, respectively, $\hat{i}_s$ (A) the current amplitude in the winding, R_{ph} (Ω) the wire resistance of each winding phase, and κ_F (N/A) and κ_T (Nm/A) the force and torque constants of the bearing and motor.

All these magnitudes can be derived directly from the previously defined models for the windings and magnetic flux. κ_F and κ_T can be analytically calculated or experimentally measured from the total force and torque applied to the rotor with current amplitude $\hat{i}_s$ as follows

$$\kappa_F = \frac{\int_{\epsilon_w} \|\boldsymbol{F}\| \mathrm{d}\epsilon_w}{\int_{\epsilon_w} \hat{i}_s \mathrm{d}\epsilon_w} = \frac{\int_{-\pi}^{\pi} \|\boldsymbol{F}\| \mathrm{d}\epsilon_w}{\hat{i}_s 2\pi}, \tag{5.2a}$$

$$\kappa_T = \frac{1}{2\hat{i}_s} \left(\left| \max_{\epsilon_w \in [-\pi,\pi]} \|\boldsymbol{T}\| \right| + \left| \min_{\epsilon_w \in [-\pi,\pi]} \|\boldsymbol{T}\| \right| \right), \tag{5.2b}$$

which corresponds to the average force and torque per current unit for all electric angles ϵ_w applied by the winding. The phase resistance can be calculated from expression

$$R_{ph} = \rho_{Cu} \frac{L_{ph}}{A_{wire}}, \tag{5.3}$$

being ρ_{Cu} the resistivity of the wire material (copper), L_{ph} the wire length of each phase as calculated in [47] for each winding type, and A_{wire} the cross-sectional area of the winding wire.

Vibrations

Another important measure for magnetically levitated electric machines is the level of vibrations generated during operation. For conventional machinery, apart from the rotor unbalance,

the main vibration sources are the imperfections in ball bearings and torque disturbances caused by the motor system such as the torque drift and ripple [10]. In the configuration studied in the present thesis, as the levitation in all degrees of freedom is performed using active magnetic bearings, asymmetries and imperfections in the windings, permanent magnets or any other component will result in the generation of vibrations by the machine. Equivalently to what is commonly known as torque disturbances and ripple for motor windings, force ripple and disturbances are generated by bearing windings.

The figures of merit used for evaluating of the level of vibrations generated by the machine are the force and torque ripple and disturbances. The ripple is defined as the variation with the electrical angle ϵ_w of the main force/torque component controlled by the winding, i.e. torque in Z for the motor, forces in X and Y for the radial bearings, and in Z for the axial bearing. The force and torque disturbances are defined as the maximum amplitude of forces/torques appearing in other direction than the main component controlled by the winding, i.e. torques in X and Y for motor, forces in Z for radial bearings, and in X and Y for axial bearing. As previously mentioned, all these components are referred to the winding reference frame as per figure 4.2.

These figures of merit can then be analytically calculated or experimentally measured, relative to the force or torque constants, as follows

$$r_F = \frac{1}{2\kappa_F} \left(\max_{\epsilon_w \in [-\pi,\pi]} \|\boldsymbol{F}\| - \min_{\epsilon_w \in [-\pi,\pi]} \|\boldsymbol{F}\| \right), \tag{5.4a}$$

$$r_T = \frac{1}{2\kappa_T} \left(\left| \max_{\epsilon_w \in [-\pi,\pi]} \|\boldsymbol{T}\| \right| - \left| \min_{\epsilon_w \in [-\pi,\pi]} \|\boldsymbol{T}\| \right| \right), \tag{5.4b}$$

$$d_F = \frac{1}{\kappa_F} \left(\max_{\epsilon_w \in [-\pi,\pi]} \|\boldsymbol{F}_d\| \right), \tag{5.4c}$$

$$d_T = \frac{1}{\kappa_T} \left(\max_{\epsilon_w \in [-\pi,\pi]} \sqrt{T_x^2 + T_y^2} \right), \tag{5.4d}$$

being r_F, r_T the force and torque ripple, respectively, d_F, d_T the force and torque disturbance, and $\boldsymbol{F}_d$ being either the force in axial direction, $\boldsymbol{F}_d = [0, 0, F_z]^\top$, for the radial bearing winding, and in radial direction, $\boldsymbol{F}_d = [F_x, F_y, 0]^\top$, for the axial bearing winding. The factor 2 is included in the ripple to account only for the amplitude with respect to the average.

5.1.2 Optimisation Problem Definition

Depending on the exact needs or the design phase in which the optimisation will be performed, a different level of generalisation can be approached: from an actuator single-objective optimisation to a general multi-objective optimisation for a group of coupled actuators (e.g. heteropolar or homopolar sides of figure 5.1).

On the one hand, due to the available electromechanical models described in section 4.1, it is possible to analytically model and study the different magnitudes required for evaluating the

efficiency in (5.1a) and (5.1b), and thus this figure of merit will be included in the optimisation procedure described hereafter.

On the other hand, the generated vibrations are mainly a result of the manufacturing and integration process, and thus difficult (if not impossible) to model analytically. From experimental measurements it is seen that highly-symmetric windings, such as rhombic (figure 4.2.b) and hexagonal (figure 4.2.c), will feature much lower force and torque ripple and disturbances than other less symmetric winding types, such as skewed (figure 4.2.a). For this reason, no analytical optimisation is required, and only a selection of a symmetric winding type is needed. The final level of ripple and disturbances are measured and validated in chapter 7.

Due to the intrinsic complexity of a fully active magnetic bearing motor, the simultaneous optimisation of several actuators (e.g. motor and radial bearing for heteropolar side and axial and radial bearings for homopolar side) needs to be expressed in the form of a multi-objective optimisation. If only one actuator needs to be optimised, the same approach can be followed by considering a single-objective optimisation instead.

Due to the independent nature of each actuator, the objective function is selected to be a weighted sum of the efficiency measures (5.1a) or (5.1b) for each actuator. In a general form, the optimisation variables will be a concatenation of the parameters for all N actuators $\boldsymbol{x} = [\boldsymbol{x}_1, \dots, \boldsymbol{x}_N]^\top$. Each actuator's parameters $\boldsymbol{x}_i$, can be composed of winding dimensions R_{wi}, R_{wo} and L_w, permanent magnet dimensions, L_{pm} and R_{pm}, back iron dimensions R_{sti}, R_{sto} and L_{st}, and winding parameters (dependent on winding type of figure 4.2) like rhombic and hexagonal opening angle ϕ_s and hexagon axial segment length L_s. The optimum set of parameters $\boldsymbol{x}^*$ will be a result of the following optimisation problem

$$\min_{\boldsymbol{x}} f(\boldsymbol{x}) := \sum_{i=1}^{N} w_i f_i(\boldsymbol{x}_i) = \sum_{i=1}^{N} \frac{w_i}{K_i(\boldsymbol{x}_i)} \tag{5.5}$$

subject to

$$\boldsymbol{g}_i(\boldsymbol{x}_i) \le \boldsymbol{0}, \qquad \boldsymbol{h}_i(\boldsymbol{x}_i) = \boldsymbol{0}, \quad \forall i \in \{1, \dots, N\}$$
$$\boldsymbol{g}_{ij}(\boldsymbol{x}_i, \boldsymbol{x}_j) \le \boldsymbol{0}, \quad \boldsymbol{h}_{ij}(\boldsymbol{x}_i, \boldsymbol{x}_j) = \boldsymbol{0}, \quad \forall j > i$$

The optimisation variables are included in vector $\boldsymbol{x}_i$, which can be any combination of desired actuator parameters to optimise. The optimisation constraints will feature the individual physical and manufacturing limits in $\boldsymbol{g}_i(\boldsymbol{x}_i)$ and $\boldsymbol{h}_i(\boldsymbol{x}_i)$, as well as some further coupling between the actuators in the form of coupled inequality and equality constraints $\boldsymbol{g}_{ij}(\boldsymbol{x}_i, \boldsymbol{x}_j)$ and $\boldsymbol{h}_{ij}(\boldsymbol{x}_i, \boldsymbol{x}_j)$ that will link parameters of actuator i with j.

As many computational optimisation algorithms are designed for minimisation, the objective function is defined as a linear combination of K_i^{-1}, being the inverse of the bearing K_B and motor constants K_M as defined in (5.1a) and (5.1b), resulting in a minimisation the phase resistance R_{ph} and thus Joule losses P_{Joule}, while maximising the force κ_F or torque constants κ_T. This selection of objective function, as previously stated, allows the maximisation of the
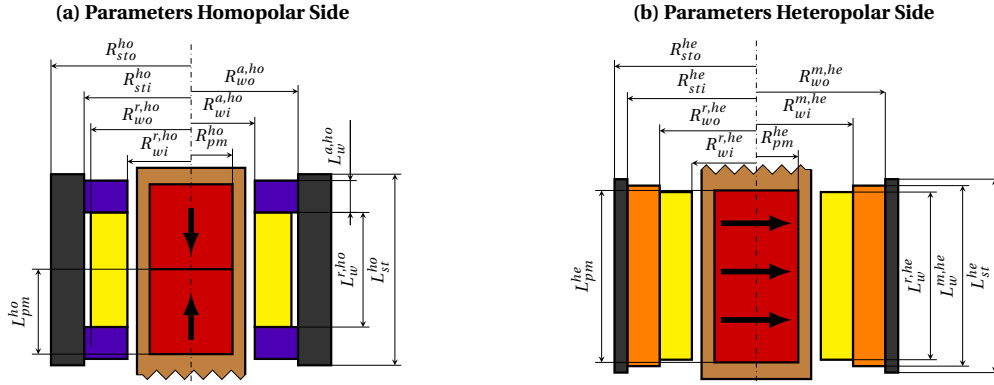
Figure 5.2 – Geometric parameters of homopolar (left) and heteropolar (right) sides, *ho* and *he* respectively, including permanent magnet R_{pm}, L_{pm}, winding R_w, L_w, and back iron R_{st}, L_{st} radius and length, of axial *a* radial *r* bearings and motor *m*.

efficiency independently on the working conditions of each actuator and thus independently on the required input current for its operation.

Furthermore, N weighting factors $\boldsymbol{w} = [w_1, \ldots, w_N]^\top$ are included to add the possibility of prioritising some actuators over others to better adapt to certain use cases where not all actuators are equally required, and to normalise the weight of each objective function $f_i(\boldsymbol{x}_i)$ that may result from combining functions with different units ($\sqrt{W}$/Nm and $\sqrt{W}$/N) and actuators with different volumes.

The optimisation problem defined in (5.5) can be solved by using any non-linear computational optimisation algorithm. In this thesis, MATLAB's built-in function *fmincon* is employed to handle the constrained non-linear optimisation.

5.1.3 Actuators Optimisation

Due to the inherent higher complexity of a fully active magnetic bearing motor, multiple actuators are present in the same system sharing resources. The optimisation of the complete system can then be done by studying all the different actuators either all at once by the multi-objective optimisation, or one by one with the single-objective optimisation. In this section, the general optimisation procedure previously introduced will be applied to maximise the efficiency of the studied fully active magnetic bearing motor developed by Celeroton.

For all the performed optimisations the following considerations are taken:

- The electromagnetic models presented in [47] are employed for an accurate and efficient execution of the optimisation. The models are capable of providing the force k_F and torque k_T constants of each actuator, as well as the phase resistance R_{ph} of the windings.

- For radial bearings and motor, the winding type selection is done by the following priority: hexagonal > rhombic > skewed, due to the increase in efficiency and flexibility

resulting from the additional degrees of freedom ϕ_s, L_s in hexagonal, and ϕ_s in rhombic windings, as defined in Fig. 4.2. Heteropolar radial bearing and motor will employ hexagonal windings, whereas homopolar radial bearing will feature rhombic winding due to manufacturing limitations and tooling availability.

- The copper filling factor of the windings is considered constant for each actuator, taking as a reference the value experimentally obtained by manufacturing.

- Both heteropolar and homopolar sides are optimised using back iron for improved efficiency.

- The total volume of the actuators is considered fixed, corresponding to the one employed in the original machine in order to reuse the same stator parts and compare machines with equivalent size.

- Due to the impact of the weighting factors in multi-objective optimisations, all are set to $w_i = 1$ to preserve the physical meaning of the objective function and equally prioritise all actuators, with the only exception of the motor one, set to $w_i^{m,he} = R_{max}^{he}$ as a change of units.

- The winding properties for optimum efficiency, denoted as $\boldsymbol{x}_i^*$, are obtained using MATLAB's *fmincon* function, employing sequential quadratic programming (SQP) solver to solve the small-case and dense problem.

- The selected winding properties for manufacturing, denoted as $\boldsymbol{x}_i^+$, will be the closest to the resulting optimum when taking into account the limitations due to the manufacturing process, material and tooling availability.

- The original winding properties, denoted as $\boldsymbol{x}_i^o$, are then compared to the optimisation results. The original machine is described in [104].

- A parametric sweep of the main optimisation variables is performed as a sensitivity analysis and its results are included in Fig. 5.3.

The main geometric parameters employed as variables in the optimisation are graphically represented in figure 5.2 for both homopolar and heteropolar sides. The optimisation of the machine is performed in two approaches. In the first optimisations (1 to 4) it is considered that the dimensions of all actuators are fixed (except for the homopolar axial winding in order to choose the back iron size), and only the winding parameters are optimised. For the last optimisations (5-6), multi-objective optimisations including winding and back iron dimensions are performed for the homopolar and heteropolar sides in order to investigate if further improvement can be achieved by considering the couplings between actuators. Finally, the selected parameters for manufacturing the optimised machine are investigated analytically to estimate the efficiency improvement with respect to the original machine.

Table 5.1 – Analytical results of single and multi-objective optimisations obtained using *fmincon* and manufactured windings. Superscript † denote a parameter that is considered fixed in a specific optimisation.

Parameter	Op. 1 a,ho	Op. 2 r,ho	Op. 3 m,he	Op. 4 r,he	Op. 5 a,ho	Op. 5 r,ho	Op. 6 m,he	Op. 6 r,he	Manufactured a,ho	Manufactured r,ho	Manufactured m,he	Manufactured r,he
L_w (mm)	$3^\dagger$	$10^\dagger$	$16^\dagger$	$16^\dagger$	2.62	10.77	16	16	3	10	16	16
R_{wi} (mm)	$4.75^\dagger$	$4.75^\dagger$	$6.5^\dagger$	$4.75^\dagger$	4.75	4.75	5.77	4.75	4.75	4.75	6.5	4.75
R_{wo} (mm)	6.19	$6.2^\dagger$	$9.5^\dagger$	$6.5^\dagger$	6.63	6.63	8.58	5.74	7.38	6.2	9.5	6.5
ϕ_s (°)	-	147	139	85	-	149	144	85.9	-	90	90	90
L_s (mm)	-	-	3.5	6.5	-	-	3.64	6.80	-	-	7.5	8.5
w_i (-)	1	1	10	1	1	1	10	1	1	1	10	1
$\frac{K_i}{w_i}$ $\left(\frac{\text{N}}{\sqrt{\text{W}}}\right)$	0.312	0.402	0.219	0.451	0.311	0.464	0.250	0.407	0.284	0.351	0.199	0.457
$\left(\sum \frac{w_i}{K_i}\right)^{-1}$	0.176 $\frac{\text{N}}{\sqrt{\text{W}}}$			0.147 $\frac{\text{N}}{\sqrt{\text{W}}}$	0.186 $\frac{\text{N}}{\sqrt{\text{W}}}$		0.155 $\frac{\text{N}}{\sqrt{\text{W}}}$		0.157 $\frac{\text{N}}{\sqrt{\text{W}}}$		0.139 $\frac{\text{N}}{\sqrt{\text{W}}}$	

Optimisation 1: *Homopolar Axial Bearing*

In this optimisation both axial winding outer radius and back iron inner radius will be chosen in such a way that the efficiency of the axial bearing winding is maximised. For this purpose it is considered that the single-objective optimisation will maximise the bearing efficiency defined as $K_B^{a,ho}$, being the variable to adjust the outer winding radius $x_1 = R_{wo}^{ao}$, and considering both the length $L_w^{a,ho}$ and inner radius R_{wi}^{ao} fixed to preserve the stator dimensions. The single-objective optimisation can then be expressed as

$$\min_{R_{wo}^{a,ho}} f_1(R_{wo}^{a,ho}) := \frac{w_1^{a,ho}}{K_B^{a,ho}} = \frac{1}{K_B^{a,ho}}, \tag{5.6}$$

subject to

$$R_{wi}^{a,ho} \leq R_{wo}^{a,ho} \leq R_{max}^{ho}, \quad R_{wo}^{a,ho} = R_{sti}^{ho}.$$

As weighting factor, in order to be able to directly compare the results between optimisations, the same value that is employed in optimisation 5 is used here, being $w_1^{a,ho} = 1$. The inverse of the objective function defined in (5.6) is plotted in figure 5.3.a, where the optimum, x_1^*, results in an efficiency increase of 37.2 % with respect to the original actuator with parameters x_1^o and no back iron. This efficiency increase is a combined result of a more efficient positioning of the winding, with all winding volume closer to the permanent magnet, and the addition of back iron. These results are summarised in table 5.1 and will be validated experimentally in chapter 7.
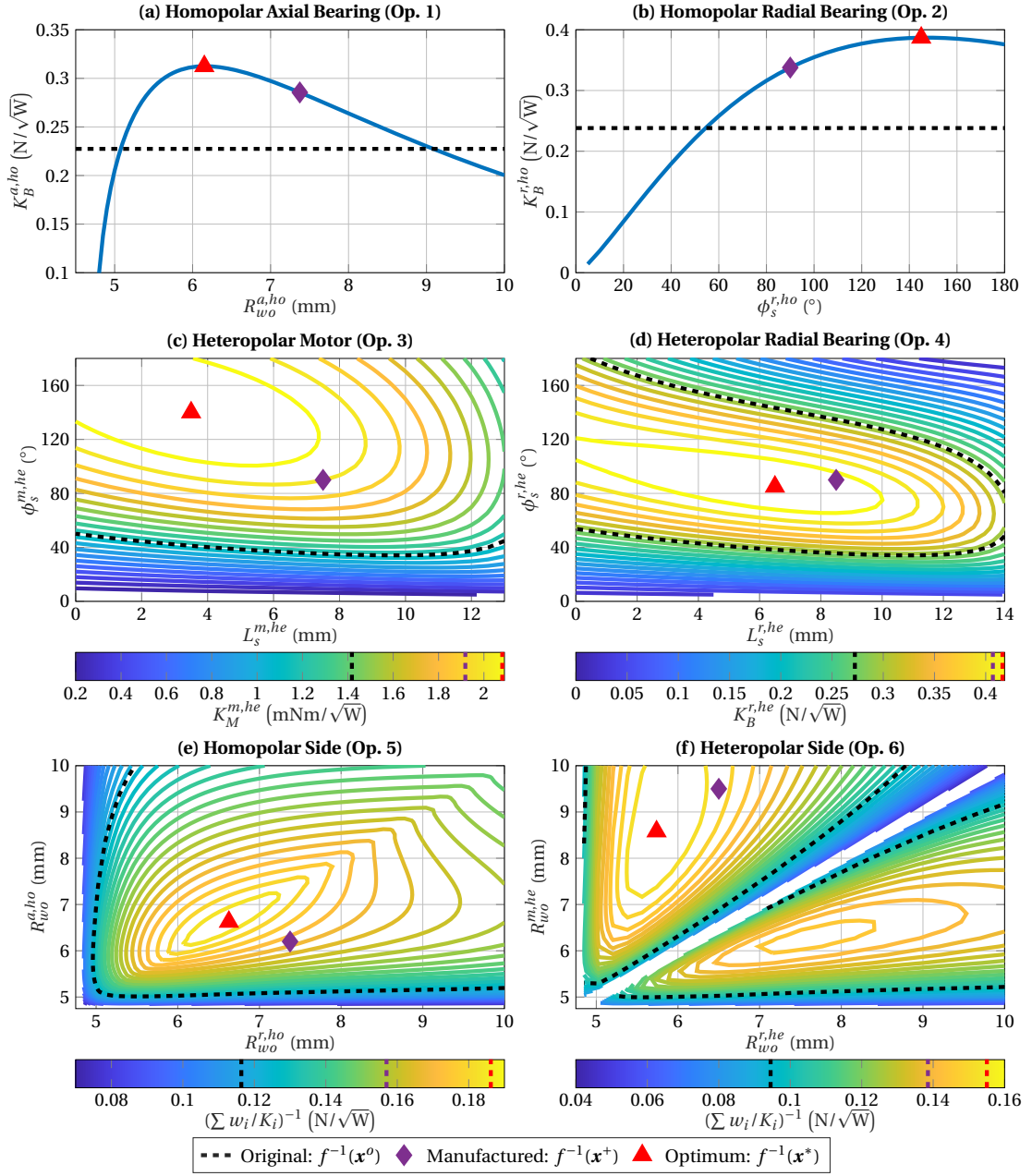
Figure 5.3 – Single and multi-objective optimisation results. Single-objective optimisations: homopolar axial (a) and radial bearing (b), heteropolar motor (c) and radial bearing (d) windings. Multi-objective optimisations: homopolar (e) and heteropolar (f) sides. All figures show the efficiency measure as per (5.1a) and (5.1b), thus being $f_i^{-1}(x_i)$.

Optimisation 2: *Homopolar Radial Bearing*

For this bearing there exist three options for selecting the winding type: skewed, rhombic and hexagonal. The skewed one is discarded due to the high force ripple and disturbances featured with this winding, caused by the layered winding structure of rather short and thick

dimensions, as it will be shown in chapter 7. The hexagonal type is also discarded due to the maximum length constraint of the winding, making it impossible to manufacture.

The rhombic winding type will be then optimised considering fixed winding dimensions ($R_{wi}^{r,ho}$, $R_{wo}^{r,ho}$ and $L_w^{r,ho}$) and a back iron with inner radius R_{sti}^{ho} resulting from the previous optimisation. The single-objective optimisation is performed by adjusting the opening angle of the rhombus $x_2 = \phi_s^{r,ho}$, seeking a maximisation of the bearing factor $K_B^{r,ho}$, by solving the following problem:

$$\min_{\phi_s^{r,ho}} f_2(\phi_s^{r,ho}) := \frac{w_2^{r,ho}}{K_B^{r,ho}} = \frac{1}{K_B^{r,ho}}, \tag{5.7}$$

subject to

$$0° \leq \phi_s^{r,ho} \leq 180°.$$

The same weighting factor that is employed in optimisation 5 is also used here, being $w_2^{r,ho} = 1$. The inverse of the objective function is plotted in figure 5.3.b, showing an optimum, x_2^*, that yields an increase in efficiency of 68.8 % with respect to the original bearing winding without back iron. This efficiency increase is again a combined result of a more efficient winding and the addition of back iron. If the optimisation is executed without back iron and thus no reluctance forces, the optimum would still result in an efficiency increase of 43.6 %. As before, the results are summarised in Table 5.1 and experimentally validated in chapter 7.

Optimisation 3: *Heteropolar Motor*

The three options of winding types for this winding are again: skewed, rhombic and hexagonal. The original system employed a skewed winding type, but it featured considerable torque disturbances in radial direction, and thus it is targeted to reduce such components by using a highly symmetric winding type such as rhombic and hexagonal. The latter is finally selected due to the increased torque density as a result of the additional degree of freedom with respect to the rhombic one, while keeping a high symmetric structure.

The two free parameters to adjust will be the opening angle of the hexagon $\phi_s^{m,he}$ and the length of the hexagon's axial segment $\boldsymbol{x}_3 = [\phi_s^{m,he}, L_s^{m,he}]^\top$, while the dimensions of the winding are fixed. It is again sought to maximise the efficiency of the winding defined as the motor constant, $K_M^{m,he}$. The single-objective optimisation problem is then defined as

$$\min_{\boldsymbol{x}_3} f_3(\boldsymbol{x}_3) := \frac{w_3^{m,he}}{K_M^{m,he}} = \frac{R_{max}^{he}}{K_M^{m,he}}, \tag{5.8}$$

subject to

$$0° \leq \phi_s^{m,he} \leq 180°, \quad 0 \leq L_s^{m,he} \leq L_w^{m,he}.$$

As weighting factor, the same one that is employed in optimisation 6 is also used here, being $w_3^{m,he} = R_{max}^{he}$, allowing the possibility of directly comparing with bearing factors due to the

change in units and normalisation of the results. In figure 5.3.c, the inverse of the objective function is shown, where the optimum, $\boldsymbol{x}_3^*$, results in an increase in motor constant (efficiency) of 55.2 % with respect to the original skewed winding $\boldsymbol{x}_3^o$. These figures are summarised in Table 5.1 and experimentally validated in chapter 7.

Optimisation 4: *Heteropolar Radial Bearing*

The exact same approach and optimisation problem as the motor winding can be performed for this winding. The hexagonal winding is optimised by seeking the maximum bearing constant, $K_B^{r,he}$, varying the opening angle of the hexagon and the length of the axial segment, $\boldsymbol{x}_4 = [\phi_s^{r,he}, L_s^{r,he}]^\top$, while considering the winding dimensions and the copper filling factor fixed. The single-objective optimisation problem is defined as

$$\min_{\boldsymbol{x}_4} f_4(\boldsymbol{x}_4) := \frac{w_4^{r,he}}{K_B^{r,he}} = \frac{1}{K_B^{r,he}}, \tag{5.9}$$

subject to

$$0° \leq \phi_s^{r,he} \leq 180°, \quad 0 \leq L_s^{r,he} \leq L_w^{r,he}.$$

The selected weighting factor is selected as in optimisation 6, being $w_4^{r,he} = 1$. This resulting objective function is shown in figure 5.3.d, where the optimum, $\boldsymbol{x}_4^*$, yields an expected increase of bearing constant of 57.9 % with respect to the original system $\boldsymbol{x}_4^o$. These results are included in Table 5.1 and are also experimentally validated in chapter 7.

Optimisation 5: *Homopolar Side*

In this case, a multi-objective optimisation is studied for the homopolar side, by searching the optimal winding dimensions and parameters of axial and radial bearings. The objective function is defined as a linear combination of the inverse of the actuators' bearing constants in order to maximise its combined efficiency, varying the dimensions and parameters of the radial bearing, $\boldsymbol{x}_5^{r,ho} = [L_w^{r,ho}, R_{wi}^{r,ho}, R_{wo}^{r,ho}, \phi_s^{r,ho}]^\top$, and axial bearing winding, $\boldsymbol{x}_5^{a,ho} = [L_w^{a,ho}, R_{wi}^{a,ho}, R_{wo}^{a,ho}]^\top$. The multi-objective optimisation problem is defined as

$$\min_{\boldsymbol{x}_5} f_5(\boldsymbol{x}_5) := \frac{w_5^{r,ho}}{K_B^{r,ho}} + \frac{w_5^{a,ho}}{K_B^{a,ho}} = \frac{1}{K_B^{r,ho}} + \frac{1}{K_B^{a,ho}}, \tag{5.10}$$

subject to

$$0 \leq L_w^{r,ho} \leq L_{max}^{ho}, \quad R_{min}^{ho} \leq R_{wi}^{r,ho} \leq R_{wo}^{r,ho}, \quad R_{wi}^{r,ho} \leq R_{wo}^{r,ho} \leq R_{max}^{ho}, \quad 0° \leq \phi_s^{r,ho} \leq 180°,$$
$$0 \leq L_w^{a,ho} \leq L_{max}^{ho}, \quad R_{min}^{ho} \leq R_{wi}^{a,ho} \leq R_{wo}^{a,ho}, \quad R_{wi}^{a,ho} \leq R_{wo}^{a,ho} \leq R_{max}^{ho},$$

$$2L_w^{a,ho} + L_w^{r,ho} \leq L_{max}^{ho}, \quad R_{sti}^{ho} = \max\left(R_{wo}^{a,ho}, R_{wo}^{r,ho}\right).$$

In the first group of constraints, the physical constraints for each actuator are defined, including the maximum available space in the stator casing as L_{max}^{ho}, R_{min}^{ho} and R_{max}^{ho}, whereas in the second set the couplings between actuators are specified, mainly the fact that the radial bearing is located between the two axial coils and that the inner radius of the back iron is limited by the thickest coil, as in figure 5.1. The weighting factors for the multi-objective optimisation are selected as $w_5^{r,ho} = 1$ and $w_5^{a,ho} = 1$ for the radial and axial bearings, respectively, in order to give the same weight to both actuators.

The results of the optimisation are included in Table 5.1. It can be seen that these results do not greatly differ from the ones obtained with optimisations 1-2. As expected, the inner radii of the windings is fixed as close as possible from the permanent magnet to capture more magnetic flux. Furthermore, the optimum is obtained with a slightly longer radial bearing winding and shorter axial windings. For the remaining parameters, in order to better study the dependency of the objective function, a parametric sweep is performed for the outer radii of radial and axial bearing windings and its results are included in figure 5.3.e. As ϕ_s of the rhombic radial bearing is independent from the remaining parameters, only the optimum for each winding dimension is considered in the figure.

The optimum will result in an increase of 55.6 % with respect to the original machine $\boldsymbol{x}_5^o$ as per [104] with no back iron, and of 2.9 %, with respect to the system resulting from optimisations 1 and 2.

Optimisation 6: *Heteropolar Side*

In this case, a multi-objective optimisation is studied for the heteropolar side, by searching the optimal winding dimensions and parameters of radial bearing and motor windings. The objective function is defined as a linear combination of the inverse of the motor and bearing constants in order to maximise the efficiency of both actuators, varying the dimensions and parameters of the radial bearing, $\boldsymbol{x}_6^{r,he} = [L_w^{r,he}, R_{wi}^{r,he}, R_{wo}^{r,he}, \phi_s^{r,he}, L_s^{r,he}]^\top$, and motor winding, $\boldsymbol{x}_6^{m,he} = [L_w^{m,he}, R_{wi}^{m,he}, R_{wo}^{m,he}, \phi_s^{m,he}, L_s^{m,he}]^\top$. The multi-objective optimisation problem is defined as

$$\min_{\boldsymbol{x}_6} f_6(\boldsymbol{x}_6) := \frac{w_6^{r,he}}{K_B^{r,he}} + \frac{w_6^{m,he}}{K_M^{m,he}} = \frac{1}{K_B^{r,he}} + \frac{R_{max}^{he}}{K_M^{m,he}}, \tag{5.11}$$

subject to

$$0 \le L_w^{r,he} \le L_{max}^{he}, \quad R_{min}^{he} \le R_{wi}^{r,he} \le R_{wo}^{r,he}, \quad R_{wi}^{r,he} \le R_{wo}^{r,he} \le R_{max}^{he}, \quad 0° \le \phi_s^{r,he} \le 180°,$$
$$0 \le L_w^{m,he} \le L_{max}^{he}, \quad R_{min}^{he} \le R_{wi}^{m,he} \le R_{wo}^{m,he}, \quad R_{wi}^{m,he} \le R_{wo}^{m,he} \le R_{max}^{he}, \quad 0° \le \phi_s^{m,he} \le 180°,$$
$$0 \le L_s^{r,he} \le L_w^{r,he}, \quad 0 \le L_s^{m,he} \le L_w^{m,he},$$

$$\left| R_{wo}^{m,he} - R_{wo}^{r,he} \right| > 0, \quad R_{sti}^{he} = \max(R_{wo}^{m,he}, R_{wo}^{r,he}),$$
$$R_{wi}^{m,he} = R_{wo}^{r,he}, \quad \text{if } R_{wo}^{r,he} < R_{wo}^{m,he},$$
$$R_{wi}^{r,he} = R_{wo}^{m,he}, \quad \text{if } R_{wo}^{r,he} > R_{wo}^{m,he}.$$

In a similar manner to the optimisation of the homopolar side, in the first group of constraints, the physical constraints for each actuator are defined, with the maximum available space L_{max}^{he}, R_{min}^{he} and R_{max}^{he}, and, in the second set, the couplings between actuators are specified. These couplings consist of the fact that the bearing is located at the inner part and the motor winding in the outer, as in figure 5.1. The weighting factors for the multi-objective optimisation are selected as $w_6^{r,he} = 1$ and $w_6^{m,he} = R_{max}^{he}$ for the radial bearing and motor, respectively, in order to normalise and convert to equivalent units for both actuators.

The numerical results of the optimisation are included in Table 5.1. From these results it can be seen that, as expected, the inner radius of the bearing winding is fixed as close as possible to the permanent magnet, $R_{wi}^{m,he} = R_{min}^{he}$, and the length of both windings is $L_w = L_{max}^{he}$ to capture the maximum flux possible, and thus these parameters could be removed from the analysis to reduce the computational complexity of the optimisation. The dependency of the bearing and motor efficiency with respect to the outer radii of the windings is included in figure 5.3.f. As parameters ϕ_s and L_s of motor winding are independent from the ones of the bearing, and *vice versa*, only the optimum for each winding dimensions is considered in the figure.

The optimum yields an increase of 64 % with respect to the original system $\boldsymbol{x}_6^o$ as in [104], and of 5.4 % with respect to the resulting actuator from optimisations 3-4. The upper triangle in the results represent the case where the motor winding is located at the outer part of the machine and the radial bearing in the inner part ($R_{wo}^{m,he} > R_{wo}^{r,he}$), which corresponds to the current arrangement of actuators, whereas the lower triangle represents the opposite case with the motor in the inner part ($R_{wo}^{m,he} < R_{wo}^{r,he}$). From the results it can be seen that the former arrangement results in a more efficient machine than the latter.

Manufactured Optimised System

Considering the manufacturing limitations and raw material availability for the back iron, the exact configurations resulting from all the previous optimisations cannot be realised. As optimisations 1-4 already considered the majority of these limitations, they are used as a basis for the manufacturing. Then, the closest available winding and stator parameters to these optimums are selected and manufactured, whose exact dimensions and efficiency as defined in previous optimisations is included in table 5.1. With respect to the original system defined in [104], the analytical models show that the manufactured system will result in the expected efficiency increases detailed in table 5.2, which can be summarised as:

1. *Homopolar axial bearing*: the manufactured bearing would result in a 20.3 % increase in efficiency, as per optimisation 1 (5.6), according to available analytical models.

2. *Homopolar radial bearing*: the manufactured bearing will result in an efficiency increase of 38.7 %, as per optimisation 2 (5.7), according to the employed analytical models.

3. *Heteropolar motor*: the manufactured motor is expected to have an efficiency increase

Table 5.2 – Analytical calculations of original and manufactured optimised winding properties, including bearing K_B and motor K_M constants, force κ_F and torque κ_T constants, and winding phase resistance R_{ph}.

Funct.	Stator			K_B, K_M		κ_F, κ_T		R_{ph}
	Winding	Side	Iron					
Axial Bearing	Original (Ax.)	Hom	w/o	0.236	N/$\sqrt{W}$	1.004	N/A	18.1 Ω
	Manufact. (Ax.)	Hom	w/	0.284	N/$\sqrt{W}$	0.895	N/A	9.93 Ω
	Relative Difference:			+20.3 %		−10.9 %		−45.1 %
Radial Bearing	Original (Sk.)	Hom	w/o	0.253	N/$\sqrt{W}$	0.408	N/A	2.60 Ω
	Manufact. (Rh.)	Hom	w/	0.351	N/$\sqrt{W}$	0.603	N/A	2.95 Ω
	Relative Difference:			+38.7 %		+47.8 %		+13.5 %
Motor	Original. (Sk.)	Het	w/	1.490	mNm/$\sqrt{W}$	1.273	mNm/A	0.73 Ω
	Manufact. (Hx.)	Het	w/	1.997	mNm/$\sqrt{W}$	2.146	mNm/A	1.16 Ω
	Relative Difference:			+34.0 %		+68.6 %		+58.9 %
Radial Bearing	Original (Sk.)	Het	w/	0.324	N/$\sqrt{W}$	0.387	N/A	1.43 Ω
	Manufact. (Hx.)	Het	w/	0.457	N/$\sqrt{W}$	0.678	N/A	2.20 Ω
	Relative Difference:			+41.1 %		+75.2 %		+53.9 %

of 34.0 %, as per optimisation 3 (5.8), according to employed analytical models.

4. *Heteropolar radial bearing*: the manufactured bearing would result in an increase of 41.1 % in efficiency, as per optimisation 4 (5.9).

5. *Homopolar side*: the manufactured homopolar radial and axial bearings will result in a global increase of 28.6 % in efficiency for the homopolar side, as per optimisation 5 (5.10).

6. *Heteropolar side*: the manufactured heteropolar radial bearing and motor will result in a global increase of 36.2 % in efficiency for the heteropolar side, as per optimisation 6 (5.11).

These results will be experimentally measured and validated in chapter 7 through a measurement of each actuator's forces or torques and phase resistances. Furthermore, these static measurements are completed by the measurement of the power consumption of the system during operation, and thus directly quantifying the efficiency increase.

5.2 Hybrid Magnetic Bearing Motor Optimisation

Depending on the use case, having a total of six degrees of freedom actively controlled may impose an excessive cost or complexity for the viability of magnetic bearings in a given application. Each actively controlled degree of freedom requires additional sensing, actuation and computing power that may be prohibitive in some cases.
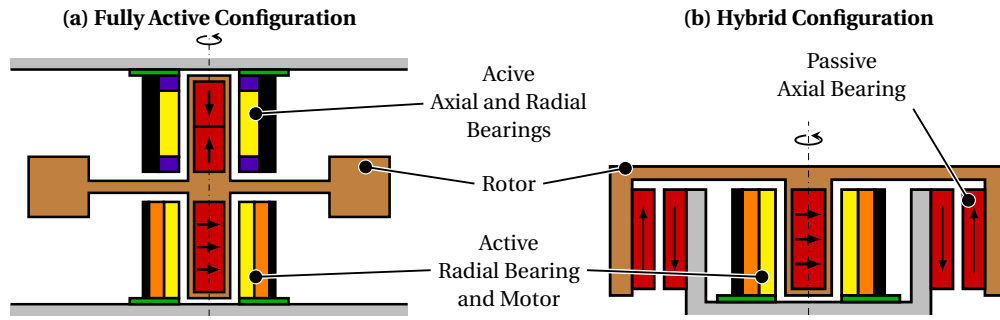
Figure 5.4 – Schematic cross section of fully active and hybrid magnetic bearing reaction wheels.

For this reason, it may be preferred to sacrifice some of the performance of a fully active magnetic bearing (AMB) system and include some degrees of freedom that are passively stabilised. Such a configuration is named a hybrid magnetic bearing (HMB) system, which combines active and passive magnetic bearings. Note that a fully passive magnetic bearing configuration employing paramagnetic or ferromagnetic materials is not possible as a result of Earnshaw's theorem [30].

As it can be observed from the closed-loop models defined in chapter 3 and from the experimental measurements in chapter 7, the most critical dynamics and vibrations are in radial direction, as unbalance, shaft bow and other disturbances are predominantly radial. Furthermore, axial dynamics are generally decoupled from radial dynamics and a simple single-input single-output (SISO) control is usually sufficient for its stabilisation.

For this reason in order to simplify the general topology of the studied actuator without greatly affecting its stability, performance and vibration suppression capabilities, an arrangement of permanent magnet rings is included in the rotor rim to passively stabilise the axial displacements. The location of the rings at the outer part of the rotor and stator, at a relatively big radius from the rotation axis also allows the passive stabilisation of the radial tilting of the rotor. To maintain complete functionality of the machine, it is then needed to actively control the radial displacements and the torsional (motor) dynamics of the rotor. The heteropolar side of the original machine, featuring a radial bearing and motor is considered for the stabilisation of these degrees of freedom, resulting in a configuration such as the one graphically shown in figure 5.4.b, where it is compared to the fully active configuration in figure 5.4.a.

The simplification of the magnetic bearing topology to include a hybrid configuration comes at the expense of the inability of actively suppressing radial torque vibrations. As torque vibrations are generally less critical than forces, specially in space applications, where a force generated by the reaction wheel, usually located at a relatively big distance from the satellite's centre of mass, would generate a much greater torque than the one generated at the actuator itself, the performance hit of the passive stabilisation of these degrees of freedom would still be minimum.

Two main configurations are considered for the passive stabilisation of axial and tilting degrees
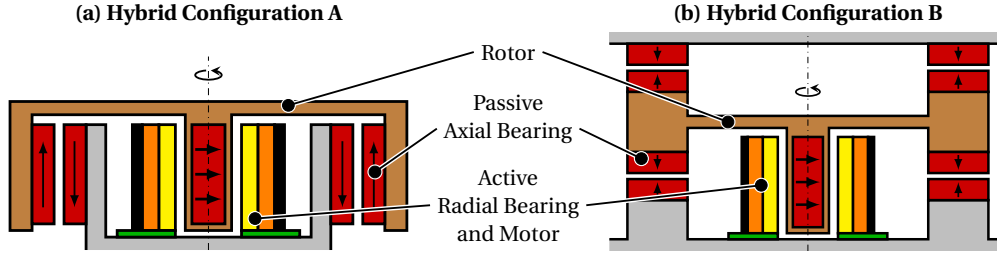
Figure 5.5 – Schematic cross section of studied hybrid magnetic bearing reaction wheel topologies with attractive (a) or repulsive configurations (b).

of freedom, which are shown in figure 5.5, featuring either attractive or repulsive arrangements of permanent magnets. The previously defined models for calculating the forces, torques and stiffness for both configurations enable the possibility of precisely dimensioning the passive structures to target a stable and high-performance system.

5.2.1   Optimisation Problem Definition

Whereas the optimisation procedure presented in section 5.1 can still be employed for the active parts of the hybrid configuration, a different procedure needs to be followed for the dimensioning and selection of the appropriate passive magnetic bearing configuration.

As shown in the validation of the passive magnetic bearing (PMB) models in section 4.3, the passive stabilisation of axial and tilting degrees of freedom, with stiffness coefficients $k > 0$, imposes a destabilising effect in radial direction, with stiffness coefficient $k < 0$, which need to be overcome by the active radial bearing. For this reason, the ultimate goal is the selection of a passive configuration that guarantees stable behaviour for the whole target speed range, while not greatly disturbing the radial dynamics.

In this analysis no detailed design of such a machine is envisioned, and only a high-level validation of such a concept is sought. In order to achieve this objective, the closed-loop dynamics, defined in chapter 3, and the electromagnetic active and passive magnetic bearing models, detailed in chapter 4, are employed, and the following design flow is proposed:

1. **System design**, $\{A\}$.

   - *Inputs*: dimensioning of rotor, active and passive elements.
   - *Method*: electromagnetic models of active and passive magnetic bearings.
   - *Output*: system high-level parameters for rotordynamics models.
     - *Physical parameters*: rotor mass, m, inertia, I_p, I_t, centre of gravity eccentricity, ϵ_w, and main axis of inertia tilt, χ.
     - *Magnetic parameters*: magnetic stiffness in radial direction, k_{11}, angular direction, k_{22}, and axial direction, k_{33}, and active bearing force constant, κ_F. No

damping (d_n and d_r) nor crossed element in stiffness (k_{12}, k_{13} and k_{23}) are considered.

2. **Reduced rotordynamics definition**, $\boldsymbol{P_{red}}$.

   - *Inputs*: $m, \epsilon, k_r, \kappa_F$.
   - *Method*: Jeffcott rotor rotordynamics model (only linear dynamics).
   - *Output*: system plant dynamic system for controller design P_{red}.

3. **Controller/observer design**, $\boldsymbol{R}$.

   - *Inputs*: P_{red} and closed-loop requirements and goals.
   - *Method*: pole-placement for homogeneous performance and equal comparison of bearings.
   - *Output*: controller and observer dynamic systems R.

4. **Full rotordynamics definition**, $\boldsymbol{P_{full}}$.

   - *Inputs*: $m, I_p, I_t, \epsilon, \chi, k_{11}, k_{22}, k_{33}, \kappa_F$.
   - *Method*: five degrees-of-freedom rotordynamics model (complete axial and radial linear and angular dynamics).
   - *Output*: system plant dynamic system for closed-loop system analysis P_{full}.

5. **Closed-loop analysis**.

   - *Inputs*: P_{full}, R.
   - *Method*: frequency and time-based analysis, considering closed-loop poles, Campbell diagram and unbalance response.
   - *Outputs*: stability and performance check through unbalance response. If closed-loop system is not stable or unbalance response not acceptable (excessive orbits or vibrations), iterate from steps 1-5.

In order to have a direct comparison with the available fully active magnetic bearing system, a hybrid magnetic bearing machine with similar dimension of actuators is considered. The main factors that determine the practical use of a reaction or momentum wheel are the maximum angular momentum storage capacity $L_{max} = I_p \Omega_{max}$ and torque T_{max}. In a similar way, for conventional motors, its size is mainly defined by its maximum power $P_{max} = T_{max}\Omega_{max}$. Considering that the same heteropolar side of the fully active magnetic bearing motor, T_{max} remains unchanged and the two remaining degrees of freedom are both I_p and Ω_{max}. It is then chosen to target a design which will feature the same order of magnitude of maximum angular momentum storage capacity.

As only a high-level design is envisioned, in the following section, the viability of such configurations is analysed through the study of stability and behaviour of the closed-loop systems.

Table 5.3 – Passive magnetic bearing (PMB) dimensions for configurations A and B, as defined in figure 4.4. All radial and axial dimensions are expressed in mm.

System	r_1	r_2	r_3	r_4	z_1	z_2	z_3	z_4
Config. A	16	23.5	24	31	-2	2	-2	2
Config. B	19	23	19	23	-4.25	-0.25	0.25	4.25

5.2.2 Viability Validation and Closed-Loop Analysis

In this section, the final high-level design of the hybrid magnetic bearing machine is described. The previously defined design flow is executed and the final results are explained for each of the steps.

System Design

For simplicity, the analysis is only focused on the passive magnetic bearing and its influence on the closed-loop system. It is then considered that the active magnetic bearing and motor are obtained through the optimisation shown in section 5.1, featuring the properties and dimensions summarised in table 5.1 for optimisation 6.

To perform the dimensioning of the machine, the following considerations are taken:

- A total rotor mass similar to the fully active rotor is targeted.

- For comparison between configurations A and B of the passive bearing, a similar total permanent magnet volume in both rotor and stator is considered.

- The maximum speed is chosen in such a way that the total angular momentum is equal or greater than the one of the fully active machine.

- No critical speed should be present in the considered speed range. For this reason, the passive stiffness in axial and tilting directions should be such that the axial and conical modes of the rotordynamic system are always higher than the rotation frequency.

- A minimum thickness of 4 mm in either radial or axial direction is imposed for the permanent magnet rings.

As no detailed rotor design is intended, the simple rotor configurations shown in figure 5.6 is considered to calculate its mass and inertia. For both configurations, the rotor can be divided in rim, spokes and shaft, and the only materials employed are titanium, with density $\rho_{Ti} = 4.506\,\text{g/cm}^3$, and Samarium-Cobalt magnets, with density $\rho_{SmCo} = 8.5\,\text{g/cm}^3$. To simplify the calculation, the spokes are considered as massless, and the shaft to be like the heteropolar side of the fully active configuration, being a cylindrical permanent magnet and a titanium rotor sleeve.
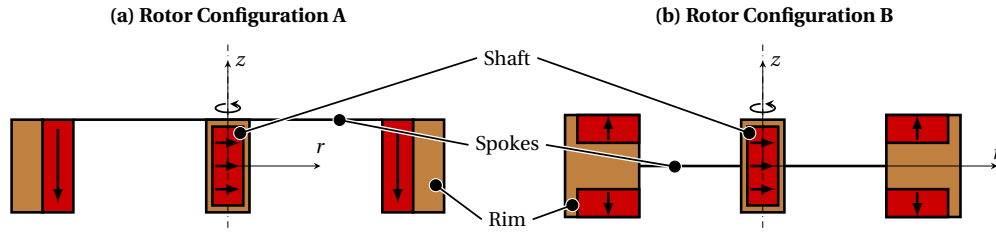
Figure 5.6 – Simplified hybrid magnetic bearing rotor structure for mass and inertia calculations with titanium and Samarium-Cobalt permanent magnet rim and shaft with massless spokes.

Table 5.4 – Closed-loop system parameters of rotordynamics model for fully active (AMB) and hybrid magnetic bearing (HMB) system configurations A and B.

System	Param.	Value		Param.	Value		Param.	Value	
AMB	m	71	g	I_t	18.9	kgmm^2	I_p	23.8	kgmm^2
	k_{11}	-0.3	N/mm	k_{22}	-0.1	Nm/rad	k_{33}	0.071	N/mm
	Ω_{max}	20	krpm	V_{PM}	1.00	cm^3	L_{max}	49.79	mNms
	ϵ	10	μm	χ	100	μrad			
HMB Conf. A	m	94.9	g	I_t	36.3	kgmm^2	I_p	72.1	kgmm^2
	k_{11}	-44.6	N/mm	k_{22}	26.7	Nm/rad	k_{33}	89.2	N/mm
	Ω_{max}	8	krpm	V_{PM}	9.06	cm^3	L_{max}	60.42	mNms
	ϵ	6.68	μm	χ	79.8	μrad			
HMB Conf. B	m	97.8	g	I_t	23.6	kgmm^2	I_p	45.3	kgmm^2
	k_{11}	-67.2	N/mm	k_{22}	28.0	Nm/rad	k_{33}	134.5	N/mm
	Ω_{max}	10	krpm	V_{PM}	8.94	cm^3	L_{max}	47.39	mNms
	ϵ	6.68	μm	χ	135.7	μrad			

Then, the rotor rim for each passive bearing configuration is:

- **Configuration A**: the rim is composed of an outer titanium rim of 3 mm of thickness and an inner magnet ring with dimensions r_3, r_4, z_3, z_4 as defined in table 5.3.

- **Configuration B**: the rim is composed of an outer titanium rim of 3 mm of thickness, two permanent magnet rings with dimensions r_3, r_4, z_3, z_4 as defined in table 5.3 and axially separated by 5 mm titanium.

In table 5.3, the final passive magnetic bearing dimensions for both configurations are defined, and in table 5.4, the main high-level parameters resulting from a system with such dimensions, calculated using the electromagnetic models validated in chapter 4. Also, for comparison, the high-level parameters of the studied fully active systems are shown.

It can be seen that the repulsive configuration (B) requires two pairs of permanent magnet rings instead of a single pair for the attractive configuration (A). The dimensions are then chosen to contain an equivalent total permanent magnet volume in rotor and stator.

The unbalance magnitude of the rotor is chosen within the allowed balancing limits for rotating machinery of equivalent size with balancing grade G6.3 provided by [14].

Reduced Rotordynamics

The design of the radial bearing controller is performed using a rotordynamic model that only considers the radial displacements, which corresponds to the Jeffcott rotor model defined in equations (3.3) and (3.4).

It is assumed that there is no damping in the system, that the radial bearing forces are applied at the center of gravity of the rotor and that the position sensors directly measure the rotor radial displacements. Under these assumptions the rotordynamics model can be defined as

$$M_q\ddot{\boldsymbol{q}} + K_q\boldsymbol{q} = U_q\boldsymbol{u},$$
$$\boldsymbol{y} = W_q\boldsymbol{q} \tag{5.12}$$

being M_q, K_q, as defined in (3.4), $U_q = \kappa_F^{r,he} = 0.5\,\text{N/A}$, and $W_q = I$, $\boldsymbol{q}$ the Jeffcott rotor generalised coordinates, $\boldsymbol{u}$ the radial bearing currents and $\boldsymbol{y}$ the position sensor measurements. Reformulating in state-space representation, considering $\boldsymbol{x}_P = [\boldsymbol{q}^\top, \dot{\boldsymbol{q}}^\top]^\top$ the plant dynamics are

$$P_{red} = \begin{cases} \dot{\boldsymbol{x}}_P(t) = A_P\boldsymbol{x}_P(t) + B_P\boldsymbol{u}(t) = \begin{bmatrix} O & I \\ -M_q^{-1}K_q & O \end{bmatrix}\boldsymbol{x}_P(t) + \begin{bmatrix} O \\ M_q^{-1}U_q \end{bmatrix}\boldsymbol{u}(t), \\ \boldsymbol{y}(t) = C_P\boldsymbol{x}_P(t) = \begin{bmatrix} W_q & O \end{bmatrix}\boldsymbol{x}_P(t) = \begin{bmatrix} I & O \end{bmatrix}\boldsymbol{x}_P(t). \end{cases} \tag{5.13}$$

Controller/Observer Design

Having defined the dynamics of the system to control, the controller and observer is designed by considering a full-state feedback control technique. An observer with matrix gain L_{SF} will estimate the system states, and a controller with gain matrix K_{SF} will stabilise the system to its reference position.

The design of L_{SF} and K_{SF} is performed by pole placement, to guarantee similar behaviour between the studied configurations. To simplify the analysis, continuous-time controller and observer are studied, and the performance is chosen by the desired closed-loop poles of observer $s_L = [-1.1, -1]\,\text{kHz}$ and controller $s_K = [-0.15, -0.12]\,\text{kHz}$.

Then, the radial position observer and controller can be combined into the following dynamic system in state-space representation

$$R = \begin{cases} \dot{\boldsymbol{x}}_R(t) = A_R\boldsymbol{x}_R(t) + B_R\boldsymbol{y}(t) = (A_P - B_PK_{SF} - L_{SF}C_P)\boldsymbol{x}_R(t) + L_{SF}\boldsymbol{y}(t), \\ \boldsymbol{u}(t) = C_R\boldsymbol{x}_R(t) = -K_{SF}\boldsymbol{x}_R(t), \end{cases} \tag{5.14}$$

where it is considered that the reference position is always 0. Note that, as opposed to chapter 3, to simplify the notation R considers both controller and observer.

Full Rotordynamics

In order to fully analyse the behaviour of the rotor in all directions, the closed-loop analysis is performed considering the five degrees-of-freedom model defined in equations (3.3) and (3.8).

The equations of motion of a rotating body with no damping and generalised coordinates $\boldsymbol{q} = [r_c, \phi_c, z_c]$, including radial displacement r_c, tilting ϕ_c and axial displacements z_c, result in

$$M_q \ddot{\boldsymbol{q}}(t) + G_q(\Omega)\dot{\boldsymbol{q}}(t) + K_q \boldsymbol{q}(t) = U_q \boldsymbol{u}(t) + V_q \boldsymbol{u}_d(t),$$
$$\boldsymbol{y}(t) = W_q \boldsymbol{q}(t)$$

(5.15)

being M_q, K_q, G_q, as defined in (3.8), with only diagonal elements of stiffness $k_{12} = k_{13} = k_{23} = 0$, U_q, V_q and W_q defined as

$$U_q = \begin{bmatrix} \kappa_F^{r,he} \\ 0 \\ 0 \end{bmatrix}, \quad V_q = \Omega^2 \begin{bmatrix} m\epsilon e^{j\alpha} \\ \chi(I_t - I_p)e^{j\beta} \\ 0.1 m\epsilon e^{j\alpha} \end{bmatrix}, \quad W_q = \begin{bmatrix} 1 & 0 & 0 \end{bmatrix},$$

(5.16)

and the physical parameters as defined in table 5.4. An harmonic disturbance in axial direction with one tenth of the radial unbalance magnitude is artificially included to clearly see any possible resonance in this direction in the closed-loop system unbalance response.

The state-space representation of such a system is

$$P_{full} = \begin{cases} \dot{\boldsymbol{x}}_P(t) = A_P \boldsymbol{x}_P(t) + B_P \boldsymbol{u}(t) + B_P' \boldsymbol{u}_d(t) = \\ \quad = \begin{bmatrix} O & I \\ -M_q^{-1}K_q & -M_q^{-1}G(\Omega) \end{bmatrix} \boldsymbol{x}_P(t) + \begin{bmatrix} O \\ M_q^{-1}U_q \end{bmatrix} \boldsymbol{u}(t) + \begin{bmatrix} O \\ M_q^{-1}V_q \end{bmatrix} \boldsymbol{u}_d(t), \\ \boldsymbol{y}(t) = C_P \boldsymbol{x}_P(t) = \begin{bmatrix} W_q & O \end{bmatrix} \boldsymbol{x}_P(t). \end{cases}$$

(5.17)

Note that only the radial displacements are measured and actively controlled and thus the tilting and axial degrees of freedom need to be passively stable.

Closed-Loop Analysis

Considering the interconnections graphically shown in figure 5.7, where it is considered that the reference position is always set to $\boldsymbol{x}_{ref} = 0$, and subject to the harmonic excitation $\boldsymbol{u}_d = e^{j\Omega t}$, it is possible to study the closed-loop stability of the system and its unbalance
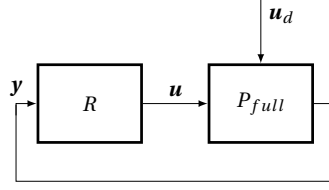
Figure 5.7 – Simplified general closed-loop diagram of hybrid magnetic bearing system with controller and observer R, and full rotordynamics P_{full} for stability analysis.

response.

Such an analysis can be performed by considering the sensitivity functions from the unbalance excitation $\boldsymbol{u}_d$ to plant states $\boldsymbol{x}_P$ and controller actuation $\boldsymbol{u}$, denoted as S_{ux} and S_{uu}, respectively. As the measurements $\boldsymbol{y}$ only account for the radial displacements, the complete system analysis is performed by considering the states $\boldsymbol{x}_P$ instead.

Defining the closed-loop system states as $\boldsymbol{x} = [\boldsymbol{x}_P^\top, \boldsymbol{x}_R^\top]^\top$, S_{ux} and S_{uu} result in

$$S_{ux} = \begin{cases} \dot{\boldsymbol{x}}_P(t) = A\boldsymbol{x}(t) + B\boldsymbol{u}_d(t), \\ \boldsymbol{x}_P(t) = C_{ux}\boldsymbol{x}(t), \end{cases} \qquad S_{uu} = \begin{cases} \dot{\boldsymbol{x}}(t) = A\boldsymbol{x}(t) + B\boldsymbol{u}_d(t), \\ \boldsymbol{u}(t) = C_{uu}\boldsymbol{x}(t), \end{cases} \qquad (5.18)$$

being

$$A = \begin{bmatrix} A_P & B_P C_R \\ B_R C_P & A_R \end{bmatrix}, \quad B = \begin{bmatrix} B_P' \\ O \\ O \end{bmatrix}, \quad C_{ux} = \begin{bmatrix} I & O \end{bmatrix}, \quad C_{uu} = \begin{bmatrix} O & C_R \end{bmatrix}. \qquad (5.19)$$

The closed-loop system is stable if no eigenvalue of matrix A is located at the right half plane (RHP), i.e. all eigenvalues have zero or negative real part. Furthermore, to guarantee that the rotor displacements and actuator currents under unbalance excitation do not exceed some reasonable limits, the unbalance response of the closed-loop systems S_{ux} and S_{uu} can be studied either in frequency or time domain.

Firstly, the closed-loop poles are shown in figure 5.8 as Campbell and decay-rate plots. It can be seen that all radial poles are located at the desired locations chosen by the pole-placement controller and observer, and that both tilting and axial modes have, as expected, no damping and they are located at the imaginary axis. On the one hand, due to the disk-shaped rotor, i.e. $I_p > I_t$, there is no critical speed for the radial tilting dynamics, as the conical or tilting modes never cross the unbalance excitation frequency Ω. On the other hand, the speed-independent axial modes do eventually cross Ω, and the maximum rotational speed will then be fixed by this critical speed.

Secondly, considering the unbalance magnitude given by the standard [14] for rotating machinery of equivalent size with balancing grade G6.3, as defined in table 5.4, the unbalance response of the hybrid magnetic bearing systems is shown in figure 5.9.
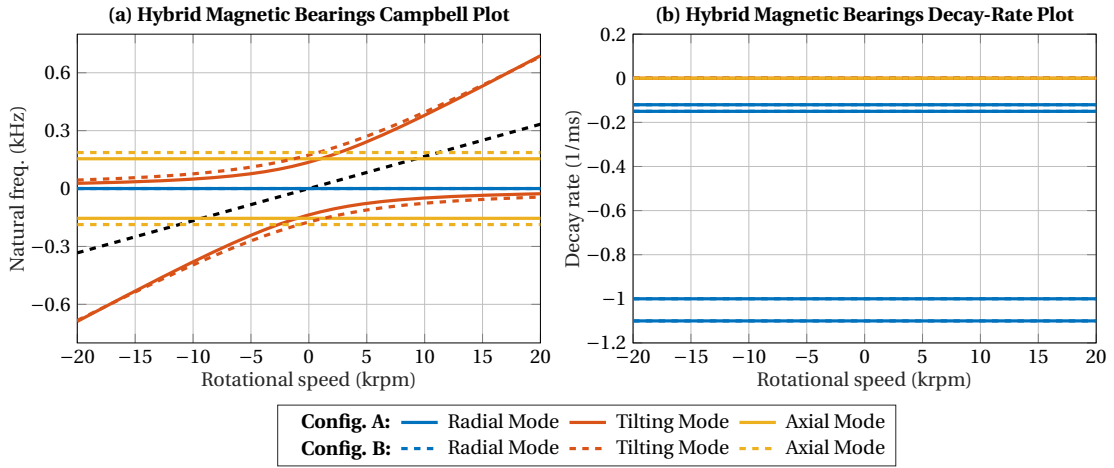
Figure 5.8 – Campbell and decay-rate plots of hybrid magnetic bearing systems defined by high-level parameters from table 5.4. Rotordynamic modes as a function of rotor speed are shown for both hybrid systems with attractive (config. A) and repulsive (config. B) passive magnetic bearings.
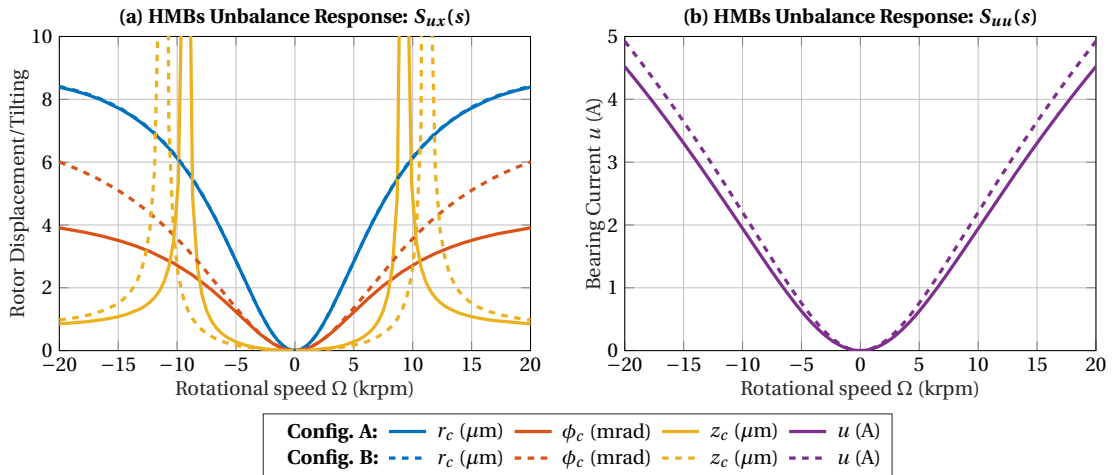
Figure 5.9 – Unbalance response of hybrid magnetic bearing systems defined by high-level parameters from table 5.4. Rotor radial displacements r_c, radial tilting ϕ_c, axial displacements z_c and actuator currents u are shown as a function of rotor speed for both hybrid systems with attractive (config. A) and repulsive (config. B) passive magnetic bearings under unbalance excitation.

It can be seen that the critical speeds for the axial degrees of freedom appear at approximately 9 krpm and 11 krpm for configurations A and B, respectively, and for this reason, the maximum speed is chosen at 8 krpm and 10 krpm to avoid infinitely big rotor displacements, which in practice would result in a rotor crash. Furthermore, the applied currents to stabilise the rotor in radial direction are not excessively high, being below 3 A for both cases for the considered Ω_{max}, which could be applied by the existing bearing and power converter.

Whereas no damping has been considered for the analysis, in practice, some damping should be considered, as a result from the induced voltage in the radial bearing and motor windings when the rotor is displaced from its centre. This behaviour would only stabilise the system

due to its energy dissipation, which would result in a damping of the harmonic disturbances such as the rotor unbalance or shaft bow.

These high-level results show that both configurations could be further investigated and eventually manufactured in order to obtain a more simple magnetic bearing topology for applications where big inertia disks are required, such as reaction or momentum wheels for space applications, or kinetic energy storage wheels for terrestrial applications.

5.3   Conclusions

In this chapter, two main developments are presented: first, a general optimisation procedure for active magnetic bearings and motors is described, and second, a hybrid magnetic bearing topology is designed and its viability validated.

The main contributions of the chapter are the following:

- A general optimisation procedure for active magnetic bearings and motors is presented.
    - The optimisation maximises the efficiency of the general machine or single actuator.
    - It allows considering the possible interactions between actuators for a general machine optimisation where several actuators share some given resources, as in self-bearing machines.
    - The optimisation is applied to the studied fully active magnetic bearing system resulting in a greatly improved efficiency when compared to the original machine.
- A hybrid magnetic bearing configuration that combines active and passive magnetic bearings is presented and analysed.
    - The hybrid magnetic bearing simplifies the magnetic bearing configuration, by actively controlling only three (radial displacements and motor torque) of the six degrees of freedom of the rotor.
    - The passive magnetic bearings with both repulsive and attractive configurations are designed and dimensioned.
    - The preliminary high-level design is analysed at system level through rotordynamics analysis using the tools described in chapter 3.
    - Both configurations show promising capabilities and their viability is proven by high-level closed-loop system analysis.

6 Harmonic Disturbance Suppression for Magnetic Bearings

In this chapter, a greatly stable harmonic force rejection control technique is presented and its stability and performance is analysed for the studied fully active magnetic bearing system. The proposed generalised notch filter is based on the unbalance and resonance suppression control originally proposed in [120], and features the advantage of not requiring any gain or parameter selection for guaranteeing its stability for a broad range of speeds. Due to the intrinsic differences between the piezoelectric active bearings featured in [120] and magnetic bearings, its stability for magnetically levitated rotors is analytically analysed and experimentally validated using a fully active slotless Lorentz-type magnetic bearing motor.

Firstly, in section 6.1, a brief description of the main previously available unbalance control techniques is presented, including their limitations. In section 6.2, the general structure of the proposed generalised notch filter is presented, including the required modifications for its implementation on a real system and its general stability criterion is derived. Afterwards, the stability of the technique is investigated in detail for the studied magnetic bearing system in section 6.3. The experimental measurements of the harmonic force rejection control technique is included in chapter 7, achieving a complete suppression of the first three harmonics of the actuating currents and thus significantly reducing the vibrations generated by the machine during operation by at least one order of magnitude over its whole speed range.

A similar analysis to the one performed in this chapter has been carried out in [50], where the proposed generalised notch filter is described, analysed and implemented for the studied fully active magnetic bearing system.

6.1 Harmonic Disturbance Suppression Techniques

Whereas rotor balancing can considerably reduce the magnitude of one of the main sources of vibrations, allowing the operation of the machine for much longer time and at higher speeds, in practice it is impossible to achieve a perfect rotor balancing [14] and thus some residual vibrations will always be present. In some applications such as optics [121] or in

97

space [10] where vibrations are critical for the precision of the measurement equipment, some additional isolation is necessary, by adding for example a passive [22] or even active [23] isolation platforms.

The absence of mechanical contact between rotor and stator in magnetically levitated rotors enables the possibility of actively controlling and reducing the vibrations generated during rotation. These approaches are commonly known as vibration or unbalance force rejection control (UFRC) techniques and have seen increasing interest in the last decades [122]–[125].

One of the most extended unbalance control techniques that was proposed in [123], known as generalised notch filter, has seen broad expansion in industry and it has been successfully employed for suppressing harmonic disturbances in magnetically levitated rotating machines [30]. The main reason of its success is its adaptive nature, not requiring any model of the noise and vibration to suppress, only requiring an estimation or measurement of the rotor speed.

Nevertheless, its implementation requires the selection of tunable parameters in a gain matrix for stable operation over a broad speed range and often requires a gain-scheduling approach. More recent approaches target at solving these stability issues by substituting the gain matrix with a phase shift [124], or by employing a polarity shift [125], but still requiring the adaptation of the parameters with speed to guarantee a stable system.

As initially proposed in [120], an independent development for piezoelectric active bearings resulted in a stable unbalance and resonance control technique that greatly reduced the stability problems of previous unbalance control implementations, with no gain adaptation required for stable operation. In [120], the stability of the approach was generally proven analytically and experimentally for rotating machinery including single or multiple piezo-electric bearing actuators, which feature intrinsic stable passive stiffness. Whereas these conditions do not hold for magnetic bearing systems, with unstable open-loop dynamics, the employed unbalance and resonance control technique show promising possibilities for magnetic bearings.

To highlight the main characteristics of the conventional generalised notch filter originally proposed in [123], a brief presentation of its structure and characteristics is performed here-after.

6.1.1   Conventional Generalised Notch Filter

Considering a general closed-loop system shown in Fig. 6.1.a, with controller R and plant P, it is possible to suppress the l-th harmonic component of the measurement signal $\boldsymbol{y}$ by considering a conventional generalised notch filter N_f as presented in [123].

The internal structure of such a generalised notch filter is graphically represented in figure

(a) Closed-Loop with Conventional N_f

(b) Closed-Loop with Proposed N_f

(c) Conventional Generalised Notch Filter N_f

(d) Proposed Generalised Notch Filter N_f
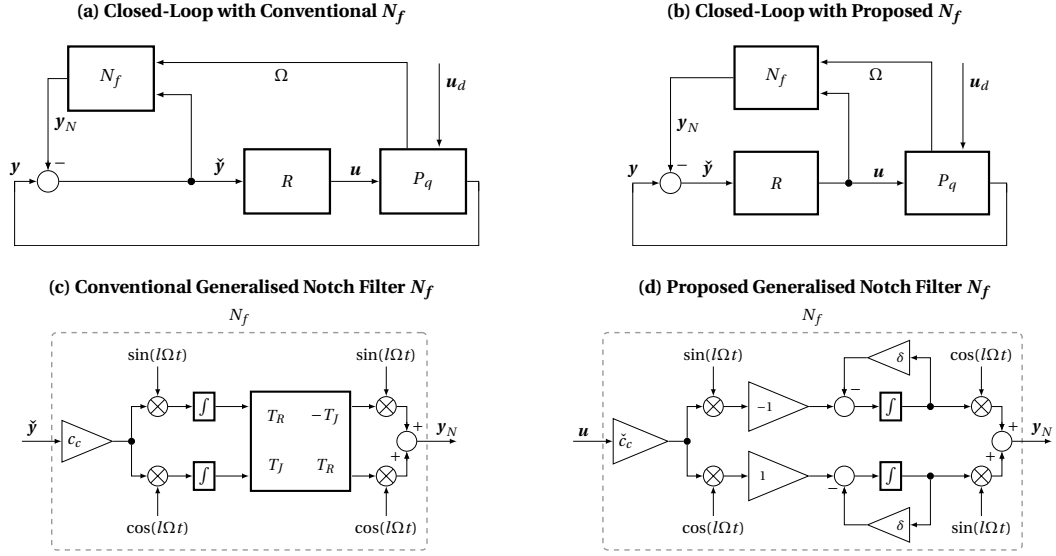
Figure 6.1 – Simplified general closed-loop (top) and internal structure (bottom) of conventional (left) or proposed (right) generalised notch filter N_f, with controller R and rotordynamics P_q.

6.1.c, which corresponds to the dynamic system N_f described by

$$\boldsymbol{y}_N(t) = \begin{bmatrix} \sin(\Omega t)I & \cos(\Omega t) \end{bmatrix} \begin{bmatrix} T_R & -T_J \\ T_J & T_R \end{bmatrix} \int_0^t c_c \begin{bmatrix} \sin(\Omega \tau)I \\ \cos(\Omega \tau)I \end{bmatrix} \check{\boldsymbol{y}}(\tau)\mathrm{d}\tau \qquad (6.1)$$

being I an identity matrix, Ω the rotational speed of the rotor, c_c the rate of convergence of the filter which also defines the bandwidth of the notch, and T_R, T_J two real-valued gain matrices. The dynamic system defined in expression (6.1) corresponds to the following linear differential equation

$$\ddot{\boldsymbol{y}}_N + \Omega^2 \dot{\boldsymbol{y}}_N = c_c(T_R \dot{\check{\boldsymbol{y}}} - \Omega T_J \check{\boldsymbol{y}}). \qquad (6.2)$$

Defining $T_N = T_R + jT_J$ as complex gain matrix, and $\overline{T}_N = T_R - jT_J$ its complex conjugate, being $j = \sqrt{-1}$ the imaginary unit, it is possible to reformulate the differential equation (6.2) as a state-space system, resulting in

$$\dot{\boldsymbol{x}}_N(t) = A_N \boldsymbol{x}_N(t) + B_N \check{\boldsymbol{y}}(t) = \begin{bmatrix} j\Omega I & O \\ O & -j\Omega I \end{bmatrix} \boldsymbol{x}_N(t) + c_c \begin{bmatrix} T_N \\ \overline{T}_N \end{bmatrix} \check{\boldsymbol{y}}(t),$$

$$\boldsymbol{y}_N(t) = C_N \boldsymbol{x}_N(t) = \frac{1}{2} \begin{bmatrix} I & I \end{bmatrix} \boldsymbol{x}_N(t), \qquad (6.3)$$

being O a zero matrix and $\boldsymbol{x}_N$ the internal states of the notch. If a matrix T_N is found such that the closed-loop system is stable, this generalised notch filter actuating over frequency Ω is able to suppress any harmonic component from the measured signal $\boldsymbol{y}$. These harmonic disturbances commonly appear due to unbalance forces, and preventing the closed-loop system to react to these disturbances results in a considerable reduction in generated vibrations and power consumption.

99

As explained in [123], different options exist for choosing the values of matrix T_N that will result in a stable closed-loop system. These techniques rely on the identification and adaptation of T_N depending on the closed-loop dynamics at each speed Ω in terms of the sensitivity transfer function matrix (TFM) $S(s)$. This results in the necessity of selecting a gain-scheduled matrix $T_N(\Omega)$ to guarantee stability over a broad speed range.

The generalised notch filter defined in expression (6.3) can be generalised to suppress not only disturbances appearing synchronous to the rotation speed Ω, but also in higher harmonics $l \in \{1, 2, \ldots, n_h\}$ by simply considering $l\Omega$ instead. Nevertheless, doing so implies the selection of either a single $T_N(\Omega)$ such that the system is stable for all n_h harmonics, or a different $T_N(\Omega)$ for each l-th harmonic.

This necessity of finding an appropriate structure for $T_N(\Omega)$ to guarantee the closed-loop stability can limit the applicability of this UFRC. The generalised notch filter proposed hereafter is developed to overcome these limitations and facilitate the implementation of multi-harmonic force rejection control for magnetic bearing systems.

6.2   Proposed Generalised Notch Filter

Following the development of equations presented in [120], the resulting general closed-loop diagram with the proposed generalised notch filter N_f is shown in figure 6.1.b. The filter takes the position controller output currents $\boldsymbol{u}(t)$ as input to generate an harmonic signal $y_N(t)$ to be removed from the input signal to the position controller $\check{\boldsymbol{y}}(t)$. This is achieved for the l-th harmonic by considering

$$
\begin{aligned}
\dot{\boldsymbol{x}}_{Nl}(t) &= A_{Nl}\boldsymbol{x}_{Nl}(t) + B_{Nl}\boldsymbol{u}(t) = \begin{bmatrix} jl\Omega I & O \\ O & -jl\Omega I \end{bmatrix} \boldsymbol{x}_{Nl}(t) + c_c \frac{\Omega}{|\Omega|} \begin{bmatrix} jI \\ -jI \end{bmatrix} \boldsymbol{u}(t), \\
\boldsymbol{y}_{Nl}(t) &= C_{Nl}\boldsymbol{x}_{Nl}(t) = \frac{1}{2} \begin{bmatrix} I & I \end{bmatrix} \boldsymbol{x}_{Nl}(t).
\end{aligned}
\tag{6.4}
$$

The stability of such configuration relies on the use of a fixed structure, and thus absence of any gain matrix, and the use of the controller output, $\boldsymbol{u}$, as input signal to the filter. It is also clear that one requisite for employing such a generalised notch filter is that a measurement or estimation of the rotor speed Ω is necessary.

The complete vibration control is obtained by combining the expression (6.4) for all $l \in \{1, 2, \ldots, n_h\}$ harmonics that will be suppressed, resulting in $\boldsymbol{x}_N = [\boldsymbol{x}_{N1}^\top, \ldots, \boldsymbol{x}_{Nn_h}^\top]^\top$ and

$$
\begin{aligned}
\dot{\boldsymbol{x}}_N(t) &= A_N\boldsymbol{x}_N(t) + B_N\boldsymbol{u}(t) = \begin{bmatrix} A_{N1} & \cdots & O \\ \vdots & \ddots & \vdots \\ O & \cdots & A_{Nn_h} \end{bmatrix} \boldsymbol{x}_N(t) + \begin{bmatrix} B_{N1} \\ \vdots \\ B_{Nn_h} \end{bmatrix} \boldsymbol{u}(t), \\
\boldsymbol{y}_N(t) &= C_N\boldsymbol{x}_N(t) = \begin{bmatrix} C_{N1} & \cdots & C_{Nn_h} \end{bmatrix} \boldsymbol{x}_N.
\end{aligned}
\tag{6.5}
$$

For a configuration that will suppress n_h harmonics on a system with n_q degrees of freedom, $\boldsymbol{u} \in \mathbb{C}^{n_q}$ and $\boldsymbol{y} \in \mathbb{C}^{n_q}$, the notch state-space matrices will have dimensions $A_N \in \mathbb{C}^{2n_q n_h \times 2n_q n_h}$, $B_N \in \mathbb{C}^{2n_q n_h \times n_q}$ and $C_N \in \mathbb{C}^{n_q \times 2n_q n_h}$.

6.2.1 Implementation

To implement the proposed harmonic disturbance suppression algorithm into a real system, it is necessary to transform the dynamic system defined in (6.4) into an algorithm that a digital signal processor (DSP) or embedded controller can compute in real-time.

To address these aspects, the following steps are taken:

1. To prevent rotor orbits of infinite amplitude at resonance speeds, a virtual stiffness δ is included into (6.4), as done in [120], which results in

$$
\begin{aligned}
\dot{\boldsymbol{x}}_{Nl}(t) &= (A_{Nl} - A_{\delta})\boldsymbol{x}_{Nl}(t) + B_{Nl}\boldsymbol{u}(t) \\
\boldsymbol{y}_{Nl}(t) &= C_{Nl}\boldsymbol{x}_{Nl}(t),
\end{aligned}
\tag{6.6}
$$

with $A_{\delta} = \delta I$. If $\delta \neq 0$ the integration of the notch states $\boldsymbol{x}_{Nl}$ is slowed down, acting against both the increase in orbits and a perfect harmonic suppression.

2. Using the similarity transformation F_l for the l-th harmonic and its time derivative

$$
\begin{aligned}
\boldsymbol{x}_{Nl}(t) &= F_l\check{\boldsymbol{x}}_{Nl}(t) = \begin{bmatrix} e^{jl\Omega t}I & O \\ O & e^{-jl\Omega t}I \end{bmatrix}\check{\boldsymbol{x}}_{Nl}(t), \\
\dot{\boldsymbol{x}}_{Nl}(t) &= \dot{F}_l\check{\boldsymbol{x}}_{Nl}(t) + F_l\dot{\check{\boldsymbol{x}}}_{Nl}(t) = A_{Nl}F_l\check{\boldsymbol{x}}_{Nl}(t) + F_l\dot{\check{\boldsymbol{x}}}_{Nl}(t),
\end{aligned}
\tag{6.7}
$$

and defining $\check{c}_c = c_c \Omega/|\Omega|$, it is possible to reformulate expression (6.6) using $\check{\boldsymbol{x}}_{Nl}(t)$ instead, resulting in

$$
\begin{aligned}
\dot{\check{\boldsymbol{x}}}_{Nl}(t) &= -A_{\delta}\check{\boldsymbol{x}}_{Nl}(t) + F_l^{-1}B_{Nl}\boldsymbol{u}(t) = -\delta\check{\boldsymbol{x}}_{Nl}(t) + \check{c}_c\begin{bmatrix} je^{-jl\Omega t}I \\ -je^{jl\Omega t}I \end{bmatrix}\boldsymbol{u}(t), \\
\boldsymbol{y}_{Nl}(t) &= C_{Nl}F_l\check{\boldsymbol{x}}_{Nl}(t) = \begin{bmatrix} \frac{e^{jl\Omega t}}{2}I & \frac{e^{-jl\Omega t}}{2}I \end{bmatrix}\check{\boldsymbol{x}}_{Nl}(t).
\end{aligned}
\tag{6.8}
$$

3. Considering Euler's formula, the complex exponentials are expressed only in terms of pure real numbers and trigonometric functions $\sin(l\Omega t)$ and $\cos(l\Omega t)$ as follows

$$
\begin{aligned}
\dot{\check{\boldsymbol{x}}}_{Nl}(t) &= -\delta\check{\boldsymbol{x}}_{Nl}(t) + \check{c}_c\begin{bmatrix} -\cos(l\Omega t)I \\ \sin(l\Omega t)I \end{bmatrix}\boldsymbol{u}(t), \\
\boldsymbol{y}_{Nl}(t) &= \begin{bmatrix} \sin(l\Omega t)I & \cos(l\Omega t)I \end{bmatrix}\check{\boldsymbol{x}}_{Nl}(t),
\end{aligned}
\tag{6.9}
$$

and as graphically represented in Fig. 6.1.d.

4. The system is discretised using Euler's method and the sampling frequency f_s of the

controller, resulting in

$$\check{\boldsymbol{x}}_{Nl}[k+1] = \left(1 - \frac{\delta}{f_s}\right)\check{\boldsymbol{x}}_{Nl}[k] + \frac{\check{c}_c}{f_s}\begin{bmatrix} -\cos(l\Omega t_k)I \\ \sin(l\Omega t_k)I \end{bmatrix}\boldsymbol{u}[k],$$

$$\boldsymbol{y}_{Nl}[k] = \begin{bmatrix} \sin(l\Omega t_k)I & \cos(l\Omega t_k)I \end{bmatrix}\check{\boldsymbol{x}}_{Nl}[k].$$

(6.10)

5. The discrete-time equations are combined for the $l \in \{1, 2, \ldots, n_h\}$ harmonics to be suppressed using (6.5).

Interestingly, it can be observed that expressions (6.9) and (6.10) correspond to a similar formulation to the one previously presented in [123], which is defined in Appendix 6.1.1, but considering no gain matrix, i.e. having a fixed structure being $T_R = O$ and $T_J = I$, and using as input to the filter the controller's output $\boldsymbol{u}$ instead of input $\check{\boldsymbol{y}}$.

6.2.2 General Stability Condition

Considering the interconnections of the closed-loop scheme shown in figure 6.1.b, with TFMs $P_q(s)$, $R(s)$ and $N_f(s)$ for plant, controller and notch dynamics, the loop TFM $L(s)$ of the configuration results in

$$L(s) = P_q(s)R(s)(I + N_f(s)R(s))^{-1}. \tag{6.11}$$

The stability is then guaranteed if the closed-loop sensitivity TFM, calculated as

$$S(s) = (I + L(s))^{-1} = (I + P_q(s)R(s) + N_f(s)R(s))^{-1}, \tag{6.12}$$

has no poles located in the right half-plane (RHP). The proposed notch TFM $N_f(s)$ can be calculated from the state-space representation using $N_f(s) = C_N(sI - A_N)^{-1}B_N$, and considering here $l = 1$ for simplicity, which results in

$$N_f(s) = -\frac{\check{c}_c\Omega}{s^2 + \Omega^2}I, \tag{6.13}$$

being $\check{c}_c = c_c\Omega/|\Omega|$. Substituting into (6.12), the closed-loop poles are calculated from the characteristic polynomial of $S(s)$, resulting in

$$\begin{aligned} 0 &= \det(I + P_q(s)R(s) + N_f(s)R(s)) \\ &= \det((s^2 + \Omega^2)I - \check{c}_c\Omega R(s)(I + P_q(s)R(s))^{-1}) \\ &= \det((s^2 + \Omega^2)I + j\check{c}_c\Omega(jR(s)\check{S}(s)). \end{aligned} \tag{6.14}$$

Note that $(I + P_q(s)R(s))^{-1}$ is the sensitivity TFM of the closed-loop system without notch filter, and to simplify the notation it is denoted here as $\check{S}(s) = (I + P_q(s)R(s))^{-1}$.

It can be seen that if $\check{c}_c = 0$ the closed-loop system is stable, having a set of poles over the imaginary axis $s = \pm j\Omega$. As $\check{c}_c$ is chosen small enough to guarantee a sufficient narrow band of

the generalised notch filter, following the procedure performed in [123], it is possible to obtain a general condition of stability for each rotor speed Ω by linearising the resulting closed-loop poles around $s = \pm j\Omega$ for $\check{c}_c = 0$.

The closed-loop is stable for sufficiently small convergence rates of the proposed notch filter $\check{c}_c \ll \Omega$ if for each speed Ω it is satisfied that

$$\left.\frac{\partial s(\check{c}_c)}{\partial \check{c}_c}\right|_{\check{c}_c=0} = -\frac{1}{2}\mathrm{eig}(jR(j\Omega)\check{S}(j\Omega)) < 0. \tag{6.15}$$

When comparing to the stability criteria obtained in [123] for the conventional generalised notch filter, it is possible to identify the parallelisms with the results derived here. As previously mentioned, the proposed configuration corresponds to an open-loop notch filter dynamics of N_f defined in [123] but with a fixed gain matrix structure $T_N = jI$. Furthermore, the different arrangement of N_f in the closed-loop results in a stability criteria depending on $jR(j\Omega)\check{S}(j\Omega)$, instead of $T_N(\Omega)\check{S}(j\Omega)$ in the conventional notch filter.

Whereas the results obtained here define a theoretical stability condition for the closed-loop system, its formulation can be difficult to use in practical applications. For this reason, the dynamics of the closed-loop system are particularised hereafter for the studied magnetic bearing system, providing a detailed stability analysis for the fully active magnetic bearing motor here investigated.

6.3 Stability Analysis for Studied Magnetic Bearing System

Before implementing the proposed generalised notch filter into the real system, it is necessary to study in more detail the stability of such an harmonic disturbance rejection technique for its configuration. It is first necessary to define the equations of each element of the closed-loop system.

As detailed in chapter 3, it is possible to select the level of complexity and considered aspects in the closed-loop simulation model. To simplify the initial stability analysis procedure, the following assumptions have been considered:

- The current control loop is considered fast enough to have an influence on the position control, i.e. $R_{cc} = I$.

- The reference set point for the position control loop is always zero, i.e. $\boldsymbol{x}_{ref} = 0$.

- Linear and ideal bearing and position sensor models are considered, i.e. the models defined in equations (3.10) and (3.11) are used, respectively.

- Due to the previous assumption, radial and axial dynamics are completely decoupled, allowing a decoupled radial and axial position control design.

- As external disturbances in the generalised force vector $\boldsymbol{f}$, only unbalance forces are considered, which are purely radial.

The closed-loop scheme presented in figure 3.4 can then be simplified to the one graphically shown in figure 6.1.b. The dynamics of the plant P_q, controller R and generalised notch filter N_f, can be expressed in state-space representation as

$$P_q = \begin{cases} \dot{\boldsymbol{x}}_P(t) = A_P \boldsymbol{x}_P(t) + B_P \boldsymbol{u}(t) + B_P' \boldsymbol{u}_d(t), \\ \boldsymbol{y}(t) = C_P \boldsymbol{x}_P(t), \end{cases} \tag{6.16a}$$

$$R = \begin{cases} \dot{\boldsymbol{x}}_R(t) = A_R \boldsymbol{x}_R(t) + B_R(\boldsymbol{y}(t) - \boldsymbol{y}_N(t)), \\ \boldsymbol{u}(t) = C_R \boldsymbol{x}_R(t) + D_R(\boldsymbol{y}(t) - \boldsymbol{y}_N(t)), \end{cases} \tag{6.16b}$$

$$N_f = \begin{cases} \dot{\boldsymbol{x}}_N(t) = A_N \boldsymbol{x}_N(t) + B_N \boldsymbol{u}(t), \\ \boldsymbol{y}_N(t) = C_N \boldsymbol{x}_N(t), \end{cases} \tag{6.16c}$$

being $\boldsymbol{u}$ the bearing currents, $\boldsymbol{y}$ the sensor measurements, $\boldsymbol{x}$ the state vector and A, B, C, D the state-space matrices with the subscripts P, R, N referring to the plant, controller or notch, respectively. Input $\boldsymbol{u}_d$ accounts for unbalance or any other harmonic disturbance force acting on the rotating system.

Considering the interconnections between elements, being $\check{\boldsymbol{y}}(t) = \boldsymbol{y}(t) - \boldsymbol{y}_N(t)$, the excitation harmonic forces $\boldsymbol{u}_d(t)$ as input, and the the rotor displacements measured by sensors $\boldsymbol{y}(t)$ or actuating currents $\boldsymbol{u}(t)$ as outputs, the stability and general behaviour of the system can be analysed. These closed-loop systems can be viewed as a sensitivity transfer function from an input disturbance to plant's output S_{uy} or to controller's output S_{uu}.

The closed-loop systems S_{uy} and S_{uu} both feature the state-space vector $\boldsymbol{x} = [\boldsymbol{x}_P^\top, \boldsymbol{x}_R^\top, \boldsymbol{x}_N^\top]^\top$ and their state-space representations are defined as

$$S_{uy} = \begin{cases} \dot{\boldsymbol{x}}(t) = A\boldsymbol{x}(t) + B\boldsymbol{u}_d(t), \\ \boldsymbol{y}(t) = C_{uy}\boldsymbol{x}(t), \end{cases} \quad , \quad S_{uu} = \begin{cases} \dot{\boldsymbol{x}}(t) = A\boldsymbol{x}(t) + B\boldsymbol{u}_d(t), \\ \boldsymbol{u}(t) = C_{uu}\boldsymbol{x}(t). \end{cases} \tag{6.17}$$

Note the similar state-space equations for both dynamic systems, only differing on the output equation. The resulting state-space matrices for both systems are

$$A = \begin{bmatrix} A_P + B_P D_R C_P & B_P C_R & -B_P D_R C_N \\ B_R C_P & A_R & -B_R C_N \\ B_N D_R C_P & B_N C_R & A_N - B_N D_R C_N \end{bmatrix}, \quad B = \begin{bmatrix} B_P' \\ O \\ O \end{bmatrix}, \quad \begin{aligned} C_{uy} &= \begin{bmatrix} C_P & O & O \end{bmatrix}, \\ C_{uu} &= \begin{bmatrix} D_R C_P & C_R & -D_R C_N \end{bmatrix}. \end{aligned} \tag{6.18}$$

The closed-loop system will be stable if no eigenvalues of matrix A are located in the RHP. In the following sections, the structure of each component of the closed-loop system shown in

figure 6.1, i.e. rotordynamics equations P_q, the controller dynamics R, and generalised notch filter N_f, will be particularised and its stability analysed for some cases.

To simplify the notation the dependency on time (t) will be dropped in the following expressions.

6.3.1   Rotordynamics Model: P

As previously developed in chapter 3 for the four and five degrees-of-freedom models, the rotor is considered as a rigid body with mass m, non-vanishing polar and transverse moments of inertia I_p and I_t, suspended over two compliant bearings b_1 and b_2 with stiffness k, and non-rotating and rotating damping coefficients d_n and d_r.

For convenience, the equations of motion described in chapter 3 are repeated here. Considering the generalised coordinate vector $\boldsymbol{q} = [r_c, \phi_c]^\top$ in complex coordinates, the linearised equations of motion from expression (3.6) and ideal sensor models from (3.11) are

$$M_q \ddot{\boldsymbol{q}} + \left(D_q + G_q(\Omega)\right) \dot{\boldsymbol{q}} + \left(K_q + H_q(\Omega)\right) \boldsymbol{q} = U_q \boldsymbol{u} + V_q(\Omega) \boldsymbol{u}_d,$$
$$\boldsymbol{y} = W_q \boldsymbol{q} \tag{6.19}$$

being M_q the mass matrix, D_q the passive damping matrix, $G_q(\Omega)$ the gyroscopic matrix, K_q the passive stiffness matrix, $H_q(\Omega)$ the circulatory matrix, U_q the ideal bearing force matrix, $V_q(\Omega)$ the unbalance or harmonic disturbance matrix, and W_q the sensor output matrix. To simplify the analysis, matrix V_q only accounts for unbalance forces as defined in [108], and thus $\boldsymbol{u}_d = e^{j\Omega t}$, but could be generalised to account for any other harmonic disturbance.

Finally, the state-space representation of the equations of motion in (3.3) results in the state-space matrices

$$A_P = \begin{bmatrix} A_{Pqq} & A_{Pq\dot{q}} \\ A_{P\dot{q}q} & A_{P\dot{q}\dot{q}} \end{bmatrix} = \begin{bmatrix} O & I \\ -M_q^{-1}(K_q + H_q(\Omega)) & -M_q^{-1}(D_q + G_q(\Omega)) \end{bmatrix},$$
$$B_P = \begin{bmatrix} B_{Pq} \\ B_{P\dot{q}} \end{bmatrix} = \begin{bmatrix} O \\ M_q^{-1}U_q \end{bmatrix}, \qquad B_P' = \begin{bmatrix} B'_{Pq} \\ B'_{P\dot{q}} \end{bmatrix} = \begin{bmatrix} O \\ M_q^{-1}V_q(\Omega) \end{bmatrix}, \tag{6.20}$$
$$C_P = \begin{bmatrix} C_{Pq} & C_{P\dot{q}} \end{bmatrix} = \begin{bmatrix} W_q & O \end{bmatrix},$$

being the state vector $\boldsymbol{x}_P = [\boldsymbol{q}^\top, \dot{\boldsymbol{q}}^\top]^\top$.

6.3.2   Controller: R

Considering the multi-variable state feedback controller defined in chapter 3, with state-pace observer with matrix gain L_{SF} and controller with matrix gain K_{SF}, and the model of the system dynamics to be controlled in equations (6.16a) and (6.20), it is possible to express the resulting dynamic system of such a controller in state-space representation as defined in

(6.16b).

Due to the use of a digital processor, such as a digital signal processor (DSP), the controller needs to be implemented in discrete-time. Firstly, the design of the controller is performed in discrete-time, and secondly, for the stability analysis, a zero-order hold is considered for converting the discrete-time controller into the continuous-time equations defined in (6.16b).

Employing a first-order forward Euler discretisation of the rotordynamics model P_q in equation (6.20) with sampling period T_s, including process $\boldsymbol{w}$ and measurement $\boldsymbol{v}$ noise the resulting discrete-time system dynamic model $\tilde{P}_q$ is defined as

$$\tilde{P}_q = \begin{cases} \boldsymbol{x}_P[k+1] = \tilde{A}_P \boldsymbol{x}_P[k] + \tilde{B}_P \boldsymbol{u}[k] + \boldsymbol{w}[k] = (I + T_s A_P) \boldsymbol{x}_P[k] + T_s B_P \boldsymbol{u}[k] + \boldsymbol{w}[k], \\ \boldsymbol{y}[k] = \tilde{C}_P \boldsymbol{x}_P[k] + \boldsymbol{v}[k] = C_P \boldsymbol{x}_P[k] + \boldsymbol{v}[k]. \end{cases} \quad (6.21)$$

If an integral error $\boldsymbol{e}_I$, the estimated position $\hat{\boldsymbol{q}}$ and velocity $\hat{\dot{\boldsymbol{q}}}$ are included into the controller state vector $\boldsymbol{x}_R = [\boldsymbol{e}_I^\top, \hat{\boldsymbol{q}}^\top, \hat{\dot{\boldsymbol{q}}}^\top]^\top$, the controller gain K_{SF} can be separated in $K_{SF} = [K_i, K_p, K_d]$, being K_i, K_p, and K_d the integral, proportional and derivative gain matrices, and the observer gain in $L_{SF} = [L_p^\top, L_d^\top]^\top$ with only proportional L_p and derivative parts L_d. The resulting controller state-space matrices are

$$\tilde{R} = \begin{cases} \boldsymbol{x}_R[k+1] = \tilde{A}_R \boldsymbol{x}_R[k] + \tilde{B}_R \boldsymbol{y}[k] = \\ \quad = \begin{bmatrix} O & I & O \\ -\tilde{B}_{Pq}K_i & \tilde{A}_{Pqq} - \tilde{B}_{Pq}K_p - L_p\tilde{C}_{Pq} & \tilde{A}_{Pq\dot{q}} - \tilde{B}_{Pq}K_p - L_p\tilde{C}_{P\dot{q}} \\ -\tilde{B}_{P\dot{q}}K_i & \tilde{A}_{P\dot{q}q} - \tilde{B}_{P\dot{q}}K_p - L_d\tilde{C}_{Pq} & \tilde{A}_{P\dot{q}\dot{q}} - \tilde{B}_{P\dot{q}}K_p - L_d\tilde{C}_{P\dot{q}} \end{bmatrix} \boldsymbol{x}_R[k] + \begin{bmatrix} O \\ L_p \\ L_d \end{bmatrix} \boldsymbol{y}[k], \\ \boldsymbol{u}[k] = \tilde{C}_R \boldsymbol{x}_R[k] = \begin{bmatrix} -K_i & -K_p & -K_d \end{bmatrix} \boldsymbol{x}_R[k]. \end{cases}$$
$$(6.22)$$

Note that as done in chapter 5 for the hybrid magnetic bearing system analysis, R considers both controller and observer dynamics.

The design of observer L_{SF} and controller K_{SF} gain matrices is then done by solving the linear-quadratic-gaussian (LQG) problem for optimal control as follows:

- **Linear-quadratic regulator (LQR), $\boldsymbol{K_{SF}}$**: the infinite-horizon discrete-time linear-quadratic controller gain K_{SF} is calculated by minimising the cost function

$$\min \left\{ \sum_{k=0}^{\infty} \left(\boldsymbol{x}_R^\top[k] Q_K \boldsymbol{x}_R[k] + \boldsymbol{u}^\top[k] R_K \boldsymbol{u}[k] + 2\boldsymbol{x}_R^\top[k] N_K \boldsymbol{u}^\top[k] \right) \right\}, \quad (6.23)$$

subject to the plant dynamics (6.21) and $\boldsymbol{u}[k] = -K_{SF}\boldsymbol{x}_R[k]$. For this case the weight

Table 6.1 – Closed-loop system parameters of rotordynamics P_q, LQG controller R and generalised notch filter N_f employed for stability analysis.

System	Param.	Value	Param.	Value	Param.	Value
P_q	m	0.071 kg	k_{11}	-0.3 kN/m	d_n	0 Nsm
	I_t	18.9 kgmm^2	k_{12}	-0.1 Nm/m	d_r	0 Nsm
	I_p	23.8 kgmm^2	k_{22}	-1 Nm/rad	κ_F	0.4 N/A
	l_b	± 0.03 m	ϵ	10 μm	χ	100 μrad
	l_s	± 0.04 m				
R	q_{Lp}	10^0 m^2/s^2	q_{Ld}	10^9 m^2/s^4	r_L	10^{-9} m^2
	q_{Ki}	10^8 m^{-2}s^{-2}	q_{Kp}	10^9 m^{-2}	q_{Kd}	10^3 s^2/m^2
	r_K	10^2 A^{-2}				
N_f	c_c	10^{-7} -	n_h	3 -		

matrices Q_K, R_K and N_K are chosen as

$$Q_K = \begin{bmatrix} q_{Ki}I & O & O \\ O & q_{Kp}I & O \\ O & O & q_{Kd}I \end{bmatrix}, \quad R_K = r_K I, \quad N_K = \begin{bmatrix} O \\ O \\ O \end{bmatrix}. \tag{6.24}$$

- **Kalman filter or linear-quadratic estimator (LQE), L_{SF}**: the infinite-horizon linear-quadratic estimator or Kalman filter with gain L_{SF} is calculated such that the steady-state error between real x and estimated $\hat{x}$ is minimised, i.e.

$$\min\left\{ \lim_{k\to\infty} E\left[x[k] - \hat{x}[k]\right] \right\}, \tag{6.25}$$

subject to the plant dynamics (6.21) and assuming that the additive process w and measurement noise v in plant dynamics and measurement equations (6.21) follow a normal distribution with zero mean and covariance matrices

$$E\left[w^\top w\right] = Q_L = \begin{bmatrix} q_{Lp}I & O \\ O & q_{Ld}I \end{bmatrix}, \quad E\left[v^\top v\right] = R_L = r_L I, \quad E\left[w^\top v\right] = O, \tag{6.26}$$

being q_L and r_L the weighting factors of optimisation (6.25), defining the variance of process and measurement noise.

The design of the controller K_{SF} and estimator L_{SF} gains is performed by simply choosing the associated weighting factors q and r in matrices (6.24) and (6.26).

Other control techniques can be considered for the stabilisation of the rotor's position, such as pole-placement for another centralised position control or a simple PID for a decentralised controller, as described in [50].
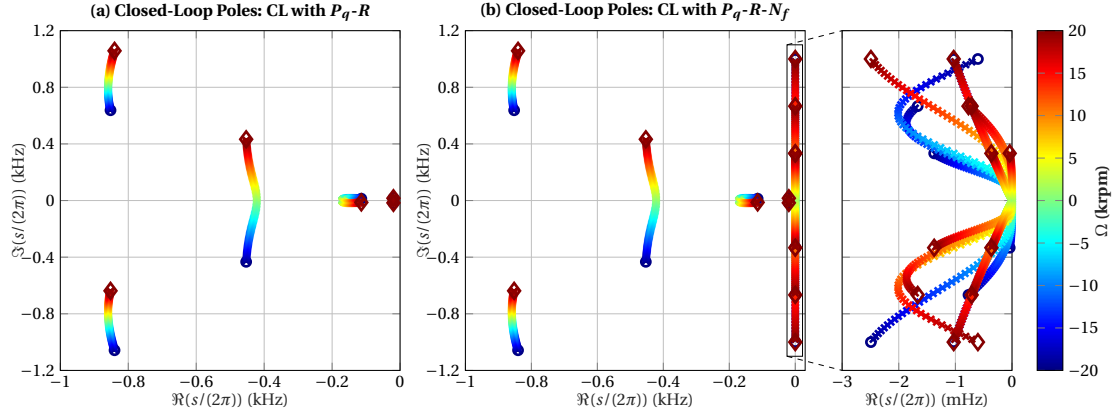
Figure 6.2 – Closed-loop poles of controlled system without (left) and with proposed notch filter (right) with detailed zoom of poles located close to imaginary axis.

6.3.3 Closed-Loop Stability

Having defined the structure of all matrices in equations (6.16a) for the plant dynamics P_q, (6.16b) for the controller R and (6.16c) for the generalised notch filter N_f, it is possible to analyse more precisely the behaviour of the closed-loop system of the studied fully active magnetic bearing motor by using the analysis tools described in chapter 3. As mentioned in chapter 3, due to the assumption of slow varying rotor speed Ω, the linear parameter-varying (LPV) system can be studied by considering a linear system dynamics for each rotor speed.

Firstly, the closed-loop system is stable if no eigenvalue of the state matrix A in (6.17) is located at the right half-plane (RHP). Secondly, the performance of the closed-loop system can be verified by calculating the unbalance response of the sensitivity functions defined in expressions (6.17), which yields the rotor displacements y and actuation currents u of the system excited by a harmonic disturbance corresponding to the rotor unbalance. The studied system, including dynamics, controller and notch, features the parameters included in table 6.1.

It is worth mentioning that, even though the poles of the open-loop generalised notch filter N_f are located at $\pm j l \Omega$, as clearly visible from the notch state matrix A_N in (6.4), its use in the closed-loop system will slightly deviate the poles from the imaginary axis.

To simplify the initial controller design, it is considered that the controller K_{SF} and estimator L_{SF} gains are calculated for each speed Ω in the range from -20 krpm to 20 krpm. In practice, a gain-scheduling approach with a few set of matrices is calculated off-line and stored in memory as a look-up table, allowing fast switching in real-time between controllers for different speeds.

A stable configuration with and without the proposed generalised notch filter is obtained choosing the weighting factors as specified in Table 6.1, resulting in the closed-loop poles shown in figure 6.2.a for R and in figure 6.2.b for N_f. Note the change in scale used for the
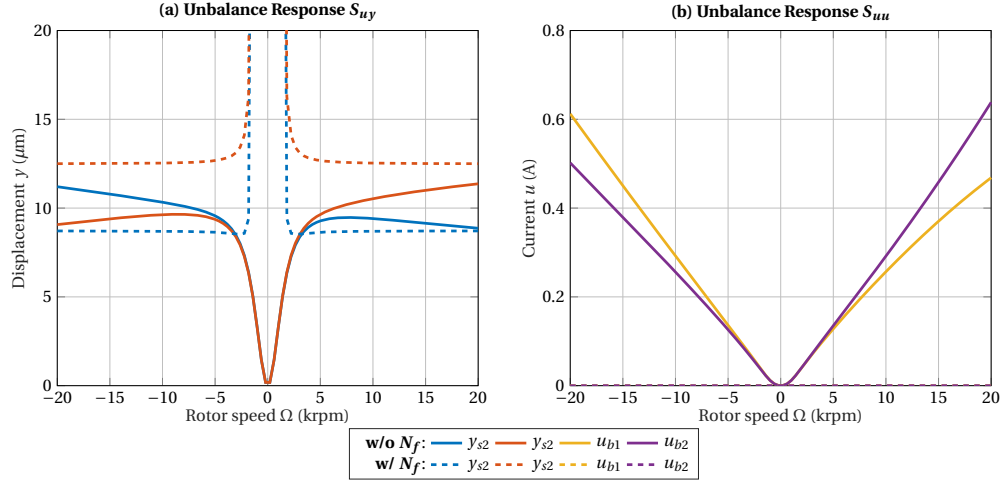
Figure 6.3 – Unbalance response of closed-loop system for rotor displacements at sensor planes (left) and bearing currents (right) with and without the proposed generalised notch filter.

x-axis to clearly visualize the impact of the closed-loop in the notch filter poles.

The resulting poles of N_f in the closed-loop are curved into the left half-plane (LHP) for lower speeds and subsequently approach the imaginary axis for higher speeds. At sufficiently high speeds, the notch poles will eventually crossing to the RHP if the estimator and controller poles are not fast enough. This can be observed in figure 6.2.d in the pole branch that bends towards the imaginary axis, which will eventually cross to the RHP for $|\Omega| > 20$ krpm. This situation could be avoided if other position control technique is employed, such as decentralised PID control, as shown in [50], but it is not deemed necessary for this case as the stability is guaranteed for the whole speed range of the system.

Even though the controller poles s_K do have a minor effect on the notch closed-loop poles, the main limiting factor of the stability is the location of the observer poles s_L. This effect can be seen as a delay between the estimated states and real states due to the rate of convergence of the state estimator, resulting in instabilities at higher speeds.

The unbalance response of the closed-loop system with the state feedback controller is also included in figure 6.3, showing the exact same behaviour with notch as the closed-loop system with PID controller for both displacements y and currents u. To prevent infinitely big orbits, in practice, the notch filter needs to be enabled for $|\Omega| > \Omega_{th}$.

To simplify the explanation of the results, only the radial dynamics have been analysed here. An equivalent study has been performed for the axial dynamics to choose the position controller and observer parameters for a stable operation with and without the proposed notch filter. In this case, due to the lower amplitude of the third harmonic for axial dynamics, it is chosen to suppress only two harmonics $n_h = 2$.

After studying the stability of the closed-loop system, the designed controller, estimator and

generalised notch filter are implemented into the real system, and the effectiveness of the proposed harmonic force rejection technique is experimentally quantified by measuring the reduction in vibrations and actuator currents. These results are detailed in section 7.

6.4 Conclusions

In this chapter, a highly stable harmonic disturbance suppression technique for magnetic bearing systems has been presented and validated. The proposed approach considerably reduces the stability problems shown in other unbalance control techniques, not requiring a time-consuming gain matrix nor phase shift fine-tuning for yielding a stable closed-loop system, and thus being easily extended to suppress multiple harmonics.

The main contributions of the chapter are:

- An harmonic force rejection force control technique is proposed, which features the following characteristics:

  - Due to its adaptive nature, it does not require any predefined noise nor vibration model.

  - It requires an estimation of measurement of the rotor speed.

  - Its internal structure does not have any gain nor phase parameter that needs to be adapted to guarantee stable operation over a broad speed range.

  - It is based on an unbalance and resonance control approach originally developed for rotating machinery employing active piezoelectric bearings, with stable open-loop dynamics.

- The general stability condition for a closed-loop system with the proposed harmonic force control is derived.

  - As opposed to the rotordynamics case with piezoelectric active bearings, no unconditional stability is obtained due to the unstable open-loop dynamics of magnetic bearings.

  - The stability condition sets the boundaries for controller design to guarantee a stable closed-loop system.

- The proposed vibration rejection technique is successfully implemented and tested on the studied fully active magnetic bearing system. Experimental validation of the approach is included in chapter 7.

7 Experimental Results and Validation

Having performed the analytical developments of a novel micro-vibration measurement technique for active magnetic bearings, closed-loop magnetic bearing models, electromagnetic force and torque models for active and passive magnetic bearings and motors, machine optimisation and harmonic force suppression techniques, it is now necessary to validate such developments experimentally.

In this chapter, the experimental results and validation for all the analyses presented in previous chapters are shown. Firstly, in section 7.1, all test benches employed for the validation of the different models are introduced and described. Secondly, the current-to-force micro-vibration measurement technique, proposed in chapter 3, is validated in section 7.2, by comparison to a state-of-the-art micro-vibration characterisation measurement equipment. Afterwards, the proposed electromagnetic models for active magnetic bearings defined in chapter 4 are validated in section 7.3. Subsequently, the experimental measurements of the optimisation results of the studied fully active magnetic bearing system, as performed in chapter 5, are described in section 7.4, consisting of the quantification of the main force and torque characteristics and the machine's efficiency. Finally, in section 7.5, the micro-vibration characterisation of the studied machine is performed, including the experimental validation of the harmonic force suppression technique proposed in chapter 6.

7.1 Experimental Test Benches

For the validation of the different analytical models or designs presented in the previous chapters different equipment has been employed. Due to the different nature of the model or design, several configurations need to be tested using various measurement set-ups. In this section, the employed equipment for the experimental validation of the previously presented models and techniques is detailed.
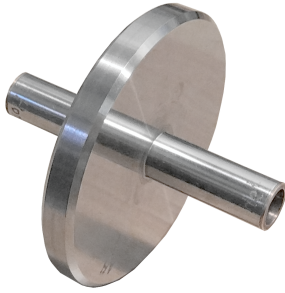
(a) Spokeless Reaction Wheel **(b) Spoked Reaction Wheel**
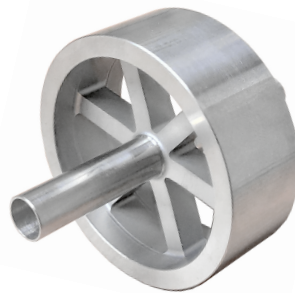
Figure 7.1 – Spokeless and spoked reaction wheel rotors of studied fully active magnetic bearing system.

7.1.1   Measured Equipment

The basic configuration of the studied fully active magnetic bearing system is presented in chapter 2, which corresponds to the initial state as detailed in [104]. During the development of the present thesis, several modifications or additions are performed to improve different characteristics of the fully active magnetic bearing system or to study new features for a more complete understanding of the system.

In terms of hardware, the following options will be available for comparison in the upcoming sections:

1. **Rotors**: to characterise the closed-loop behaviour for rotors with different mass and inertia and to identify some possible rotor-dependent vibration sources, two main rotor configurations are studied.

   - *Spokeless Reaction Wheel*: rotor with solid inertial disk as shown in figure 7.1.a. Due to the flat axial surface in the disk, this rotor allows the use of a more precise eddy-current axial position sensor.

   - *Spoked Reaction Wheel*: rotor with solid inertial rim, linked to the rotor shaft by six spokes as shown in figure 7.1.b. This rotor is controlled using the axial position derived from the magnitude of the stray flux measured by Hall sensors.

2. **Stators**: two main configurations have been studied for performance and efficiency comparison between different skewed, rhombic and hexagonal windings.

   - *Original Machine*: stator parts as described in chapter 2 and [104], consisting of skewed radial bearing and motor windings with heteropolar side with back iron, and homopolar side without iron.

   - *Optimised Machine*: stator parts resulting from the optimisation described in chapter 5, consisting of hexagonal and rhombic radial bearing and motor windings with back iron in both heteropolar and homopolar sides.
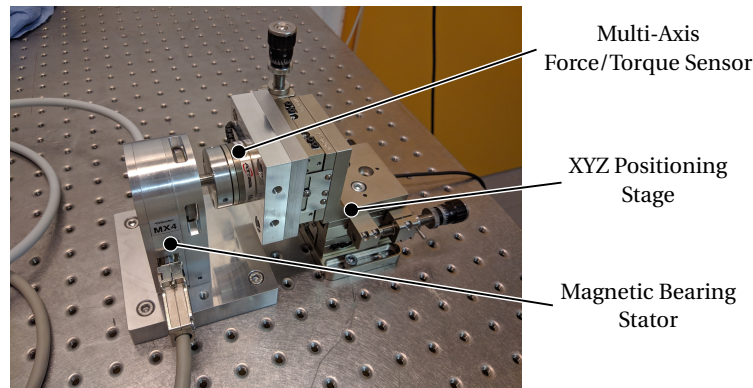
Figure 7.2 – Dedicated force and torque measurement test bench featuring a six-component force/-torque sensor and three-axis linear positioning stage.

Having two rotors of each type and considering the efficiency limitations of the original machine, the studied configurations are the following:

- **Configuration 1**: original machine with first spokeless reaction wheel rotor.
- **Configuration 2**: optimised machine with first spokeless reaction wheel rotor.
- **Configuration 3**: optimised machine with second spokeless reaction wheel rotor.
- **Configuration 4**: optimised machine with first spoked reaction wheel rotor.
- **Configuration 5**: optimised machine with second spoked reaction wheel rotor.

7.1.2 Measurement Set-Ups

In order to validate the models or quantify the impact of the design and optimisations described in previous chapters, the following test equipment is employed:

- *Active electromagnetic force and torque*: test bench consisting of a positioning stage and a six-component force and torque sensor capable of measuring the exerted forces and torques of magnetic bearings and motor.

- *Micro-vibration characterisation*: test bench consisting of a multi-component dynamometer employed for measuring the generated vibrations of the machine during operation.

Force and Torque Measurement Test Bench

A dedicated set-up for the measurement of the winding forces and torques has been developed and it is shown in figure 7.2. The test bench consists of fixed stator, where the studied windings are located, and a Thorlabs XYZ positioning stage, over which a 6-component ATI Mini 40-E force and torque sensor is mounted. Over the FT sensor a rotor with the diametrically magnetised or axially magnetised permanent magnets is fixed. After centring the rotor, a
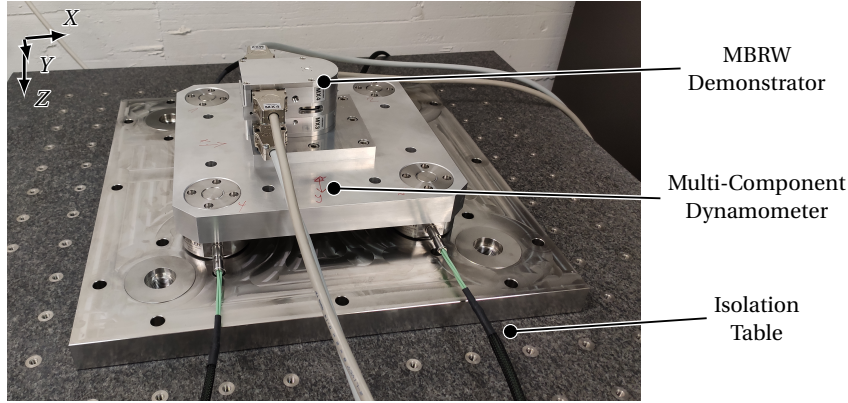
Figure 7.3 – Micro-vibration measurement test set-up featuring a multi-component dynamometric platform, a big seismic mass over pneumatic isolators as isolation table and the studied fully active magnetic bearing system.

rotating current, with a varying phase angle $\epsilon_w \in [-\pi, \pi]$, is impressed in the winding using a Celeroton CC-AMB-500 power converter, and the force and torque applied to the rotor are measured and logged using a ATI IFPMSC-4 multi-sensor interface.

Micro-Vibration Characterisation Test Bench

For validating the proposed current-to-force method as well as the simulated micro-vibrations of the developed closed-loop model, a state-of-the-art multi-component dynamometer is employed. This set-up is commonly employed for the qualification of equipment for space applications and its working principle has been introduced in chapter 3.

To summarise, the test bench consists of four three-component piezoelectric sensors fixed on one side to a big seismic mass and isolators for removing possible perturbations from the environment, and on the other fixed to the equipment to be characterised. The test set-up available at CSEM is shown in figure 7.3. The vibrations generated by the excitation forces generate a mechanical stress on the piezoelectric sensors, of type 9047C and 9048C by Kistler, and combined with a 5080A charge amplifier, also by Kistler, for signal conditioning, it is possible to measure three components of both force and torque. The voltage signals are sampled at 20 kHz for high-order harmonic disturbance identification by a dSpace MicroLabBox system with 16-bit A/D converters.

The mechanical design of the multi-component dynamometer is performed such that the first resonance mode of the structure is located at frequencies >1 kHz, guaranteeing a clean frequency spectrum up to 1 kHz. This design specification is given by the standard micro-vibration requirements for micro-vibration qualification is space applications [126]. This is achieved by the appropriate design in terms of dimensions and materials of the custom-made bottom and top plates of the dynamometer and the selection of high-stiffness piezoelectric transducers.
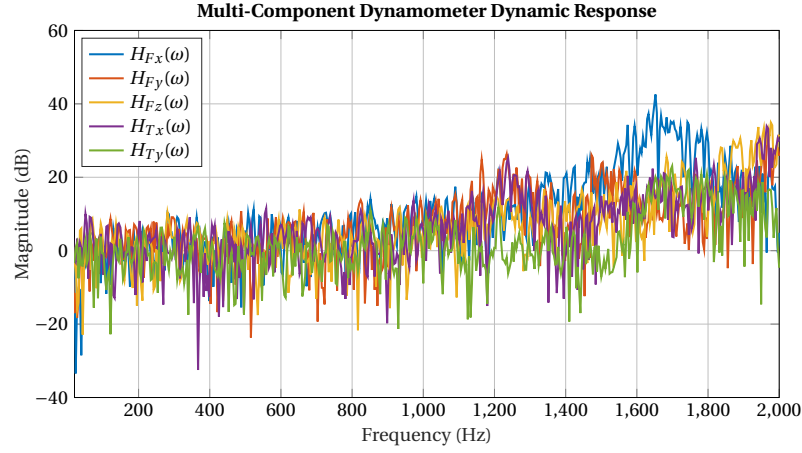
Figure 7.4 – Dynamic response $H(\omega)$ of micro-vibration characterisation test bench composed of multi-component dynamometer and studied fully active magnetic bearing system.

Furthermore, the resonance mode of the pneumatic isolators with the seismic mass is chosen to be at approximately 3 Hz to isolate low-frequency disturbances from the environment and surrounding laboratories.

7.2 Current-to-Force Measurements and Validation

To validate the proposed current-to-force micro-vibration measurement technique, a comparison with the micro-vibration level measured by an external state-of-the-art multi-component dynamometric platform shown in figure 7.3 is performed. This measurement validation set-up has been selected because it is extensively used for qualification and micro-vibration characterisation of space equipment, as mentioned in chapter 3.

7.2.1 Dynamic Characterisation of Measurement Equipment

It is first needed to guarantee that the measurement equipment does not greatly influence the vibration measurements. If there is a structural resonance in the studied frequency range, it would be necessary to also consider the dynamic response of the structure in the comparison, as done in [44].

Considering that the proposed current-to-force method directly measures the forces and torques supported by bearings $\boldsymbol{f}_b$, and that the reference multi-component dynamometer directly measures the forces supported by its transducers $\boldsymbol{f}_t$, the transformation from one to

the other can be defined as the transfer function matrix $H(\omega)$

$$
\boldsymbol{f}_t = \begin{bmatrix} F_{x,t} \\ F_{y,t} \\ F_{z,t} \\ T_{x,t} \\ T_{y,t} \end{bmatrix} = \begin{bmatrix} H_{Fx}(\omega) & 0 & 0 & 0 & 0 \\ 0 & H_{Fy}(\omega) & 0 & 0 & 0 \\ 0 & 0 & H_{Fz}(\omega) & 0 & 0 \\ 0 & 0 & 0 & H_{Tx}(\omega) & 0 \\ 0 & 0 & 0 & 0 & H_{Ty}(\omega) \end{bmatrix} \begin{bmatrix} F_{x,b} \\ F_{y,b} \\ F_{z,b} \\ T_{x,b} \\ T_{y,b} \end{bmatrix} = H(\omega)\boldsymbol{f}_b. \quad (7.1)
$$

The dynamic response of the structure $H(\omega)$, composed by the measurement equipment and the measured item, can be investigated by experimental modal testing using, for instance, a miniature impact hammer to excite the structure [44]. In this case, as the excitation forces are directly measured by means of the actuator currents during levitation, it is also possible to extract the dynamic response of the structure by comparing the current-to-force and dynamometer measurements at stand-still. This transfer function $H(\omega)$ is shown in figure 7.4.

As opposed to the situation presented in [44], the employed measurement set-up presents a considerably higher stiffness, featuring its first resonance mode at 1.6 kHz, and thus not disturbing the investigated frequency range up to 1 kHz. For this reason, and also due to the considerable noise in the measured $H(\omega)$, it is assumed that the structure has no effect on the excitation and measured forces, i.e. $H(\omega) = I$, and thus current-to-force and dynamometer micro-vibration measurements can be directly compared, and all subscripts b and t will be dropped hereafter.

7.2.2 Micro-Vibration Level Comparison

The validation is performed by covering the complete speed range of the fully active magnetic bearing system, from -20 krpm to 20 krpm in steps of 0.2 krpm, and measuring simultaneously the forces by both methods: current-to-force and dynamometric platform.

Furthermore, two hardware configurations are studied for a more complete validation: configurations 3 and 4 defined in section 7.1, i.e. the optimised machine stator combined with a spokeless or spoked reaction wheel rotor. Due to the thermal limitations of the original machine stator, it is not possible to cover the complete speed range for the heavier spoked rotor, and thus this validation is not possible. The current-to-force comparison with the original machine and spokeless rotor is performed in [44].

For the current-to-force method, the analytical bearing force constants κ_F, obtained by the electromagnetic models described in chapter 4, are employed. The exact values for the optimised machine are included in table 7.4.

The same analysis procedure presented in chapter 3 is performed for both dynamometer and current-to-force measurements to perform the comparison: the force and torque measurements in the time domain for each constant speed step are transformed to the frequency domain by a fast Fourier transform (FFT). The force and torque amplitude for each speed and
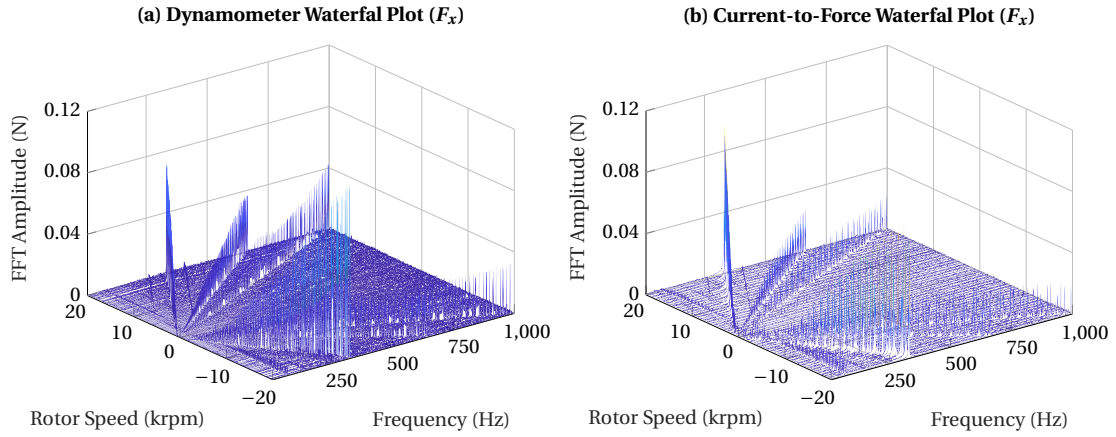
Figure 7.5 – Waterfall plot comparison between multi-component dynamometer and current-to-force micro-vibration measurements for configuration 4 (spoked reaction wheel rotor and optimised machine).

Table 7.1 – Roor mean square (RMS) absolute and relative difference between the proposed method and the reference dynamometer's measurements for configurations with spokeless and spoked rotors.

RMS	e_{Fx} [mN]	e_{Fy} [mN]	e_{Fz} [mN]	e_{Tx} [mNm]	e_{Ty} [mNm]
Spokeless RW Rotor	36.29 5.01%	28.67 3.50%	3.289 1.85%	1.5888 17.76%	1.6635 17.24%
Spoked RW Rotor	10.76 8.95%	10.93 10.95%	33.874 7.68%	0.78628 9.47%	0.30318 4.71%

frequency is then merged in a waterfall plot, as shown in figure 7.5 for both dynamometer and current-to-force methods. All forces and torques are expressed under the motor centre of mass reference frame, with axes parallel to the ones shown in figure 7.3.

To better compare both approaches, a worst-case plot is employed, where the maximum force and torque amplitude for all speeds at each frequency is taken, as shown in figure 7.6. In the top row, the comparison between dynamometer and current-to-force is performed for the configuration with a spokeless reaction wheel rotor, and with spoked rotor in the bottom row.

For both methods, it can clearly be seen that the current-to-force micro-vibration measurement method provides a force and torque magnitude similar to the one given by the state-of-the-art multi-component dynamometric platform. To quantify the accuracy in all force and torque components, the root mean square (RMS) of the difference between dynamometer and current-to-force in absolute magnitude or relative to the maximum peak of each component is included in table 7.1.

In these quantitative results it can be seen that whereas the current-to-force measurements better match the micro-vibration measurements for the three components of the force for the spokeless rotor, from 2 % to 5 % of difference, the torques present a much higher deviation,
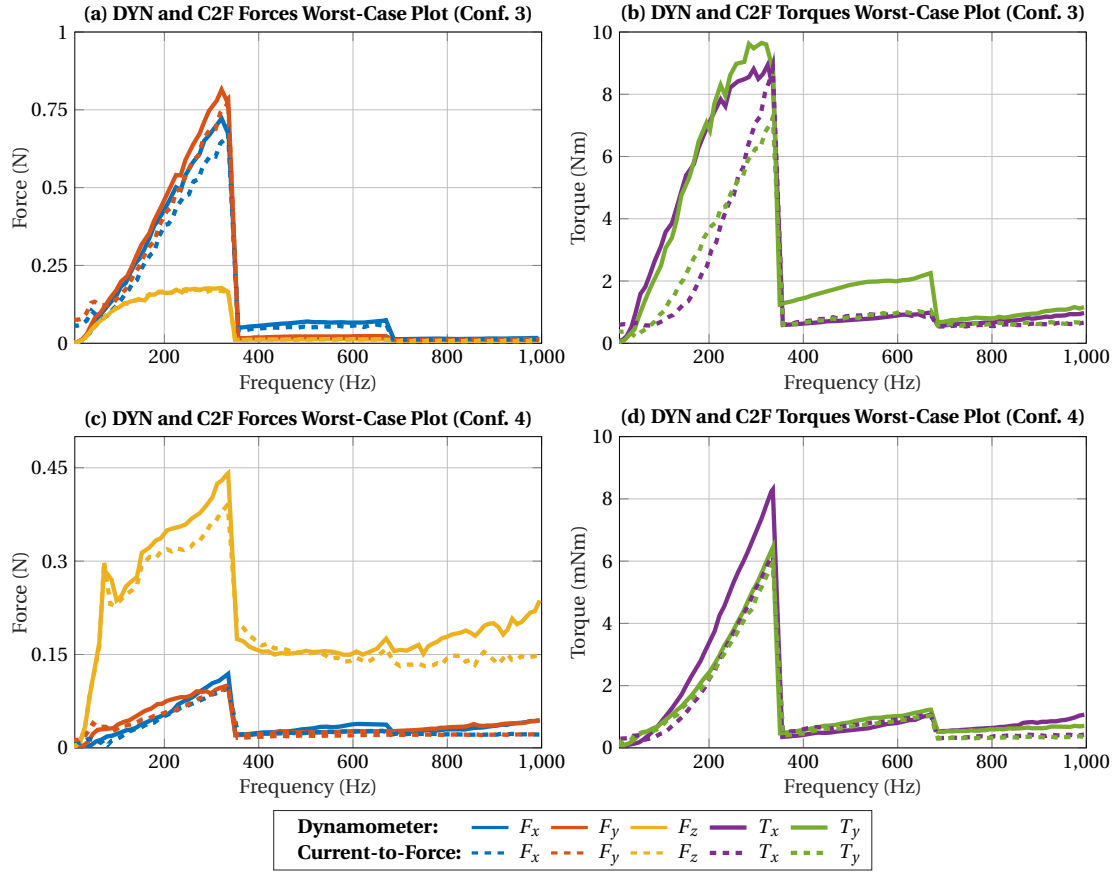
Figure 7.6 – Current-to-force micro-vibration measurement method validation results for configurations with spokeless and spoked reaction wheel (RW) rotors. Worst-case plots comparing dynamometer (DYN) and current-to-force (C2F) measurements of configurations 3 (top), with spokeless RW rotor, and 4 (bottom), with spoked RW rotor, for forces (left) and torques (right).

around 17 %. This situation may be due to the reduced axial length of the spokeless rotor, imposing a reduced resolution for the torques. Regarding the spoked rotor, a more consistent deviation is measured, being between 5 % and 11 % of relative difference.

In any case, the current-to-force method shows to be considerably accurate when compared with a state-of-the-art micro-vibration multi-component dynamometer. This method enables the possibility of considering an on-line micro-vibration measurement that could be employed during operation for possible fault detection or even control parameter adjustment if a deterioration of the performance is seen.

It is worth highlighting the notable difference in the magnitude of the forces in axial direction when employing the eddy-current or hall sensor axial position measurement. The higher sensitivity and reduced disturbances in the eddy-current axial sensor allows for a much lower magnitude of axial vibrations, as it can be seen in figures 7.6.a and 7.6.b.

7.3   Active Force and Torque Models Validation

In this section, the electromechanical models for slotless motors and magnetic bearings presented in chapter 4 are validated. The experimental measurement of the force and torque using a dedicated test bench is performed to validate the proposed models for the different studied configurations. Furthermore, the computational efficiency and accuracy of the proposed approach is compared to other analytical methods.

7.3.1   Force and Torque Magnitude Validation

All force and torque models are validated by comparing the experimental measurements taken using the dedicated test bench in figure 7.2 with the model calculations. For all validations the same test procedure is used:

1. Rotor is fixed to force/torque sensor with fixed orientation. Its magnetisation direction is considered to be along the X-axis.
2. The stator with the winding type to be tested is fixed to the measurement test bench.
3. A rotating current of amplitude $\hat{i}_s = 1\,\text{A}$ is applied, whose electric phase angle ϵ_w is varied in 41 steps to cover a whole revolution $\epsilon_w \in [-\pi, \pi]$.
4. All six components of forces and torques are measured and logged using the Force/-Torque ATI sensor.
5. The previous steps of the test are replicated using the models defined in chapter 4, including reluctance forces for all radial bearing windings and radial torques of motor windings from (4.25).
6. Comparison between measured and analytical forces/torques is performed.

All forces and torques are expressed under the winding's reference frame, shown in figure 4.2. For validation, the following combinations of field distribution and winding types have been studied:

- **Skewed winding**: the cases of the original machine as per [104], i.e. heteropolar motor and radial bearing with back iron, and homopolar radial bearing without iron.
- **Rhombic winding**: the cases for which hexagonal winding is not possible to be manufactured, i.e. homopolar radial bearing with and without back iron, due to the reduced length of this winding.
- **Hexagonal winding**: all possible cases where manufacturing is possible with available tools, i.e. heteropolar motor and radial bearing winding with and without back iron.
- **Axial winding**: only the original winding as per [104], i.e. homopolar without iron, and a new winding (with modified dimensions in order to fit inside back iron) at the homopolar side with back iron.
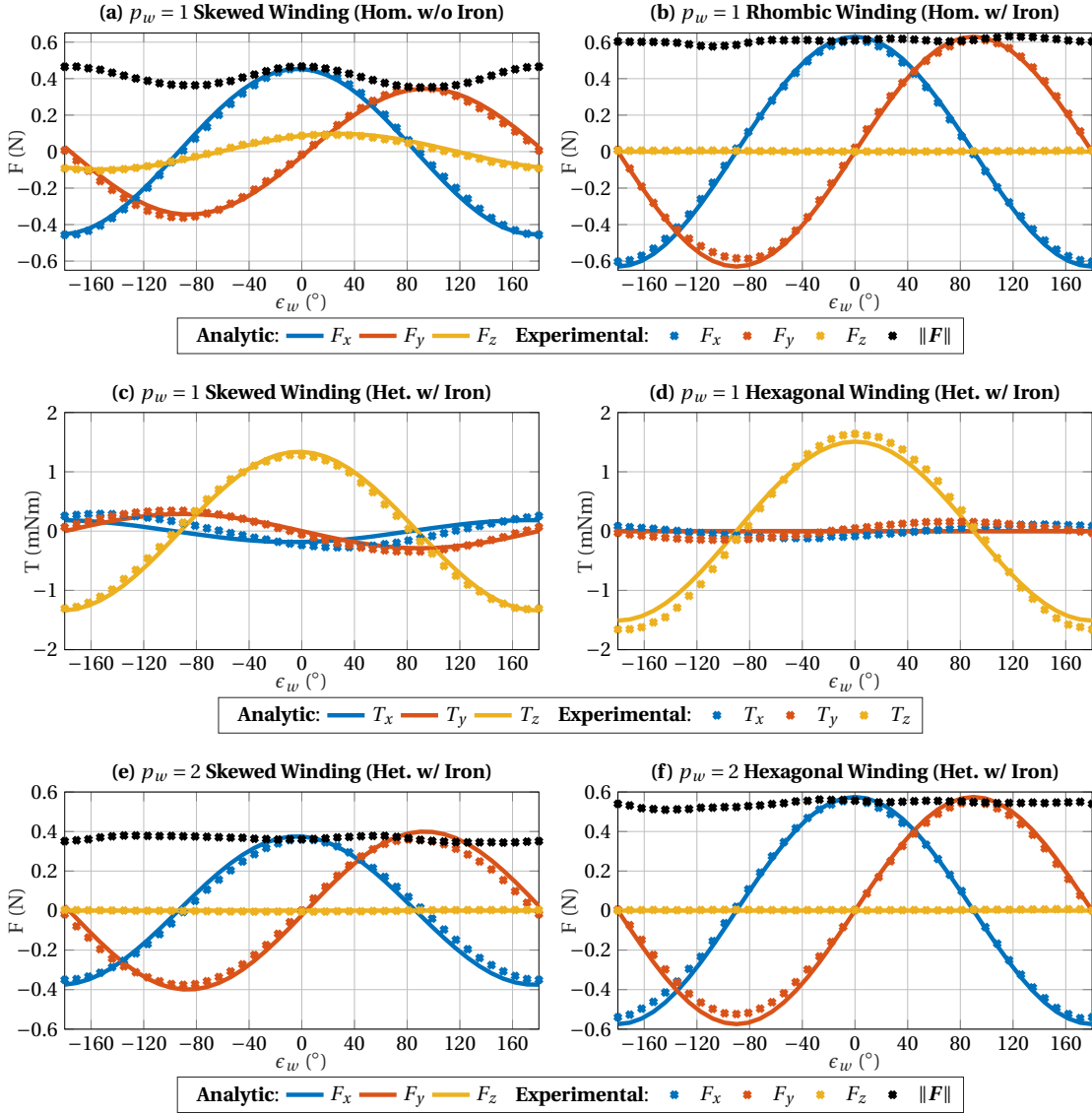
Figure 7.7 – Analytical and experimental forces and torques for skewed, rhombic and hexagonal windings. All plots are arranged in rows with windings for the same function: (a) and (b) homopolar radial bearing windings, (c) and (d) motor windings, and (e) and (f) heteropolar radial bearing windings.

A comparison between original (skewed) and new (rhombic or hexagonal) windings with the same functionality is included in figure 7.7. As only the most representative cases are included in figure 7.7, a quantitative comparison between models and experimental measurements for all combinations (winding types on hetero- and homopolar sides with and without back iron), is included in Table 7.2.

Due to the importance of winding resistance for the estimation of losses in machine design and optimisation, the analytical value obtained using the calculation described in (5.3) is compared to the resistance of each phase measured experimentally in Table 7.2 for 20 °C.

Table 7.2 – Analytical (an.) and experimental (exp.) data for validation of F/T models for all manufactured test windings. Units with superscript * represent motor torque measurements in mN m/A. All resistance measurements are taken at 20°C

Funct.	Winding		Stator		Fig.	κ_F, κ_T (N/A)		Err.	R_{ph} (Ω)		Err.
	Type	p_w	Side	Iron		Exp.	An.	(%)	Exp.	An.	(%)
Motor	Sk.	1	Het	w/	7.7.c	1.299*	1.338*	3.0	0.70	0.68	2.9
	Hx.	1	Het	w/o	-	1.192*	1.106*	7.2	0.79	0.73	7.6
	Hx.	1	Het	w/	7.7.d	1.648*	1.509*	8.4	0.79	0.73	7.6
Radial Bearing	Sk.	2	Het	w/	7.7.e	0.364	0.387	6.3	1.53	1.43	6.5
	Hx.	2	Het	w/o	-	0.524	0.523	0.2	2.1	1.97	6.2
	Hx.	2	Het	w/	7.7.f	0.541	0.574	6.1	2.1	1.97	6.2
	Sk.	1	Hom	w/o	7.7.a	0.411	0.408	0.7	2.58	2.60	0.8
	Rh.	1	Hom	w/o	-	0.515	0.495	3.9	3.0	2.98	0.7
	Rh.	1	Hom	w/	7.7.b	0.608	0.567	6.7	3.0	2.98	0.7
Axial Bearing	Ax.	-	Hom	w/o	-	0.991	1.004	1.3	19	18.1	4.8
	Ax.	-	Hom	w/	-	0.891	0.948	6.4	9.7	9.6	1.0

- *Skewed winding*: the measured windings correspond to the system as defined in previous publications, i.e. [104]: 1 pole-pair radial bearing winding on homopolar side without back iron, figure 7.7.a, 1 pole-pair motor winding on heteropolar side with back iron, 7.7.c, and 2 pole-pairs heteropolar radial bearing winding with back iron, 7.7.e.

  The main novelty in the skewed winding model estimations, with respect to [101] and [44], relies on the ability of estimating force and torque asymmetries and the consideration of reluctance forces for radial forces and torques, as more clearly seen in Fig 7.7.a and 7.7.c. This is mainly due to the relatively high thickness of both heteropolar motor and homopolar radial bearing windings, making each phase's layer thick, and thus increasing the winding asymmetries causing the force and torque ripple and disturbances.

  It can be seen in both figure 7.7 and table 7.2 that the model accurately predicts, not only the magnitude of force κ_F and torque κ_T constants, but also the force and torque asymmetries, specially for figure 7.7.a.

- *Rhombic winding*: for this type of windings, only the forces generated by the radial bearing winding with $p_w = 1$ for the homopolar side without and with back iron are measured, included in figure 7.7.b for the latter.

  As in the previous case, both figure 7.7 and table 7.2 show an accurate matching between the model and the measured forces. It is also noticeable in this case, thanks to the high symmetry of the rhombic winding, that both the variation of force magnitude with the phase angle ϵ_w and axial forces are drastically reduced when compared to the equivalent skewed winding in 7.7.a.

  Being the radial bearing winding next to the back iron, the effect of the reluctance forces are considerably noticeable for this case, resulting in an increase of about 40 % with

respect to the Lorentz forces alone.

- *Hexagonal winding*: as previously stated, the following configurations have been measured: 1 pole-pair motor winding in the heteropolar side without and with back iron and a 2 pole-pairs radial bearing winding again in the heteropolar side without and with back iron. The cases with back iron are shown in figure 7.7.d and figure 7.7.f, while the numerical results for all cases are included in Table 7.2.

  Like in the previous cases, the results show a good matching between the model and the measurements. It is worth highlighting again the identified effect of the back iron in the measured forces and torques: while a considerable increase in the torque constant κ_T ($\approx 38\,\%$) and reduction of radial torques for the motor winding ($\approx 11\,\%$), this effect is much less intense for the radial bearing force constant κ_F (increase of $\approx 4\,\%$), due to the relatively high distance to the back iron as the motor winding lies between them.

- *Axial winding*: two different windings with different dimensions and number of turns had to be used for performing the test with and without back iron due to the difficulty of holding the two halves of the winding. Furthermore no figure is included due linear behaviour of the winding, creating only axial force proportional to the input current and no radial force. The comparison between the model and experimental measurements in included in Table 7.2. It can be seen the positive effect of the back iron in the measurements: even if a reduction of 49 % in the number of turns (and thus wire length and resistance), the bearing force constant κ_F is only slightly reduced ($-10\,\%$).

7.3.2   Computational Efficiency

A key element of the electromagnetic models of the magnetic bearings and motor that defines their computational requirements is the magnetic flux density distribution employed for calculating the force and torques. As previously mentioned, one of the main advantages of the proposed models is the use of accurate and computationally efficient 3D flux models that rely on the use of elliptic integrals, as described in chapter 4. In this section the proposed models are compared to other analytical approaches such as 2D models [116] and 3D models based on Fourier series expansions [113]–[115].

All approaches are implemented in MATLAB using built-in functions, apart from *EIFun18* toolbox presented in [127] for elliptic integral calculations. The execution time of each approach is measured using the same computer and taking the average of five repetitions, running 64-bit Windows 10 Pro, 64-bit MATLAB R2020a and featuring an Intel Core i7-8565U CPU, being all results summarised in table 7.3.

As the 2D model and 3D model with Fourier-Bessel series expansions are targeted for configurations with back iron, not all comparisons can be performed. In all cases, the 2D model is the fastest to execute, in the order of tens of millisecond, followed by the proposed 3D model with elliptic integrals (3D EI), in the order of seconds, and lastly the 3D model with series expansion

Table 7.3 – Accuracy and execution time comparison between analytical models for magnetic flux density distribution: two-dimensional (2D), three-dimensional with elliptic integrals (3DEI) and with Fourier-Bessel series expansion (3DFB). For execution time calculations, columns with Λ include the execution time of (4.9). Values with superscript [*] represent motor torque measurements in mN m/A.

Funct.	Winding		Stator		κ_F, κ_T (N/A)				Execution time (s)				
	Type	p_w	Side	Iron	Exp.	2D	3DEI	3DFB	2D	2DΛ	3DEI	3DEIΛ	3DFB
Motor	Sk.	1	Het	w/	1.31[*]	1.22[*]	1.29[*]	1.30[*]	0.02	1.70	1.06	3.38	11.3
	Hx.	1	Het	w/o	1.19[*]	-	1.11[*]	-	-	-	1.05	-	-
	Hx.	1	Het	w/	2.15[*]	1.99[*]	2.14[*]	2.15[*]	0.02	1.97	1.22	3.38	11.8
Radial Bearing	Sk.	2	Het	w/	0.38	0.35	0.42	0.42	0.02	2.23	2.54	5.05	28.2
	Hx.	2	Het	w/o	0.52	-	0.52	-	-	-	2.51	-	-
	Hx.	2	Het	w/	0.64	0.56	0.68	0.67	0.02	2.30	2.53	4.99	26.3
	Sk.	1	Hom	w/o	0.39	-	0.38	-	-	-	2.48	-	-
	Rh.	1	Hom	w/o	0.52	-	0.50	-	-	-	2.88	-	-
	Rh.	1	Hom	w/	0.59	-	0.60	0.60	-	-	2.54	4.87	10.4
Axial Bearing	Ax.	-	Hom	w/o	0.99	-	1.00	-	-	-	0.84	-	-
	Ax.	-	Hom	w/	0.89	-	0.90	0.90	-	-	0.80	2.91	3.48

(3D FB), in the order of tens of second when considering 50 harmonics. On the accuracy side, the 3D FB and 3D EI show equivalent results, whereas the 2D model shows a greater difference with respect to the experimental measurements. In general terms, the proposed 3D EI model proves to have the broadest applicability and a great accuracy while being computationally light, enabling the possibility of including such models into a numerical optimisation for actuator design.

Note that different windings have been employed for some cases in this comparison with respect to the previous validation of the force and torque in table 7.2.

7.4 Final Electromagnetic Design Measurements

In this section, the properties of the magnetic bearing machine resulting from the optimisations presented in chapter 5 are experimentally validated. Two analyses are performed for validating the optimisation results: firstly, the generated forces and torques, as well as winding resistances are measured and compared with the analytical results, and secondly, the power consumption during operation is measured to quantify the resulting machine efficiency.

7.4.1 Force and Torque Measurements

The dedicated set-up for the measurement of the winding forces and torques, shown in figure 7.2, is employed. For all windings the same test procedure was used:

1. Rotor is fixed to force/torque sensor with fixed orientation. Its magnetisation direction

Table 7.4 – Experimental measurements of original and optimised winding properties, including bearing K_B and motor K_M constants, force κ_F and torque κ_T constants, winding phase resistance R_{ph}, and force and torque ripple r_F, r_T and disturbances d_F, d_T, for homopolar axial and radial bearings, and heteropolar radial bearing and motor. Values with superscript * represent motor torque measurements in $mNm/\sqrt{W}$ or mNm/A.

| Funct. | Stator | | | Fig. | K_B, K_M $(N/\sqrt{W})$ | κ_F, κ_T (N/A) | R_{ph} (Ω) | r_F, r_T (%) | d_F, d_T (%) |
	Winding	Side	Iron						
Axial Bearing	Orig. (Ax.)	Hom	w/o	-	0.227	0.991	19.0	1.89	1.83
	Opt. (Ax.)	Hom	w/	-	0.286	0.891	9.70	3.77	1.59
	Relative Difference (%):				+25.8	−10.1	−48.9	+1.88	−0.24
Radial Bearing	Orig. (Sk.)	Hom	w/o	7.7.a	0.239	0.394	2.73	14.06	39.81
	Opt. (Rh.)	Hom	w/	7.7.b	0.343	0.594	3.00	3.54	1.33
	Relative Difference (%):				+43.76	+50.6	+9.8	−10.5	−38.5
Motor	Orig. (Sk.)	Het	w/	7.7.c	1.409^*	1.312^*	0.87	0.66	42.60
	Opt. (Hx.)	Het	w/	7.7.d	1.964^*	2.152^*	1.20	0.09	16.64
	Relative Difference (%):				+39.4	+64.1	+38.5	−0.6	−25.9
Radial Bearing	Orig. (Sk.)	Het	w/	7.7.e	0.286	0.380	1.77	7.07	1.71
	Opt. (Hx.)	Het	w/	7.7.f	0.413	0.644	2.43	3.89	1.20
	Relative Difference (%):				+44.5	+69.6	+37.7	−3.2	−0.5

is used as the reference X-axis for the measurements ($\phi_z = 0$).

2. The stator with the winding type to be tested is fixed to the measurement test bench. The windings tested are skewed, rhombic, hexagonal and axial (concentrated) windings.

3. A rotating current of amplitude $\hat{i}_s = 1\,\text{A}$ is applied, whose electric phase angle ϵ_w is varied in 41 steps to cover a whole revolution $\epsilon_w \in [-\pi, \pi]$.

4. The six components of forces and torques applied to the rotor are simultaneously measured using the Force/Torque ATI sensor.

All forces and torques are expressed under the winding's reference frame, being X- and Y-components radial and Z-component axial. Furthermore each winding phase resistance is measured using a digital multimeter.

The measured forces for all windings were shown in figure 7.7 for the validation of the electromagnetic models of the bearings and motor. The original windings correspond to the left column of plots, i.e. homopolar radial bearing with skewed windings in figure 7.7.a, heteropolar motor with skewed windings in 7.7.c, and heteropolar radial bearing with skewed windings in 7.7.e. The optimised windings results are shown in the right column of plots, i.e. homopolar radial bearing with rhombic windings in figure 7.7.b, heteropolar motor with hexagonal windings in 7.7.d, and heteropolar radial bearing with hexagonal windings in 7.7.f. Furthermore, the quantitative results of bearing/motor constant (K_B, K_M), force/torque constant (κ_F, κ_T), winding phase resistance (R_{ph}), force/torque ripple (r_F, r_T), and force/torque disturbance

(d_F, d_T), are summarised in table 7.4.

As analytically calculated, a considerable increase in efficiency for all actuators is measured, ranging between 25 % and 45 % with respect to the original actuators [104], showing the great accuracy of the analytical models. This drastic increase is a result of the combined action of more efficient windings for motor and radial bearing windings, and the addition of back iron for the radial and axial homopolar bearings. Furthermore, as shown in the force magnitudes in figure 7.7, both disturbances and ripple in force or torque are also considerably reduced for all cases where possible (with the exception of the axial bearing where a marginal increase is experienced).

7.4.2 Power Consumption Measurements

To quantify the effect of the efficiency increase during operation, the power consumption of the magnetic bearing system is experimentally measured using a ZES Zimmer LMG670 power analyser. This power analyser is able to simultaneously measure the three-phase or single-phase voltage and currents of a single actuator and calculate its active P_w, reactive Q_w and apparent $|S_w| = \sqrt{P_w^2 + Q_w^2}$ power consumption. A tachometer signal is also fed into the power analyser to synchronise rotational speed and power consumption measurements.

In order to fully characterise the power consumption of the machine, the following test plan is undertaken:

1. Connect a single actuator (bearing or motor) of a machine to the power analyser.
2. Position the machine in horizontal orientation, with gravity actuating in radial direction.
3. Apply a speed profile from -20 krpm to 20 krpm in steps of 0.5 krpm and acceleration of 500 rpm/s while logging tachometer and power consumption at a sampling rate of 10 Hz.
4. Repeat steps 2-3 for vertical orientation, with gravity actuating in axial direction.
5. Repeat steps 1-4 for all actuators: heteropolar radial bearing, heteropolar motor, homopolar radial bearing and homopolar axial bearings.
6. Repeat steps 1-5 for the remaining machine, to cover both original and optimised machines.

The results are then separated in steady-state and transient power consumption, measured at constant speed in figure 7.8 and during acceleration in figure 7.9, respectively. It can be seen that for all actuators and configurations an important reduction in power consumption is obtained as a result of the optimisation described in chapter 5, and thus considerable increase in efficiency.

A quantitative comparison of the power consumption is included in table 7.5. All maximum, minimum and average values for all speeds of active P_w, reactive Q_w and apparent $|S_w|$
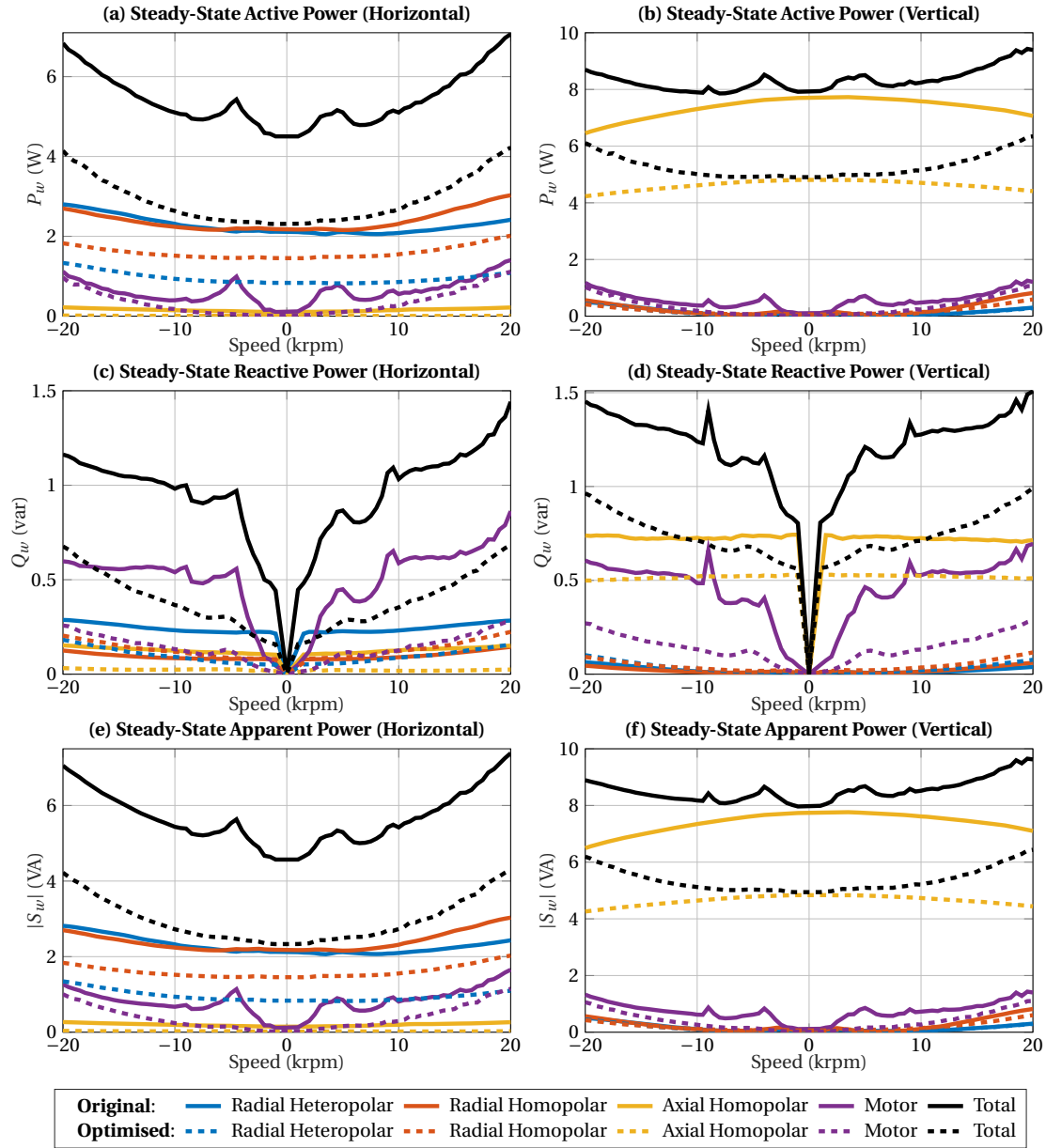
Figure 7.8 – Active P_w, reactive Q_w and apparent $|S_w|$ power consumption measurements at constant speeds for all actuators in original and optimised machines in two orientations: (a)-(c)-(e) horizontal, with gravity in radial direction, and (b)-(d)-(f) vertical, with gravity in axial direction.

power consumption is shown for both original and optimised machines, including the relative improvement resulting from the optimisation. Furthermore, the comparison is performed for each actuator independently as well as the total power consumption resulting from the combination of all actuators. Due to the different load acting on each actuator depending on the working conditions, such as constant speed/acceleration or horizontal/vertical orientations, the values included in table 7.5 correspond to the condition in which the actuator is more demanded. More specifically, the comparison for each actuator is performed under the
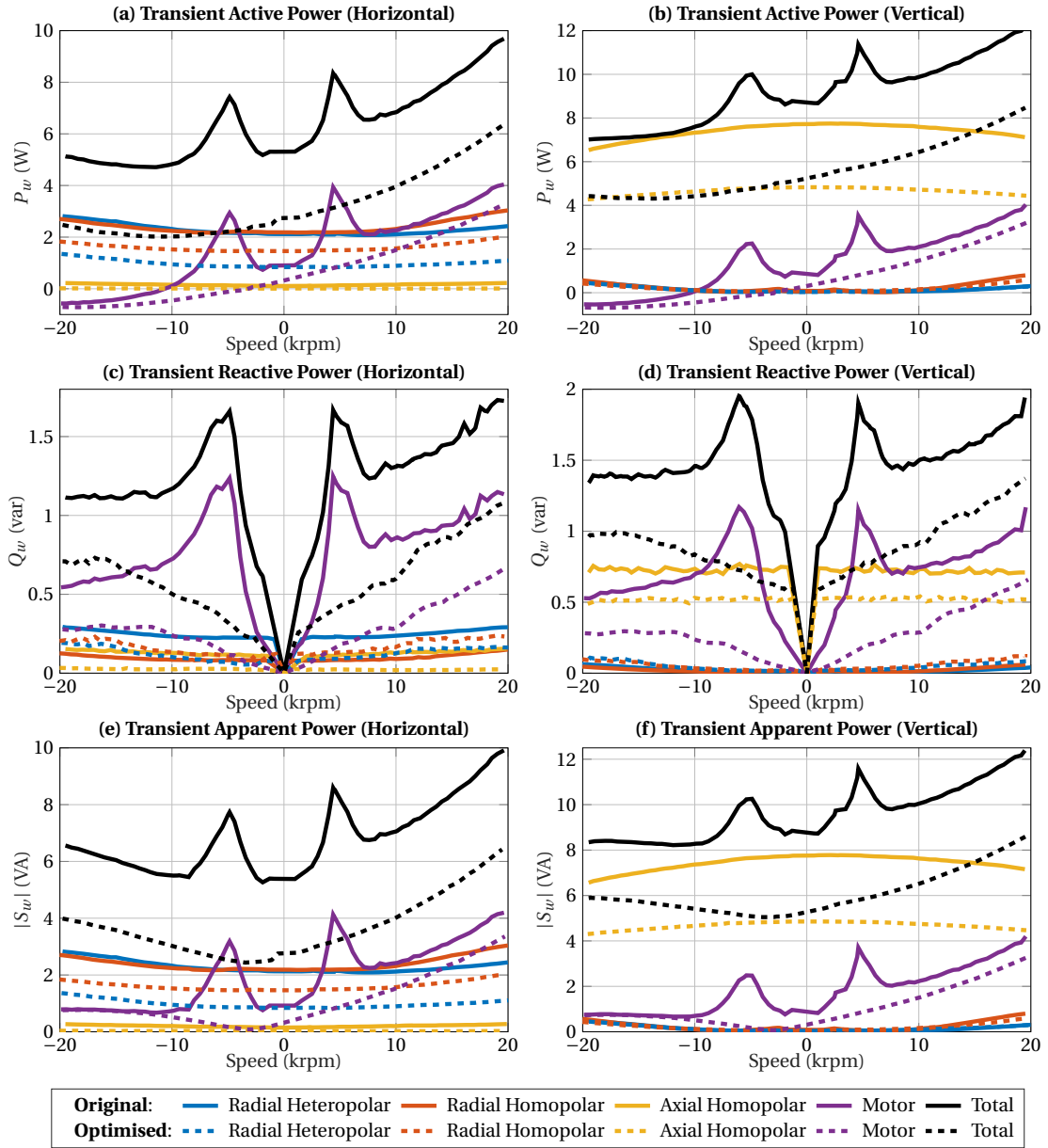
Figure 7.9 – Active, reactive and apparent power consumption measurements during acceleration from −20 krpm to 20 krpm for all actuators in original and optimised machines in two orientations: (a)-(c)-(e) horizontal, with gravity in radial direction, and (b)-(d)-(f) vertical, with gravity in axial direction.

following conditions:

- *Heteropolar Radial Bearing*: steady-state and horizontal orientation (SS Hor).

- *Homopolar Radial Bearing*: steady-state and horizontal orientation (SS Hor).

- *Homopolar Axial Bearing*: steady-state and vertical orientation (SS Ver).

- *Heteropolar Motor*: transient and horizontal orientation (Tr Hor) during acceleration from 0 krpm to 20 krpm.

Table 7.5 – Power consumption comparison between original and optimised machine in steady-state conditions for all actuators and total consumption. SS and Tr denote steady-state or transient conditions, while Hor and Ver horizontal or vertical configurations, respectively. In dark green and red the values with relative difference greater than 50 % are highlighted.

Act.	Case	*P* (W)			*Q* (var)			|*S*| (VA)		
		max	min	avg	max	min	avg	max	min	avg
Het. Radial	Orig (SS Hor)	2.80	2.05	2.27	0.29	0.21	0.24	2.82	2.06	2.29
	Opt (SS Hor)	1.33	0.82	0.95	0.18	0.05	0.10	1.35	0.82	0.96
	Diff. (%):	−52.4	−60.0	−58.2	−36.5	−76.5	−60.3	−52.2	−60.1	−58.2
Hom. Radial	Orig (SS Hor)	3.03	2.16	2.39	0.14	0.08	0.10	3.03	2.16	2.39
	Opt (SS Hor)	2.02	1.45	1.60	0.22	0.08	0.13	2.03	1.45	1.61
	Diff. (%):	−33.5	−32.7	−33.1	+55.0	+0.66	+35.8	−33.1	−32.6	−32.9
Hom. Axial	Orig (SS Ver)	7.73	6.45	7.36	0.74	0.70	0.73	7.76	6.49	7.40
	Opt (SS Ver)	4.81	4.23	4.62	0.53	0.50	0.52	4.84	4.26	4.65
	Diff. (%):	−37.8	−34.4	−37.2	−28.6	−29.3	−28.6	−37.7	−34.4	−37.1
Motor	Orig (Tr Hor)	4.14	-0.58	1.62	1.26	0.15	0.77	4.29	0.67	2.02
	Opt (Tr Hor)	3.36	-0.72	0.61	0.68	0.02	0.27	3.43	0.08	1.07
	Diff. (%):	−18.8	+23.8	−62.6	−46.1	−86.6	−65.0	−20.0	−88.2	−47.1
Total	Orig (SS Hor)	7.06	4.50	5.46	1.44	0.44	0.97	7.38	4.57	5.71
	Opt (SS Hor)	4.22	2.31	2.91	0.68	0.16	0.39	4.30	2.33	2.99
	Diff. (%):	−40.2	−48.7	−46.7	−52.6	−64.2	−59.7	−41.8	−49.0	−47.7
	Orig (SS Ver)	9.43	7.86	8.33	1.51	0.80	1.23	9.65	7.96	8.55
	Opt (SS Ver)	6.35	4.90	5.28	0.99	0.56	0.74	6.44	4.94	5.37
	Diff. (%):	−32.7	−37.6	−36.6	−34.2	−30.3	−39.7	−33.3	−38.0	−37.1

- *Total*: steady-state for both horizontal and vertical orientations (SS Hor and SS Ver).

From table 7.5, it can be seen that there is a considerable improvement in efficiency and power consumption for all actuators, and more importantly for the total consumption of the machine during operation. As the windings of the actuators represent mainly resistive loads, the total apparent power is mainly composed of active power, with the only exception of the motor windings.

The biggest reduction is obtained for the heteropolar side of the machine, resulting in a radial bearing with an average reduction of almost 60 % in power consumption, and the motor, whose consumption is reduced in 50 % to 65 %. For the homopolar side, the power reduction ranges from 37 % of the axial bearing, to 33 % of the radial bearing, with the only exception of the reactive power on the homopolar radial bearing, due to the inductance increase as a result of the optimisation. The power consumption is mainly resistive, and thus the impact of the reactive power is minimal for the studied machine. Regarding the total power consumption, an average reduction of 47 % is obtained in horizontal, and of 37 % in vertical orientation.

(a) C2F Waterfal F_x Plot w/o Notch (Conf. 3) **(b) C2F Waterfal F_x Plot w/ Notch (Conf. 3)**
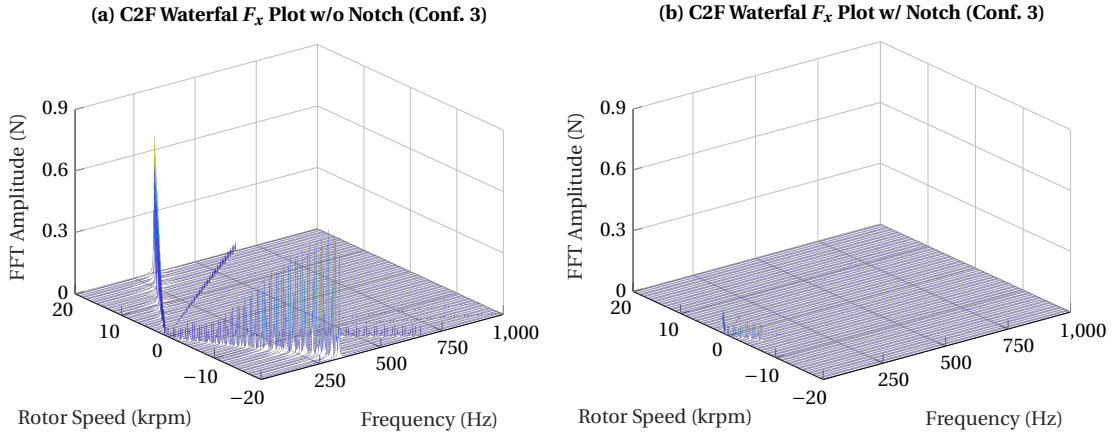
Figure 7.10 – Waterfall plots of current-to-force (C2F) micro-vibration measurements without (left) and without (right) the proposed generalised notch filter for configuration 3 (optimised machine with spokeless RW rotor).

7.5 Micro-Vibration Measurements

In this last section, the characterisation of the generated micro-vibrations by the studied fully active magnetic bearing system is performed. As mentioned in section 7.1, different hardware configurations need to be tested to quantify the influence of the different rotors and stators in the magnitude of the exported micro-vibrations. The characterisation is then performed with both current-to-force and multi-component dynamometer micro-vibration measurement methods, as the former accounts only for the active electromagnetic forces, i.e. Lorentz forces, whereas the latter also accounts for passive stiffness or other passive electromagnetic and mechanical forces.

Furthermore, the effect of the harmonic force suppression control proposed in chapter 6 is measured for each configuration by comparing the measured micro-vibrations with and without the generalised notch filter. The multi-harmonic suppression technique is enabled for the first three harmonics $n_h = 3$ in radial direction, and two $n_h = 2$ in axial direction for rotational speeds above a certain threshold $|\Omega| > \Omega_{th} = 4\,\mathrm{krpm}$.

As a result of the much higher efficiency of the optimised machine, as shown in the previous section, only this stator is capable of covering the complete studied speed range, from $-20\,\mathrm{krpm}$ to $20\,\mathrm{krpm}$, with any rotor with and without generalised notch filter. All studied configurations are defined in section 7.1. Only the most representative cases will be graphically shown, completed by the quantitative results summarised in table 7.6.

Due to the multiple combinations of hardware to test, the analysis of the generated micro-vibrations is investigated as follows: first, the effect of the proposed generalised notch filter is verified, followed by a study of the influence of the employed stator and rotor.
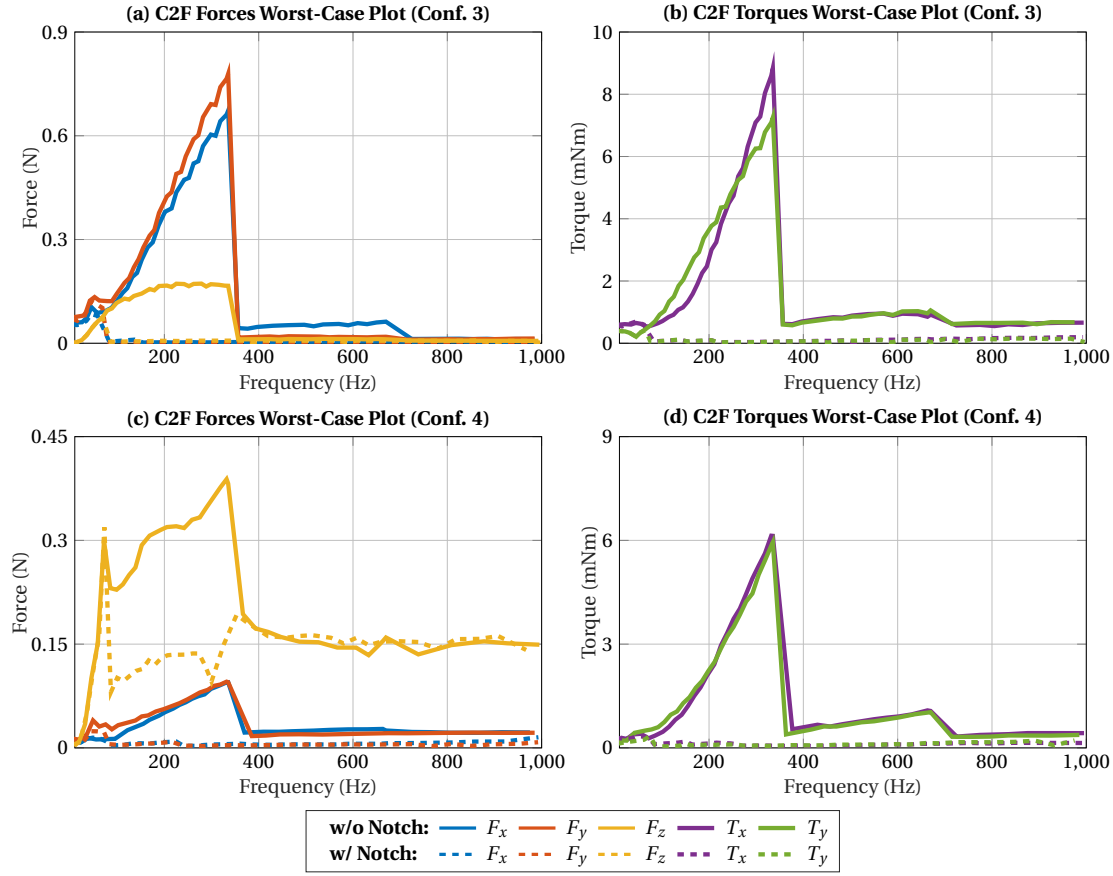
Figure 7.11 – Current-to-force (C2F) micro-vibration measurements of forces (left) and torques (right) with and without the proposed generalised notch filter for configurations 3 (top), with optimised machine and spokeless RW rotor, and 4 (bottom), with optimised machine with spoked RW rotors.

Effect of Generalised Notch Filter

Firstly, the effect of the proposed generalised notch filter using the current-to-force method is analysed, which directly considers the actuator currents, and thus show the effect on the signal that is used as input to the filter. As analytically shown in chapter 6, the proposed technique should completely suppress any component at the desired harmonics.

As shown in the waterfall plots comparing the current-to-force measurements for configuration 3 with and without generalised notch filter, in figure 7.10, and in the worst-case plots for configurations 3 and 4, in figure 7.11, the proposed generalised notch filter successfully suppresses any narrow-band actuator current with a frequency at any of the first three harmonics. This behaviour matches the analytical results described in chapter 6. The same behaviour is seen for the remaining configurations.

When considering the micro-vibration measurements taken by the multi-component dynamometer, as shown in figures 7.12 and 7.13 for the waterfall plots of configuration 3 and 4, and in figure 7.14 for the worst-case plots of configurations 3 and 4, it can be seen that some

(a) DYN Waterfal F_x Plot w/o Notch (Conf. 3)

(b) DYN Waterfal F_x Plot w/ Notch (Conf. 3)

(c) DYN Waterfal F_z Plot w/o Notch (Conf. 3)

(d) DYN Waterfal F_z Plot w/ Notch (Conf. 3)

Figure 7.12 – Waterfall plots of multi-component dynamometer (DYN) micro-vibration measurements with and without the proposed generalised notch filter for configuration 3 (optimised machine with spokeless reaction wheel rotor).

residual harmonic forces are still present in some cases.

On the one hand, for axial forces, the filtering of the axial position controller currents shown in the current-to-force measurements results also in a complete suppression of the generated axial vibrations measured by the dynamometer, as shown in figures 7.12.c and 7.12.d.

On the other hand, for radial forces and torques, the filtering of radial position controller currents is not translated into a complete suppression of radial vibrations, as it can be seen in figures 7.12.a and 7.12.b, for example. Whereas all unbalance forces and higher harmonic disturbances are completely removed, a residual first harmonic of constant amplitude can now be seen.

The effect of the proposed generalised notch filter is quantitatively summarised in table 7.6, where the maximum amplitude of the first, second and third harmonic forces and torques measured by the multi-component dynamometer for $|\Omega| > \Omega_{th}$ and all studied configurations is shown. It can be seen that the proposed harmonic force suppression control technique

(a) DYN Waterfal F_x Plot w/o Notch (Conf. 4)

(b) DYN Waterfal F_x Plot w/ Notch (Conf. 4)

(c) DYN Waterfal F_z Plot w/o Notch (Conf. 4)

(d) DYN Waterfal F_z Plot w/ Notch (Conf. 4)
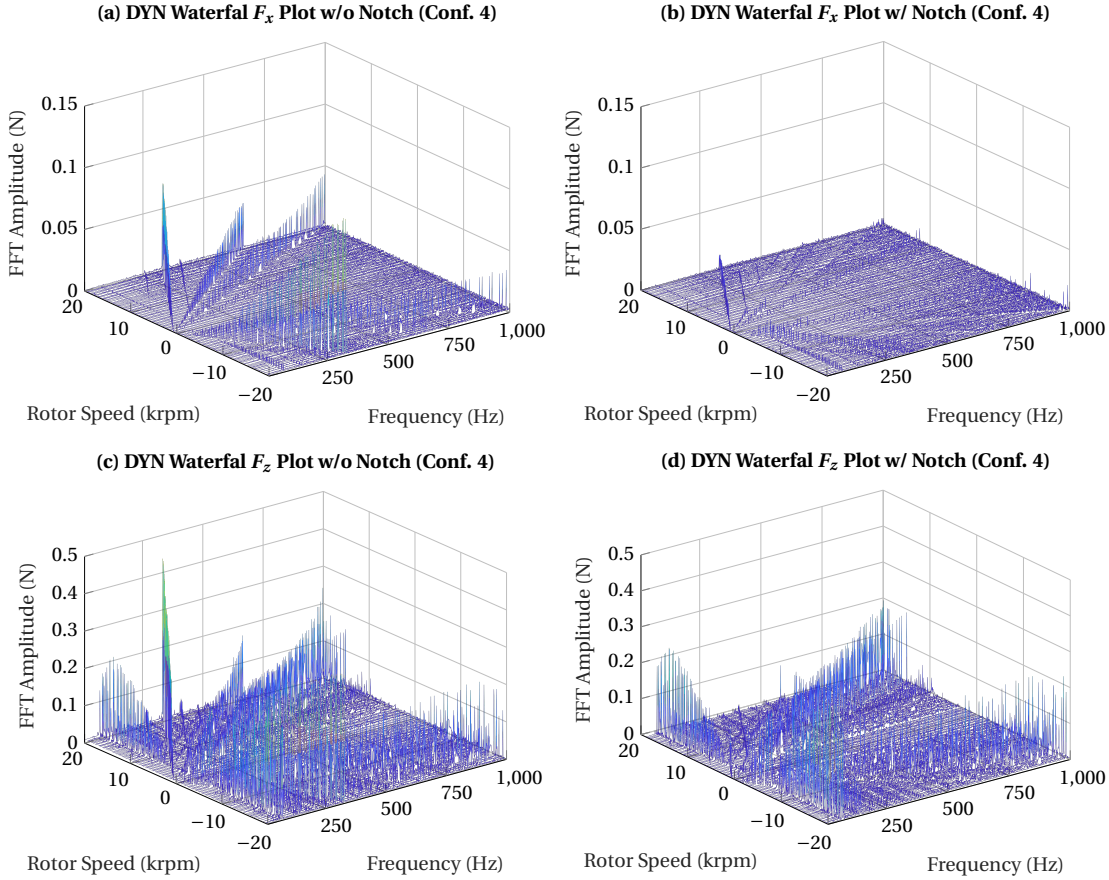
Figure 7.13 – Waterfall plots of multi-component dynamometer (DYN) micro-vibration measurements with and without the proposed generalised notch filter for configuration 4 (optimised machine with spoked reaction wheel rotor).

successfully reduces considerably the magnitude of the exported forces and torques, generally achieving at least one order of magnitude reduction.

For every studied configuration, the current-to-force measurements at standstill $\Omega = 0\,\mathrm{rpm}$ or very low speeds show that the first harmonic currents do not feature zero amplitude, but a small ripple is present, as shown in figure 7.11 at 0 Hz. A rotating system under unbalance forces, a quadratic dependency with speed is expected, as described in chapter 3, and thus showing a disturbance with amplitude proportional to Ω^2. This ripple amplitude at $\approx 0\,\mathrm{rpm}$ measured by the current-to-force method corresponds to the first harmonic disturbance measured by the dynamometer when the notch filter is enabled.

This implies that the closed-loop position controller is actively compensating an angle-dependent passive disturbance in the system, such as a shaft bow or an angle-dependent bearing force constant κ_F. When the notch filter is enabled, this compensation is suppressed due to its appearance at a frequency equal to the rotation speed. It can be seen though, that the amplitude of such disturbance varies with the considered configuration, and thus, the
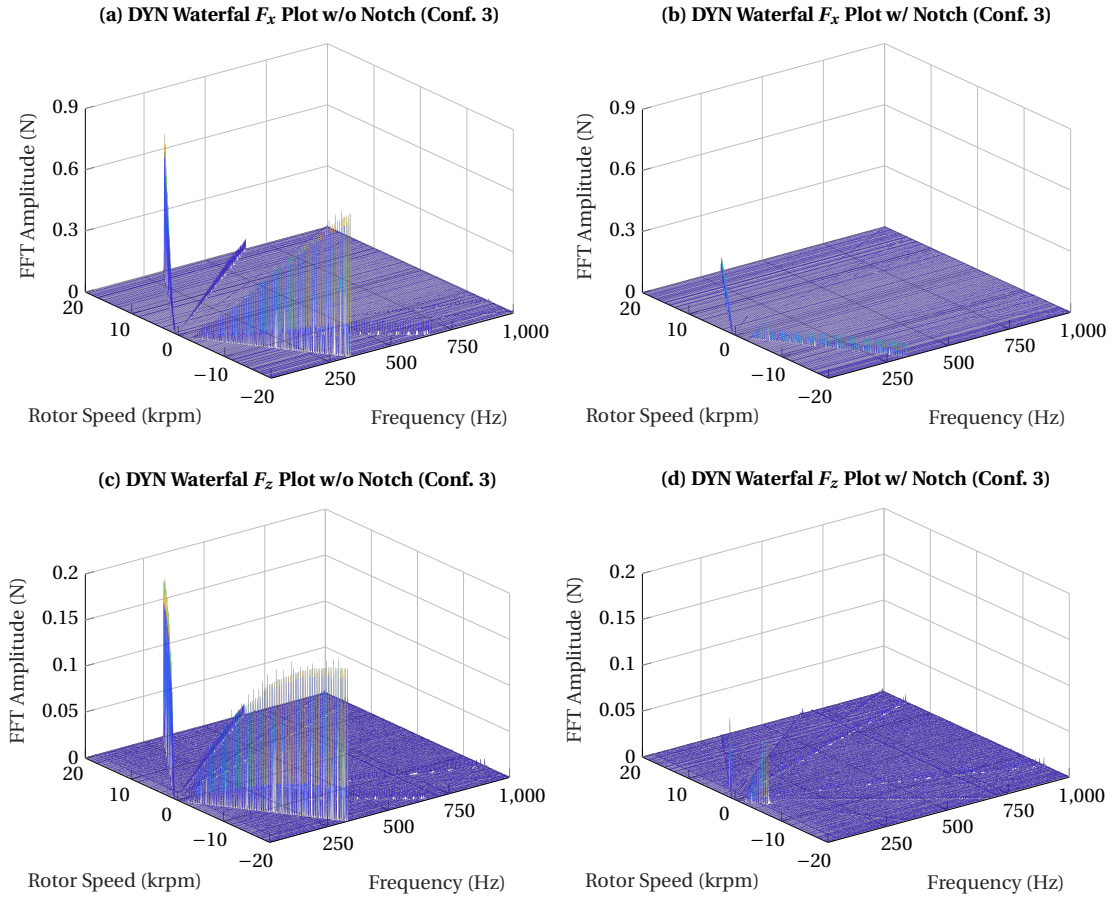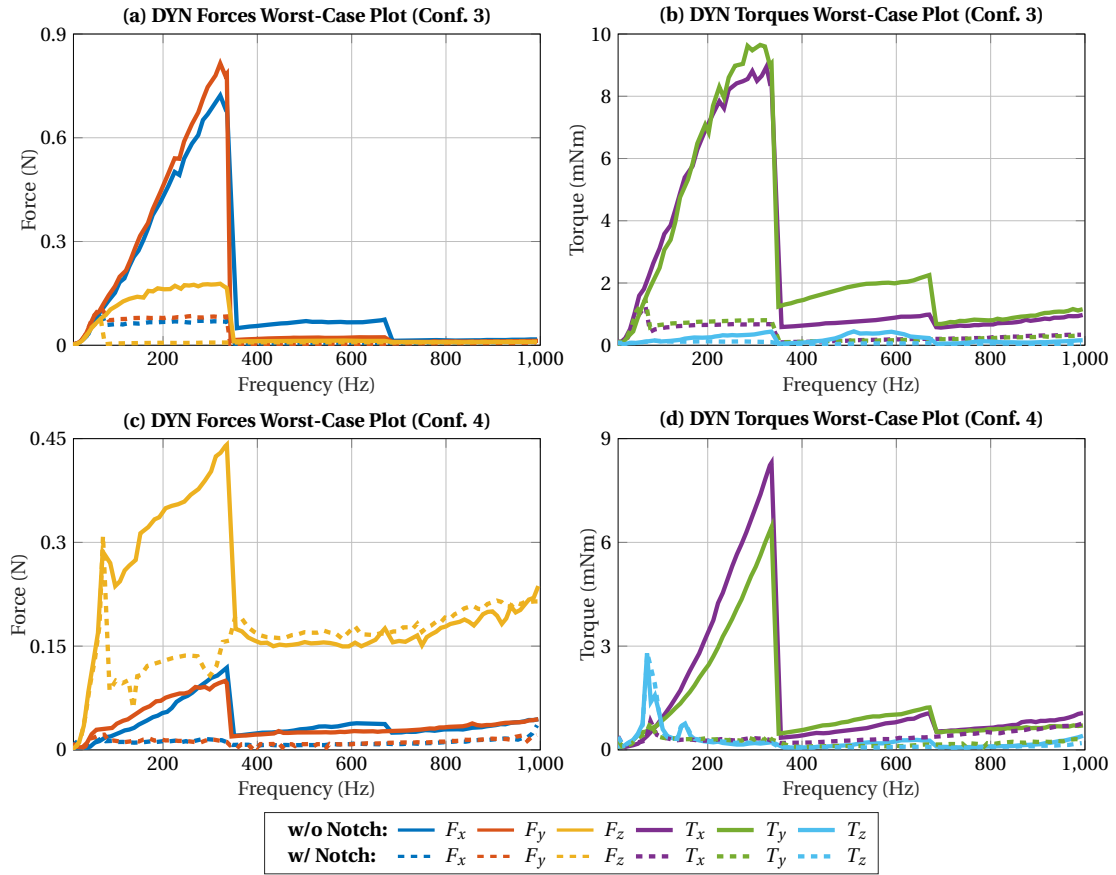
Figure 7.14 – Multi-component dynamometer (DYN) micro-vibration measurements with and without the proposed generalised notch filter for configurations 3 and 4 (optimised machine with spokeless and spoked reaction wheel rotors).

effect of the stator and rotor on these residual vibrations is investigated hereafter.

It is worth highlighting the impact of the employed axial displacement sensor on the level of exported vibrations. For configurations 1-3 that use the eddy-current position sensor, the level of disturbances is considerably low, and they can be easily suppressed by the proposed generalised notch filter, as shown in figures 7.12.d and 7.14.a. For configurations 4-5 that employ the hall-effect position sensor, not only the general magnitude of disturbances is higher, but there are also many more components, e.g. up to four harmonics, parallels to these harmonics or even constant-frequency disturbances, which reduces the impact of the proposed notch filter for reducing the maximum vibrations. Even though the first and second harmonics are successfully suppressed, many other disturbances still remain.

This situation could be improved by simply adding a conductive flat surface, e.g. an additional metallic disk-shaped sheet over the rotor spokes, to preserve the high inertia-to-mass ratio of the rotor, while enabling the possibility of employing the eddy-current axial position sensor.

Table 7.6 – Maximum amplitude of each harmonic of micro-vibrations measured by multi-component dynamometer (DYN) for all studied configurations with and without generalised notch filter. The definition of the configurations is available in section 7.1.

System	Harm.	Notch	F_x (N)	F_y (N)	F_z (N)	T_x (mNm)	T_y (mNm)	T_z (mNm)
Conf. 1	1	w/o	0.2969	0.2254	0.0709	2.8744	3.3561	0.4757
	1	w/	0.0745	0.0778	0.0044	0.9510	1.0094	0.4439
	2	w/o	0.0490	0.0501	0.0324	1.9282	1.9786	0.4802
	2	w/	0.0086	0.0073	0.0068	0.2475	0.3028	0.1702
	3	w/o	0.0576	0.0370	0.0236	1.1053	2.4119	1.1771
	3	w/	0.0076	0.0041	0.0071	0.1046	0.2258	0.0893
Conf. 2	1	w/o	0.3868	0.3697	0.0244	4.7255	4.2299	0.5556
	1	w/	0.0717	0.0771	0.0024	1.0038	1.2018	0.3324
	2	w/o	0.0927	0.0541	0.0262	1.8083	2.3167	0.6045
	2	w/	0.0022	0.0052	0.0077	0.0754	0.0759	0.0643
	3	w/o	0.0934	0.0481	0.0706	1.3350	5.3547	1.4910
	3	w/	0.0038	0.0081	0.0074	0.1554	0.1720	0.0930
Conf. 3	1	w/o	0.7223	0.8150	0.1779	8.9477	9.6489	0.4386
	1	w/	0.0708	0.0846	0.0021	0.6832	0.8052	0.1413
	2	w/o	0.0742	0.0235	0.0136	0.9848	2.2534	0.4456
	2	w/	0.0019	0.0033	0.0087	0.1017	0.0469	0.0722
	3	w/o	0.0134	0.0130	0.0058	0.9796	1.1779	0.1767
	3	w/	0.0068	0.0050	0.0045	0.0646	0.1325	0.0537
Conf. 4	1	w/o	0.1188	0.0998	0.4412	8.3018	6.4377	1.5764
	1	w/	0.0159	0.0163	0.0500	0.4820	0.5139	1.9068
	2	w/o	0.0385	0.0188	0.1756	1.0616	1.2248	0.2957
	2	w/	0.0036	0.0061	0.1592	0.3608	0.1324	0.3348
	3	w/o	0.0453	0.0457	0.2438	1.0969	0.7611	0.4566
	3	w/	0.0577	0.0379	0.2139	0.6256	0.3089	0.4289
Conf. 5	1	w/o	0.0939	0.0806	0.1384	6.4006	5.1149	1.3028
	1	w/	0.0311	0.0347	0.0534	0.8801	0.8729	1.0838
	2	w/o	0.0376	0.0587	0.2263	1.0509	0.7837	0.3064
	2	w/	0.0040	0.0063	0.1589	0.1434	0.1893	0.1021
	3	w/o	0.0362	0.0599	0.2716	1.4445	0.6323	0.2604
	3	w/	0.0346	0.0253	0.2896	0.6992	0.2361	0.2371

Effect of Stator

Unfortunately, due to the limited efficiency of the original machine, it is not possible to perform all possible stator comparisons. Only the first spokeless reaction wheel rotor can be fully tested with both stators, being configurations 1 and 2 for the original and optimised machines, respectively.

As a linear-quadratic-gaussian (LQG) position controller is used, it is not possible to use the exact same controller parameters, as there are different bearing force constants for both stators. Furthermore, the thermal limits of the original stator forces the selection of a less stiff controller, resulting in lower unbalance forces, as it can be seen in table 7.6 for the magnitude of the first harmonic without notch for configurations 1 and 2.

It can be seen that the use of a more symmetric windings in configuration 2 considerably reduces the axial disturbances resulting from cross-couplings between radial and axial bearings. This effect has been clearly identified by comparing the homopolar radial bearing forces of the original machine with skewed windings in figure 7.7.a with the ones of the optimised machine with rhombic windings in figure 7.7.b.

When comparing the residual radial disturbances with the notch enabled between configurations 1 and 2, no noticeable difference can be seen, implying that the main source of such disturbances is not the possible asymmetries of windings or negative stiffness of the machine. Due to the addition of back iron on the homopolar side in the optimised machine, the negative stiffness is considerably increased, but this is not translated into an increase of residual first harmonic disturbances.

Preliminary comparisons between both stators with the remaining rotors show the equivalent results, implying that the stator does not influence significantly the residual first harmonic disturbances.

Effect of Rotor

Focusing now on the influence of the rotors on the generated vibrations, many more comparisons can be performed. Using the optimised machine for all comparisons, it is possible to study all four available rotors, corresponding to configurations 2 to 5.

The first obvious difference in all comparisons, as shown in figures 7.12 and 7.13 and table 7.6, is the unbalance vibrations when no harmonic force suppression is enabled due to different rotor unbalance. For conventional ball bearing motors this magnitude is the main factor that defines the level of generated vibrations. As proven here, the use of magnetic bearings enables the possibility of suppressing this component by means of a generalised notch filter.

When the proposed harmonic suppression technique is enabled, as shown in table 7.6, the use of different rotors shows a noticeable effect on the residual first harmonic disturbance. The main possible causes of such behaviour are a possible shaft bow, which would generate a first harmonic disturbance of constant amplitude, as described in [108] and chapter 3, or an asymmetric magnetisation of the permanent magnets, which would generate an angle-dependent variation of the bearing force constant κ_F.

Due to the imposed geometric tolerances on the rotor by design, manufactured from a single titanium block, the shaft bow is deemed unlikely to be the cause of these vibrations. The

harmonic vibrations caused by shaft bow are a combined actuation of a physical curvature of the rotor shaft and stiffness of the bearings. To create a force of such magnitude, the shaft bow would have to be of considerable magnitude due to the very low magnetic stiffness characteristic of slotless machines. Furthermore, previously mentioned, no considerable influence is seen on the residual first harmonic when employing a different stator with different stiffness.

A preliminary study of the permanent magnet magnetisation has been undertaken, making use of an external three-axis hall probe and centring system, showing an important deviation from the ideal magnetisation, specially for the axially-magnetised permanent magnets of the homopolar side. Whereas a more in depth analysis needs to be performed to fully characterise such behaviour, knowing that a possible source of disturbances is the magnetisation of the employed permanent magnets, to overcome this limitation for the most demanding applications, a more strict manufacturing and magnetisation process could be imposed, or if a magnet characterisation test bench is available, a selection of the most symmetric magnets on a given batch could be performed.

In any case, all the performed modifications in the system, such as the use of more efficient and symmetric winding types or the implementation of a multi-harmonic vibration suppression technique, significantly reduce the magnitude of the generated forces and torques by the system, achieving an improvement of one order of magnitude for the majority of cases.

7.6   Conclusions

In this chapter, the experimental validation of the models, optimisations and control techniques presented in the previous chapters is performed.

The main contributions presented in this chapter can be summarised as follows:

- The experimental validation of the proposed current-to-force micro-vibration measurement method presented in chapter 3 has been performed.

- The electromechanical models of slotless active magnetic bearings and motors, presented in chapter 4 have been experimentally validated.

- The optimisation of the fully active magnetic bearing system described in chapter 5 has been experimentally analysed by measuring the key efficiency and force symmetry figures of merit of the resulting machine.

- The effect of the generalised notch filter proposed in chapter 6 has been experimentally quantified, showing a significant reduction in the magnitude of the generated vibrations.

8 Conclusions

8.1 Summary

Throughout the development of the present thesis, a study of the main aspects of magnetic bearing systems for space applications has been performed. The availability of very-low disturbance and intelligent actuators are a strategic goal identified by the European Space Agency (ESA) to enable the development of novel high-precision platforms for future high-performance scientific and Earth observation missions. Magnetic bearings (MB) are identified as a key technology to achieve these goals in actuators such as reactions wheels (RWs) employed for attitude and orbit control systems (AOCS) for satellites. The contact-less and friction-less operation of magnetically levitated rotors results in a virtually infinite lifetime, with no maintenance required and no need of lubrication. Moreover, the absence of contact also reduces the emitted micro-vibrations during rotation by the suppression of most bearing-related disturbances, and if intelligent control techniques are employed, also the main speed-dependent vibrations, such as unbalance forces.

A compact ultra-high-speed magnetic bearing and motor topology has been proposed and developed by the Swiss Federal Institute of Technology in Zurich (ETHZ) and Celeroton AG, with promising capabilities for space applications. The topology of this actuator is a dual hetero/homopolar, slotless, self-bearing and permanent-magnet synchronous motor (PMSM). The fully active, Lorentz-type magnetic bearing consists of a heteropolar self-bearing motor that applies motor torque and radial forces on one side of the rotor's axis, and a homopolar machine that exerts axial and radial forces, allowing the active control of all rotor's six degrees of freedom. This machine is the basis in which the work of this thesis is based on, focusing on the analysis of the key aspects for space applications, such as micro-vibrations, machine efficiency and system complexity.

As a result of the complexity of magnetic bearing systems, and specially of active magnetic bearings (AMB), which require sensing, actuation and computational power to stabilise the otherwise unstable dynamic system consisting of a rotor levitated by electromagnetic forces, multiple factors simultaneously interfere and influence the system under levitation. These

factors can be as diverse as sensor noise, high-frequency disturbances due to pulse-width modulation (PWM), permanent magnet (PM) magnetisation imperfections and asymmetries, inhomogeneous back iron material, manufacturing imperfections and asymmetries in windings, rotor unbalance, computation delays, or fixed-point rounding errors, among many others.

Through modelling and measurement of the studied fully active magnetic bearing system, some of these factors and disturbances can be analytically or experimentally quantified. In order to be able to account for such a wide variety of disturbances and assess its possible impact on the rotor behaviour and generated vibrations, a modular closed-loop simulation model for magnetic bearing systems is developed. Depending on the specific analysis or needs, different level of abstraction and simplification is possible for the different elements of the closed-loop systems, such as position and current control, bearing, motor, sensor and rotordynamic models. For instance, such a model can be employed for controller design in its most simplified form, with all linear and ideal elements, or for stability and performance assessment of different implemented controllers or unbalance force rejection techniques before its implementation on the real system, facilitating and boosting development phases.

Whereas the micro-vibration characterisation is regularly performed in space applications to guarantee that the actuator's noise signature does not compromise the mission's objectives and payload performance, it usually requires an extensive measurement campaign using costly state-of-the-art equipment, consisting of a multi-component dynamometric platform. Due to the limited availability of such equipment, this characterisation is generally performed in late stages of development, which could be greatly penalising for complex systems such as magnetic bearing actuators, which could profit from early identification and corrections to minimise development risks. For such systems, and specially for fully active magnetic bearings, where all bearing forces are known due to the active control of all rotor's degrees of freedom, it exists the possibility of extracting the mechanical vibrations of the actuator during operation by measuring the actuator's currents.

Even though this proposed micro-vibration measurement technique, named current-to-force (C2F) method, would not substitute the conventional characterisation using a dynamometer (DYN), it enables the possibility of measuring the systems vibrations from early development stages without any external equipment, as only internal current measurements are required, which are usually already available for control purposes. This current-to-force micro-vibration measurement technique is presented, implemented and validated by comparison with a conventional multi-component dynamometer, showing great accuracy to be employed as reference measurements to quantify the impact of any design or control modification in the magnitude of the generated vibrations. Furthermore, it allows the possibility of monitoring the behaviour of the system during operation and if necessary adapt certain control parameters for optimal performance.

As common in rotating machinery, the main source of vibrations is the residual unbalance

of the rotor, which generates a synchronous rotating vibration with magnitude proportional to the square of the rotor speed. Due to the physical contact between rotor and stator in conventional motors, the magnitude of the generated vibrations is directly linked to the rotor unbalance and thus any improvement can only be achieved through better rotor balancing. In magnetic bearings, this limitation no longer exists as a result of the magnetic levitation of the rotor, which allows the free rotation of the rotor about its main axis of inertia, preventing any reaction to the rotor unbalance. The techniques to achieve this are commonly known as unbalance force rejection control (UFRC) which rely on the injection and removal of synchronous harmonic signals into the control loop. If the residual rotor unbalance is perfectly known, it is possible to directly adapt the reference position of the position controller in order to force the force-free rotation of the rotor. It is not only really difficult but also considerably time consuming to accurately measure the residual unbalance of each tested rotor, and for this reason, the most extended techniques rely on some adaptation of amplitude and phase of the injected harmonic signal.

One of the most extended adaptive unbalance force rejection techniques is known as generalised notch filter due to its structure, similar to a notch filter but with a gain matrix that allows improved stability. Nevertheless, the difficulty in finding stable values for this gain matrix or phase shift generally requires the implementation of a gain-scheduled technique to achieve a stable closed-loop over broader speed ranges. To overcome these limitations, a new generalised notch filter, originally proposed for piezoelectric active bearings, which does not require any parameter adaptation to guarantee stability, is successfully implemented and tested in the studied fully active magnetic bearing system. These improved stability properties greatly simplify the implementation of multi-harmonic force rejection control to suppress not only unbalance forces but also higher harmonic disturbances. The stability of such configurations is studied for magnetic bearing systems and its implementation results in a reduction in generated vibrations of at least one order of magnitude.

Having considerably reduced the magnitude of the micro-vibrations during operation, other crucial aspect to consider in magnetic bearings for space applications is the machine efficiency, due to the maximum power consumption limitations from the satellite. For conventional motors the maximum power consumption is defined by the maximum torque at maximum speed that the actuator is capable of providing, but for magnetic bearing systems, also the power consumption of the bearings during levitation needs to be accounted for. Whereas the machine power consumption for levitation in orbit is negligible due to the micro-gravity conditions, the magnetic bearings need to counteract any external effort, such as the gyroscopic forces appearing on the rotor during satellite manoeuvre. Furthermore, the magnetic bearing need to have sufficient load capacity to levitate and operate the rotor on-ground to be able to perform the required qualification tests, at least in some constraint conditions.

All these conditions define the constraints and requirements imposed on the magnetic bearing and motor design and dimensioning. For this reason, it is desired to achieve a maximisation of the machine efficiency by minimising the machine losses during operation. For fully active

magnetic bearing motors, the formulation of such an optimisation problem requires finding a global optimum between the different actuators that usually share resources, greatly complicating the manual selection of the multiple variables for all magnetic bearings and motor. A global optimisation technique for magnetic bearing systems is proposed and successfully employed to maximise the efficiency of the studied machine. This optimisation procedure seeks the maximisation of the weighted sum of all the considered actuator's bearing and motor constants, defined as the ratio between the applied force or torque and the Joule losses in the windings. The advantage of employing such a definition of efficiency is its general applicability, being independent on the load cases and working conditions, and the possibility of deriving it analytically from the electromagnetic models of each actuator.

For slotless machines, the winding type greatly limits the maximum efficiency that the machine can achieve, and thus it is of crucial interest to perform a careful analysis for its selection. The original studied machine featured skewed winding types for all radial and motor actuators, which showed limited efficiency due to the fact that its geometry is fully determined by the overall winding dimensions, being the axial component of the wire, the one that determines the effective force and torque, defined by the winding's pole pairs and axial length. Furthermore, the micro-vibration analysis of the studied fully active magnetic bearing reveals that the residual vibrations remaining after suppression of the unbalance forces are mainly a result of magnetic bearing disturbances, including permanent magnet and winding asymmetries and manufacturing imperfections. As a result of the higher symmetry and additional degrees of freedom in the winding geometry, rhombic and hexagonal slotless winding types are identified as the most promising options for both increasing machine efficiency and improving both force and torque symmetry, and thus reducing bearing-dependent disturbances.

In order to accurately choose the winding properties through the optimisation, it is necessary to develop a electromagnetic models of all actuator types, including different permanent magnet arrangements, with and without back iron, and different winding types. These models need to be computationally light in order to be able to employ them in the developed optimisation. For this reason, the proposed models for slotless magnetic bearings and motors are based on the analytical evaluation of the magnetic flux density distribution, required for the Lorentz force calculation, using elliptic integrals, for which efficient algorithms exist. This formulation allows the evaluation of the three-dimensional flux in the machine airgap, achieving greater accuracy than common two-dimensional approximations and being capable of estimating some force and torque disturbances and asymmetries.

In parallel to the model definition, a manufacturing process to produce such types of windings in-house is developed, enabling the possibility to physically manufacture and test such windings in the studied machine. The resulting optimisation of the studied fully active machine, including the limitations in the newly-developed manufacturing process, yields considerable machine efficiency increases, ranging from 25 % to 45 % depending on the actuator when measuring the bearing and motor constants, and resulting in average power consumption reductions from 30 % to 60 % during operation. These results could be further improved if

some of the manufacturing limitations are overcome, such as the maximum opening angle of the rhombus and hexagon that defines the maximum flux linkage that the winding can capture, which could result in additional 10 % to 20 % efficiency increase, as analytically estimated by the available models.

Although the achieved performance and efficiency results proven throughout the thesis, in some applications, the necessity of actively controlling all rotor degrees of freedom, and its associated actuator, sensing and computational power, may result in a system complexity and cost that will not make such a configuration attractive. An alternative is to consider the passive stabilisation of some degrees of freedom which would result in a much simpler actuator that could retain a significant part of its performance and even increase its efficiency. For these reasons, in space applications, hybrid magnetic bearing (HMB) systems, that combine both active (AMB) and passive (PMB) magnetic bearings, are the most extended configuration. Therefore, a HMB configuration is proposed, which guarantees the high performance and low vibrations due to the actively-controlled radial degrees of freedom, keeping a configuration equivalent to the heteropolar side of the studied machine, while passively stabilising the axial displacements and radial tilting by means of a single arrangement of permanent magnets in the rotor rim. Such a configuration would result in a much compact actuator, with reduced axial length, allowing higher inertia-to-mass ratio for space applications.

The design of such a hybrid system is performed employing the available magnetic flux density distribution models based on elliptic integrals to estimate the passive stiffness properties. Moreover, the viability and performance of the hybrid magnetic bearing actuator is analysed and proved employing the modular closed-loop magnetic bearing simulation model, showing very promising stability and performance results, encouraging the further development of such a system.

As detailed before, in the present thesis a comprehensive study of some of the key aspects of magnetic bearing systems for space application is performed, such as vibrations, efficiency and system complexity. The obtained results highlight the great possibilities that magnetic bearing systems can create for space applications, making very-low disturbance and high-performance actuators.

Finally, it is worth highlighting that even though the studied modelling and modifications are mainly focused on the studied dual hetero/homopolar, slotless, self-bearing and PMSM configuration, the proposed electromagnetic and closed-loop models, optimisation procedure, current-to-force micro-vibration measurement technique and multi-harmonic force rejection control can be employed in most magnetic bearing configurations. More precisely, the electromagnetic models can be employed for any slotless magnetic bearing or motor, whereas the remaining contributions are broadly applicable to any rotating machine featuring magnetic bearings.

8.2 Outlook

Having analysed the identified key aspects of magnetic bearings for space applications, some open points should be investigated to further strengthen the research and results obtained throughout the present thesis. These open points can be summarised as follows:

- *Fully active magnetic bearing system scaling.* The analysis and modifications undertaken in this thesis have been performed maintaining the same machine overall dimensions in order to have a fair comparison with the original machine and directly quantify their impact. Nevertheless, some high-performance missions where magnetic bearings would be of most interest would require a reaction wheel of bigger size, and thus the scaling of such system is currently being investigated.

- *Analysis of residual vibrations.* Whereas the use of high-symmetric winding types and the proposed multi-harmonic force rejection control is proven successful in considerably reducing the emitted micro-vibrations, by at least one order of magnitude, some residual vibrations are identified. It is identified that the permanent magnet imperfections greatly affect the magnitude of these remaining vibrations, and a detailed investigation is on-going.

- *Experimental testing of hybrid magnetic bearing system.* Due to the successful simulation validation of the proposed hybrid magnetic bearing system, a detailed design and manufacturing of such a configuration needs to be performed to experimentally analyse its behaviour and make its development progress.

As mentioned in [15], an on-going collaboration between the German space equipment manufacturer Astro- und Feinwerktechnik Adlershof GmbH (AFW), the Swiss high-speed drive manufacturer Celeroton AG (CEL), and the Swiss Center for Electronics and Microtechnology (CSEM), targets the design of a magnetic bearing reaction wheel that can profit from the results presented in this dissertation and address the main open points mentioned before.

A Elliptic Integrals

The complete elliptic integrals of the first, $K(m)$, second, $E(m)$, and third kind, $\Pi(n, m)$ employed for the definition of the magnetic flux density distribution generated by permanent magnets are

$$K(m) = \int_0^{\pi/2} \frac{1}{\sqrt{1 - m\sin^2 t}} \, \mathrm{d}t, \tag{A.1a}$$

$$E(m) = \int_0^{\pi/2} \sqrt{1 - m\sin^2 t} \, \mathrm{d}t, \tag{A.1b}$$

$$\Pi(n, m) = \int_0^{\pi/2} \frac{1}{(1 - n\sin^2 t)\sqrt{1 - m\sin^2 t}} \, \mathrm{d}t. \tag{A.1c}$$

Furthermore, the derivatives of the elliptic integrals with respect to their parameters m and n are defined as follows

$$\frac{\partial K}{\partial m}(m) = \frac{1}{2m} \left[\frac{1}{1 - m} E(m) - K(m) \right], \tag{A.2a}$$

$$\frac{\partial E}{\partial m}(m) = \frac{1}{2m} \left[E(m) - K(m) \right], \tag{A.2b}$$

$$\frac{\partial \Pi}{\partial n}(n, m) = \frac{1}{2n(n-1)} \left[\frac{n}{m-n} E(m) + K(m) + \frac{n^2 - m}{m - n} \Pi(n, m) \right], \tag{A.2c}$$

$$\frac{\partial \Pi}{\partial m}(n, m) = \frac{1}{2(n-m)} \left[\frac{1}{m-1} E(m) + \Pi(n, m) \right]. \tag{A.2d}$$

For the evaluation of the elliptic integrals, the MATLAB toolbox *EIFun18* presented in [127] is employed, which allows a much faster evaluation of the functions than MATLAB's own implementation, specially when employing matrix arguments, as required for numerically integrating the magnetic flux density expressions for evaluating force and torque in the magnetic bearings.

B Slotless Windings Parametrisations

In order to complete the description of the current density distribution and Lorentz force for slotless skewed, rhombic, hexagonal and axial windings, as generally described in chapter 4, the unitary directing vector $\boldsymbol{e}_v$, infinitesimal winding volume $\mathrm{d}V$, area $A_\perp$ and phase wire length L_{ph} and the volume integration limits V need to be defined.

To summarise, having the definition of the winding parametrisation vector for skewed $\boldsymbol{v}^{sk}(\rho, \phi, \alpha)$, rhombic $\boldsymbol{v}^{rh}(\rho, \phi, \alpha)$, hexagonal $\boldsymbol{v}^{hx}(\rho, \phi, \alpha)$ and axial $\boldsymbol{v}^{ax}(\rho, \phi, \alpha)$ windings as performed in chapter 4, the integration limits $\rho \in [\rho_i, \rho_o]$, $\phi \in [\phi_i, \phi_o]$ and $\alpha \in [\alpha_i, \alpha_o]$ to cover the whole winding volume, the unitary directing vector $\boldsymbol{e}_v$, the infinitesimal winding volume $\mathrm{d}V$, the area $A_\perp$ and phase wire length L_{ph} can be calculated using the following general expressions

$$V = [\rho_i, \rho_o] \times [\phi_i, \phi_o] \times [\alpha_i, \alpha_o], \tag{B.1a}$$

$$\boldsymbol{e}_v = \frac{\boldsymbol{v}'(\rho, \phi, \alpha)}{\left\| \boldsymbol{v}'(\rho, \phi, \alpha) \right\|} = \frac{\frac{\partial \boldsymbol{v}}{\partial \phi}}{\left\| \frac{\partial \boldsymbol{v}}{\partial \phi} \right\|}, \tag{B.1b}$$

$$\mathrm{d}V = \left| \frac{\partial(v_x, v_y, v_z)}{\partial(\rho, \phi, \alpha)} \right| \mathrm{d}\rho \mathrm{d}\phi \mathrm{d}\alpha = \left| (\rho \, \mathrm{d}\boldsymbol{\alpha} \times \mathrm{d}\boldsymbol{\rho}) \cdot \frac{\partial \boldsymbol{v}}{\partial \phi} \, \mathrm{d}\phi \right|, \tag{B.1c}$$

$$A_\perp = \frac{1}{2} \int_{\rho_i}^{\rho_o} \int_{\alpha_i}^{\alpha_o} \frac{\mathrm{d}V}{\left\| \frac{\partial \boldsymbol{v}}{\partial \phi} \right\| \mathrm{d}\phi}, \tag{B.1d}$$

$$L_{ph} = \frac{N}{\rho_o - \rho_i} \int_{\rho_i}^{\rho_o} \int_{\phi_i}^{\phi_o} \left\| \frac{\partial \boldsymbol{v}}{\partial \phi} \right\| \mathrm{d}\phi \mathrm{d}\rho, \tag{B.1e}$$

where the factor $1/2$ in $A_\perp$ is included to consider that two overlapping wires need to share a given volume, and the average winding loop length for the winding thickness $\rho \in [\rho_i, \rho_o]$ is employed to calculate the phase wire length L_{ph}.

Furthermore, the resulting integral for calculating the generated Lorentz force $\boldsymbol{F}_L$ and torque $\boldsymbol{T}_L$ by each winding type is also defined hereafter.

B.1 Skewed Windings

The integration limits $\rho \in \left[\rho_i^{sk}, \rho_o^{sk} \right]$, $\phi \in \left[\phi_i^{sk}, \phi_o^{sk} \right]$ and $\alpha \in \left[\alpha_i^{sk}, \alpha_o^{sk} \right]$, the unitary directing vector $\boldsymbol{e}_v^{sk}$, the infinitesimal winding volume dV^{sk}, the area $A_\perp^{sk}$ and phase wire length L_{ph}^{sk} for a skewed winding as defined in (4.17) results in

$$
\begin{aligned}
V_{n,h}^{sk} &= \left[\rho_i^{sk}, \rho_o^{sk} \right] \times \left[\phi_i^{sk}, \phi_o^{sk} \right] \times \left[\alpha_i^{sk}, \alpha_o^{sk} \right] = \left[R_{wi} + \frac{R_{wo} - R_{wi}}{m_w/n}, R_{wi} + \frac{R_{wo} - R_{wi}}{m_w/(n+1)} \right] \\
&\quad \times \left[0, \frac{2\pi}{p_w} \right] \times \left[\frac{2\pi n}{m_w p_w} + \frac{2h\pi}{p_w} - \frac{\pi}{m_w p_w}, \frac{2\pi n}{m_w p_w} + \frac{2h\pi}{p_w} + \frac{\pi}{m_w p_w} \right],
\end{aligned}
\tag{B.2a}
$$

$$
\boldsymbol{e}_v^{sk} = \frac{1}{\sqrt{\rho^2 + \left(\frac{p_w L_w}{\pi} \right)^2}} \begin{bmatrix} -\rho \sin(\phi + \alpha) \\ \rho \cos(\phi + \alpha) \\ \pm \frac{p_w L_w}{\pi} \end{bmatrix},
\tag{B.2b}
$$

$$
dV^{sk} = \frac{p_w L_w}{\pi} d\phi \rho \, d\alpha \, d\rho,
\tag{B.2c}
$$

$$
A_\perp^{sk} = \frac{L_w}{m_w} \left(\sqrt{\left(\rho_o^{sk} \right)^2 + \left(\frac{p_w L_w}{\pi} \right)^2} - \sqrt{\left(\rho_i^{sk} \right)^2 + \left(\frac{p_w L_w}{\pi} \right)^2} \right),
\tag{B.2d}
$$

$$
\begin{aligned}
L_{ph}^{sk} &= \frac{N\pi}{R_{no} - R_{ni}} \left[\rho_o^{sk} \sqrt{\left(\rho_o^{sk} \right)^2 + \left(\frac{p_w L_w}{\pi} \right)^2} + \frac{p_w^2 L_w^2}{\pi^2} \log \left(\rho_o^{sk} + \sqrt{\left(\rho_o^{sk} \right)^2 + \left(\frac{p_w L_w}{\pi} \right)^2} \right) \right. \\
&\quad \left. - \rho_i^{sk} \sqrt{\left(\rho_i^{sk} \right)^2 + \left(\frac{p_w L_w}{\pi} \right)^2} - \frac{p_w^2 L_w^2}{\pi^2} \log \left(\rho_i^{sk} + \sqrt{\left(\rho_i^{sk} \right)^2 + \left(\frac{p_w L_w}{\pi} \right)^2} \right) \right],
\end{aligned}
\tag{B.2e}
$$

where it has been considered, due to the manufacturing process, that each phase is in an independent layer in radial direction, and thus occupying each one third of the thickness.

Considering each winding phase, $n \in \{0, \ldots, m_w - 1\}$, and pole, $h \in \{0, \ldots, p_w - 1\}$, volume $V_{n,h}^{sk}$ and summing up for all of them, the total Lorentz force and torque can be expressed by substituting all previous expressions into (4.1a) and (4.1b) resulting in the form

$$
\boldsymbol{F}_L^{sk} = \frac{1}{2} \sum_{n=0}^{m_w-1} \sum_{h=0}^{p_w-1} \iiint_{V_{n,h}^{sk}} \frac{J^{sk}}{\sqrt{\frac{1}{\rho^2} + \frac{\pi^2}{p_w^2 L_w^2}}} \begin{bmatrix} -\rho \sin(\phi + \alpha) \\ \rho \cos(\phi + \alpha) \\ \pm \frac{p_w L_w}{\pi} \end{bmatrix} \times \boldsymbol{B}(\rho, \phi, \alpha) \, d\phi \, d\alpha \, d\rho,
\tag{B.3a}
$$

$$
\boldsymbol{T}_L^{sk} = \frac{1}{2} \sum_{n=0}^{m_w-1} \sum_{h=0}^{p_w-1} \iiint_{V_{n,h}^{sk}} \frac{J^{sk}}{\sqrt{\frac{1}{\rho^2} + \frac{\pi^2}{p_w^2 L_w^2}}} \boldsymbol{v}^{sk}(\rho, \phi, \alpha) \times \begin{bmatrix} -\rho \sin(\phi + \alpha) \\ \rho \cos(\phi + \alpha) \\ \pm \frac{p_w L_w}{\pi} \end{bmatrix} \times \boldsymbol{B}(\rho, \phi, \alpha) \, d\phi \, d\alpha \, d\rho,
\tag{B.3b}
$$

being $\boldsymbol{B}(\rho, \phi, \alpha) = \boldsymbol{B}(\boldsymbol{v}^{rh}(\rho, \phi, \alpha))$, the flux $\boldsymbol{B}$ evaluated at each position identified by the winding parametrisation $\boldsymbol{v}^{sk}$, and the current density magnitude J^{sk} as generally defined in (4.16). The choice of sign in $\boldsymbol{e}_v$ will depend on the value of ϕ as per (4.18).

B.2 Rhombic Windings

The integration limits $\rho \in [\rho_i^{rh}, \rho_o^{rh}]$, $\phi \in [\phi_i^{rh}, \phi_o^{rh}]$ and $\alpha \in [\alpha_i^{rh}, \alpha_o^{rh}]$, the unitary directing vector $\boldsymbol{e}_v^{rh}$, the infinitesimal winding volume dV^{rh}, the area $A_\perp^{rh}$ and phase wire length L_{ph}^{rh} for a skewed winding as defined in (4.19) results in

$$V_{n,h}^{rh} = \left[\rho_i^{rh}, \rho_o^{rh}\right] \times \left[\phi_i^{rh}, \phi_o^{rh}\right] \times \left[\alpha_i^{rh}, \alpha_o^{rh}\right] = [R_{wi}, R_{wo}] \times [0, 2\phi_s]$$
$$\times \left[\frac{2\pi n}{m_w} + \frac{h\pi}{p_w} - \frac{\pi/2}{m_w p_w}, \frac{2\pi n}{m_w} + \frac{h\pi}{p_w} + \frac{\pi/2}{m_w p_w}\right], \tag{B.4a}$$

$$\boldsymbol{e}_v^{rh} = \frac{1}{\sqrt{\rho^2 + \left(\frac{L_w}{\phi_s}\right)^2}} \begin{bmatrix} \mp\rho\sin(v_\varphi^{rh}(\phi,\alpha)) \\ \pm\rho\cos(v_\varphi^{rh}(\phi,\alpha)) \\ \pm\frac{L_w}{\phi_s} \end{bmatrix}, \tag{B.4b}$$

$$dV^{rh} = \frac{L_w}{\phi_s} d\phi \rho d\alpha d\rho, \tag{B.4c}$$

$$A_\perp^{rh} = \frac{\pi L_w}{2\phi_s p_w m_w}\left(\sqrt{R_{wo}^2 + \left(\frac{L_w}{\phi_s}\right)^2} - \sqrt{R_{wi}^2 + \left(\frac{L_w}{\phi_s}\right)^2}\right), \tag{B.4d}$$

$$L_{ph}^{rh} = \frac{2p_w N\phi_s}{R_{wo} - R_{wi}}\left[R_{wo}\sqrt{R_{wo}^2 + \left(\frac{L_w}{\phi_s}\right)^2} + \frac{L_w^2}{\phi_s^2}\log\left(R_{wo} + \sqrt{R_{wo}^2 + \left(\frac{L_w}{\phi_s}\right)^2}\right)\right.$$
$$\left. - R_{wi}\sqrt{R_{wi}^2 + \left(\frac{L_w}{\phi_s}\right)^2} - \frac{L_w^2}{\phi_s^2}\log\left(R_{wi} + \sqrt{R_{wi}^2 + \left(\frac{L_w}{\phi_s}\right)^2}\right)\right]. \tag{B.4e}$$

Substituting in this case all previous expressions into (4.1a) and (4.1b), integrating over each phase and pole winding volume $V_{n,h}^{rh}$ and summing up all their contributions, the total Lorentz force $\boldsymbol{F}_L^{rh}$ and torque $\boldsymbol{T}_L^{rh}$ generated by a rhombic winding is

$$\boldsymbol{F}_L^{rh} = \frac{1}{2}\sum_{n=0}^{m_w-1}\sum_{h=0}^{p_w-1}\iiint_{V_{n,h}^{rh}}\frac{(-1)^h J^{rh}}{\sqrt{\frac{1}{\rho^2} + \frac{\phi_s^2}{L_w^2}}}\begin{bmatrix} \mp\rho\sin(v_\varphi^{rh}(\phi,\alpha)) \\ \pm\rho\cos(v_\varphi^{rh}(\phi,\alpha)) \\ \pm\frac{L_w}{\phi_s} \end{bmatrix} \times \boldsymbol{B}(\rho,\phi,\alpha)\,d\phi\,d\alpha\,d\rho, \tag{B.5a}$$

$$\boldsymbol{T}_L^{rh} = \frac{1}{2}\sum_{n=0}^{m_w-1}\sum_{h=0}^{p_w-1}\iiint_{V_{n,h}^{rh}}\frac{(-1)^h J^{rh}}{\sqrt{\frac{1}{\rho^2} + \frac{\phi_s^2}{L_w^2}}}\boldsymbol{v}^{rh}(\rho,\phi,\alpha) \times \begin{bmatrix} \mp\rho\sin(v_\varphi^{rh}(\phi,\alpha)) \\ \pm\rho\cos(v_\varphi^{rh}(\phi,\alpha)) \\ \pm\frac{L_w}{\phi_s} \end{bmatrix} \times \boldsymbol{B}(\rho,\phi,\alpha)\,d\phi\,d\alpha\,d\rho, \tag{B.5b}$$

being $\boldsymbol{B}(\rho,\phi,\alpha) = \boldsymbol{B}(\boldsymbol{v}^{rh}(\rho,\phi,\alpha))$, and the current density magnitude J^{rh} as generally defined in (4.16). Note the change in polarity in the current for every pole of the winding included in factor $(-1)^h$. Again, the choice of sign in $\boldsymbol{e}_v$ will depend on the value of ϕ as per (4.20a) and (4.20b).

B.3   Hexagonal Windings

The integration limits $\rho \in [\rho_i^{hx}, \rho_o^{hx}]$, $\phi \in [\phi_i^{hx}, \phi_o^{hx}]$ and $\alpha \in [\alpha_i^{hx}, \alpha_o^{hx}]$, the unitary directing vector $\boldsymbol{e}_v^{hx}$, the infinitesimal winding volume $\mathrm{d}V^{hx}$, the area $A_\perp^{hx}$ and phase wire length L_{ph}^{hx} for a hexagonal winding as defined in (4.21) results in

$$
\begin{aligned}
V_{n,h}^{hx} &= \left[\rho_i^{hx}, \rho_o^{hx}\right] \times \left[\phi_i^{hx}, \phi_o^{hx}\right] \times \left[\alpha_i^{hx}, \alpha_o^{hx}\right] \\
&= [R_{wi}, R_{wo}] \times \left[0, 2\phi_s\right] \times \left[\frac{2\pi n}{m_w} + \frac{h\pi}{p_w} - \frac{\pi/2}{m_w p_w}, \frac{2\pi n}{m_w} + \frac{h\pi}{p_w} + \frac{\pi/2}{m_w p_w}\right],
\end{aligned}
\tag{B.6a}
$$

$$
\boldsymbol{e}_{v,\mathscr{D}}^{hx} = \frac{1}{\sqrt{\rho^2 + \frac{(L_w - L_s)^2}{\phi_s^2}}} \begin{bmatrix} \mp\rho \sin(v_\varphi^{hx}(\phi,\alpha)) \\ \pm\rho \cos(v_\varphi^{hx}(\phi,\alpha)) \\ \pm\frac{L_w - L_s}{\phi_s} \end{bmatrix}, \quad \boldsymbol{e}_{v,\mathscr{S}}^{hx} = \begin{bmatrix} 0 \\ 0 \\ \pm 1 \end{bmatrix},
\tag{B.6b}
$$

$$
\mathrm{d}V_{\mathscr{D}}^{hx} = \frac{L_w - L_s}{\phi_s} \mathrm{d}\phi \rho \,\mathrm{d}\alpha \mathrm{d}\rho, \quad \mathrm{d}V_{\mathscr{S}}^{hx} = \mathrm{d}\phi \rho \,\mathrm{d}\alpha \mathrm{d}\rho,
\tag{B.6c}
$$

$$
A_{\perp\mathscr{D}}^{hx} = \frac{\pi(L_w - L_s)}{2\phi_s p_w m_w} \left(\sqrt{R_{wo}^2 + \left(\frac{L_w - L_s}{\phi_s}\right)^2} - \sqrt{R_{wi}^2 + \left(\frac{L_w - L_s}{\phi_s}\right)^2}\right), \quad A_{\perp\mathscr{S}}^{hx} = \frac{\pi\left(R_{wo}^2 - R_{wi}^2\right)}{2m_w p_w},
\tag{B.6d}
$$

$$
\begin{aligned}
L_{ph}^{hx} &= 4 p_w N L_s \\
&+ \frac{2 p_w N \phi_s}{R_{wo} - R_{wi}} \left[R_{wo}\sqrt{R_{wo}^2 + \left(\frac{L_w - L_s}{\phi_s}\right)^2} + \left(\frac{L_w - L_s}{\phi_s}\right)^2 \log\left(R_{wo} + \sqrt{R_{wo}^2 + \left(\frac{L_w - L_s}{\phi_s}\right)^2}\right)\right. \\
&\left. - R_{wi}\sqrt{R_{wi}^2 + \left(\frac{L_w - L_s}{\phi_s}\right)^2} - \left(\frac{L_w - L_s}{\phi_s}\right)^2 \log\left(R_{wi} + \sqrt{R_{wi}^2 + \left(\frac{L_w - L_s}{\phi_s}\right)^2}\right)\right].
\end{aligned}
\tag{B.6e}
$$

To facilitate the calculations for this winding type, it is assumed that the whole winding volume is occupied by wire, resulting in a different current density for the axial and diagonal segments of the hexagon due to a different phase belt area. The normal vector of these surfaces $\boldsymbol{e}_v^{hx}$ is separated in two domains: diagonal, $\mathscr{D}$, and straight (axial), $\mathscr{S}$, segments defined in (4.22a).

In a similar way to the previous windings, the total Lorentz force $\boldsymbol{F}_L^{hx}$ and torque $\boldsymbol{T}^{hx}$ generated by an hexagonal winding can be calculated by

$$
\boldsymbol{F}_L^{hx} = \frac{1}{2} \sum_{n=0}^{m_w-1} \sum_{h=0}^{p_w-1} \iiint_{V_{n,h}^{hx}} (-1)^h J^{rh} \boldsymbol{e}_v^{hx}(\rho,\phi,\alpha) \times \boldsymbol{B}(\rho,\phi,\alpha) \,\mathrm{d}V^{hx},
\tag{B.7a}
$$

$$
\boldsymbol{T}_L^{hx} = \frac{1}{2} \sum_{n=0}^{m_w-1} \sum_{h=0}^{p_w-1} \iiint_{V_{n,h}^{hx}} (-1)^h J^{hx} \boldsymbol{v}^{hx}(\rho,\phi,\alpha) \times \boldsymbol{e}_v^{hx}(\rho,\phi,\alpha) \times \boldsymbol{B}(\rho,\phi,\alpha) \,\mathrm{d}V^{hx}.
\tag{B.7b}
$$

In this case J^{hx}, $\boldsymbol{e}_v^{hx}$ and $\mathrm{d}V^{hx}$ change not only in sign but also in magnitude, as defined in (B.6d), (B.6b) and (B.6c), respectively, depending on the value of ϕ as per (4.22a) and (4.22b).

B.4 Axial Windings

The integration limits $\rho \in \left[\rho_i^{ax}, \rho_o^{ax}\right]$, $\phi \in \left[\phi_i^{ax}, \phi_o^{ax}\right]$ and $\alpha \in \left[\alpha_i^{ax}, \alpha_o^{ax}\right]$, the unitary directing vector $\boldsymbol{e}_v^{ax}$, the infinitesimal winding volume $\mathrm{d}V^{ax}$, the area $A_\perp^{ax}$ and phase wire length L_{ph}^{ax} for a skewed winding as defined in (4.23) results in

$$V^{ax} = \left[\rho_i^{ax}, \rho_o^{ax}\right] \times \left[\phi_i^{ax}, \phi_o^{ax}\right] \times \left[\alpha_i^{ax}, \alpha_o^{ax}\right] = [R_{wi}, R_{wo}] \times [0, 2\pi] \times \left[-\frac{L_w}{2}, \frac{L_w}{2}\right], \quad \text{(B.8a)}$$

$$\boldsymbol{e}_v^{ax} = \begin{bmatrix} -\sin(\phi) \\ \cos(\phi) \\ 0 \end{bmatrix}, \tag{B.8b}$$

$$\mathrm{d}V^{ax} = \mathrm{d}\phi \rho \mathrm{d}\alpha \mathrm{d}\rho, \tag{B.8c}$$

$$A_\perp^{ax} = L_w(R_{wo} - R_{wi}), \tag{B.8d}$$

$$L_{ph}^{ax} = \frac{2\pi N(R_{wo}^2 - R_{wi}^2)}{R_{wo} - R_{wi}}. \tag{B.8e}$$

The total Lorentz force and torque generated by an axial winding is calculated as follows

$$\boldsymbol{F}_L^{ax} = 2 \iiint_{V^{ax}} J^{ax} \rho \begin{bmatrix} -\sin(\phi) \\ \cos(\phi) \\ 0 \end{bmatrix} \times \boldsymbol{B}(\rho, \phi, \alpha) \, \mathrm{d}\phi \, \mathrm{d}\alpha \, \mathrm{d}\rho, \tag{B.9}$$

where the factor 2 is considered to include the force and torque generated by both ring coils that compose the axial winding.

C Geometric Transformations for Passive Stiffness Calculation

In order to calculate the attraction or repulsive force and torque between a pair of permanent magnets as a function of a given relative displacement, it is necessary to define the geometric transformations that converts the magnetic flux density distribution generated by one permanent magnet expressed under the other's reference frame. This transformation allows the evaluation of the volume integral integral defined in expressions (4.31a) and (4.31b).

For all the considered geometric transformations, four different reference frames are defined: two inertial (fixed) frames centred at stator and bearing centre, $S\{C', X', Y', Z'\}$ and $S\{O', x', y', z'\}$, respectively, and two non-inertial reference frames linked to the rotor centre of gravity and bearing, $S\{C, X, Y, Z\}$ and $S\{O, x, y, z\}$, respectively. In the following expressions only the lower pair of PM rings will be shown, but equivalent transformations can be performed for the bearing's upper pair of rings.

C.1 Axial Displacement

The position in Cartesian coordinates of any point P, defined by the cylindrical coordinates (r, φ, z), of the integration volume V (rotor's permanent magnet), subject to an axial displacement Δz, as shown in figure C.1, with respect to the stator-linked bearing reference frame $S\{O', x', y', z'\}$, can be simply expressed by

$$P(\Delta z) = \begin{bmatrix} r'_p \cos\varphi'_p \\ r'_p \sin\varphi'_p \\ z'_p \end{bmatrix} = \begin{bmatrix} r_p \cos\varphi_p \\ r_p \sin\varphi_p \\ z_p + \Delta z \end{bmatrix} \implies \begin{cases} r' = r, \\ \varphi' = \varphi, \\ z' = z + \Delta z. \end{cases} \tag{C.1}$$

When considering this axial displacement, the purely axial magnetisation vector $\boldsymbol{M}_{rot} = [0, 0, -M_z]^\top$ of the rotor permanent magnet ring remains unchanged and thus the projection of the external field over the magnetisation direction B_M and its gradient in Cartesian coordinates
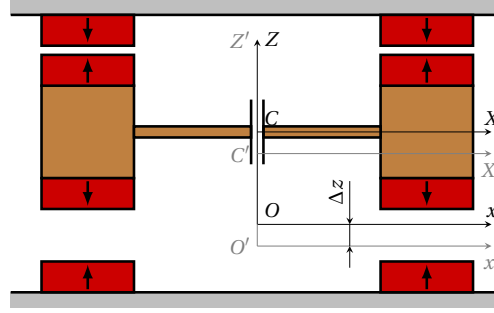
Figure C.1 – Schematic cross-section of axial displacement with reference frame definition.

can be simply computed by

$$B_M(r, \varphi, z) = \boldsymbol{M}_{rot} \cdot \boldsymbol{B}_{st} = \begin{bmatrix} 0 \\ 0 \\ -M_z \end{bmatrix} \cdot \begin{bmatrix} B_r(r', z') \cos\varphi' \\ B_r(r', z') \sin\varphi' \\ B_z(r', z') \end{bmatrix} = -M_z B_z(r', z'), \tag{C.2a}$$

$$\nabla B_M(r, \varphi, z) = \begin{bmatrix} \frac{\partial B_M}{\partial r'}(r', \varphi', z') \cos\varphi' - \frac{1}{r'} \frac{\partial B_M}{\partial \varphi'}(r', \varphi', z') \sin\varphi' \\ \frac{\partial B_M}{\partial r'}(r', \varphi', z') \sin\varphi' + \frac{1}{r'} \frac{\partial B_M}{\partial \varphi'}(r', \varphi', z') \cos\varphi' \\ \frac{\partial B_M}{\partial z'}(r', \varphi', z') \end{bmatrix} = -M_z \begin{bmatrix} \frac{\partial B_z}{\partial r'}(r', z') \cos\varphi' \\ \frac{\partial B_z}{\partial r'}(r', z') \sin\varphi' \\ \frac{\partial B_z}{\partial z'}(r', z') \end{bmatrix},$$
$$\tag{C.2b}$$

with r', z' as defined in expression (C.1), the partial derivatives as in (4.30a), (4.30b), (4.30c), and (4.30d), being then the force at an infinitesimal permanent magnet volume $\mathrm{d}V$

$$\mathrm{d}\boldsymbol{F}(\Delta z) = \nabla (\boldsymbol{M}_{rot} \cdot \boldsymbol{B}_{st}) \, \mathrm{d}V = \begin{bmatrix} \mathrm{d}F_{x'} \\ \mathrm{d}F_{y'} \\ \mathrm{d}F_{z'} \end{bmatrix} = -M_z \begin{bmatrix} \frac{\partial B_z}{\partial r'}(r', z') \cos\varphi' \\ \frac{\partial B_z}{\partial r'}(r', z') \sin\varphi' \\ \frac{\partial B_z}{\partial z'}(r', z') \end{bmatrix} \mathrm{d}V. \tag{C.3}$$

The total force $\boldsymbol{F}$ applied to the rotor magnets subject to a given axial displacement Δz is calculated by substituting expression (C.3) into (4.31a). Note that due to the symmetry of the problem, only axial force will be present after the integration, and no torque is generated in this case.

C.2 Radial Displacement

In the case of experiencing a radial displacement Δx, as shown in figure C.2a, the position in Cartesian coordinates of any point P, of the rotor's PM ring, with respect to the stator PM reference frame $S\{O', x', y', z'\}$, can be expressed by performing the transformation graphically
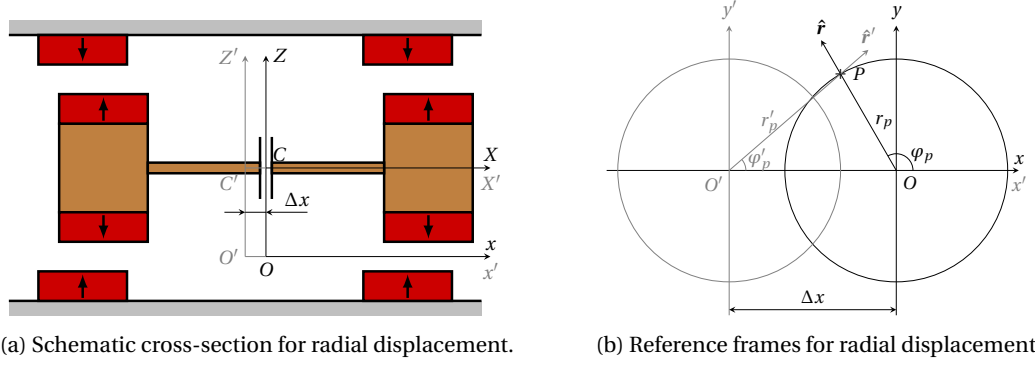
(a) Schematic cross-section for radial displacement.

(b) Reference frames for radial displacement.

Figure C.2 – Geometric transformation for radial displacement.

shown in figure C.2b as

$$
P(\Delta x) = \begin{bmatrix} r_p' \cos\varphi_p' \\ r_p' \sin\varphi_p' \\ z_p' \end{bmatrix} = \begin{bmatrix} r_p \cos\varphi_p + \Delta x \\ r_p \sin\varphi_p \\ z_p \end{bmatrix} \implies \begin{cases} r' = \sqrt{r^2 + \Delta x^2 + 2r\Delta x \cos\varphi}, \\ \varphi' = \operatorname{atan}\left(\frac{r\sin\varphi}{r\cos\varphi + \Delta x}\right), \\ z' = z. \end{cases} \tag{C.4}
$$

When considering this radial displacement Δx, the magnetisation vector $\boldsymbol{M}_{rot} = [0,0,-M_z]^\top$ of the rotor permanent magnet ring remains unchanged and thus the projection of the external field and its gradient can be simply computed by

$$
B_M(r,\varphi,z) = \boldsymbol{M}_{rot} \cdot \boldsymbol{B}_{st} = \begin{bmatrix} 0 \\ 0 \\ -M_z \end{bmatrix} \cdot \begin{bmatrix} B_r(r',z')\cos\varphi' \\ B_r(r',z')\sin\varphi' \\ B_z(r',z') \end{bmatrix} = -M_z B_z(r',z'), \tag{C.5a}
$$

$$
\nabla B_M(r,\varphi,z) = \begin{bmatrix} \frac{\partial B_M}{\partial r'}(r',\varphi',z')\cos\varphi' - \frac{1}{r'}\frac{\partial B_M}{\partial \varphi'}(r',\varphi',z')\sin\varphi' \\ \frac{\partial B_M}{\partial r'}(r',\varphi',z')\sin\varphi' + \frac{1}{r'}\frac{\partial B_M}{\partial \varphi'}(r',\varphi',z')\cos\varphi' \\ \frac{\partial B_M}{\partial z'}(r',\varphi',z') \end{bmatrix} = -M_z \begin{bmatrix} \frac{\partial B_z}{\partial r'}(r',z')\cos\varphi' \\ \frac{\partial B_z}{\partial r'}(r',z')\sin\varphi' \\ \frac{\partial B_z}{\partial z'}(r',z') \end{bmatrix}
$$
$$
\tag{C.5b}
$$

with r',φ',z' as defined in expression (C.4), the partial derivatives as in (4.30a), (4.30b), (4.30c), and (4.30d), and the force at an infinitesimal permanent magnet volume $\mathrm{d}V$

$$
\mathrm{d}\boldsymbol{F}(\Delta x) = \nabla\left(\boldsymbol{M}_{rot} \cdot \boldsymbol{B}_{st}\right)\mathrm{d}V = \begin{bmatrix} \mathrm{d}F_{x'} \\ \mathrm{d}F_{y'} \\ \mathrm{d}F_{z'} \end{bmatrix} = -M_z \begin{bmatrix} \frac{\partial B_z}{\partial r'}(r',z')\cos\varphi' \\ \frac{\partial B_z}{\partial r'}(r',z')\sin\varphi' \\ \frac{\partial B_z}{\partial z'}(r',z') \end{bmatrix} \mathrm{d}V. \tag{C.6}
$$

As before, the total force $\boldsymbol{F}$ applied to the rotor magnets subject to a given axial displacement Δz is calculated by substituting expression (C.6) into (4.31a). Due to the radial displacement towards x direction, only force in x direction and no torque will be present.
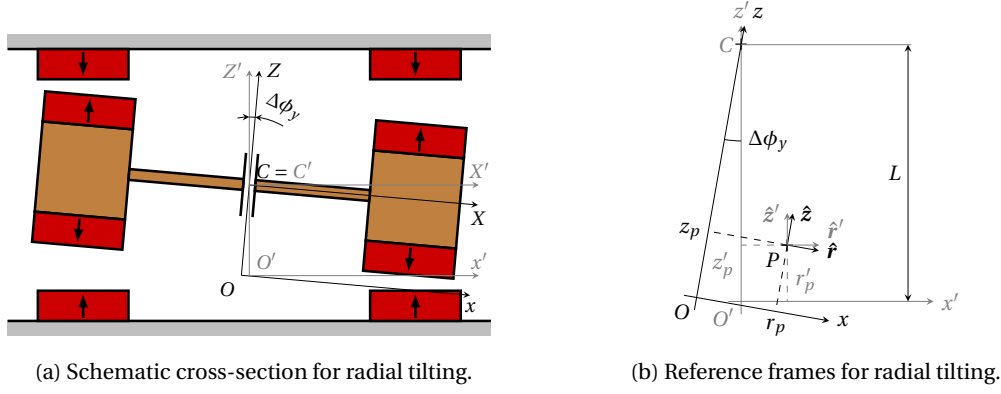
153

(a) Schematic cross-section for radial tilting.

(b) Reference frames for radial tilting.

Figure C.3 – Geometric transformation for radial tilting.

C.3   Radial Tilting

In the case of experiencing a tilt $\Delta\phi_y$, as shown in figure C.3a for a rotation about Y'-axis, another geometric transformation is also required. This tilting is not defined at the bearing centre (point O), but at the rotor centre of gravity (point C). Thus, by considering a rotation about axis Y passing by the rotor centre C, the position in Cartesian coordinates of any point P of the rotor's permanent magnet, with respect to the stator-linked bearing reference frame $S\{O', x', y', z'\}$, can be expressed performing the transformation shown in figure C.3b as follows

$$
P(\Delta\phi_y) = \begin{bmatrix} r_p' \cos\varphi_p' \\ r_p' \sin\varphi_p' \\ z_p' \end{bmatrix} = \begin{bmatrix} \cos\phi_y & 0 & \sin\phi_y \\ 0 & 1 & 1 \\ -\sin\phi_y & 0 & \cos\phi_y \end{bmatrix} \begin{bmatrix} r_p \cos\varphi_p \\ r_p \sin\varphi_p \\ z_p - L \end{bmatrix} + \begin{bmatrix} 0 \\ 0 \\ L \end{bmatrix} =
$$
$$
= \begin{bmatrix} r_p \cos\varphi_p \cos\Delta\phi_y + (z_p - L)\sin\Delta\phi_y \\ r_p \sin\varphi_p \\ L - r_p \cos\varphi_p \sin\Delta\phi_y + (z_p - L)\cos\Delta\phi_y \end{bmatrix},
$$

(C.7)

resulting in the following transformation $(r, \varphi, z) \mapsto (r', \varphi', z')$

$$
P(\Delta\phi_y) \implies \begin{cases} r' = \sqrt{(r\cos\varphi\cos\Delta\phi_y + (z-L)\sin\Delta\phi_y)^2 + (r\sin\varphi)^2}, \\ \varphi' = \operatorname{atan}\left(\frac{r\sin\varphi}{r\cos\varphi\cos\Delta\phi_y + (z-L)\sin\Delta\phi_y}\right), \\ z' = L - r\sin\varphi\sin\Delta\phi_y + (z-L)\cos\Delta\phi_y. \end{cases}
$$

(C.8)

In this case, the magnetisation vector $\boldsymbol{M}_{rot} = [0, 0, -M_z]^\top$ of the rotor permanent magnet ring is rotated by $\Delta\phi_y$ about Y, and thus the projection of the external field and its gradient can be

computed as follows

$$B_M(r,\varphi,z) = \boldsymbol{M}_{rot} \cdot \boldsymbol{B}_{st} = \begin{bmatrix} \cos\Delta\phi_y & 0 & \sin\Delta\phi_y \\ 0 & 1 & 1 \\ -\sin\Delta\phi_y & 0 & \cos\Delta\phi_y \end{bmatrix} \begin{bmatrix} 0 \\ 0 \\ -M_z \end{bmatrix} \cdot \begin{bmatrix} B_r(r',z')\cos\varphi' \\ B_r(r',z')\sin\varphi' \\ B_z(r',z') \end{bmatrix} =$$

$$= -M_z(\sin\Delta\phi_y B_r(r',z')\cos\varphi' + \cos\Delta\phi_y B_z(r',z')), \tag{C.9a}$$

$$\nabla B_M(r,\varphi,z) = \begin{bmatrix} \frac{\partial B_M}{\partial r'}(r',\varphi',z')\cos\varphi' - \frac{1}{r'}\frac{\partial B_M}{\partial \varphi'}(r',\varphi',z')\sin\varphi' \\ \frac{\partial B_M}{\partial r'}(r',\varphi',z')\sin\varphi' + \frac{1}{r'}\frac{\partial B_M}{\partial \varphi'}(r',\varphi',z')\cos\varphi' \\ \frac{\partial B_M}{\partial z'}(r',\varphi',z') \end{bmatrix} =$$

$$= -M_z \begin{bmatrix} \cos\varphi'\left(\sin\Delta\phi_y\frac{\partial B_r(r',z')}{\partial r'}\cos\varphi' + \cos\Delta\phi_y\frac{\partial B_z(r',z')}{\partial r'}\right) + \frac{B_r(r',z')\sin^2\varphi'}{r'}\sin\Delta\phi_y \\ \sin\varphi'\left(\sin\Delta\phi_y\frac{\partial B_r(r',z')}{\partial r'}\cos\varphi' + \cos\Delta\phi_y\frac{\partial B_z(r',z')}{\partial r'}\right) - \frac{B_r(r',z')\sin 2\varphi'}{2r'}\sin\Delta\phi_y \\ \sin\Delta\phi_y\frac{\partial B_r(r',z')}{\partial z'}\cos\varphi' + \cos\Delta\phi_y\frac{\partial B_z(r',z')}{\partial z'} \end{bmatrix},$$

$$\tag{C.9b}$$

with r', φ', z' as defined in expression (C.8), the partial derivatives as in (4.30a), (4.30b), (4.30c), and (4.30d), resulting in the force and torque at an infinitesimal permanent magnet volume dV

$$d\boldsymbol{F}(\Delta\phi_y) = \begin{bmatrix} dF_{x'} \\ dF_{y'} \\ dF_{z'} \end{bmatrix} = \nabla(\boldsymbol{M}_{rot} \cdot \boldsymbol{B}_{st})\,dV =$$

$$= -M_z \begin{bmatrix} \cos\varphi'\left(\sin\Delta\phi_y\frac{\partial B_r(r',z')}{\partial r'}\cos\varphi' + \cos\Delta\phi_y\frac{\partial B_z(r',z')}{\partial r'}\right) + \frac{B_r(r',z')\sin^2\varphi'}{r'}\sin\Delta\phi_y \\ \sin\varphi'\left(\sin\Delta\phi_y\frac{\partial B_r(r',z')}{\partial r'}\cos\varphi' + \cos\Delta\phi_y\frac{\partial B_z(r',z')}{\partial r'}\right) - \frac{B_r(r',z')\sin 2\varphi'}{2r'}\sin\Delta\phi_y \\ \sin\Delta\phi_y\frac{\partial B_r(r',z')}{\partial z'}\cos\varphi' + \cos\Delta\phi_y\frac{\partial B_z(r',z')}{\partial z'} \end{bmatrix} dV,$$

$$\tag{C.10a}$$

$$d\boldsymbol{T}(\Delta\phi_y) = \begin{bmatrix} dT_{x'} \\ dT_{y'} \\ dT_{z'} \end{bmatrix} = \boldsymbol{r}' \times d\boldsymbol{F}(\Delta\phi_y) = \begin{bmatrix} r'\cos\varphi' \\ r'\sin\varphi' \\ z'-L \end{bmatrix} \times \begin{bmatrix} dF_{x'} \\ dF_{y'} \\ dF_{z'} \end{bmatrix} = \begin{bmatrix} r'\sin\varphi' dF_{z'} - (z'-L)dF_{y'} \\ -r'\cos\varphi' dF_{z'} + (z'-L)dF_{x'} \\ r'\cos\varphi' dF_{y'} - r'\sin\varphi' dF_{x'} \end{bmatrix}.$$

$$\tag{C.10b}$$

The total force and torque is obtained by substituting expressions (C.10a) and (C.10b) into (4.31a) and (4.31b), respectively. In this case, due to the problem's symmetry, only $dT_{y'}$ will be non zero.

Bibliography

[1]   ESA Earth Observation Portal (eoPortal) Directory, *SPOT-4 - Satellite Missions*. [Online].
Available: https://directory.eoportal.org/web/eoportal/satellite-missions/s/spot-4.

[2]   ——, *SPOT-5 - Satellite Missions*. [Online]. Available: https://directory.eoportal.org/
web/eoportal/satellite-missions/s/spot-5.

[3]   ——, *SWOT (Surface Water Ocean Topography) - Satellite Missions*. [Online]. Available:
https://directory.eoportal.org/web/eoportal/satellite-missions/s/swot.

[4]   ——, *GAIA (Global Astrometric Interferometer for Astrophysics) - Satellite Missions*.
[Online]. Available: https://directory.eoportal.org/web/eoportal/satellite-missions/
content/-/article/gaia-satellite-mission.

[5]   ——, *Euclid: Mapping the geometry of the dark Universe - Satellite Missions*. [Online].
Available: https://directory.eoportal.org/web/eoportal/satellite-missions/e/euclid.

[6]   ——, *JWST (James Webb Space Telescope) - Satellite Missions*. [Online]. Available: https:
//directory.eoportal.org/web/eoportal/satellite-missions/content/-/article/jwst-
content.

[7]   H. Jeffcott, "The lateral vibration of loaded shafts in the neighbourhood of a whirling
speed — The effect of want of balance.", *The London, Edinburgh, and Dublin Philo-
sophical Magazine and Journal of Science*, vol. 37, no. 219, pp. 304–314, Mar. 1919, ISSN:
1941-5982. DOI: 10.1080/14786440308635889.

[8]   "Discussion on "testing steam turbines and steam turbo-generators", New York, De-
cember 9, 1910. (see proceedings for December, 1910)", *Proceedings of the American
Institute of Electrical Engineers*, vol. 30, no. 2, pp. 357–375, Feb. 1911, ISSN: 0097-2444.
DOI: 10.1109/PAIEE.1911.6659755.

[9]   Harisberger, Breed, and Wilkins, "Experience with bearings and vibration conditions
of large hydroelectric units: Waterwheel construction and governing: A study of irregu-
larity of reaction in francis turbines", *Journal of the A.I.E.E.*, vol. 43, no. 3, pp. 261–262,
Mar. 1924, ISSN: 0095-9804. DOI: 10.1109/JAIEE.1924.6534046.

[10]   H. Heimel, "Spacewheel Microvibration: Sources, Appearance, Countermeasures", in
8th International ESA Conference on Guidance, Navigation & Control Systems, Karlovy
Vary, Czech Republic, 2011.

Bibliography

[11] M. P. Le, "Micro-disturbances in reaction wheels", PhD thesis, Eindhoven University of Technology, 2017, p. 166.

[12] O. Matsushita, M. Tanaka, H. Kanki, M. Kobayashi, and P. Keogh, *Vibrations of Rotating Machinery*, ser. Mathematics for Industry. Tokyo: Springer Japan, 2017, vol. 16, ISBN: 978-4-431-55455-4. DOI: 10.1007/978-4-431-55456-1.

[13] ——, *Vibrations of Rotating Machinery - Volume 2. Advanced Rotordynamics: Applications of Analysis, Troubleshooting and Diagnosis*. Tokyo, Japan: Springer Japan, 2019, p. 577, ISBN: 978-4-431-55453-0. DOI: 10.1007/978-4-431-55453-0.

[14] "Mechanical vibration — Rotor balancing — Part 11: Procedures and tolerances for rotors with rigid behaviour", International Organization for Standardization, Geneva, CH, ISO 21940-11:2016 Standard, Nov. 2016.

[15] IPC Technology Harmonisation Advisory Group (IPC-THAG), "European Space Technology Harmonisation, Technology Harmonisation Dossier: AOCS Sensors and Actuators", European Space Agency, ESA/IPC/THAG(2020)3 Technical Note, 2020.

[16] A. Samuel and B. Lechable, "An Overview on AEROSPATIALE Magnetic Bearing Products for Spacecraft Attitude Control and for Industry", in *Spacecraft Guidance, Navigation and Control Systems, Proceedings of the 3rd ESA International Conference*, Noordwijk, the Netherlands, 1996, pp. 217–226.

[17] J. R. Wertz and W. Larson, *Space Mission Analysis and Design*, 3rd. Springer Netherlands, 1999, p. 976, ISBN: 978-0-7923-5901-2.

[18] L. Giulicchi, S.-F. Wu, and T. Fenal, "Attitude and orbit control systems for the LISA Pathfinder mission", *Aerospace Science and Technology*, vol. 24, no. 1, pp. 283–294, Jan. 2013, ISSN: 12709638. DOI: 10.1016/j.ast.2011.12.002.

[19] J. H. Saleh, F. Geng, M. Ku, and M. L. Walker, "Electric propulsion reliability: Statistical analysis of on-orbit anomalies and comparative analysis of electric versus chemical propulsion failure rates", *Acta Astronautica*, vol. 139, pp. 141–156, Oct. 2017, ISSN: 00945765. DOI: 10.1016/j.actaastro.2017.06.034.

[20] V. Lappas, W. Steyn, and C. Underwood, "Attitude control for small satellites using control moment gyros", *Acta Astronautica*, vol. 51, no. 1-9, pp. 101–111, Jul. 2002, ISSN: 00945765. DOI: 10.1016/S0094-5765(02)00089-9.

[21] E. Canuto, C. Novara, L. Massotti, D. Carlucci, and C. Perez Montenegro, *Spacecraft Dynamics and Control: The Embedded Model Control Approach*, 1st ed. Butterworth-Heinemann, 2018, p. 790, ISBN: 9780081007006. DOI: 10.1016/C2016-0-00420-5.

[22] G. Smet, G. Richardson, S. Mclaren, and A. Haslehurst, "Managing Reaction Wheel Microvibration on a High Resolution EO Small Spacecraft", in *15th European Space Mechanisms and Tribology Symposium*, Noordwijk, The Netherlands, 2013.

[23]   V. Preda, J. Cieslak, D. Henry, S. Bennani, and A. Falcoz, "Robust microvibration mitiga-
       tion and pointing performance analysis for high stability spacecraft", *International
       Journal of Robust and Nonlinear Control*, vol. 28, no. 18, pp. 5688–5716, Dec. 2018, ISSN:
       10498923. DOI: 10.1002/rnc.4338.

[24]   M. Buttery, A. Kent, R. Bingley, M. Cropper, and S. Lewis, "Ageing and Environmental
       Effects on Lubricants - A Preliminary Study", in *18th European Space Mechanisms and
       Tribology Symposium*, Munich, Germany, 2019.

[25]   Celeroton AG, *White Paper: 500'000 rpmrotational speeds thanks to magnetic bearings*.
       [Online]. Available: https://www.celeroton.com/fileadmin/user_upload/medien/
       201412_Celeroton_Magnetic_Bearing_EN.pdf.

[26]   G. L. Agrawal, "Foil Air/Gas Bearing Technology — An Overview", in *ASME 1997 In-
       ternational Gas Turbine and Aeroengine Congress and Exhibition, Volume 1: Aircraft
       Engine; Marine; Turbomachinery; Microturbines and Small Turbomachinery*, Orlando,
       Florida, USA: American Society of Mechanical Engineers, Jun. 1997, ISBN: 978-0-7918-
       7868-2. DOI: 10.1115/97-GT-347.

[27]   A. Looser, "Gas bearing with active magnetic damping for ultra-high-speed electrical
       drive systems", PhD thesis, ETH Zurich, 2013.

[28]   B. T. Paulsen, S. Morosi, and I. F. Santos, "Static, Dynamic, and Thermal Properties
       of Compressible Fluid Film Journal Bearings", *Tribology Transactions*, vol. 54, no. 2,
       pp. 282–299, Jan. 2011, ISSN: 1040-2004. DOI: 10.1080/10402004.2010.538490.

[29]   H. Bleuler, "A Survey of Magnetic Levitation and Magnetic Bearing Types.", *JSME
       international journal. Ser. 3, Vibration, control engineering, engineering for industry*,
       vol. 35, no. 3, pp. 335–342, 1992, ISSN: 0914-8825. DOI: 10.1299/jsmec1988.35.335.

[30]   G. Schweitzer and E. H. Maslen, Eds., *Magnetic Bearings: Theory, Design, and Applica-
       tion to Rotating Machinery*. Springer, 2009, ISBN: 978-3-642-00497-1.

[31]   P. A. Studer, "Magnetic Bearings for Spacecraft", NASA, Greenbelt, MD, United States,
       Tech. Rep., 1972, p. 6.

[32]   T. Wilson, "A high-temperature superconductor energy-momentum control system
       for small satellites", *IEEE Transactions on Appiled Superconductivity*, vol. 13, no. 2,
       pp. 2287–2290, Jun. 2003, ISSN: 1051-8223. DOI: 10.1109/TASC.2003.813078.

[33]   J. Tang, J. Fang, and W. Wen, "Superconducting Magnetic Bearings and Active Mag-
       netic Bearings in Attitude Control and Energy Storage Flywheel for Spacecraft", *IEEE
       Transactions on Applied Superconductivity*, vol. 22, no. 6, pp. 5 702 109–5 702 109, Dec.
       2012, ISSN: 1051-8223. DOI: 10.1109/TASC.2012.2218245.

[34]   J. Tang, K. Wang, and B. Xiang, "Stable Control of High-Speed Rotor Suspended by
       Superconducting Magnetic Bearings and Active Magnetic Bearings", *IEEE Transactions
       on Industrial Electronics*, vol. 64, no. 4, pp. 3319–3328, Apr. 2017, ISSN: 0278-0046. DOI:
       10.1109/TIE.2016.2542786.

Bibliography

[35] P. K. Sinha, *Electromagnetic Suspension: Dynamics and Control.* London, UK: IEE Control Engin. Series Nr. 30. Peregrinus Ltd, 1987.

[36] K. Davey, "Electrodynamic Maglev coil design and analysis", *IEEE Transactions on Magnetics*, vol. 33, no. 5, pp. 4227–4229, 1997, ISSN: 00189464. DOI: 10.1109/20.619718.

[37] H. M. Gutierrez and H. Luijten, "5-DOF Real-Time Control of Active Electrodynamic MAGLEV", *IEEE Transactions on Industrial Electronics*, vol. 65, no. 9, pp. 7468–7476, Sep. 2018, ISSN: 0278-0046. DOI: 10.1109/TIE.2018.2795520.

[38] N. Amati, X. De Lépine, and A. Tonoli, "Modeling of Electrodynamic Bearings", *Journal of Vibration and Acoustics*, vol. 130, no. 6, Dec. 2008, ISSN: 1048-9002. DOI: 10.1115/1.2981170.

[39] J. Van Verdeghem, V. Kluyskens, and B. Dehez, "Stability and Performance Analysis of Electrodynamic Thrust Bearings", *Actuators*, vol. 8, no. 1, p. 11, Feb. 2019, ISSN: 2076-0825. DOI: 10.3390/act8010011.

[40] J. L. Nikolajsen, "Experimental Investigation of an Eddy-Current Bearing", in *1st International Symposium on Magnetic Bearings*, Zurich, Switzerland: Springer Berlin Heidelberg, 1988.

[41] T. Hiromi, T. Katou, A. Chiba, M. A. Rahman, and T. Fukao, "A Novel Magnetic Suspension-Force Compensation in Bearingless Induction-Motor Drive With Squirrel-Cage Rotor", *IEEE Transactions on Industry Applications*, vol. 43, no. 1, pp. 66–76, 2007, ISSN: 0093-9994. DOI: 10.1109/TIA.2006.887310.

[42] T. I. Baumgartner, "A Magnetically Levitated 500 000 RPM Electrical Drive System", PhD thesis, ETH Zurich, 2013.

[43] A. Chiba, T. Fukao, O. Ichikawa, M. Oshima, M. Takemoto, and D. G. Dorrell, *Magnetic Bearings and Bearingless Drives.* Elsevier, 2005, p. 400, ISBN: 978-0-7506-5727-3. DOI: 10.1016/B978-0-7506-5727-3.X5000-7.

[44] G. Borque Gallego, L. Rossini, E. Onillon, T. Achtnich, C. Zwyssig, R. Seiler, D. Martins Araujo, and Y. Perriard, "On-line micro-vibration measurement method for Lorentz-type magnetic-bearing space actuators", *Mechatronics*, vol. 64, p. 102 283, Dec. 2019, ISSN: 09574158. DOI: 10.1016/j.mechatronics.2019.102283.

[45] ——, "Magnetic Bearing Reaction Wheel Micro-Vibration Signature Prediction", in *18th European Space Mechanisms and Tribology Symposium*, Munich, Germany, Sep. 2019.

[46] G. Borque Gallego, L. Rossini, T. Achtnich, C. Zwyssig, D. Martins Araujo, and Y. Perriard, "Force Analysis of a Slotless Lorentz-Type Active Magnetic Bearing Actuator", in *2018 21st International Conference on Electrical Machines and Systems (ICEMS)*, IEEE, Oct. 2018, pp. 75–80, ISBN: 978-89-86510-20-1. DOI: 10.23919/ICEMS.2018.8549038.

[47] G. Borque Gallego, L. Rossini, T. Achtnich, D. Martins Araujo, and Y. Perriard, "Three-Dimensional Force and Torque Models of Slotless Magnetic Bearing Machines", *IEEE/ASME Transactions on Mechatronics*, May 2020, under review.

[48] G. Borque Gallego, L. Rossini, T. Achtnich, C. Zwyssig, D. Martins Araujo, and Y. Perriard, "Force and Torque Model of Ironless Passive Magnetic Bearing Structures", in *2019 IEEE International Electric Machines & Drives Conference (IEMDC)*, IEEE, May 2019, pp. 507–514, ISBN: 978-1-5386-9350-6. DOI: 10.1109/IEMDC.2019.8785411.

[49] G. Borque Gallego, L. Rossini, T. Achtnich, D. Martins Araujo, and Y. Perriard, "Efficiency Optimisation and Vibration Reduction in Slotless Magnetic Bearing Machines", *IEEE/ASME Transactions on Industry Applications, Special Issue on Magnetically Levitated Motor Systems*, Nov. 2020, under review.

[50] ——, "Novel Generalised Notch Filter for Harmonic Vibration Suppression in Magnetic Bearing Systems", *IEEE/ASME Transactions on Industry Applications, Special Issue on Magnetically Levitated Motor Systems*, Dec. 2020, under review.

[51] P. A. Studer, "A Practical Magnetic Bearing", in *IEEE Transactions on Magnetics*, Los Angeles, CA, United States, 1977, pp. 1155–1157.

[52] ——, "Magnetic bearings for instruments in the space environment", NASA Goddard Space Flight Center, Greenbelt, MD, United States, Tech. Rep., 1978, p. 18.

[53] C. H. Henrikson, J. Lyman, and P. A. Studer, "Magnetically suspended momentum wheels for spacecraft stabilization", in *12th Aerospace Sciences Meeting*, Washington DC, United States, 1974.

[54] L. J. Veillette, "Design and development of a momentum wheel with magnetic bearings", in *8th Aerospace Mechanisms Symposium*, Hampton, VA, United States, 1973, pp. 131–143.

[55] A. V. Sabnis, G. L. Stocking, and J. B. Dendy, "Magnetically Suspended Reaction Wheels", in *9th Aerospace Mechanisms Symposium*, Cocoa Beach, FL; United States, 1974, pp. 211–234.

[56] G. L. Stocking, J. B. Dendy, and A. V. Sabnis, "Design study for a magnetically supported reaction wheel", Sperry Flight Systems, Phoenix, AZ, United States, Tech. Rep., 1974, p. 88.

[57] C. J. Pentlicki and P. C. Poubeau, "Magnetic Bearing Momentum Wheel", in *6th Communications Satellite Systems Conference*, Montreal, Canada, 1976.

[58] P. C. Poubeau, *Satellite momentum wheel*, 1976.

[59] ——, "Development of a satellite flywheel family operating on one active axis magnetic bearings", in *11th Aerospace Mechanisms Symposium*, Greenbelt, MD, United States, 1977, pp. 185–201.

[60] P. Müler, R. S. Sindlinger, and G. M. Siouris, "One-momentum wheel concepts for 3-axis satellite attitude control hardware experiences and system studies", in *Guidance and Control Conference*, Boston, MA, United States, 1975.

[61] R. S. Sindlinger, "Magnetic Bearing Momentum Wheels with Magnetic Gimballing Capability for 3-Axis Active Attitude Control and Energy Storage", in *11th Aerospace Mechanisms Symposium*, Greenbelt, MD, United States, 1977, pp. 45–55.

[62] M. Gauthier, A. Robinson, and J.-P. Roland, "An Advanced Low-Cost 2-Axis Active Magnetic Bearing", in *3rd European Space Mechanisms and Tribology Symposium*, Madrid, Spain, 1987.

[63] J.-P. Roland, "Magnetic bearing wheels for very high pointing accuracy satellite missions", in *International Symposium on Magnetic Suspension Technology*, Hampton, VA, United States, 1991, pp. 857–872.

[64] C. Bernus, P. Jamain, and J.-P. Roland, *Magnetic bearing with alternating actuators and sensors*, 1998.

[65] D. Chassoulier, *Dual-stage centring magnetic bearing*, 2009.

[66] H. Knörrchen and T. Lange, "Modular design and dynamic tests on active bearing momentum wheels", in *9th IFAC/ESA Symposium on Automatic Control in Space*, Noordwijkerhout, The Netherlands, 1982, pp. 459–468.

[67] U. Bichler and T. Eckardt, "A 3(5) Degree of Freedom Electrodynamic-Bearing Wheel for 3-Axis Spacecraft Attitude Control Applications", in *1st International Symposium on Magnetic Bearings*, Zurich, Switzerland: Springer Berlin Heidelberg, 1988, pp. 13–22. DOI: 10.1007/978-3-642-51724-2_2.

[68] ——, "A Gimbaled Low Noise Momentum Wheel", in *27th Aerospace Mechanisms Symposium*, 1993, pp. 181–196.

[69] B. Gerlach, M. Ehinger, H. Knut Raue, and R. Seiler, "Gimballing Magnetic Bearing Reaction Wheel with Digital Controller", in *11th European Space Mechanisms and Tribology Symposium*, Lucerne, Switzerland, 2005.

[70] B. Gerlach, M. Ehinger, and R. Seiler, "Low Noise Five-Axis Magnetic Bearing Reaction Wheel", in *IFAC Proceedings Volumes, 4th IFAC Symposium on Mechatronic Systems*, vol. 39, 2006, pp. 572–577, ISBN: 9783902661173. DOI: 10.3182/20060912-3-DE-2911.00100.

[71] K. Yabu-Uchi, M. Inoue, S. Akishita, C. Murakami, and O. Okamoto, "A compact magnetic bearing for gimballed momentum wheel", in *17th Aerospace Mechanisms Symposium*, Pasadena, CA; United States, 1983, pp. 333–342.

[72] C. Murakami, Y. Ohkami, O. Okamoto, A. Nakajima, M. Inoue, J. Tsuchiya, K. Yabu-uchi, S. Akishita, and T. Kida, "A new type of magnetic gimballed momentum wheel and its application to attitude control in space", *Acta Astronautica*, vol. 11, no. 9, pp. 613–619, 1984. DOI: 10.1016/0094-5765(84)90036-5.

[73] C. Murakami, A. Nakajima, S. Shingu, and Y. Shimamoto, "A Flat Magnetic Bearing Reaction Wheel", in *14th International Symposium on Space Technology and Science*, Tokyo, Japan, 1984, pp. 647–654.

[74] A. Nakajima, "Research and Development of Magnetic Bearing Flywheels for Attitude Control of Spacecraft", in *1st International Symposium on Magnetic Bearings*, Zurich, Switzerland, 1988, pp. 3–12.

[75] Y. Horiuchi, M. Inoue, and N. Sato, "Development of magnetic bearing momentum wheel for ultra-precision spacecraft attitude control", in *7th International Symposium on Magnetic Bearings*, Zurich, Switzerland, 2000, pp. 525–530.

[76] M. Scharfe, K. Meinzer, and R. Zimmermann, "Development of a Magnetic-Bearing Momentum Wheel for the AMSAT Phase 3-D Small Satellite", in *International Symposium on Small Satellites*, Annecy, France, 1996.

[77] M. Scharfe, T. Roschke, E. Bindl, and D. Blonski, "Design And Development Of A Compact Magnetic Bearing Momentum Wheel For Micro And Small Satellites", in *15th Annual/USU Conference on Small Satellites*, 2001.

[78] M. Scharfe, T. Roschke, E. Bindl, D. Blonski, and R. Seiler, "The challenges of miniaturisation for a magnetic bearing wheel", in *9th European Space Mechanisms and Tribology Symposium*, vol. 480, 2001, pp. 17–24.

[79] M. Scharfe, "Compact Magnetic Bearing Wheel: Study on the development of a Compact Magnetic Bearing Momentum Wheel for the 3-Axis Control of Microsatellites (ESA contract No 14.335/00/NL/PA)", Technical University of Dresden, Dresden, Germany, Tech. Rep., 2007, p. 43.

[80] A. Argondizza, S. Carabelli, G. Genta, and A. Tonoli, "Magnetically levitated reaction wheel for space application", in *5th International Symposium on Magnetic Suspension Technology*, Santa Barbara, CA, United States, 1999.

[81] S. Carabelli, G. Genta, M. Silvagni, and A. Tonoli, "Active Magnetic Suspension for Satellite Inertia Wheels", in *2nd EUSPEN International Conference*, Torino, Italy, 2001.

[82] ——, "Inertia Wheel on Low-Noise Active Magnetic Suspension", in *53rd International Astronautical Congress*, Houston, TX, United States, 2002.

[83] J. Seddon and A. Pechev, "3Dwheel: 3-Axis Low Noise, High-Bandwidth Attitude Actuation from a Single Momentum Wheel Using Magnetic Bearings", in *23rd Annual AIAA/USU Conference on Small Satellites*, Logan, UT, United States, 2009.

[84] J. Seddon, "3Dwheel: Attitude Control of Small Satellites Using Magnetically Levitated Momentum Wheels", PhD thesis, Surrey Space Centre (University of Surrey), 2011, p. 254.

[85] J. Fang, J. Sun, Y. Xu, and X. Wang, "A new structure for permanent-magnet-biased axial hybrid magnetic bearings", in *IEEE Transactions on Magnetics*, vol. 45, 2009, pp. 5319–5325. DOI: 10.1109/TMAG.2009.2024687.

[86] J. Fang, J. Sun, H. Liu, and J. Tang, "A Novel 3-DOF Axial Hybrid Magnetic Bearing", *IEEE Transactions on Magnetics*, vol. 46, no. 12, pp. 4034–4045, 2010, ISSN: 0018-9464. DOI: 10.1109/TMAG.2010.2074206.

[87] J. Sun and J. Fang, "A novel structure of permanent-magnet-biased radial hybrid magnetic bearing", *Journal of Magnetism and Magnetic Materials*, vol. 323, no. 2, pp. 202–208, 2011, ISSN: 03048853. DOI: 10.1016/j.jmmm.2010.08.053.

[88]   J. Sun and D. Chen, "Analysis and experiment of eddy current loss in Homopolar magnetic bearings with laminated rotor cores", *Acta Astronautica*, vol. 89, pp. 229–235, Aug. 2013, ISSN: 00945765. DOI: 10.1016/j.actaastro.2013.04.021.

[89]   J. Tang, J. Sun, J. Fang, and G. S. Sam, "Low eddy loss axial hybrid magnetic bearing with gimballing control ability for momentum flywheel", *Journal of Magnetism and Magnetic Materials*, vol. 329, pp. 153–164, 2013, ISSN: 0304-8853. DOI: http://dx.doi.org/10.1016/j.jmmm.2012.10.006.

[90]   J. Tang, C. Wang, and B. Xiang, "Gimballing Flywheel and its Novel Reluctance Force-type Magnetic Bearing with Low Eddy Loss and Slight Tilting Torque", *Journal of Magnetics*, vol. 18, no. 4, pp. 432–442, Dec. 2013, ISSN: 1226-1750. DOI: 10.4283/JMAG.2013.18.4.432.

[91]   C. Wang and J. Tang, "Design and Mathematical Analysis of a Novel Reluctance Force-Type Hybrid Magnetic Bearing for Flywheel with Gimballing Capability", *Mathematical Problems in Engineering*, vol. 2013, pp. 1–17, 2013. DOI: 10.1155/2013/836058.

[92]   J. Fang, C. Wang, and J. Tang, "Modeling and analysis of a novel conical magnetic bearing for vernier-gimballing magnetically suspended flywheel", *Proceedings of the Institution of Mechanical Engineers, Part C: Journal of Mechanical Engineering Science*, vol. 228, no. 13, pp. 2416–2425, 2014. DOI: 10.1177/0954406213517488.

[93]   J. Tang, B. Xiang, and C. Wang, "Rotor's suspension for vernier-gimballing magnetically suspended flywheel with conical magnetic bearing", *ISA Transactions*, vol. 58, pp. 509–519, 2015, ISSN: 0019-0578. DOI: http://dx.doi.org/10.1016/j.isatra.2015.05.011.

[94]   J. Tang, Z. Peng, B. Liu, and K. Wang, "Control of rotor's vernier-gimballing for a magnetically suspended flywheel", *IEEE Transactions on Industrial Electronics*, vol. 64, no. 4, pp. 2972–2981, Apr. 2017, ISSN: 0278-0046. DOI: 10.1109/TIE.2016.2636213.

[95]   "Small satellite TET-1", Astro- und Feinwerktechnik Adlershof GmbH, Berlin, Germany, Tech. Rep., 2010, p. 22.

[96]   G. Wiedermann, W. Gockel, S. Winkler, J. M. Rieber, B. Kraft, and D. Reggio, "The Sentinel-2 Satellite Attitude Control System - Challenges and Solutions", in *9th International ESA Conference on Guidance, Navigation & Control Systems*, Porto, Portugal, 2014.

[97]   F. Liebold, S. Wiegand, and R. Käso, "Analysis of micro-vibration by high resolution force sensing measurement to reduce mechanical noise", in *63rd International Astronautical Congress, Materials and Structures Symposium*, Naples, Italy, 2012.

[98]   Y. Okada, H. Konishi, H. Kanebako, and C.-W. Lee, "Lorentz Force type Self-Bearing Motor", in *Proceedings of 7th International Symposium on Magnetic Bearings*, Zurich, Switzerland, 2000, pp. 353–358.

[99] B. Dehez, F. Baudart, M. Markovic, and Y. Perriard, "Theoretical and Experimental Investigation of Flex-PCB Air-Gap Windings in Slotless BLDC Machines", *IEEE Transactions on Industry Applications*, vol. 50, no. 5, pp. 3153–3160, Sep. 2014, ISSN: 0093-9994. DOI: 10.1109/TIA.2014.2301862.

[100] B. Dehez, F. Baudart, and Y. Perriard, "Analysis of a new topology of flexible PCB winding for slotless BLDC machines", in *2017 IEEE International Electric Machines and Drives Conference (IEMDC)*, Miami, FL, USA: IEEE, May 2017, pp. 1–8, ISBN: 978-1-5090-4281-4. DOI: 10.1109/IEMDC.2017.8002019.

[101] A. Looser, T. I. Baumgartner, J. W. Kolar, and C. Zwyssig, "Analysis and Measurement of Three-Dimensional Torque and Forces for Slotless Permanent-Magnet Motors", *IEEE Transactions on Industry Applications*, vol. 48, no. 4, pp. 1258–1266, 2012.

[102] T. I. Baumgartner, R. M. Burkart, and J. W. Kolar, "Analysis and Design of a 300-W 500 000-r/min Slotless Self-Bearing Permanent-Magnet Motor", *IEEE Transactions on Industrial Electronics*, vol. 61, no. 8, pp. 4326–4336, 2014.

[103] T. I. Baumgartner and J. W. Kolar, "Multivariable State Feedback Control of a 500 000-r/min Self-Bearing Permanent-Magnet Motor", *IEEE/ASME Transactions on Mechatronics*, vol. 20, no. 3, pp. 1149–1159, 2015.

[104] C. Zwyssig, T. I. Baumgartner, and J. W. Kolar, "High-Speed Magnetically Levitated Reaction Wheel Demonstrator", in *International Power Electronics Conference - ECCE Asia (IPEC 2014)*, Hiroshima, Japan, 2014, pp. 1707–1714.

[105] M. Kaufmann, A. Tüysüz, J. W. Kolar, and C. Zwyssig, "High-Speed Magnetically Levitated Reaction Wheels for Small Satellites", in *23rd International Symposium on Power Electronics, Electrical Drives, Automation and Motion (SPEEDAM 2016)*, Anacapri, Capri, Italy, 2016, pp. 28–33.

[106] C. Zwyssig, "An Ultra-High-Speed Electrical Drive System", PhD thesis, ETH Zurich, 2008.

[107] R. Larsonneur and P. Bühler, "New Radial Sensor for Active Magnetic Bearings", in *9th International Symposium On Magnetic Bearings*, Lexington, KY, USA: University of Kentucky, 2004, pp. 495–499, ISBN: 9781604232943.

[108] G. Genta, *Dynamics of Rotating Systems*, ser. Mechanical Engineering Series. New York, NY: Springer US, 2005, ISBN: 0-387-20936-0.

[109] P.-D. Pfister and Y. Perriard, "Slotless Permanent-Magnet Machines: General Analytical Magnetic Field Calculation", *IEEE Transactions on Magnetics*, vol. 47, no. 6, pp. 1739–1752, Jun. 2011, ISSN: 0018-9464, 1941-0069. DOI: 10.1109/TMAG.2011.2113396.

[110] J. D. Jackson, *Classical Electrodynamics*, 3rd. New York: Wiley, 1998, p. 832, ISBN: 978-0-471-30932-1.

[111] E. P. Furlani, *Permanent magnet and electromechanical devices: materials, analysis, and applications*, 1st, ser. Academic Press series in electromagnetism. San Diego, Calif: Academic, 2001, ISBN: 978-0-12-269951-1.

Bibliography

[112]   A. Caciagli, R. J. Baars, A. P. Philipse, and B. W. Kuipers, "Exact expression for the magnetic field of a finite cylinder with arbitrary uniform magnetization", *Journal of Magnetism and Magnetic Materials*, vol. 456, pp. 423–432, Jun. 2018, ISSN: 03048853. DOI: 10.1016/j.jmmm.2018.02.003.

[113]   K. J. Meessen, "Electromagnetic Fields and Interactions in 3D Cylindrical Structures: Modeling and Application", PhD thesis, Technische Universiteit Eindhoven, 2012, p. 238.

[114]   B. L. J. Gysen, K. J. Meessen, J. J. H. Paulides, and E. A. Lomonova, "General Formulation of the Electromagnetic Field Distribution in Machines and Devices Using Fourier Analysis", *IEEE Transactions on Magnetics*, vol. 46, no. 1, pp. 39–52, Jan. 2010, ISSN: 0018-9464. DOI: 10.1109/TMAG.2009.2027598.

[115]   Y. N. Zhilichev, "Analytic solutions of magnetic field problems in slotless permanent magnet machines", *COMPEL - The international journal for computation and mathematics in electrical and electronic engineering*, vol. 19, no. 4, pp. 940–955, Dec. 2000, ISSN: 0332-1649. DOI: 10.1108/03321640010347385.

[116]   J. Luomi, C. Zwyssig, A. Looser, and J. W. Kolar, "Efficiency Optimization of a 100-W, 500 000-rpm Permanent-Magnet Machine Including Air Friction Losses", New Orleans, LA, USA: IEEE Industry Applications Annual Meeting, Oct. 2007, pp. 861–868, ISBN: 978-1-4244-1259-4 978-1-4244-1260-0. DOI: 10.1109/07IAS.2007.135.

[117]   S. Jumayev, J. J. H. Paulides, K. Boynov, J. Pyrhönen, and E. A. Lomonova, "3-D Analytical Model of Helical Winding PM Machines Including Rotor Eddy Currents", *IEEE Transactions on Magnetics*, vol. 52, no. 5, pp. 1–8, May 2016, ISSN: 0018-9464. DOI: 10.1109/TMAG.2015.2512987.

[118]   J.-M. Seo, J.-H. Kim, I.-S. Jung, and H.-K. Jung, "Design and Analysis of Slotless Brushless DC Motor", *IEEE Transactions on Industry Applications*, vol. 47, no. 2, pp. 730–735, Mar. 2011, ISSN: 0093-9994. DOI: 10.1109/TIA.2010.2091611.

[119]   G. Burnand, A. Thabuis, D. M. Araujo, and Y. Perriard, "Novel Optimized Shape and Topology for Slotless Windings in BLDC Machines", *IEEE Transactions on Industry Applications*, vol. 56, no. 2, pp. 1275–1283, Mar. 2020, ISSN: 0093-9994. DOI: 10.1109/TIA.2019.2956717.

[120]   S. Heindel, "Unbalance and Resonance Elimination on General Rotors with Active Bearings", PhD thesis, Technische Universität Darmstadt, 2017, p. 161.

[121]   Celeroton AG, *White Paper: Towards optical switches based on high-speed magnetic bearing motor CM-AMB-400*. [Online]. Available: https://www.celeroton.com/fileadmin/user_upload/technologie/tech-blog/Celeroton_White_Paper_Magnetic_Bearing_Motor.pdf.

[122]   C. R. Knospe, R. Hope, S. J. Fedigan, and R. D. Williams, "Experiments in the control of unbalance response using magnetic bearings", *Mechatronics*, vol. 5, no. 4, pp. 385–400, Jun. 1995, ISSN: 09574158. DOI: 10.1016/0957-4158(95)00015-W.

[123] R. Herzog, P. Buhler, C. Gahler, and R. Larsonneur, "Unbalance compensation using generalized notch filters in the multivariable feedback of magnetic bearings", *IEEE Transactions on Control Systems Technology*, vol. 4, no. 5, pp. 580–586, 1996, ISSN: 10636536. DOI: 10.1109/87.531924.

[124] Q. Chen, G. Liu, and B. Han, "Unbalance vibration suppression for AMBs system using adaptive notch filter", *Mechanical Systems and Signal Processing*, vol. 93, pp. 136–150, Sep. 2017, ISSN: 08883270. DOI: 10.1016/j.ymssp.2017.02.009.

[125] L. Gong and C. Zhu, "Vibration Suppression for Magnetically Levitated High-speed Motors Based on Polarity Switching Tracking Filter and Disturbance Observer", *IEEE Transactions on Industrial Electronics*, pp. 1–1, 2020, ISSN: 0278-0046. DOI: 10.1109/TIE.2020.2989710.

[126] M. Wagner, S. Airey, G. Piret, and M. P. Le, "European Space Agency (ESA): New Reaction Wheel Characterisation Test Facility (RCF)", in *35th AAS Guidance and Control Conference*, Breckenridge, Colorado, 2012.

[127] M. Batista, "Elfun18 – A collection of MATLAB functions for the computation of elliptic integrals and Jacobian elliptic functions of real arguments", *SoftwareX*, vol. 10, p. 100 245, Jul. 2019, ISSN: 23527110. DOI: 10.1016/j.softx.2019.100245.

Curriculum Vitae

Guzmán Borque Gallego

1110 Morges, Switzerland
✉ gborquegallego@gmail.com
Born on September 27, 1992

Education

Now - 2016	**On-going Ph.D. in Robotics, Control, and Intelligent Systems**, *Integrated Actuators Laboratory (LAI) - Swiss Federal Institude of Technology (EPFL)*.
2016 - 2014	**Master in Industrial Engineering**, *Escuela Técnica Superior de Ingenieros Industriales - Technical University of Madrid (UPM)*.
2014 - 2010	**Bachelor in Industrial Engineering**, *Escuela Técnica Superior de Ingenieros Industriales - Technical University of Madrid (UPM)*.

Professional Experience

2020 - 2016	**Ph.D. Student**, *CSEM SA*, Neuchâtel, Switzerland.
2016	**R&D Intern Engineer**, *CSEM SA*, Neuchâtel, Switzerland.
2014 - 2013	**R&D Intern Engineer**, *CAR (UPM-CSIC)*, Madrid, Spain.
2013	**Intern Engineer**, *Bull SAS - Atos SE*, Paris, France.

Publications

Journal Articles

1. G. Borque Gallego, L. Rossini, E. Onillon, T. Achtnich, C. Zwyssig, R. Seiler, D. Martins Araujo, and Y. Perriard, "On-line micro-vibration measurement method for Lorentz-type magnetic-bearing space actuators," *Mechatronics*, vol. 64, p. 102 283, Dec. 2019.

2. Under Review: G. Borque Gallego, L. Rossini, T. Achtnich, D. Martins Araujo, and Y. Perriard, "Three-Dimensional Force and Torque Models of Slotless Magnetic Bearing Machines," *IEEE/ASME Transactions on Mechatronics*, May 2020.

3. Under Review: G. Borque Gallego, L. Rossini, T. Achtnich, D. Martins Araujo, and Y. Perriard, "Efficiency Optimisation and Vibration Reduction in Slotless Magnetic Bearing Machines," *IEEE/ASME Transactions on Industry Applications, Special Issue on Magnetically Levitated Motor Systems*, Nov. 2020.

4. Under Review: G. Borque Gallego, L. Rossini, T. Achtnich, D. Martins Araujo, and Y. Perriard, "Novel Generalised Notch Filter for Harmonic Vibration Suppression in Magnetic Bearing Systems," *IEEE/ASME Transactions on Industry Applications, Special Issue on Magnetically Levitated Motor Systems*, Dec. 2020.

Conference Papers

1. G. Borque Gallego, L. Rossini, E. Onillon, and A. Karimi, "Linear Parameter-Varying Kalman Filter for angular velocity estimation of a reaction sphere actuator for satellite attitude control," in *2017 IEEE International Conference on Advanced Intelligent Mechatronics (AIM)*, Munich, Germany, Jul 2017, pp. 352–357.

2. G. Borque Gallego, L. Rossini, T. Achtnich, C. Zwyssig, D. Martins Araujo, and Y. Perriard, "Force Analysis of a Slotless Lorentz-Type Active Magnetic Bearing Actuator," in *21st International Conference on Electrical Machines and Systems (ICEMS)*, Jeju, Korea, Oct. 2018, pp. 75–80.

3. G. Borque Gallego, L. Rossini, T. Achtnich, C. Zwyssig, D. Martins Araujo, and Y. Perriard, "Force and Torque Model of Iron-less Passive Magnetic Bearing Structures," in *2019 IEEE International Electric Machines and Drives Conference (IEMDC)*, San Diego, CA, United States, May 2019, pp. 507–514.

4. G. Borque Gallego, L. Rossini, T. Achtnich, C. Zwyssig, D. Martins Araujo, and Y. Perriard, "Magnetic Bearing Reaction Wheel Micro-Vibration Signature Prediction," in *18th European Space Mechanisms and Tribology Symposium*, Munich, Germany, Sep. 2019.